Enhancing photodynamic therapy of refractory solid cancers

Weijer, R.

Publication date
2017
Document Version
Final published version
License
Other

Enhancing photodynamic therapy of refractory solid cancers

Ruud Weijer

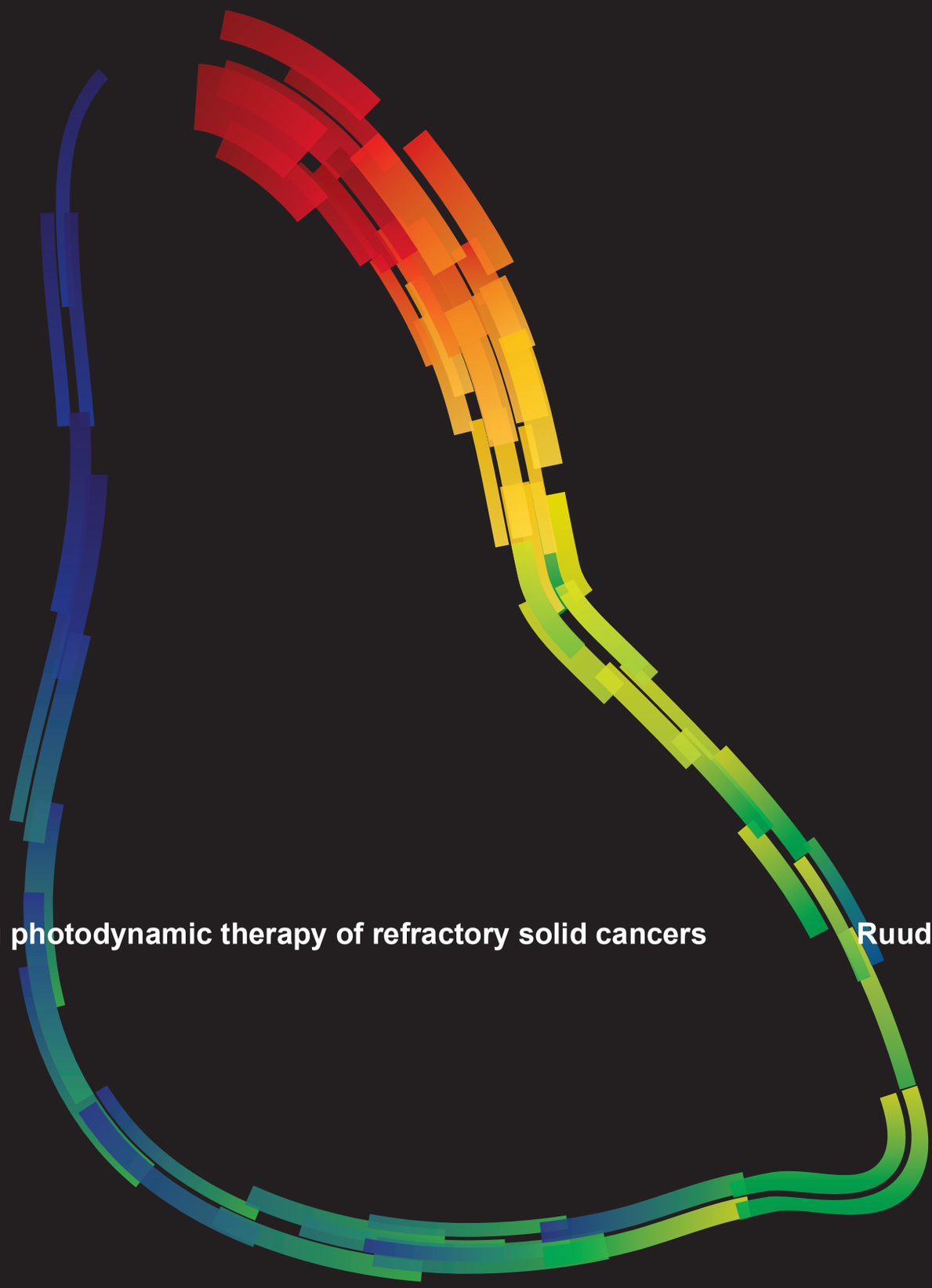

Enhancing photodynamic therapy of refractory solid cancers

Ruud Weijer

ENHANCING PHOTODYNAMIC THERAPY OF REFRACTORY SOLID CANCERS

Ruud Weijer

Enhancing photodynamic therapy of refractory solid cancers
Ruud Weijer
PhD thesis, University of Amsterdam, the Netherlands

ISBN: 978-94-6233-534-9
Layout and cover design: Ruud Weijer
Printing: Gildeprint

The research described in this thesis was sponsored by Stichting Nationaal Fonds Tegen Kanker, Amsterdam, the Netherlands; the Phospholipid Research Center, Heidelberg, Germany; and Roba Metals BV, IJsselstein, the Netherlands.

ENHANCING PHOTODYNAMIC THERAPY OF REFRACTORY SOLID CANCERS

ACADEMISCH PROEFSCHRIFT

ter verkrijging van de graad van doctor

aan de Universiteit van Amsterdam

op gezag van de Rector Magnificus

prof. dr. ir. K.I.J. Maex

ten overstaan van een door het College voor Promoties ingestelde commissie,

in het openbaar te verdedigen in de Agnietenkapel

op vrijdag 24 februari 2017, te 14:00 uur

door Ruud Weijer

geboren te Coevorden

Promotiecommissie:

Promotor:

Prof. dr. T.M. van Gulik	Universiteit van Amsterdam

Copromotor:

Dr. M. Heger	Universiteit van Amsterdam

Overige leden:

Dr. E.A.J. Rauws	Universiteit van Amsterdam
Prof. dr. E.F. Eldering	Universiteit van Amsterdam
Prof. dr. H.W.M. van Laarhoven	Universiteit van Amsterdam
Dr. S.A. Bonnet	Universiteit Leiden
Prof. dr. ir. H.J.C.M. Sterenborg	Universiteit van Amsterdam
Prof. dr. ir. C. Ince	Erasmus Medisch Centrum Rotterdam

Faculteit der Geneeskunde

Table of contents

Chapter 1 **7**
Introduction

Chapter 2 **15**
Enhancing photodynamic therapy of refractory solid cancers: Combining second-generation photosensitizers with multi-targeted liposomal delivery
Journal of Photochemistry and Photobiology C: Photochemistry Reviews (2015)

Chapter 3 **71**
Low-power photodynamic therapy induces survival signaling in perihilar cholangiocarcinoma cells
BMC Cancer (2015)

Chapter 4 **101**
Multi-OMIC profiling of survival and metabolic signaling networks in cells subjected to photodynamic therapy
Cellular and Molecular Life Sciences (2016)

Chapter 5 **145**
Inhibition of hypoxia inducible factor 1 and topoisomerase with acriflavine sensitizes perihilar cholangiocarcinomas to photodynamic therapy
Oncotarget (2015)

Chapter 6 **171**
Photodynamic therapy with liposomal zinc phthalocyanine and tirapazamine increases tumor cell death via DNA damage
Journal of Biomedical Nanotechnology (2016)

Chapter 7 **199**
Summarizing discussion and future perspectives

Appendices **203**
Summary & Nederlandse samenvatting
Portfolio
List of publications
Dankwoord
Biography

Chapter 1

Introduction

1. Background

Cancer is a global health problem and poses a significant economic burden to society as marked by an incidence of 14.1 million new cases and 8.2 million cancer-associated deaths in 2012 [1]. These numbers are likely to increase over the coming years as a result of ageing and an increased exposure to risk factors [1]. Typically, cancer patients are treated with surgery, chemotherapy, radiotherapy, or combinations thereof. However, these therapies are often associated with severe side effects and high treatment costs. In case conventional therapies fail, alternative therapies such as photodynamic therapy (PDT) may be applied.

PDT is a non-to-minimally invasive treatment modality that comprises the administration of a photosensitizer and illumination of the photosensitizer-replete tumor with laser light (**Fig. 1A**). The activated photosensitizer reacts with molecular oxygen that causes the local production of reactive oxygen species, including highly deleterious singlet oxygen in the photosensitizer-replete and illuminated tissue [2]. This creates a state of oxidative stress in the tumor, which leads to tumor cell death, tumor (micro)vasculature shutdown, thereby depleting the tumor of oxygen and nutrients, and triggers an anti-tumor immune response (reviewed in [3]). All these

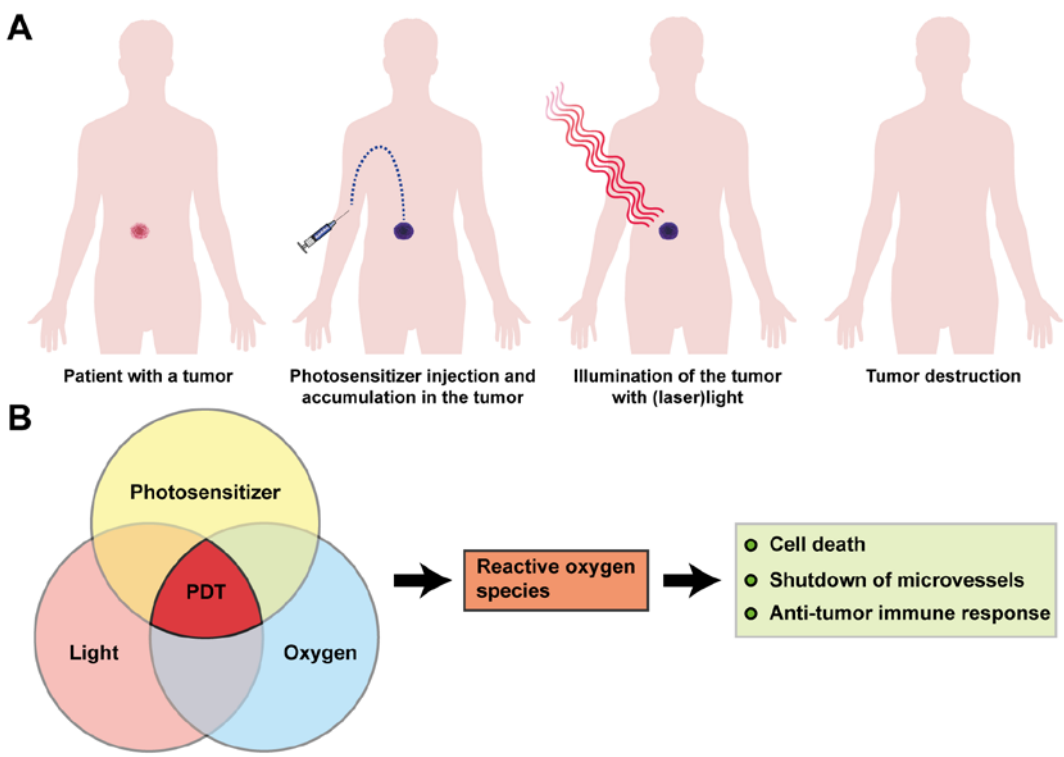

Fig. 1. Principles of photodynamic therapy (PDT). (**A**) PDT comprises the administration of photosensitizer, its accumulation in the tumor, followed by the local illumination of the tumor with light. (**B**) PDT requires three basic elements (photosensitizer + light + oxygen) to locally generate reactive oxygen species and result in tumor removal.

factors contribute to tumor removal (**Fig. 1B**).

2. Clinical status quo of photodynamic therapy

PDT is currently used for the treatment of a variety of tumor types, including cancers of the head-and-neck area, early-stage esophageal cancers, Barrett's esophagus, and skin cancers, all of which show high complete response rates [4-7] (**Fig. 2**). However, some tumor types only moderately respond to PDT, including superficial urothelial carcinoma [8], nasopharyngeal carcinoma [9], and perihilar cholangiocarcinoma [10] (**Fig. 2**).

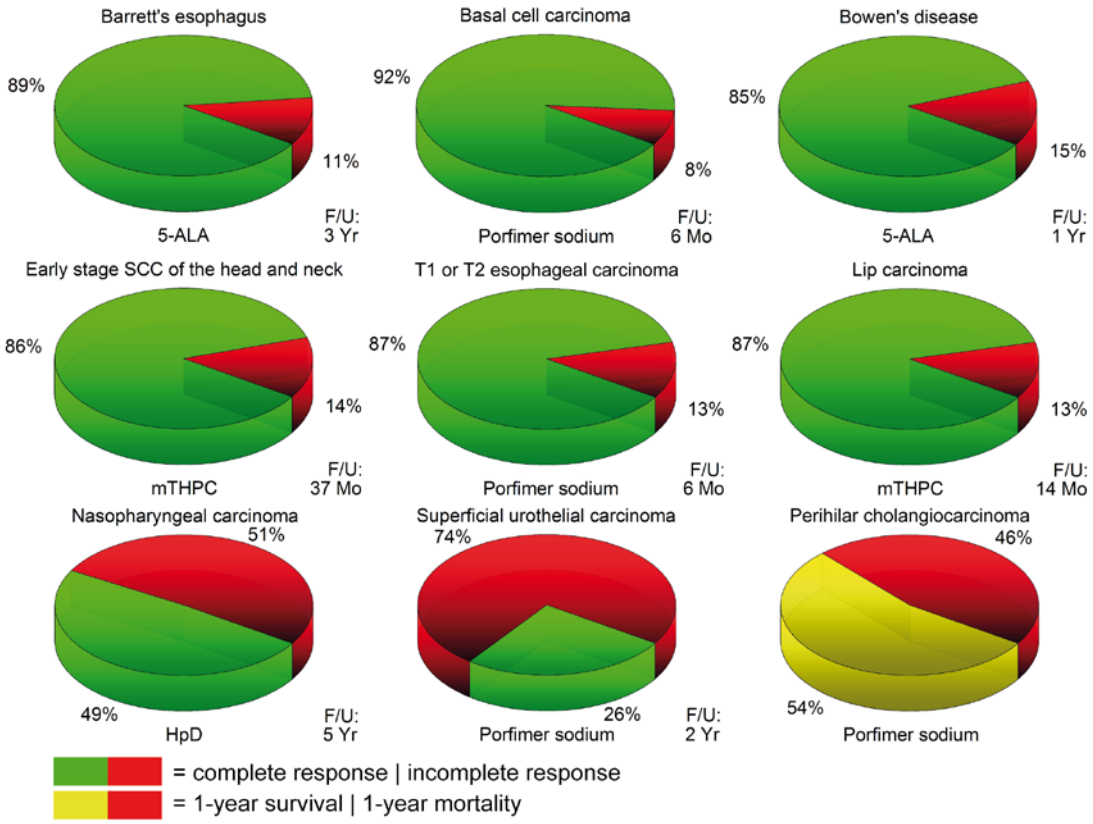

Fig. 2. Clinical PDT outcomes plotted for various types of solid cancer. The cancer subtype is indicated at the top of the pie chart and the corresponding PS is shown at the bottom. The mean percentage of patients with a complete response to PDT (*i.e.*, complete removal of the tumor) at follow up (F/U) is indicated in green, whereas the percentage of patients with an incomplete response to PDT is indicated in red (*i.e.*, residual tumor present after PDT at the time of follow up). For non-resectable perihilar cholangiocarcinoma, the yellow and red slices represent the 1-year survival and the 1-year mortality, respectively. Abbreviations: 5-ALA, 5-aminolevulinic acid; SCC, squamous cell carcinoma; mTHPC, m-tetrahydroxyphenylchlorin; T1/T2, tumor stage 1/2; HpD, hematoporphyrin derivative. Data compiled from refs [11-24].

2.1 Photodynamic therapy for perihilar cholangiocarcinoma

The work in thesis is mainly focused on optimizing PDT for the treatment of perihilar cholangiocarcinoma patients. Perihilar cholangiocarcinoma is a tumor that arises at the confluence of the common hepatic bile ducts and is often diagnosed at a late stage, at a point where only 20-30% of the patients are eligible to undergo resection [25]. The remainder of the patients will enter a palliative trajectory, inasmuch as there are no curative therapies available for non-resectable perihilar cholangiocarcinoma patients. Typically, a stent is placed in the bile ducts to restore the bile flow and to relieve patients from jaundice. However, these patients generally have a poor survival as marked by a median survival of 6-9 months post-diagnosis (stenting + palliative chemotherapy) [26]. Promising results have been achieved when stenting was combined with PDT, which resulted in a median survival of 21 months [26]. Unfortunately, PDT is not able to cure these patients and conventional PDT strategies are associated with photosensitivity issues that may last up to three months after photosensitizer administration. This may be due to long clearance times and non-specific accumulation of photosensitizer in the skin [27]. After exposure to (day)light, the photochemical reaction in the skin may produce erythema, blisters, and burn-like wounds (**Fig. 3**). The phototoxicity poses a clinical problem, especially in cancer patients that have a short life expectancy.

Driven by these promising results and a clear medical need for novel therapies, this thesis is focused on the development of a novel PDT strategy for the treatment of perihilar cholangiocarcinoma patients.

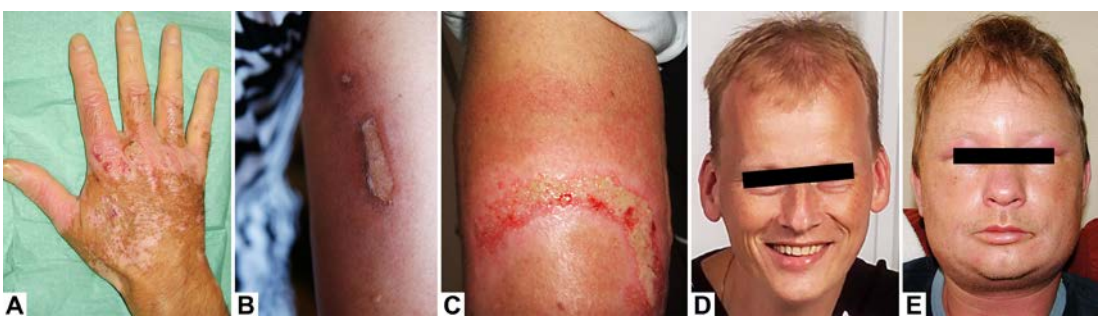

Fig. 3. Clinical phototoxicity cases in non-resectable biliary cancer patients who had undergone PDT with intravenously administered Photofrin (porfimer sodium) or Foscan (mTHPC) as a last-line treatment (palliative). Phototoxicity was most prominent in regions most susceptible to light exposure as well as the infusion site. (**A**) Photo of a hand made after healing of severe burns with blisters, 3 months after injection of Photofrin in the vena cubiti. (**B**) and (**C**) Skin lesions both 2 months after intravenous injection of mTHPC, which ultimately healed by scarring (not shown). (**D**) and (**E**) Patient before (**D**) and 3 months after Photofrin-PDT (**E**) following a visit to an amusement park. The patient was wearing light-protective clothing, including a hat, but still experienced a severe photoallergic reaction in the face as evidenced by the degree of swelling. All patients were included in a clinical trial that had been approved by the institutional review board of the Academic Medical Center, University of Amsterdam (trial number NCT01016002). The trial was discontinued after inclusion of 5 patients due to the severity of adverse events. Explicit informed consent for the publication of the images in (**D**) and (**E**) was provided in writing by the patient's spouse to Michal Heger.

3. Enhancing photodynamic therapy

In an attempt to reduce photosensitivity issues and to increase therapeutic efficacy, the work in this thesis has focused on the development of a photosensitizer multi-drug delivery platform. Conventional, clinically approved photosensitizers such as porfimer sodium (first-generation photosensitizer) and 5-aminolevulinic acid (second-generation photosensitizer) only moderately absorb light and exhibit an absorption peak that lies outside the therapeutic window (650 – 850 nm [2]). Photosensitizers that have a absorption peak in the therapeutic window suffer less from absorption by biological compounds such as hemoglobin and melanin that may limit light penetration into tissues [3]. As such, the experimental second-generation photosensitizer zinc phthalocyanine (ZnPC) was selected, which is known to have a high molar extinction coefficient (2.74×10^5 M-1 cm-1) in the red spectrum and a main absorption peak at 674 nm [28]. Also, ZnPC and other metallated phthalocyanines appear to be efficient singlet oxygen generators that are relatively non-toxic in the ground state [3].

In addition to photosensitizers with improved spectral properties, targeting could improve the photosensitizer pharmacokinetics and result in higher photosensitizer concentration in the target tissue and hence increase PDT efficacy. Photosensitizers have been incorporated in various targeting structures that include low-density lipoproteins, micelles, liposomes, solid lipid nanoparticles, gold nanoparticles, quantum dots, polymeric micelles, and polymeric nanoparticles (reviewed in [3]), which could be classified as third-generation photosensitizers. The work described in this thesis is focused on liposomes inasmuch as liposomes can be employed to encapsulate both hydrophobic and hydrophilic agents, are relatively inexpensive, have a high payload, and are relatively non-toxic. Importantly, liposomes can also be modified to impart tumor targeting properties [29]. This knowledge was utilized to develop three distinct liposomal formulations that are targeted to the pharmacologically most relevant tumor areas, which include tumor cells, tumor interstitial spaces, and tumor endothelium (described in **Chapter 2**, **Fig. 4**). In brief, all liposomal formulations are coated with polyethylene glycol (PEG) to ensure long circulation time and deter clearance by cells of the mononuclear phagocyte system [30]. While interstitially-targeted liposomes (ITLs) are passively targeted to the tumor stroma by means of the enhanced permeability and retention effect [31, 32], tumor endothelium-targeting liposomes (ETLs) have a positively charged surface that is believed to associate with the more negatively charged tumor endothelium [33]. Lastly, tumor-targeting liposomes (TTLs) bear a tumor-recognizing domain (*i.e.*, nanobody) on their surface to ensure binding to a surface receptor that is overexpressed by tumor cells.

Lastly, as a result of a sublethal fluences generated in the more distal regions of the illuminated tumor, tumor cells may activate survival pathways that result in

ineffective tumor removal. An extensive overview of the behavior of cells to PDT can be found in [34]. We hypothesized that inhibition of survival signaling following PDT may improve therapeutic efficacy and ultimately tumor recurrence. Our multi-targeting drug delivery platform may be used to both target the photosensitizer as well as inhibitors of survival pathways to the tumor (fourth-generation photosensitizer).

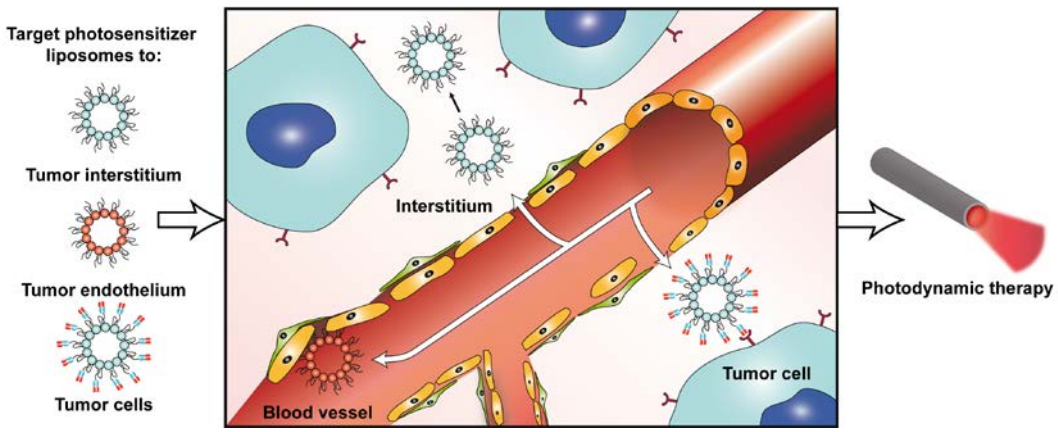

Fig. 4. Multi-targeting photosensitizer delivery platform for PDT. The PDT modality consists of three distinct liposomal formulations that are targeted to the tumor interstitial spaces (top), tumor endothelium (bottom left), and tumor cells (bottom right). After photosensitizer accumulation, the tumor area is locally illuminated with light to activate the photosensitizer.

4. Aim and outline of the thesis

The aim of this thesis was to develop a PDT strategy that could be employed for the treatment of perihilar cholangiocarcinoma based on third- or fourth-generation photosensitizers. We attempted this by (1) incorporating a photosensitizer with improved properties into a multi-targeting liposomal delivery system, (2) analyzing the molecular and cellular responses of tumor cells to PDT, and (3) pharmacologically intervening in survival programs that are activated by tumor cells after PDT.

The basis for this thesis is provided in **Chapter 2**, as it describes the rationale to use the experimental photosensitizer ZnPC in combination with a multi-targeting approach. In an attempt to gain insight into the response of PDT-recalcitrant tumor cells to PDT, perihilar cholangiocarcinoma cells were treated with PDT using ZnPC-encapsulating ITLs and the activation of survival signaling was assessed using transcriptomics (**Chapter 3**). The latter study was followed up using a multi-omic approach, as a panel of tumor-associated cells were subjected to PDT using ZnPC-encapsulating ETLs and analyzed by transcriptomics, of which perihilar cholangiocarcinoma cells were also analyzed by a proteomic- and metabolomic-based approach (**Chapter 4**). The knowledge obtained in the previous chapters was exploited in **Chapters 5** and **6** to make tumor cells more vulnerable to PDT. **Chapter 5** reveals

that combination treatment of a HIF-1 inhibitor with PDT hypersensitizes perihilar cholangiocarcinoma cells to PDT and **Chapter 6** demonstrates that the combinatorial use of the hypoxic cytotoxin tirapazamine with PDT significantly improved efficacy.

References

1. Torre LA, Bray F, Siegel RL, Ferlay J, Lortet-Tieulent J, Jemal A: Global cancer statistics, 2012. CA Cancer J Clin 2015, 65(2):87-108.
2. Plaetzer K, Krammer B, Berlanda J, Berr F, Kiesslich T: Photophysics and photochemistry of photodynamic therapy: fundamental aspects. Lasers Med Sci 2009, 24(2):259-268.
3. Weijer R, Broekgaarden M, Kos M, van Vught R, Rauws EA, Breukink E, van Gulik TM, Storm G, Heger M: Enhancing photodynamic therapy of refractory solid cancers: combining second-generation photosensitizers with multi-targeted liposomal delivery. Journal of Photochemistry and Photobiology C: Photochemistry Reviews 2015, 23:103-131.
4. de Visscher SA, Melchers LJ, Dijkstra PU, Karakullukcu B, Tan IB, Hopper C, Roodenburg JL, Witjes MJ: mTHPC-mediated photodynamic therapy of early stage oral squamous cell carcinoma: a comparison to surgical treatment. Ann Surg Oncol 2013, 20(9):3076-3082.
5. Sibille A, Lambert R, Souquet JC, Sabben G, Descos F: Long-term survival after photodynamic therapy for esophageal cancer. Gastroenterology 1995, 108(2):337-344.
6. Mackenzie GD, Dunn JM, Selvasekar CR, Mosse CA, Thorpe SM, Novelli MR, Bown SG, Lovat LB: Optimal conditions for successful ablation of high-grade dysplasia in Barrett's oesophagus using aminolaevulinic acid photodynamic therapy. Lasers Med Sci 2009, 24(5):729-734.
7. Foley P, Freeman M, Menter A, Siller G, El-Azhary RA, Gebauer K, Lowe NJ, Jarratt MT, Murrell DF, Rich P et al: Photodynamic therapy with methyl aminolevulinate for primary nodular basal cell carcinoma: results of two randomized studies. Int J Dermatol 2009, 48(11):1236-1245.
8. Nseyo UO, DeHaven J, Dougherty TJ, Potter WR, Merrill DL, Lundahl SL, Lamm DL: Photodynamic therapy (PDT) in the treatment of patients with resistant superficial bladder cancer: a long-term experience. J Clin Laser Med Surg 1998, 16(1):61-68.
9. Sun ZQ: Photodynamic therapy of nasopharyngeal carcinoma by argon or dye laser - An analysis of 137 cases. Zhonghua Zhong Liu Za Zhi 1992, 14(4):290-292.
10. Wiedmann M, Berr F, Schiefke I, Witzigmann H, Kohlhaw K, Mossner J, Caca K: Photodynamic therapy in patients with non-resectable hilar cholangiocarcinoma: 5-year follow-up of a prospective phase II study. Gastrointest Endosc 2004, 60(1):68-75.
11. Benson RC, Jr.: Laser photodynamic therapy for bladder cancer. Mayo ClinProc 1986, 61(11):859-864.
12. Copper MP, Tan IB, Oppelaar H, Ruevekamp MC, Stewart FA: Meta-tetra(hydroxyphenyl)chlorin photodynamic therapy in early-stage squamous cell carcinoma of the head and neck. ArchOtolaryngolHead Neck Surg 2003, 129(7):709-711.
13. Dougherty TJ: Photodynamic therapy (PDT) of malignant tumors. Crit RevOncolHematol 1984, 2(2):83-116.
14. Dumoulin FL, Gerhardt T, Fuchs S, Scheurlen C, Neubrand M, Layer G, Sauerbruch T: Phase II study of photodynamic therapy and metal stent as palliative treatment for nonresectable hilar cholangiocarcinoma. Gastrointest Endosc 2003, 57(7):860-867.
15. Kubler AC, de CJ, Hopper C, Leonard AG, Putnam G: Treatment of squamous cell carcinoma of the lip using Foscan-mediated photodynamic therapy. IntJOral MaxillofacSurg 2001, 30(6):504-509.
16. Mackenzie GD, Dunn JM, Selvasekar CR, Mosse CA, Thorpe SM, Novelli MR, Bown SG, Lovat LB: Optimal conditions for successful ablation of high-grade dysplasia in Barrett's oesophagus using aminolaevulinic acid photodynamic therapy. Lasers MedSci 2009, 24(5):729-734.
17. Morales A: Treatment of superficial bladder cancer. CanMedAssocJ 1980, 122(10):1133-1138.
18. Morton CA, Whitehurst C, Moseley H, McColl JH, Moore JV, Mackie RM: Comparison of photodynamic therapy with cryotherapy in the treatment of Bowen's disease. BrJDermatol 1996, 135(5):766-771.
19. Nseyo UO, Dougherty TJ, Boyle DG, Potter WR, Wolf R, Huben R, Pontes JE: Whole bladder photodynamic therapy for transitional cell carcinoma of bladder. Urology 1985, 26(3):274-280.
20. Rosenberg SJ, Williams RD: Photodynamic therapy of bladder carcinoma. UrolClinNorth Am 1986, 13(3):435-444.
21. Sibille A, Lambert R, Souquet JC, Sabben G, Descos F: Long-term survival after photodynamic therapy for esophageal cancer. Gastroenterology 1995, 108(2):337-344.
22. Sun ZQ: Photodynamic therapy of nasopharyngeal carcinoma by argon or dye laser - An analysis of 137 cases. Zhonghua ZhongLiu Za Zhi 1992, 14(4):290-292.
23. Wiedmann M, Berr F, Schiefke I, Witzigmann H, Kohlhaw K, Mossner J, Caca K: Photodynamic therapy in patients with non-resectable hilar cholangiocarcinoma: 5-year follow-up of a prospective phase II study. GastrointestEndosc 2004, 60(1):68-75.
24. Zeitouni NC, Shieh S, Oseroff AR: Laser and photodynamic therapy in the management of cutaneous malignancies. ClinDermatol 2001, 19(3):328-338.

25. Ruys AT, van Haelst S, Busch OR, Rauws EA, Gouma DJ, van Gulik TM: Long-term survival in hilar cholangiocarcinoma also possible in unresectable patients. World J Surg 2012, 36(9):2179-2186.
26. Lee TY, Cheon YK, Shim CS: Current status of photodynamic therapy for bile duct cancer. Clin Endosc 2013, 46(1):38-44.
27. Bellnier DA, Greco WR, Loewen GM, Nava H, Oseroff AR, Dougherty TJ: Clinical pharmacokinetics of the PDT photosensitizers porfimer sodium (Photofrin), 2-[1-hexyloxyethyl]-2-devinyl pyropheophorbide-a (Photochlor) and 5-ALA-induced protoporphyrin IX. Lasers Surg Med 2006, 38(5):439-444.
28. Broekgaarden M, de Kroon AI, Gulik TM, Heger M: Development and in vitro proof-of-concept of interstitially targeted zinc- phthalocyanine liposomes for photodynamic therapy. Curr Med Chem 2014, 21(3):377-391.
29. Nogueira E, Gomes AC, Preto A, Cavaco-Paulo A: Design of liposomal formulations for cell targeting. Colloids Surf B Biointerfaces 2015, 136:514-526.
30. Harding JA, Engbers CM, Newman MS, Goldstein NI, Zalipsky S: Immunogenicity and pharmacokinetic attributes of poly(ethylene glycol)-grafted immunoliposomes. Biochimica et Biophysica Acta-Biomembranes 1997, 1327(2):181-192.
31. Bovis MJ, Woodhams JH, Loizidou M, Scheglmann D, Bown SG, MacRobert AJ: Improved in vivo delivery of m-THPC via pegylated liposomes for use in photodynamic therapy. Journal of Controlled Release 2012, 157(2):196-205.
32. Buchholz J, Kaser-Hotz B, Khan T, Bleyl CR, Melzer K, Schwendener RA, Roos M, Walt H: Optimizing photodynamic therapy: In vivo pharmacokinetics of liposomal meta-(tetrahydroxyphenyl)chlorin in feline squamous cell carcinoma. Clinical Cancer Research 2005, 11(20):7538-7544.
33. Thurston G, Mclean JW, Rizen M, Baluk P, Haskell A, Murphy TJ, Hanahan D, McDonald DM: Cationic liposomes target angiogenic endothelial cells in tumors and chronic inflammation in mice. Journal of Clinical Investigation 1998, 101(7):1401-1413.
34. Broekgaarden M, Weijer R, van Gulik TM, Hamblin MR, Heger M: Tumor cell survival pathways activated by photodynamic therapy: a molecular basis for pharmacological inhibition strategies. Cancer Metastasis Rev 2015, 34(4):643-690.

Chapter 2

Enhancing photodynamic therapy of refractory solid cancers: Combining second-generation photosensitizers with multi-targeted liposomal delivery

Journal of Photochemistry and Photobiology C: Photochemistry Reviews (2015)

RUUD WEIJER
MANS BROEKGAARDEN
MILAN KOS
REMKO VAN VUGHT
ERIK A.J. RAUWS
EEFJAN BREUKINK
THOMAS M. VAN GULIK
GERT STORM
MICHAL HEGER

Abstract

Contemporary photodynamic therapy (PDT) for the last-line treatment of refractory cancers such as nasopharyngeal carcinomas, superficial recurrent urothelial carcinomas, and non-resectable extrahepatic cholangiocarcinomas yields poor clinical outcomes and may be associated with adverse events. This is mainly attributable to three factors: (1) the currently employed photosensitizers exhibit suboptimal spectral properties, (2) the route of administration is associated with unfavorable photosensitizer pharmacokinetics, and (3) the upregulation of survival pathways in tumor cells may impede cell death after PDT. Consequently, there is a strong medical need to improve PDT of these recalcitrant cancers. An increase in PDT efficacy and reduction in clinical side-effects may be achieved by encapsulating second-generation photosensitizers into liposomes that selectively target to pharmacologically important tumor locations, namely tumor cells, tumor endothelium, and tumor interstitial spaces. In addition to addressing the drawbacks of clinically approved photosensitizers, this review addresses the most relevant pharmacological aspects that dictate clinical outcome, including photosensitizer biodistribution and intracellular localization in relation to PDT efficacy, the mechanisms of PDT-induced cell death, and PDT-induced antitumor immune responses. Also, a rationale is provided for the use of second-generation photosensitizers such as diamagnetic phthalocyanines (*e.g.*, zinc or aluminum phthalocyanine), which exhibit superior photophysical and photochemical properties, in combination with a multi-targeted liposomal photosensitizer delivery system. The rationale for this PDT platform is corroborated by preliminary experimental data and proof-of-concept studies. Finally, a summary of the different nanoparticulate photosensitizer delivery systems is provided followed by a section on phototriggered release mechanisms in the context of liposomal photosensitizer delivery systems.

Keywords
Cancer, drug delivery, metallated phthalocyanines, photodynamic therapy, photosensitizers, reactive oxygen species, singlet oxygen, tumor targeting

1. Introduction

Photodynamic therapy (PDT) is a minimally-to-noninvasive treatment modality for numerous types of solid cancers. PDT involves the systemic administration of a photosensitizer (PS), accumulation of the PS in the tumor, and irradiation of the tumor with light of a wavelength that is well absorbed by the PS. Resonantly irradiated PSs undergo intersystem crossing from the singlet state to the triplet state, from which either an electron is transferred (type I photochemical reaction) or energy is donated (type II photochemical reaction) to molecular oxygen [1]. Type I reactions result in the formation of superoxide anion ($O_2^{\bullet -}$) and, in biological systems, derivative reactive oxygen and nitrogen species (ROS and RNS, respectively) [2], whereas type II reactions yield singlet oxygen ($^1O_2$). ROS/RNS are capable of (per) oxidizing biomolecules and ultimately induce tumor cell death by causing shutdown of intratumoral vasculature, tumor cell death, and an anti-tumor immune response (**Fig. 1**) [3, 4].

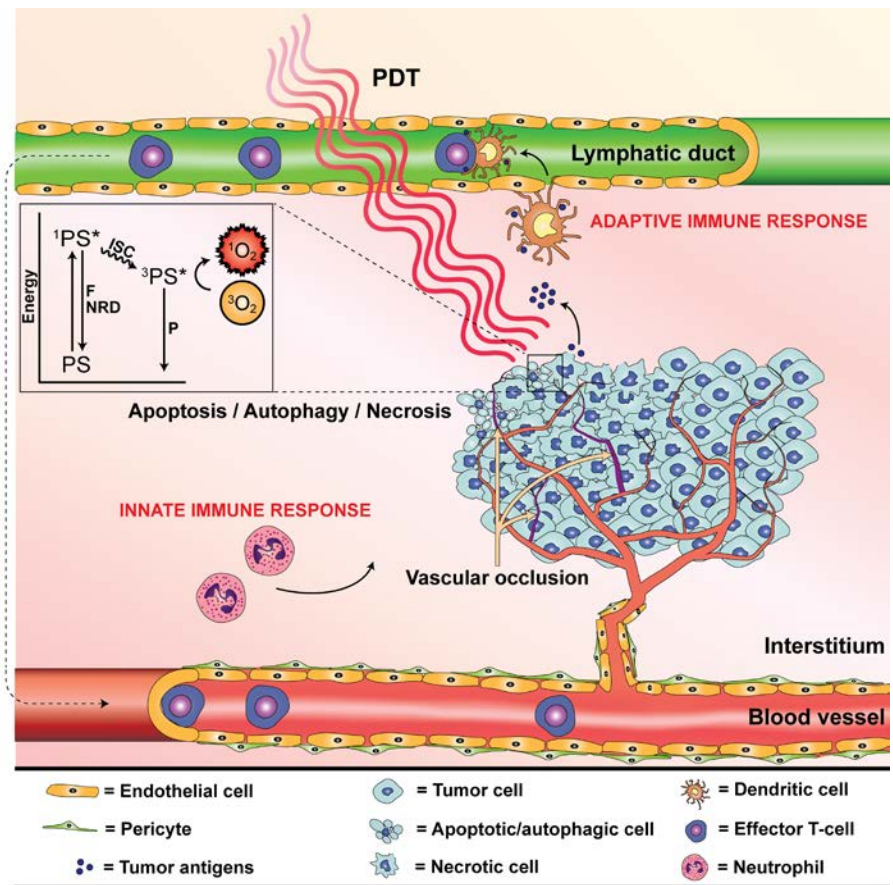

Fig. 1. Photophysical and biological mechanisms of photodynamic therapy (PDT). Tumor-replete photosensitizer (PS) molecules are activated by (laser) light to an excited singlet state photosensitizer ($^1PS^*$). The $^1PS^*$ can return to the ground state (PS) by emitting fluorescence (F) or by non-radiative decay (NRD), or can enter an excited triplet state via intersystem crossing (ISC) to yield an excited triplet state photosensitizer ($^3PS^*$). $^3PS^*$ can consequently

transfer the triplet state electron (type I photochemical reaction) or energy (type II photochemical reaction) to molecular oxygen, yielding $O_2^{\bullet -}$ and $^1O_2$, respectively (top left), or the $^3PS^*$ can return to the ground state by emitting phosphorescence (P). The generation of $O_2^{\bullet -}$ and $^1O_2$ (and its ROS/RNS derivatives) results in tumor cell death, vaso-occlusion, and an anti-tumor immune response (via the innate as well as the adaptive immune system) (Section 2.4).

While some solid cancer types respond very well to PDT [5-14], there are cancer types that are relatively recalcitrant to PDT, including superficial recurrent urothelial carcinoma [15], nasopharyngeal carcinoma [16], and extrahepatic cholangiocarcinoma [17, 18]. In addition to the therapeutic recalcitrance, systemic administration of the PS may lead to non-selective tissue damage and phototoxic reactions due to inadvertent accumulation of the PS in the skin. With respect to the latter, patients are instructed to stay inside and avoid direct exposure to sunlight until the PS has been completely cleared to prevent unbridled photochemical damage to the skin. Although PDT is still being used in specialized treatment centers, the significant burden on patients has led several treatment centers, including ours, to abandon PDT as a treatment option for terminal cancer patients due to ethical considerations [19].

Such decisions are unfortunate in light of the relatively good treatment outcomes achieved with PDT in many other types of cancer, as a result of which researchers are striving to further improve this modality while minimizing the drawbacks. The negative side-effects associated with PDT may be circumvented in several ways. Firstly, novel and more efficacious second-generation PSs with improved photophysical and photochemical properties have emerged, including chlorins and metal-coordinated phthalocyanines. These PSs are excited at longer wavelengths at which deeper light penetration into tissue and more homogeneous treatment of the tumor can be achieved. High-power laser systems have become available to accommodate PDT with these PSs. Secondly, the new generation of PSs, which are often lipophilic, can be incorporated into nanoparticulate drug delivery systems to ensure compatibility with plasma (required for intravenous administration) and to facilitate selective targeting. The targeting is expected to improve PS accumulation in the tumor [20, 21], as a result of which lower PS plasma concentrations will be required for an optimal PDT effect (compared to clinically approved PS). This should also reduce PS-associated phototoxicity. Thirdly, the use of a drug delivery system allows the co-encapsulation of adjuvant therapeutics or diagnostic/imaging agents, with which the PDT modality could be further improved.

In this review, these three aspects are addressed in light of a multi-faceted PDT modality for the treatment of recalcitrant solid cancers. Specifically, the systemic and intracellular distribution of PSs is addressed in the context of the PDT-induced model of cell death as well as the anti-tumor immune response. Next, an overview is provided of second-generation metallated phthalocyanines (PCs) as PSs and their advantages over conventional, clinically employed PSs. Following a brief overview of the different nanoparticulate PS delivery systems currently available for PDT, an exemplary PS delivery platform is introduced that is centered on zinc phthalocyanine

(ZnPC) and liposomes as an experimental PDT regimen for solid cancers.

2. Photodynamic therapy

2.1. Clinically approved photosensitizers

In the most ideal scenario, PSs should be non-toxic, should not generate toxic or mutagenic catabolites, and exhibit low-to-no dark toxicity. Moreover, ideal PSs should be chemically pure and photostable compounds that absorb maximally in the therapeutic window (650–850 nm [1]), have a high triplet state quantum yield, have a high ROS production efficiency, and accumulate selectively in the tumor tissue [22].

As detailed in **Fig. 2**, the four most frequently utilized clinical PSs include (1) hematoporphyrin derivative (HpD), (2) a semi-purified form of HpD known as porfimer sodium, (3) 5-aminolevulinic acid (5-ALA), which is a precursor of the mitochondrially produced PS protoporphyrin IX (PpIX), and (4) m-tetrahydroxyphenylchlorin (mTHPC). These PSs are associated with a considerable level of phototoxicity that is caused by long clearance times after systemic administration and extensive PS retention in the skin (**Table 1**). The profound skin toxicity applies to HpD [23] and

	Administration route	Tumor:tissue healthy ratio	Mutagenicity	Elimiation (half-life)	Photosensitivty	LD50 dark toxicity [µM]	Est. costs per treatment ($)	[Ref]
HpD	IV	NA	Yes	17 – 22 d	8-12 wk	367-1,136*	NCA	[181, 308-310]
Porfimer sodium	IV	1.7-2:1	Yes	17 d	4-12 wk	5.3	7,000	[24, 176, 187, 192, 311-313]
5-ALA	Oral / IV	2:1	Yes	5-ALA: 0.75 h	1-2 d	9,041	2000	[25, 176, 188, 314-316]
	Topical	1.7-30:1		PpIX: 8 h			250	
mTHPC	IV	2-3:1	No	45 h	2-6 wk	8.46-26.4	8,750	[26, 176, 181, 182, 186, 189, 317]
ZnPC	IV	6.3:1 [3.7-9:1]	NA	NA	NA	>5	< 100	[190, 191, 201, 301, 318]
$ZnPCS_4$	IV	NA	No	NA	NA	>31.6	< 100	[180, 319]
AlPC	IV	NA	No	NA	NA	>10	< 100	[178, 179, 320]
$AlPCS_4$	IV	10:1	No	NA	NA	>500	< 100	[33, 176, 177, 192]

Table 1. Pharmacokinetic, pharmacodynamic, and toxicity parameters of clinically applied and experimental photosensitizers. Abbreviations: LD_{50}, lethal 50% dose; est., estimated; IV, intravenous; NA, not assessed; d, day; wk, week; NCA, not commercially available; h, hour; ZnPC, zinc phthalocyanine; $ZnPCS_4$, tetrasulfonated zinc phthalocyanine; AlPC, chloroaluminum phthalocyanine; $AlPCS_4$, tetrasulfonated chloroaluminum phthalocyanine. *LD_{50} dark toxicity for HpD was calculated based on a molecular weight of 598.7 g/mol, as described in [307].

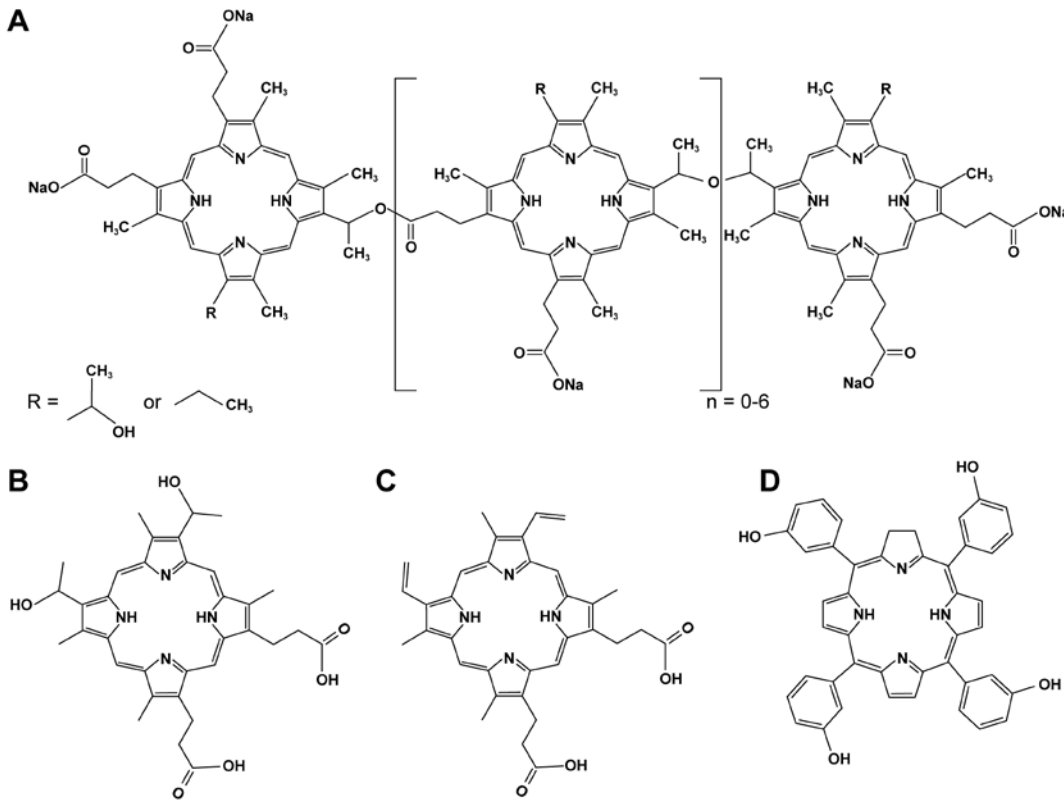

E

	Solubility	Log *P*	Q-band maximum [nm]	ε at Q-band maximum [$M^{-1} \cdot cm^{-1}$]	Triplet state quantum yield	Singlet oxygen quantum yield	[Ref]
(A) Porfimer sodium	Lipophile	8.50 (±3.34)	630	3,000	0.20	0.11	[33, 34]
(B) HpD	Lipophile	3.25 (±2.15)	630	3,000	0.83	0.56	[33-35]
(C) 5-ALA (PpIX)	Hydrophile	-1.89 (±1.08)	635	5,000	0.56	0.54	[35-37]
(D) mTHPC	Lipophile	7.40 (±2.16)	652	30,000	0.31	0.30	[35, 36, 38]

Fig. 2. Chemical structure and physicochemical properties of commonly used PSs. Chemical structure of porfimer sodium (**A**), hematoporphyrin (inasmuch as the exact chemical structure of HpD is unknown, the structure of hematoporphyrin is depicted) (**B**), PpIX (**C**), and mTHPC (**D**). The physicochemical properties are summarized in (**E**). Estimated octanol/water partition coefficients (log *P*) were obtained from [382].

porfimer sodium in particular [24], but also to a degree to PpIX [25] and mTHPC [26]. Peng *et al*. have determined the dermal distribution of porfimer sodium using highly light-sensitive video intensification microscopy, which revealed that porfimer sodium localizes to keratinized epithelium, hair (including follicles), and collagenous connective tissue [27]. Since PSs are slowly cleared from the skin by gradual

photobleaching [28], the photosensitivity caused by HpD and porfimer sodium can persist for up to 3 months.

Another limitation of the clinically approved PSs is the relatively low main absorption peak in the red spectrum (Q-band, **Fig. 3A**). The position of the Q-band maximum has several important clinical implications. First, short-wavelength red light has a lower optical penetration depth into tissue than longer-wavelength red light due to the competitive absorption by melanin (skin) and hemoglobin (skin and blood-containing tissue, including tumors) (**Fig. 3B**). The use of 630-nm light may result in insufficient PS excitation in the tumor bulk or inhomogeneous photosensitization of larger tumors due to optical shielding by blood vessels. Moving from 630-nm light to 690-nm light would significantly reduce absorption by blood, which theoretically yields a 1.67-fold increase in optical penetration depth [29]. Second, sunlight is more intense at the shorter red wavelengths (**Fig. 3B**) and may therefore account for more ROS generation by PSs with more blue-positioned Q-band maxima compared to PSs with more red-positioned Q-band maxima at equal dermal PS concentrations (**Fig. 3B**).

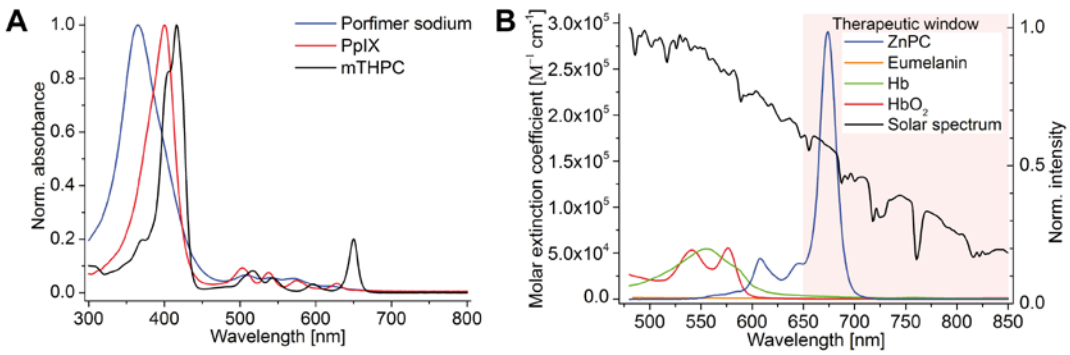

Fig. 3. (**A**) Normalized absorption spectra of porfimer sodium (in MilliQ), PpIX (in methanol), and mTHPC (in ethanol:MilliQ (49:51, v/v)). (**B**) Molar extinction coefficient of eumelanin [383], hemoglobin (Hb), oxyhemoglobin (HbO_2) [384], and zinc phthalocyanine (ZnPC, in pyridine). The solar spectrum (black trace) was recorded from direct sunlight in the 250–1,050 nm range and the spectrum was normalized to the maximum intensity (secondary y-axis). The pink area represents the therapeutic window for clinical PDT (650–850 nm).

With respect to the abovementioned factors and on the basis of the data presented in **Fig. 2**, the clinically approved PSs are not ideal. This has triggered the development of PSs with better spectral and photochemical properties and technically more sophisticated PDT modalities. Readers should note that PDT may not be the treatment of choice for bulky tumors. Bulky tumors are associated with limited optical penetration depth and extensive scattering of light, particularly when a tumor has a necrotic core. In those cases, surgical resection is preferred (when possible) and/or radiotherapy/chemotherapy. Alternatively, interstitial PDT, a PDT modality where multiple light-emitting fibers are inserted into the tumor, may be employed to completely and homogenously photosensitize the malignant tissue.

2.2. Biodistribution of photosensitizers

2.2.1. Systemic distribution

Systemically infused PSs are distributed throughout the body via the circulation, whereby the PS typically hyperaccumulates in tumor tissue due to the enhanced permeability and retention (EPR) effect. Since the tumor endothelium is highly fenestrated and the tumor interstitium lacks lymphatic drainage, PSs are more prone to accumulate and remain in tumor tissue than in healthy tissues [30].

To study the biodistribution of a PS after systemic administration, Bellnier and co-workers injected radio-isotopically (^{14}C)-labeled porfimer sodium intravenously in mammary carcinoma (SMT-F)-bearing mice [31], and found that porfimer sodium (hydrophobic, **Fig. 2**) was taken up by various organs within 7.5 h after systemic administration. The highest peak concentrations were measured in the liver, adrenal gland, and bladder, whereas lower concentrations were found in the pancreas, kidney, and spleen. Even lower concentrations were measured in the stomach, bone, lung, and heart. Although the intratumoral porfimer sodium concentration was lower than in the previously mentioned organs, the porfimer sodium concentration in the tumor was higher than in skeletal muscle, skin, and brain tissue. Another study evaluated the biodistributive behavior of mono-l-aspartyl chlorin e6 (NPe6, hydrophilic) in murine mammary carcinoma (BA)-bearing mice [32]. It was shown that the highest NPe6 concentrations were reached in the liver, kidney, and spleen, whereas the lowest concentration of NPe6 was found in the brain, muscle, and esophagus. Furthermore, a substantial amount of NPe6 was localized in the skin 1 h post-injection, although this concentration rapidly declined over a period of 96 h. At 4 h, the NPe6 tumor tissue concentration was higher than in all the examined tissues, except for the liver, kidney, adrenal gland, and spleen. Additionally, Chan *et al*. examined the biodistribution of sulfonated chloroaluminum phthalocyanines (AlPCs) in colon carcinoma (Colo 26)-xenografted mice [33]. A positive correlation was found between the degree of intratumoral PS accumulation and the degree of sulfonation (increases hydrophilicity), where tetrasulfonated AlPC ($AlPCS_4$) was associated with the highest tumor concentration. In line with earlier studies, the sulfonated AlPCs extensively accumulated in the liver and spleen in an inversely proportional manner to the degree of sulfonation ($AlPCS_1 > AlPCS_2 > AlPCS_4 > AlPCS_3$). These studies reveal that PSs typically accumulate in all organs, where the liver, spleen, lungs, and kidneys are the most prominent sites for PS accumulation. However, the uptake of PSs by internal organs does not constitute a clinical issue on the condition that the PSs do not exhibit dark toxicity, given that the organs are usually impermeable to light from the outside. In contrast, the accumulation of PSs in the skin should be minimized to prevent severe adverse events as described in Section 2.1.

The biodistributive behavior of a PS described in the previous paragraph is

dependent on its ability to: (1) refrain from aggregating, thereby avoiding preferential uptake in organs replete with cells of the mononuclear phagocyte system (*i.e.*, liver, spleen, lung) [34], (2) bind to macromolecules, including low-density lipoprotein (LDL) [35], albumin [36], and/or lipid bodies that are abundantly expressed or metabolically exacted in the tumor environment [37, 38], (3) undergo an increase in its lipophilicity (octanol/water partition coefficient or log *P*) in the more acidic tumor milieu [39], and (4) undergo pinocytosis and/or phagocytosis by tumor cells or by tumor-associated macrophages [40, 41]. It should be noted that higher intratumoral PS concentrations do not necessarily correlate positively to treatment efficacy [42], as additional factors are involved in post-PDT tumoricidal mechanisms.

The binding of PSs to biomolecules (*e.g.*, LDL, transferrin, and/or albumin or their cognate receptors) and subsequent PS internalization [43] constitutes a propitious PS delivery route to tumor cells and may positively contribute to treatment outcome. The delivery mechanism is based on the tumor cell's demand for energy and building blocks required for cell sustenance and proliferation. Accordingly, tumor cells typically exhibit elevated expression of LDL- and transferrin receptors as well as enhanced albumin uptake [44-46]. Porphyrins, for instance, have a strong affinity for LDL, transferrin, and albumin [47]. Kessel found that in mice HpD associated with both LDL and HDL and that accumulation of HpD correlated with the relative number of LDL receptors present in the respective tissue [48]. This indicates that the LDL pathway serves as a delivery route of HpD and other PSs that associate with LDL to the tumor site. PCs (including ZnPC) also associate with LDL [49] and albumin [50], as a result of which these blood-borne biomolecules can be exploited as endogenous tumor-targeting PS carriers to enhance PS tumor-to-normal tissue ratios. Typically, the binding of biomolecule-conjugated PS to the corresponding cell receptor results in endocytic internalization of the PS and subsequent delivery to lysosomes [51].

2.2.2. Intracellular distribution

Cellular uptake of the PS, either by diffusion or via the endosomal-lysosomal pathway, is followed by translocation to distinct intracellular loci depending on the PS's chemical properties. PSs typically accumulate in various organelles, including mitochondria, lysosomes, endoplasmic reticulum (ER), and the plasma membrane. Factors that influence the subcellular localization include net ionic charge, log *P* value, and the amphiphilicity of the PS. Generally, anionic PSs (net charge of ≤−2) end up in lysosomes, whereas cationic PSs are electrophoretically driven to the mitochondria [52] because the inner space of the mitochondrion is more negatively charged in tumor cells than in healthy cells [53]. Consequently, cationic PSs preferentially accrue and remain in the mitochondria of tumor cells [52, 53]. Furthermore, hydrophilic PSs tend to localize to lysosomes [54, 55], while lipophilic PSs preferentially localize to the plasma membrane and intracellular membranes, including the mitochondrial and ER

membrane [56].

With respect to the intracellular localization of clinically used PSs, 5-ALA readily localizes to mitochondria, after which the mitochondrially produced PpIX translocates to the cytosol [57]. On the other hand, HpD temporarily accumulates in the plasma membrane but quite rapidly redistributes diffusely across subcellular membranes [58]. Its derivative, porfimer sodium, localizes to the plasma membrane as well, but also shows discrete association with the Golgi apparatus [59]. While mTHPC exhibits a preference for both the ER and Golgi [60], metallated PCs preferentially accumulate in the plasma-, Golgi-, and mitochondrial-membranes [61]. Studies have further shown that a PS exhibits spatiotemporal dynamics following uptake [57-60], which will ultimately affect the mode and extent of cell death upon PDT and hence therapeutic outcome (addressed in Section 2.3). For instance, mTHPC-treated human mesothelioma-bearing nude mice were susceptible to PDT-induced necrosis over a range of drug-light intervals (12 h to 4 days), although the therapeutic efficacy significantly differed among the different drug-light intervals irrespective of the tissue PS concentration [62].

2.3. Mechanisms of photodynamic therapy-mediated cell death as function of intracellular photosensitizer localization

PDT-induced mechanisms of cell death are in part dependent on the type of PS used and hence the intracellular localization of the PS. It is believed that type II photochemical reaction-derived $^1O_2$ is the most predominant type of ROS that is produced upon PDT [63, 64], and, given that cytosolic $^1O_2$ diffusion is restricted to very short distances (~220 nm) [65], $^1O_2$ is only capable of oxidizing biomolecules in close proximity to its production site. The short diffusion distance of most ROS/RNS is beneficial to PDT insofar as ROS/RNS are usually not generated close to nuclear material [66] and hence do not result in sublethal oxidation of DNA and consequent malignant cell transformation (*e.g.*, by generation of 8-hydroxyguanine) in proximal non-cancerous cells, although exceptions do exist [67]. The short lifetimes of most ROS/RNS also preclude cell damage to peritumoral healthy tissue. Furthermore, PSs often target to more than one (sub) cellular location that, upon PDT, will result in concomitant activation of different cell death pathways, thereby limiting the efficacy of simultaneously activated cell survival pathways and stress responses after PDT (reviewed in [68]). In addition to intracellular PS localization, factors such as cell type, intracellular PS concentration, light dose, local oxygen tension, and residual energy status govern the eventual mode of cell death (*i.e.*, apoptosis versus necrosis) [69] (discussed in this section) and autophagy (addressed in Section 2.5).

As addressed in Section 2.2.2, the temporal distribution and intracellular localization of a PS is dynamic after initial cell entry. For instance, HpD, porfimer sodium, and ZnPC are initially confined to the plasma membrane, whereas at longer

incubation times (>1–2 h) the PSs become more prominently localized in distinct perinuclear areas [57, 58, 61]. Accordingly, Hsieh *et al*. demonstrated that porfimer sodium accumulates in the plasma membrane directly after uptake but, at later time points, distributes to various intracellular compartments to ultimately end up mainly in the Golgi complex [59]. Irradiation of plasma membrane-localized porfimer sodium induced necrosis-like cell death, whereas irradiation of cytoplasmically localized porfimer sodium led to cell death that was characterized by cytoplasmic vacuole formulation and cell shrinkage in the presence of an intact plasma membrane.

For illustrative purposes, the effect of PS localization on PDT efficacy was evaluated in a so-called chase experiment. Human epidermoid carcinoma (A431) cells were incubated with ZnPC-encapsulating cationic liposomes (ZnPC-ETLs, Section 4.4.3) for 10 min, after which the liposome-containing medium was replaced with fresh culture medium. After specific time intervals the cells were treated with PDT and examined for cell viability, the results of which are presented in **Fig. 4A**. These data reveal that a higher photokilling capacity was achieved when A431 cells were irradiated at early time points after incubation (<4 h) compared to later time points (>4 h). In addition, confocal microscopy experiments were performed to examine the intracellular localization of ZnPC as a function of time. As shown in **Fig. 4B**, ZnPC is highly associated with mitochondria after 30 min and to a lesser extent after 4 h. At the 4-h time point, ZnPC exhibited a more diffuse localization, which was even more pronounced after 24 h. This is in line with the previously alluded to spatiotemporal dynamics of PSs following uptake, attesting to the importance of a well-defined PDT protocol and the fact that systematic modulation of this protocol can culminate in the activation of distinct cell death pathways.

2.3.1. Organelle-specific response

The plasma membrane is the first site that PSs encounter before entering a cell. As opposed to polar PSs, which are typically transported across the plasma membrane [70] due to the hydrophobic barrier effect imposed by the lipid bilayer, lipophilic PSs usually intercalate into the acyl chain region of the lipid bilayer. PDT-mediated ROS production in the plasma membrane can cause necrosis-like cell death that is preceded by loss of plasma membrane integrity due to peroxidation of unsaturated phospholipids [71] (usually dioxetane adduct formation when $^1O_2$ is produced and peroxide formation when oxygen radicals ($^{\bullet}OH$) are generated from type I photochemical reaction-derived $O_2^{\bullet -}$ [72]). Oxidative modification of lipid constituents is associated with phospholipid packing defects and membrane permeabilization [73, 74], ultimately leading to necrosis.

Lysosome-targeted PSs may induce ROS-triggered cell death in two ways: (1) via the discharge of cathepsins from lysosomes due to lipid (per) oxidation-mediated lysosome rupture and/or (2) PDT-induced relocalization of the PS to other organelles

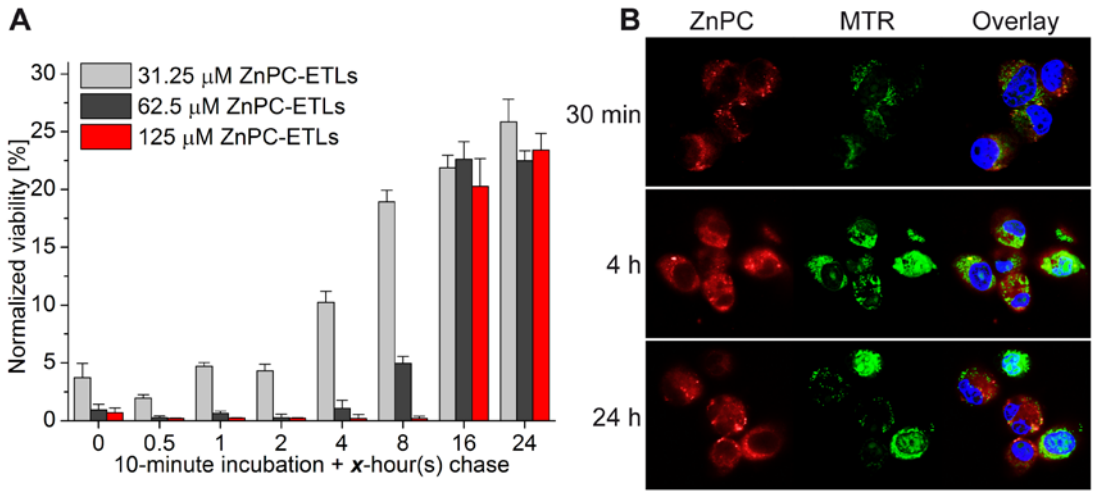

Fig. 4. (**A**) Effect of intracellular ZnPC dispersion time on PDT-induced cell death and spatiotemporal dynamics of intracellular ZnPC distribution. A431 cells were incubated with ZnPC-encapsulating cationic liposomes (ZnPC–ETLs) composed of DPPC:DC-chol:cholesterol:DSPE-PEG (66:25:5:4, molar ratio). ZnPC was incorporated at a ZnPC:lipid ratio of 0.003. Concentrations in the legend indicate final lipid concentrations. After 10 min, the medium was refreshed and cells were treated with PDT at the indicated time points (x-axis) and kept under standard culture conditions until the time of viability testing. (**B**) Intracellular ZnPC localization as a function of time. A431 cells were incubated with ZnPC-ETLs (ZnPC:lipid ratio of 0.030) for 10 min, after which the intracellular localization was visualized by confocal microscopy at different time points. ZnPC (red), MitoTracker Red (MTR, mitochondria, green), DAPI (nuclei, blue).

and subsequent induction of oxidative damage [75-77]. With respect to the first pathway, cathepsins exhibit proteolytic activity and are able to cleave BH3 interacting-domain death agonist (BID) to form truncated-BID (t-BID), which ultimately culminates in apoptosis. The second pathway comprises the redistribution of lysosomal PS molecules to other organelles such as the ER, mitochondria, and the Golgi apparatus, where site-specific damage is inflicted upon PDT.

Irradiation of PSs that localize to the ER (*e.g.*, 9-capronyloxytetrakis (methoxyethyl) porphycene (CPO) [78], hypericin [79], and mTHPC [60]) is believed to result in lipid (per) oxidation and consequent disruption of the ER membrane, accompanied by the release of Ca^{2+} as well as unfolded/misfolded proteins into the cytosol. The release of these compounds triggers Ca^{2+} signaling and the unfolded protein response (UPR), respectively. The net effect of Ca^{2+} signaling and UPR is the activation of calpain, caspase 4, and caspase 12 and ultimately caspase-mediated apoptosis [80]. Alternatively, excessive Ca^{2+} uptake by mitochondria may either lead to apoptogen release and loss of mitochondrial membrane potential followed by apoptosis [81] or mitochondrial permeability transition (MPT) ensued by ATP depletion and necrotic cell death [82]. Mitochondria-targeting PSs have been shown to rapidly induce apoptosis following photosensitization [83, 84] as a result of mitochondrial lipid peroxidation. PDT-induced mitochondrial lipid peroxidation has been demonstrated with meso-tetrakis[4-(carboxymethyleneoxy)phenyl]porphyrin (T4CPP), a (non-

exclusive) mitochondria-targeting PS [85], which resulted in $^1O_2$ generation and lipid peroxidation in isolated rat liver mitochondria and mitochondria of sarcoma 180 cells [86]. The release of pro-apoptotic factors ultimately leads to apoptosis when residual ATP levels are high enough to facilitate this energy-dependent mode of cell death [87]. Lastly, essentially three pathways have been described in which Golgi-targeting PSs induce cell death following PDT. First, ROS generation in the Golgi can cause oxidative modification and cleavage of Golgi proteins, leading to apoptosis as well as organelle fragmentation, which is an early apoptotic event [88, 89]. Second, PDT-induced apoptotic signaling seems to involve the general vesicular transport factor p115. Following PDT, p115 was shown to undergo cleavage by caspase-3 and caspase-8 and to subsequently translocate to the nucleus, where it was able to stimulate apoptosis independently of Golgi fragmentation [90]. Third, a study revealed that 2,4,5,7-tetrabromorhodamine 123 bromide, a PS that selectively incorporates into the Golgi, produced both $O_2^{\bullet -}$ and $^1O_2$ after illumination and induced apoptosis via a calcium-dependent pathway that did not involve mitochondria [91]. These results indicate that Golgi-localized PSs induce apoptosis upon PDT via cell death pathways that in some respects differ from those triggered by other organelles afflicted by PDT, and may therefore amplify other PDT-induced cell death cascades.

2.4. Photodynamic therapy-mediated immune response: the role of damage-associated molecular patterns (DAMPs)

The initiation of an anti-tumor immune response is one of the main secondary mechanisms by which PDT orchestrates anti-tumor effects [92-94]. The requirement of the immune system in the PDT-induced removal of solid cancers has been clearly demonstrated in murine tumor models. Immunocompetent mammary sarcoma (EMT6)-bearing mice treated with porfimer sodium showed a complete response rate up to 90 days post-PDT [95]. In contrast, immunodeficient EMT-6 tumor-bearing mice treated under the same conditions only exhibited initial tumor destruction. At later time points (>25 days), all immunodeficient mice had recurrent tumors [95]. These findings indicate that PDT results in direct tumor destruction, whereas prolonged tumor-free survival relies on a functional immune system. The PDT-induced anti-tumor immune response essentially comprises the initiation of a sterile inflammatory response, the maturation of dendritic cells (DCs), the presentation of tumor-associated antigens (TAAs) by DCs, the priming of a specific $CD8^+$ cytotoxic T-lymphocyte (CTL) response [96], and the removal of cancer cells, as summarized in **Fig. 1** and further discussed in Section 2.4.3. Over the last years, it has become evident that damage-associated molecular patterns (DAMPs) exposed or released by PDT-treated cells play a major role in anti-tumor immunity by promoting sterile inflammation and DC maturation [97, 98].

2.4.1. Damage-associated molecular patterns

DAMPs are specific molecules that emanate from stressed and dying cells and act as danger signals for the host immune system. In case of PDT, DAMPs play a crucial role in initiating and augmenting the pro-inflammatory response following therapy [99-101]. DAMPs have predominantly non-immunological functions and are normally sequestered within the cell. Once secreted, released, or surface-exposed by stressed, dying, and dead cells, the DAMPs are recognized by various receptors on immune cells, which includes the family of pattern recognition receptors (PRRs). The binding results in various pro-inflammatory effects such as maturation, activation, and antigen processing/presentation on antigen-presenting cells (APCs) such as DCs and macrophages [100]. An overview of the best characterized DAMPs that are released after PDT is provided in **Fig. 5** in the context of the mode of cell death induced by PDT as well as the immunological effects.

2.4.2. Damage-associated molecular pattern release following photodynamic therapy

Heat shock proteins (HSPs) are chaperone proteins that facilitate the correct folding and transport of newly synthesized proteins. Increased expression of HSPs protects the cell under stress conditions by stabilizing unfolded proteins, promoting proteasomal degradation, and preventing apoptosis [102]. Moreover, in stressed cells the overexpressed HSPs can be surface exposed and/or released into the extracellular environment, where they exhibit immunostimulatory properties [102]. HSPs bind to numerous receptors, including Toll-like receptor 2 (TLR2), TLR4, and cluster of differentiation 91 (CD91) [103-106], resulting in the activation of various innate immune cells and anti-tumor immune responses. HSP-initiated signaling through TLR2 and TLR4 has been associated with nuclear factor kappa-light-chain-enhancer of activated B cells (NF-κB) activation (mediates a pro-inflammatory response), DC maturation, and cytokine production [107]. Signaling via CD91 results in phagocytosis, NF-κB activation, and antigen presentation [108-110]. HSPs are the best-characterized DAMPs associated with PDT and can be released extracellularly and/or exposed on the cell surface following PDT treatment [111-115]. It seems that PDT modalities that trigger apoptosis primarily instigate the surface exposure of HSPs such as HSP60 and HSP70 [111], whereas PDT regimes that primarily cause necrosis are associated with the extracellular release of HSPs such as HSP70 and HSP90 [116].

Calreticulin is a Ca^{2+}-binding protein that mainly resides in the lumen of the ER, where it functions as a chaperone and is involved in Ca^{2+} signaling [117, 118]. Calreticulin exposed on the cell membrane (ecto-CRT) acts as an eat-me signal and engages in the recognition and phagocytic engulfment of apoptotic cells by APCs [119], a process mediated by CD91 on APCs [109]. Calreticulin also functions as one of the main DAMPs in immunogenic apoptosis (also termed immunogenic cell death, ICD) [120], as ecto-CRT facilitates the DC-mediated phagocytosis of cancer cells undergoing

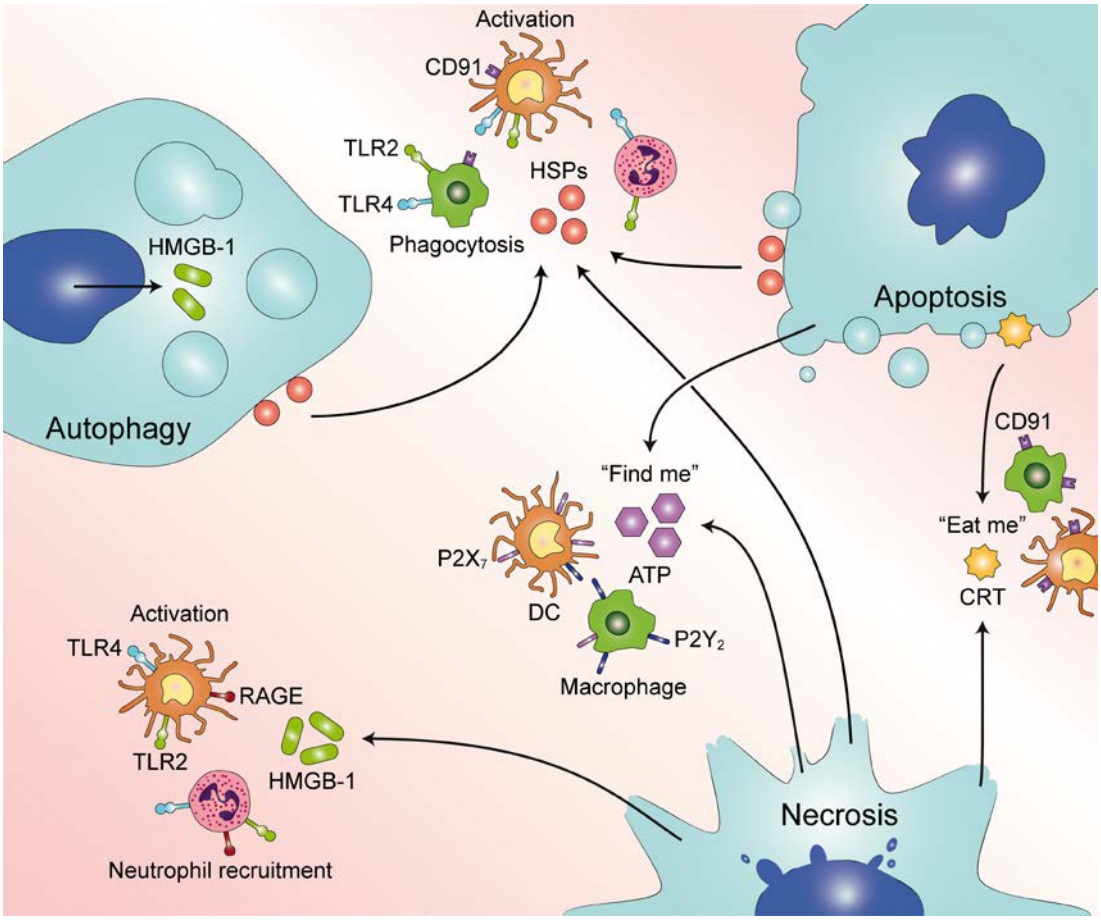

Fig. 5. Apoptotic cells (top right) expose and/or release heat shock protein 60 (HSP60) and HSP70. In addition, HSP70 is liberated by necrotic (bottom) and autophagic cells (top left). HSPs interact with immune cells via Toll-like receptor 2 (TLR2), TLR4, and CD91, which leads to immune cell activation. In addition, apoptotic cells express and/or release calreticulin (CRT), culminating in DC and macrophage activation via CD91. Necrotic cells release CRT as a result of membrane perturbation. Both apoptotic and necrotic cells release ATP that interacts with the P2Y2 and P2X7 receptor. Necrosis is accompanied by the release of high mobility group box-1 (HMGB-1), resulting in DC activation and neutrophil recruitment via TLR2, TLR4, and receptor for advanced glycation end products (RAGE) on these cells. In response to oxidative stress, HMGB-1 may act as an important regulator of autophagic cell death [385].

ICD, resulting in antigen presentation and an anti-tumor adaptive immune response [121]. Hypericin-PDT can for instance induce ICD through site-specific oxidative damage to the ER [122]. Both pre-apoptotic ecto-CRT and late apoptotic/secondary necrotic extracellularly released calreticulin have been found following hypericin-PDT *in vitro* [109, 123, 124].

High mobility group box-1 (HMGB-1) has been identified as a nuclear DNA-binding protein involved in DNA organization and gene transcription [125]. HMGB-1 can be actively secreted by immune cells [126, 127] or passively released by necrotic cells [128, 129]. Extracellular HMGB-1 acts as a DAMP by inducing inflammation

[129], stimulating cytokine production [130, 131], enhancing neutrophil recruitment [132], and activating DCs [133]. More recently, it has been demonstrated that apoptotic [134] and autophagic [135] cells also release HMGB-1. HMGB-1 exerts its pro-inflammatory functions through interactions with a range of receptors, including but not limited to receptor for advanced glycation end products (RAGE), TLR2, and TLR4 [136, 137]. Very few studies have been conducted on the release of HMGB-1 from PDT-treated cells and the relative importance of this DAMP in the PDT-induced immune response. Korbelik *et al*. reported that PDT with porfimer sodium resulted in the release of HMGB-1 from necrotic cells into the blood stream of mice as early as 1 h post-PDT [138]. A study by Tracy *et al*. showed that HMGB-1 is one of the DAMPs released from necrotic cells treated with PDT using 2-(1-hexyloxyethyl)-2-devinylpyropheophorbide-a (HPPH, localizes to mitochondria) or HPPH-galactose (localizes to lysosomes) [116]. However, cells undergoing apoptotic cell death did not release significant amounts of HMGB-1 following PDT with HPPH or HPPH-galactose [116]. Moreover, no significant HMGB-1 release was detected from T24 cells treated with hypericin-PDT under ICD-inducing conditions [124], altogether suggesting that HMGB-1 signaling after PDT is dependent on the mode of cell death.

Extracellularly released ATP has been identified as a very potent find-me signal for monocytes, macrophages, and DCs [139]. Elliott *et al*. reported that the ATP/UTP receptor P2Y2 on phagocytes is a critical sensor for extracellular ATP, which in turn promotes phagocyte recruitment [139]. Moreover, ATP has been identified as a ligand for P2X7 purinergic receptors on DCs. ATP binding to this receptor can lead to the activation of the NLR family, pyrin domain containing 3 (NLRP3) inflammasome; a caspase 1 activation complex that stimulates DC maturation and subsequent secretion of IL-1β, an important chemokine for the priming of T cells and hence the induction of an anti-tumor adaptive immune response [140, 141]. Garg *et al*. showed that hypericin-PDT-treated human bladder carcinoma (T24) cells undergoing ICD secrete ATP in the pre-apoptotic phase [109]. Unfortunately, the extracellular release of ATP following PDT has only been investigated using hypericin as PS in the paradigm of ICD [109, 124]. It should be noted that oxidized ATP has been reported to act as an inhibitor of P2RX7, thereby impeding proliferation and effector functions of T cells [142]. This means that ATP belongs to the class of redox-sensitive DAMPs such as HMGB-1, which are susceptible to oxidation-induced inactivation in terms of immunostimulatory properties.

2.4.3. Photodynamic therapy-induced anti-tumor immunity

The mechanisms whereby PDT activates and potentiates anti-tumor immunity have been extensively researched. However, the exact molecular mechanisms that lead to the PDT-induced enhancement of anti-tumor immunity have yet to be fully elucidated. Here, a brief overview of the mechanisms involved in the transition from

focused, PDT-induced oxidative stress to a systemic anti-tumor immune response is addressed. For more detailed reports on PDT-induced anti-tumor immunity the readers are referred to other reviews [96, 115, 143-145].

PDT-induced oxidative stress results in extended tumor tissue injury. The host perceives this injury as localized trauma and is provoked to launch an inflammatory response mediated by the innate immune system [146]. DAMPs released by PDT-stressed cells act as danger signals intended to assist the host in recognizing the injured self. This PDT-induced activation of the innate immune system constitutes a multistep process that involves the initiation of a massive, acute, and sterile inflammatory response, cytokine release, complement activation, and recruitment and activation of innate immune cells (*e.g.*, neutrophils, DCs, macrophages) [96]. Different DAMPs play major roles in these processes (Section 2.4.2). Ultimately, this rapidly expanding, relatively non-specific innate immune response gives rise to the much slower developing adaptive immune response and hence anti-tumor immunity. The anti-tumor immune response is initiated by the presentation of TAAs, released from dying and dead cancer cells, by DCs to naive T cells, resulting in the generation of tumor-specific CTLs that attack and remove residual cancer cells. Moreover, the DAMPs interact with various receptors expressed by DCs (**Fig. 5**), which stimulates DC maturation that culminates in increased surface levels of major histocompatibility complex (MHC) classes I and II, and other co-stimulatory proteins [147], rendering fully mature DCs much more effective at presenting TAAs to T cells.

The involvement of CTLs in PDT-mediated anti-tumor immunity was first observed by Canti *et al.* [148]. In a subsequent study it was demonstrated that the growth inhibition of EMT6 tumors after porfimer sodium-mediated PDT is dependent on CTLs [149]. Recent studies showed that PDT-treated tumor cells stimulate DCs and their ability to present TAAs, resulting in the generation of tumor-specific CTLs [123, 124].

The involvement of the adaptive immune system, and more specifically DCs and T cells, in PDT-induced tumor eradication enables the manifestation of abscopal effects, which is absolutely critical for good clinical outcomes of PDT given that PDT may not affect all cancer cells in a tumor equally (Section 2.1) and PDT-subjected cancer cells may activate survival pathways to revert cell death signaling (Section 2.5). The eradication of distant tumor cells that were not exposed to PDT has been observed not only in a murine syngeneic cancer model [149], but also in a clinical setting [150]. Other clinical studies that point towards the potency of PDT to induced anti-tumor immune responses have been published for vulval intraepithelial neoplasia [151], basal cell carcinoma [152], and both actinic keratosis and Bowen's disease [153].

2.5. Photosensitizer concentration- and light dosage-dependent cell responses

Two important factors in the cell's response to PDT are intracellular PS concentration and fluence rate (W/cm^2 in an infinitesimal tissue volume) and, by inference, the extent of ROS generation and consequent degree of oxidation. Tumor cells can cope with PDT-induced damage by activating one or more of several possible survival- and stress-response pathways, comprising (1) an immediate early stress response that promotes tumor cell proliferation, (2) an antioxidant response that results in de novo synthesis of antioxidants, (3) a hypoxia stress response that restores energy homeostasis and induces angiogenesis, (4) a pro-inflammatory signaling response that governs angiogenesis and invasion, (5) an ER stress response that aims to restore ER homeostasis, and (6) autophagy that involves recycling of damaged cell components as part of promoting cell survival. The first five cell survival pathways have been reviewed in detail by Broekgaarden *et al.* in light of PDT [68]. The ER stress response following PDT [80, 154] has not been completely characterized and likely applies predominantly to PSs that localize to or near the ER given the short diffusion distance of ROS/RNS. Consequently, the PS concentration- and light dose-dependent cell responses will be illustrated in the context of autophagy, which constitutes a better elucidated and more ubiquitous response mechanism than the ER stress response. For all responses, however, an oxidative damage threshold generally applies that governs the fate of a cell in that cells must possess sufficient residual metabolic capacity to remediate oxidative damage. When the oxidative damage threshold is crossed and the level of damage exceeds the restorative capacity, cells will typically actualize cell death programs.

Autophagy generally constitutes a cytoprotective mechanism through which cells recycle damaged and degraded organelles. Under certain conditions, autophagic pathways may be directed at promoting autophagic cell death upon continued exposure to stress conditions (reviewed in [155]). With respect to PDT, Kessel and Reiners [156] demonstrated that at lower PS dosages, PDT with CPO (targets to the ER) and mesochlorin (localizes to mitochondria) induced pro-survival autophagy, whereas both autophagic cell death and apoptosis were induced at higher dosages of either PS at equal radiant exposure. Cell death was presumably caused by loss of B-cell CLL/lymphoma 2 (BCL2) [157, 158], which is confined to the mitochondria and/or ER, insofar as photo-oxidative loss of BCL2 can trigger both apoptosis and autophagy. As oxidative stress is known to be destructive to BCL2 [158, 159], the oxidation-mediated release of autophagy-regulated protein beclin 1 (BECN1) from its BCL2 complex may induce autophagy following PDT [160, 161] and consequent cell death.

Comparable results have been reported for the mode of autophagy as a function of light dosage. Low-dose PDT is typically associated with pro-survival autophagy, during which cells (L1210 cells, murine leukemia) recycle damaged and degraded cell organelles to remediate injury and facilitate survival [156, 162]. Correspondingly, low-dose PDT with mitochondria- or ER-targeting PSs (CPO and mesochlorin,

respectively) resulted in a greater degree of cell death when autophagy-related protein 7 (ATG7), a protein involved in autophagy induction, was silenced in a knockdown derivative cell line (L1210/Atg7$^-$) [156, 163]. Conversely, higher-dose PDT induced autophagic cell death rather than survival and augmented the extent of photokilling [156, 163]. It should be noted that these effects may in part be attributable to oxidative stress-dependent debilitation of autophagosome formation, particularly when ER- or mitochondria-targeted PSs are used [156, 163].

Taken altogether, these findings indicate that autophagy contributes to cell survival after low-dose PDT but cell death after high-dose PDT. Since it has been postulated that there is an equilibrium state between apoptosis and autophagy [164, 165], suppression of autophagy following PDT may exacerbate oxidative stress-induced cell demise.

3. Metallated phthalocyanines as photosensitizers for photodynamic therapy

3.1. Metallated phthalocyanines

Metallated PCs are synthetic second-generation PSs comprising a fully conjugated, symmetrical macrocyclic structure containing a centrally positioned, coordinated, multivalent metal cation such as Al^{3+}, Ga^{3+}, Zn^{2+}, Cu^{2+}, Fe^{2+}, or Co^{2+} (**Fig. 6A–D**). The type of metal dictates the photophysical properties of the PS [166]; closed-shell diamagnetic metal-containing PCs (Al^{3+}, Ga^{2+}, Zn^{2+}) exhibit higher triplet state quantum yields (Φ_T) and longer-lived triplet states than paramagnetic metal-containing PCs (Co^{2+}, Cu^{2+}, Fe^{2+}) [167].

The diamagnetic PCs, and particularly ZnPC and AlPC, are very suitable PSs for PDT due to several pronounced advantages. Firstly, these PCs have a molar absorptivity (ε) in the order of ~10^5 M^{-1} cm^{-1} and a strong Q-band in the mid-red wavelength range (absorption maximum at ~674 nm for AlPC and ZnPC), *i.e.*, well within the therapeutic window (650–850 nm) (**Fig. 6E–I**) [168]. Secondly, the non-functionalized diamagnetic PCs exhibit Φ_Ts of 0.3–0.5 [169] and triplet state lifetimes of >200 μs (reviewed in [170]). Moreover, the triplet states are amply energetic (1.21–1.31 eV) to generate $^1O_2$ (0.98 eV) [171], altogether accounting for considerable $^1O_2$ generation during PDT (**Fig. 6J–M**) relative to other PSs, and particularly the first-generation PSs. Thirdly, the synthesis of PCs is simple, cheap, and versatile in that any di- or tri-valent metal cation can be incorporated and the six-membered ring of the isoindole groups can be modified by conjugation of functional groups (*e.g.*, sulfonate) to alter the chemical properties (*e.g.*, log *P*) without drastically affecting the photophysical properties (**Fig. 6A–E**). In some instances, however, functionalization may change the photochemical properties, as was observed for tetrasulfonated ZnPC ($ZnPCS_4$) (**Fig. 6L**) but not for $AlPCS_4$ (**Fig. 6M**).

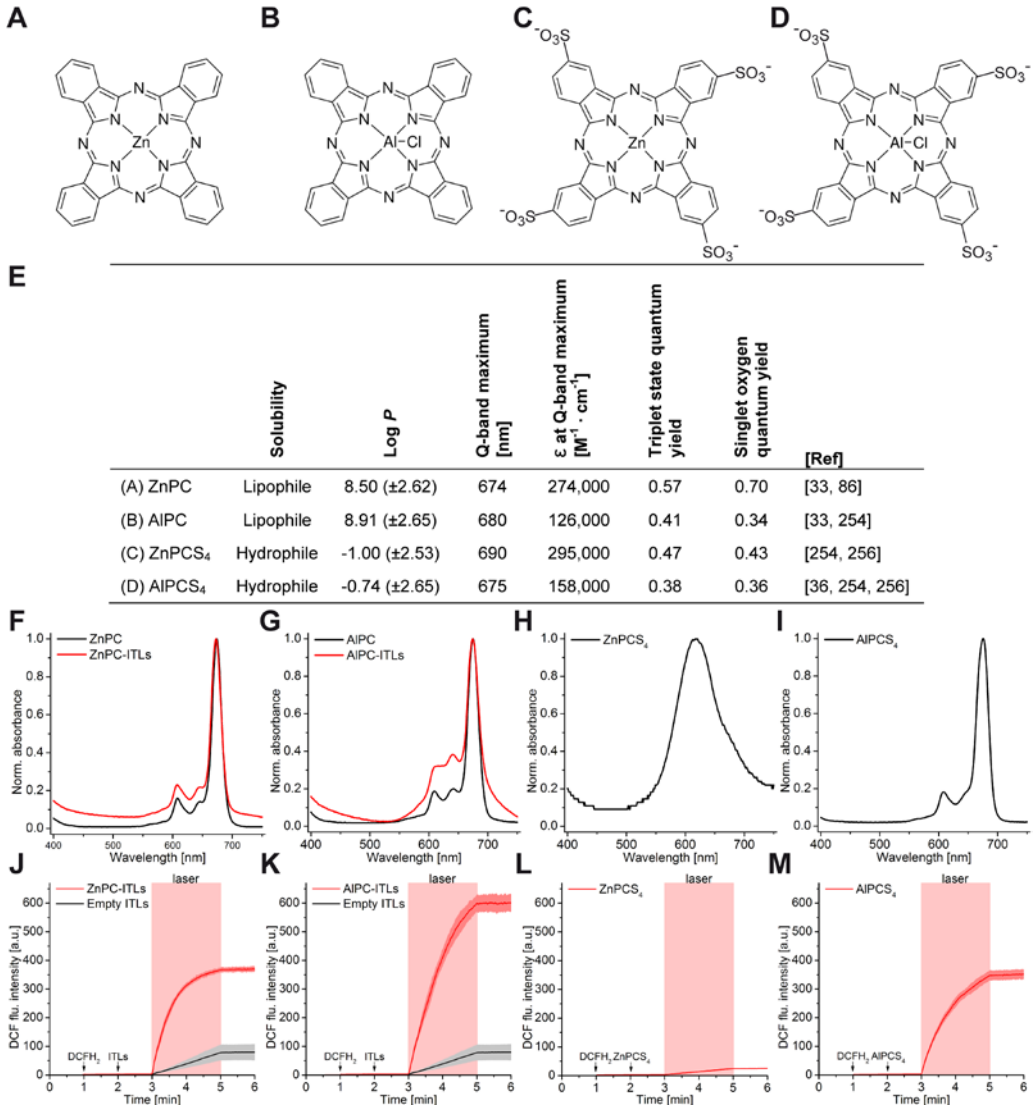

	Solubility	Log *P*	Q-band maximum [nm]	ε at Q-band maximum [$M^{-1} \cdot cm^{-1}$]	Triplet state quantum yield	Singlet oxygen quantum yield	[Ref]
(A) ZnPC	Lipophile	8.50 (±2.62)	674	274,000	0.57	0.70	[33, 86]
(B) AlPC	Lipophile	8.91 (±2.65)	680	126,000	0.41	0.34	[33, 254]
(C) $ZnPCS_4$	Hydrophile	-1.00 (±2.53)	690	295,000	0.47	0.43	[254, 256]
(D) $AlPCS_4$	Hydrophile	-0.74 (±2.65)	675	158,000	0.38	0.36	[36, 254, 256]

Fig. 6. Chemical structures of ZnPC (**A**), AlPC (**B**), tetrasulfonated ZnPC ($ZnPCS_4$) (**C**), and tetrasulfonated AlPC ($AlPCS_4$) (**D**). The physicochemical properties are provided in (**E**). Estimated octanol/water partition coefficients (log *P*) were obtained from [382]. Normalized absorption spectra are provided of ZnPC dissolved in pyridine and ZnPC encapsulated in liposomes (ZnPC-ITLs, composed of DPPC:DSPE-PEG (96:4, molar ratio) at a ZnPC:lipid ratio of 0.003) (**F**), AlPC dissolved in pyridine and AlPC encapsulated in liposomes (AlPC-ITLs, composed of DPPC:DSPE-PEG (96:4, molar ratio) at an AlPC:lipid ratio of 0.003) (**G**), tetrasulfonated ZnPC ($ZnPCS_4$) in MilliQ (**H**), and tetrasulfonated AlPC ($AlPCS_4$) in MilliQ (**I**), both at a 1.5-μM final PS concentration. The ROS-generating capacity of ZnPC-ITLs (**J**), AlPC-ITLs (**K**), $ZnPCS_4$ in physiological buffer [74] (**L**), and $AlPCS_4$ in physiological buffer (**M**) during PDT (pink area) was determined using the oxidation-sensitive fluorogenic probe 2',7'-dichlorodihydrofluorescein ($DCFH_2$), prepared as described in [386]. The mean ± SD DCF fluorescence intensities are plotted for $n = 3$ experiments and the experiment was carried out according to [74].

3.2. Advantages of metallated phthalocyanines over conventional photosensitizers

An important advantage of metallated PCs over clinical first-generation PSs such as HpD, porfimer sodium, and 5-ALA as well as the second-generation PS mTHPC is that the PC Q-band maximum of ~675 nm lies more favorably in the therapeutic window (**Fig. 3B** and **Fig. 6E**), accounting for greater optical penetration depth and more homogeneous photon distribution throughout the target tissue. Diamagnetic PCs also exhibit an ε that is several orders of magnitude greater than that of traditional PSs (**Fig. 2E**), resulting in more effective photon absorption at a wavelength at which there is less competitive absorption and scattering by tissue [4]. A higher ε in combination with a larger Φ_T further lowers the intratumoral PS concentration that is required for a therapeutic response, thereby reducing PDT-related side effects such as phototoxicity as a lower PS dose suffices [172].

Another beneficial aspect of PCs is that they do not exhibit notable toxicity [173]. With respect to phototoxicity, it is well-documented that the clinically approved PSs elicit considerably longer photosensitivity, and thus potential phototoxicity, than the metallated PCs, which have not been associated with skin phototoxicity to date (**Table 1**). The photosensitivity of HpD and porfimer sodium, for example, extends to as much as 4–12 weeks after PS administration, which corresponds to the time patients must be kept away from light exposure. This is mainly due to a combination of factors, including long elimination half-life of the PSs (**Table 1**), long clearance times from the skin (**Table 1**), and a relatively unfavorable spectral overlap with sunlight (**Fig. 3B**) [174, 175]. The photosensitivity of mTHPC is also quite extensive, namely 2–4 weeks, while that of 5-ALA is clinically manageable. However, the use of 5-ALA is associated with other drawbacks related to its photophysical properties (**Fig. 2E**) and unfavorable pharmacokinetics (*i.e.*, low tumor:healthy tissue ratio) after systemic administration (**Table 1**), as addressed below.

In regard to the toxicity profiles of the clinically approved PSs, Berlanda *et al.* studied the dark toxicity of mTHPC (both Foscan and its polyethylene glycol (PEG)-conjugated derivative, Fospeg), porfimer sodium, and 5-ALA, amongst others, in A431 cells [176]. The lethal 50% dose (LD_{50}) for non-irradiated Foscan, Fospeg, porfimer sodium, and 5-ALA was 8, 246, 5, and 9040 μM, respectively. The LD_{50} value for $AlPCS_4$ could not be calculated as its dark toxicity did not fall below 50% at concentrations up to 200 μM. Similarly, Amin *et al.* found no dark toxicity of $AlPCS_4$ up to a concentration of 500 μM in bladder cancer (T24) cells [177]. A summary of the dark toxicity LD_{50} values is provided in **Table 1**. In addition, PCs appear to be non-genotoxic compounds. PDT with AlPC induced considerable oxidative damage and cell death in human oral keratinocytes *in vitro*, but without inducing a genotoxic response, as confirmed by the comet assay [178]. These results were corroborated in another study employing AlPC-PDT [179]. Similarly, $ZnPCS_4$ is not genotoxic upon PDT *in vitro* [180], although its utility in PDT is limited due to the relatively poor ROS-generating capacity (**Fig. 6L**).

With respect to clinically approved PSs, mTHPC did not induce DNA damage in human myeloid leukemia (K562) and nasopharyngeal carcinoma (CNE2 and HK1) cells under dark conditions or following PDT [181, 182]. In contrast, considerable DNA damage was observed in K562 cells after HpD-PDT [181]. Other *in vitro* studies showed that treatment of cells with 5-ALA resulted in mutagenic effects after exposure to visible light [183]. Chromosomal aberrations and formation of micronuclei were also detected under dark conditions [184]. Of note, as the photoactive product of 5-ALA, namely PpIX, is produced in mitochondria, it is conceivable that most of the genomic aberrations might be confined to mitochondrial DNA, which is a typical target for DNA modifications, even during regular energy metabolism [185].

The safety:efficacy ratio of a compound is also an important parameter in pharmacology, as it reflects the 'clinical worthwhileness' of a drug. In case of PDT, this ratio can be calculated by dividing the PS LD_{50} (*i.e.*, dark toxicity) by the PS LD_{50} following PDT. The safety:efficacy values for Foscan, Fospeg, porfimer sodium, and 5-ALA in A431 cells were 268, 4695, 3, and 23, respectively [176], whereby the lower values indicate a less favorable balance between dark toxicity and PDT efficacy. The safety:efficacy ratio of $AlPCS_4$ could not be derived in this study, as the dark toxicity was too low to calculate an LD_{50} value. The safety:efficacy ratio of Foscan in two biliary tract cancer cell lines (gall bladder cancer and bile duct cancer cells) was 356 and 410, respectively [186].

Moreover, the tumor:healthy tissue ratio is a critical *in vivo* pharmacokinetic parameter because it relates PDT efficacy to biodistribution and potential (photo) toxicity. Theoretically, a high tumor:healthy tissue ratio is likely to improve therapeutic outcome and reduce drug accumulation in healthy tissue, which is inherently proportional to the level of undesired side effects. For example, porfimer sodium exhibited a tumor:skin ratio of only 1.7:1 in a hamster melanoma model [187]. Similarly, intravenously or intravesically injected 5-ALA resulted in a tumor:bladder wall ratio of 2:1 in an orthotopic rat bladder tumor model [188]. Slightly higher tumor:normal adjacent mucosa ratios of 2–3:1 were observed for mTHPC after intravenous injection in patients with different types of solid cancer [189]. In case of diamagnetic PCs, the majority of studies on these PSs have employed liposomal formulations (discussed in the next section) as a delivery vehicle. In a fibrosarcoma mouse model using ZnPC liposomes, tumor:muscle ratios (muscle tissue adjacent to the fibrosarcoma) of 7.5:1 [190] and 9:1 [191] were found 18 to 24 h post-injection, respectively. Furthermore, Chan and colleagues showed that the uptake of sulfonated AlPC in Colo 26 tumor-bearing mice was dependent on the degree of sulfonation [33]. Whereas $AlPCS_4$ accumulated in tumors at a 10:1 tumor:adjacent tissue ratio, lower ratios were observed with a lower degree of sulfonation. Accordingly, monosulfonated AlPC appeared to have the lowest tumor:adjacent tissue ratio (*i.e.*, <2:1). Similar tumor:tissue ratios (*i.e.*, 10:1) for $AlPCS_4$ were observed in mice bearing melanoma tumors, which peaked 18

h after systemic administration [192]. The tumor:tissue ratios of the most common clinical and experimental PSs are listed in **Table 1**.

Lastly, the high log *P* value of metallated PCs (**Fig. 6E**) is responsible for the distribution of these PSs to a wide variety of lipophilic compartments (Sections 2.2.2 and 4.4.2). PDT of metallated PC-containing cells will therefore induce oxidative damage at multiple intracellular sites that are critical to cell viability and function (Section 2.3). As addressed in Section 2.3.1, the mode of cell death depends on intracellular PS localization and thus the origin of PDT-induced damage. Given that metallated PCs localize to multiple intracellular sites, PDT with these PSs will activate different modes of cell death that will ultimately result in necrotic, apoptotic, necroptotic, and/or autophagic cell death. The concomitant activation of different cell death pathways will therefore increase the probability that a tumor cell is terminated after PDT through the 'cumulative cell death induction effect' rather than salvaged by activated survival and/or stress response mechanisms [68]. Consequently, the cytotoxic potential of irradiated PCs is theoretically higher per mole compound in a cell than for PSs that target to a single location, such as lutetium texaphyrin [193], verteporfin [194], and hypericin [79], where only one specific cell death induction pathway dominates.

In the final analysis, compared to clinically approved PSs, diamagnetic PCs have a more red-shifted Q-band maximum and superior molar absorptivity, which facilitates deeper light penetration, a higher efficiency of light absorption at clinically relevant wavelengths, and extensive ROS generation at comparably lower intratumoral PS concentrations. The generation of ROS occurs at multiple cellular locations, which enables optimal PDT efficacy due to the cumulative cell death induction effect. Moreover, diamagnetic PCs exhibit no dark toxicity or genotoxicity, even after irradiation. Lastly, the diamagnetic PCs are associated with a higher safety:efficacy ratio and tumor:healthy tissue ratio, altogether making these metallated PCs more suitable for PDT compared to conventional PSs. Unfortunately, a direct comparison regarding the therapeutic efficacy of clinical PSs and diamagnetic PCs could not be made inasmuch as the effectiveness (*e.g.*, LD_{50} value) is dependent on several variables such as irradiance, cumulative radiant exposure, wavelength/molar absorptivity, and cell/tumor tissue type, which widely differ among studies.

4. Multi-targeted photosensitizer-encapsulating nanoparticulate delivery systems for photodynamic therapy

A major obstacle in oncopharmacology is specific delivery of drugs to the tumor, as is for instance problematic with most orally or intravenously administered chemotherapeutics. The unspecific uptake of chemotherapeutic agents by healthy tissue causes all sorts of sequelae that impose a significant burden on patient well-being and quality of life. As a result, numerous chemotherapeutic agents have been

encapsulated in nanoparticulate drug delivery systems to improve drug solubility, to ensure improved delivery to the tumor and enhanced therapeutic efficacy, and to reduce chemotherapy-associated side effects (reviewed in [195]).

4.1. Non-liposomal photosensitizer carrier and delivery systems

Nanoparticulate PS delivery systems can be classified into lipid-based and non-lipid based delivery systems. Both types of delivery systems are described in **Table 2**, including the physico-chemical attributes as well as the advantages and disadvantages in terms of PS delivery. The lipid-based delivery systems include LDL, micelles, and solid lipid nanoparticles, all of which are water-compatible carriers suitable for the encapsulation of hydrophobic PSs (**Table 2**). LDL is an endogenous blood-borne particle composed of (free and esterified) cholesterol, phospholipids, triglycerides, and a single apoliporotein B-100 that the body uses for the transport of lipophilic biomolecules (*e.g.*, cholesterol) to cells. Micelles comprise small-diameter particles composed of a phospholipid monolayer that, in case of normal-phase micelles, contain an acyl chain-based core and the hydrophilic head groups positioned at the phospholipid–water interface. Solid lipid nanoparticles are composed of a solid lipid core that is stabilized by a surfactant layer, albeit the composition can be highly variable. The micelles and solid lipid nanoparticles can be functionally modified to accommodate a specific pharmacokinetic purpose, including PEGylation to enhance circulation half-life [196, 197] and the conjugation of ligands for *e.g.*, immunotargeting [198, 199], whereas this is less applicable to LDL due to its intrinsic targeting properties. LDL has been employed for intratumoral PS delivery [200, 201] via its cognate LDL receptor (LDLR). However, this delivery system may lack targeting specificity inasmuch as the LDLR is not exclusively present on tumor cells and a variety of malignant tissues lack overexpression of LDLR (reviewed in [202]).

Of the non-lipid based nanoparticles, dendrimers, polymeric micelles, and polymers are capable of encapsulating hydrophobic as well as hydrophilic PSs (**Table 2**). Dendrimers are supramolecular assemblies typically composed of branched polyaminoamides that can be synthesized in a controlled manner with a high monodispersity (reviewed in [203, 204]). However, the *in vivo* toxicity data for dendrimers is currently unavailable, which limits the prospects for clinical applicability. Polymeric micelles are nanoparticles that are usually composed of amphiphilic polymers, including PEG-based phospholipid conjugates and poloxamers [205]. Although polymeric micelles have a high structural stability and low toxicity (**Table 2**), the development of these nanoparticles may be hampered by technical difficulties in specific polymer synthesis and efficient drug incorporation methods on an industrial-scale basis [206]. Alternatively, polymeric nanoparticles are generally composed of biodegradable polymers, including polyglycolic acid, polylactic acid, and poly(lactic-co-glycolic acid), which are generally non-toxic [207]. Although polymeric

Lipid-based	Size [nm]	Carrier material	Encapsulated PS	(Dis)advantages	[Ref]
Liposomes	15 – 1,000	Hydrophobic Hydrophilic	5-ALA [321], AlPC [255], AlPCS4 [257], mTHPC [236], porfimer sodium [322], temocene [323], ZnPC [74]	+ Versatility + Non-toxic + Payload - Stability - PS transfer	[324]
Low-density lipoprotein	18 – 25	Hydrophobic	Bacteriochlorin e6 bisoleate [325], hematoporphyrin [200], SiPC [326], ZnPC [201]	+ Endogenous carrier + Drugs are protected + Circulation time - Specificity - Requires overexpression of LDLR	[202]
Micelles	2 – 20	Hydrophobic	Cl2SiPC [327], HexSiPC [327], temocene [328], ZnPC [329]	+ Synthesis + Shelf-life + Low viscosity - Low solubilization - Potential surfactant toxicity	[330]
Solid lipid nanoparticles	50 – 1,000	Hydrophobic	Hypericin [331], mTHPC [332]	+ Easy to scale up + Water-based technology + Biocompatibility - Particle growth - Drug loading capacity	[333]
Other					
Dendrimers	1 – 100	Hydrophobic Hydrophilic	5-ALA [334], SiPC [335]	+ Monodispersity + Versatility + High payload - Lack of *in vivo* toxicity data - Preparation is laborious	[203]
Gold nanoparticles	1 – 100	Hydrophobic Hydrophilic	5-ALA [336], PpIX [337], ZnPC [338]	+ Physico-chemical properties of gold + Synthesis + Versatility - Potential toxicity - Costs	[339]
Polymeric micelles	10 – 100	Hydrophobic Hydrophilic	mTHPC [340], Pc 4 [341], porfimer sodium [342], ZnPC [343]	+ Structural stability + Payload + Low toxicity - Synthesis - No universal incorporation method	[344]
Polymeric nanoparticles	10 – 1,000	Hydrophobic Hydrophilic	5-ALA [345], mesochlorin e6 [346]	+ Versatility + Biocompatibility + Synthesis - Encapsulation efficiency - Stability	[208]
Quantum dots	2 – 100	Hydrophobic Hydrophilic	AlPCS4 [214], chlorin e6 [347], PpIX [348], Rose Bengal [349]	+ Unique optical properties + Tunable surface properties - Limited knowledge on clinical use - Potential toxicity - Compatibility in biological environments	[350]

Table 2. Overview of lipid- and non-lipid-based nanoparticles that have been used for the delivery of photosensitizers. Abbreviations: AlPCS4, tetrasulfonated chloroaluminumphthalocyanine; Cl2SiPC, dichlorosilicon phthalocyanine; HexSiPc, bis(tri-*n*-hexylsiloxy)silicon phthalocyanine; LDLR, low-density lipoprotein receptor; Pc 4, silicon phthalocyanine 4; SiPC, silicon phthalocyanine.

nanoparticles may be attractive as a delivery vehicle, there are still some difficulties to overcome, including a poor encapsulation efficiency [208, 209] and a poor PS stability in solution [210].

In contrast, gold nanoparticles and quantum dots are nanoparticles with unique physico-chemical and optical properties, respectively [211]. Gold nanoparticles that are coupled to PSs have been associated with increased $^1O_2$ upon irradiation as a result of surface plasmon resonance (reviewed in [212]), allowing these particles to be used for PDT as well as photothermal therapy. Moreover, the excitation wavelength is tunable to wavelengths in the far red [213], enabling deep light penetration and relatively homogenous irradiation of bulkier tumors. Quantum dots are semiconductor nanocrystals that function as light acceptor for subsequent PS activation via fluorescence resonance energy transfer [214]; the PS therefore has to be conjugated to the quantum dots in order to achieve a photodynamic effect. Although gold nanoparticles and quantum dots are attractive for PDT, the nanoparticles may be quite toxic (**Table 2**) and therefore limited in terms of clinical applicability.

Inasmuch as the nanoparticulate PS delivery systems addressed in this section may not be ideal for clinical PDT (**Table 2**), the following sections will focus on liposomes for intratumoral PS delivery. Although liposomes are not superior to the abovementioned PS delivery systems *per se*, the combination of advantages (next section) makes liposomes very suitable for PS targeting to tumors.

4.2. Liposomal photosensitizer carrier and delivery systems

To date, the Food and Drug Administration has approved liposomal formulations of two anti-cancer drugs, daunorubicin and doxorubicin, and various anti-cancer formulations are under evaluation in clinical trials [215, 216]. It is somewhat surprising that none of these drugs include a PS, given the fact that the clinical implementation of PDT is primarily hampered by ethical issues related to phototoxicity (which can be alleviated by encapsulation) while the therapy is very effective for several cancer types (Section 1). At this moment, clinical phase I/II trials with liposome-encapsulated PSs are being conducted exclusively with verteporfin (Fospeg). Of note, it is not expected that PDT with liposome-encapsulated first-generation PSs will result in better therapeutic outcomes compared to liposome-encapsulated second-generation PSs, given that the majority of drawbacks of the first-generation PSs as addressed in Section 3.2 will remain an issue.

In case of PDT with second-generation PSs (metallated PCs), liposomal encapsulation (in which case it is referred to as a third-generation PS) is advantageous [217] for several reasons. First, liposomes are able to encapsulate hydrophilic and lipophilic molecules and hence render the highly lipophilic second-generation PSs compatible with plasma. Second, liposomal incorporation resolves PS aggregation in aqueous solutions such as biological fluids, which negatively affects Φ_T and

ROS generation [218-220]. Third, due to the high payload, a single liposome could theoretically deliver a sufficient amount of PS to a cell to cause lethal oxidative stress following PDT. As a result, less liposomal PS can be administered to patients to achieve equal intratumoral PS levels compared to unencapsulated PS. Moreover, unencapsulated PSs have a tendency to extravasate and accumulate in the skin. Liposomal encapsulation minimizes PS accumulation in the skin [221, 222], which will not only reduce phototoxicity but also further improve PS bioavailability for tumor targeting. Fourth, additional pharmacological compounds can be co-encapsulated in a single delivery system (in which case it is referred to as a fourth-generation PS) for further improvement of therapeutic efficacy. Finally, in addition to the inherent non-toxicity of neutral phospholipids [223, 224], *i.e.*, typically the main lipid constituents of liposomal drug delivery systems [225], liposomes can easily be modified compositionally to facilitate the unique prerequisites of the drug delivery system and to accommodate a specific physiological context. For instance, liposome uptake by cells of the mononuclear phagocyte system can be considerably forestalled by proper sizing [226] and by the conjugation of PEG to component phospholipids, usually phosphatidylethanolamine [227-230]. It has been proposed that (1) the presence of a "dense conformational cloud" by the PEG polymers over the liposome surface [231], (2) the repulsive interactions between PEG-grafted membranes and blood constituents [232], (3) the hydrophilicity of PEGylated formulations [233], and (4) the decreased rate of plasma protein adsorption on the hydrophilic surface of PEGylated liposomes [234] impose so-called 'stealth' properties [235]. Consequently, PEGylated liposomes are targeted to tumors by means of the EPR effect, which facilitates higher tumor:healthy tissue ratios and tumor killing capacity compared to their unencapsulated equivalents [236, 237]. Inclusion of PEG chains further enables the design of immunoliposomes capable of homing to the target site through the attachment of antibodies, antigen-binding fragments (Fab' fragments), or nanobodies to a chemically modified distal end of a liposome-grafted PEG chain [238-241]. As for the stealth liposomes, the use of drug-encapsulating immunoliposomes is associated with greater *in vivo* target selectivity and improved cytostatic efficacy (**Table 3**). More detailed information on the utility of PS encapsulation into lipid-based delivery systems is available elsewhere [21].

In light of the advantages of liposomal encapsulation of metallated PCs and the proven *in vivo* efficacy of stealth liposomes and immunoliposomes, the remainder of this review will mainly focus on second-generation PC-encapsulating liposomes for the treatment of solid tumors. Three different liposomal formulations will be addressed from the perspective of a comprehensive multi-targeting modality. Inasmuch as diamagnetic PCs exhibit similar photochemical and photophysical properties (Section 3.1), ZnPC is used as a model PS in many instances.

Target	Antibody	Cancer subtype	Liposomal composition	Drug	Response	[Ref]
CD19	Anti-CD19 mAb	B-cell lymphoma	HSPC:Chol:mPEG	Doxorubicin	Improved survival compared to untargeted liposomes.	[351]
CD19	Anti-CD19 mAb Anti-CD19 Fab	B-cell lymphoma	SM:Chol:mPEG	Doxorubicin Vincristin	Significantly more effective than untargeted liposomes or free drug.	[352]
EGFR	IMC-C225 Fab	Breast cancer	DSPC:Chol:mPEG	Various	Significant anti-tumor effects and superior to untargeted liposomes.	[264]
EGFR	EMD72000 Fab IMC-C225 Fab	Breast cancer, colorectal cancer	DSPC:Chol:mPEG	Doxorubicin	High uptake in various EGFR-overexpressing cell lines.	[353]
EGFR	EGFR mAb	Non-small cell lung cancer	DOPE:CHEMS: PDP-PEG-DOPE	Gemcitabine	Significant tumor reduction in A549 tumor-bearing nude mice.	[354]
EGFR	EGFR mAb	Glioblastoma multiforme	Soy PC:Chol: mPEG:PEG-PE		Significantly enhanced accumulation and uptake.	[355]
EGFR	EGFR mAb	Ovarian carcinoma	HSPC:Chol:mPEG	Doxorubicin	Accumulation was comparable to control liposomes.	[356]
GD2	Anti-GD2 mAb Anti-GD2 Fab	Neuroblastoma	HSPC:Chol:mPEG	Doxorubicin	Complete inhibition of metastatic growth in a nude mouse model.	[357]
HBEGF	Anti-HBEGF Fab	Breast cancer	HSPC:Chol:mPEG	Doxorubicin	Tumor regression in MDA-MB-231 tumor-bearing mice.	[266]
HER-2	Anti-HER2 scFV	Breast cancer	POPC:Chol:m-PEG	Doxorubicin	Significant decrease in tumor size compared to untargeted liposomes.	[358]
HER-2	Anti-HER2 Fab	Breast cancer	EPC:Chol:mPEG	PE38KDEL	Receptor-specific binding and internalization *in vitro*.	[359]
HER-2	Anti-HER2 Fab	Breast cancer	POPC:Chol: mPEG	HPTS (probe)	The uptake correlated with the cell surface expression of HER2 *in vitro*.	[360]
IGF-1R	1H7 mAb	Pancreatic carcinoid cancer	HSPC:Chol:mPEG	Doxorubicin	Superior antitumor efficacy compared to control liposomes.	[361]
MT1-MMP	222-1D8 Fab	Fibrosarcoma	HSPC:Chol:mPEG	Doxorubicin	Significant suppression of tumor growth, independent of tumor accumulation.	[362]
VCAM-1	Anti-VCAM-1 mAb	Multiple myeloma	Soy PC:Chol: cyanur-PEG-PE		Selective targeting of tumor vessels.	[363]
VEGFR	DC101 Fab	Hepatocellular carcinoma	PC:mPEG	Doxorubicin	Significant delay of tumor growth up to 7 weeks.	[364]
VEGFR	DC101 Fab	Colon cancer, breast cancer, pancreatic cancer	DSPC:Chol:mPEG	Doxorubicin	Superior therapeutic efficacy and selective abolishment of the tumor vasculature.	[365]

Table 3. Summary of experimental *in vivo* studies with immunoliposomes. Abbreviations: CHEMS, cholesteryl hemisuccinate; Chol, cholesterol; DOPE, dioleoyl phosphatidylethanolamine; DSPC, distearoyl phosphatidylcholine; EGFR, epidermal growth factor receptor (HER1); EPC, egg phosphatidylcholine; Fab antigen-binding fragment; GD2, ganglioside GD2; HBEGF, heparin-binding EGF-like growth factor; HPTS, 8-hydroxypyrene-1,3,6-trisulphonic acid; HSPC, hydrogenated soy phosphatidylcholine; IGF-1R; insulin-like growth factor 1 receptor; ILs, immunoliposomes; mAb, monoclonal antibody; mPEG, methoxy polyethylene glycol; MT1-MMP, membrane

type-1 matrix metalloproteinase; PC, phosphatidylcholine; PDP-PEG-DOPE, 3-(2-pyridyldithio)propionic acid-polyethylene glycol-DOPE; PEG-PE, polyethyleneglycol-phosphatidylethanolamine; POPC, palmitoyloleoyl phosphatidylcholine; scFV, single-chain variable fragment; SM, egg sphingomyelin; VCAM-1, vascular cell adhesion molecule 1; VEGFR, vascular endothelial growth factor receptor.

4.3. Phthalocyanine-encapsulating liposomes

Metallated PC-containing liposomes have been employed for a broad array of clinical applications, including the treatment of cutaneous leishmaniasis [242], antineoplastic therapy [190, 243, 244], and diagnostic applications in atherosclerosis [245]. For the treatment of solid cancers, ZnPC has been conjugated to LDL [201] and serum albumin for systemic administration [246], encapsulated into various nanoparticulate drug delivery systems for intravenous infusion [244, 247-249], and formulated in a mixture of oleic acid and propylene glycol for topical administration [250]. With respect to liposomal formulations, *in vivo* studies demonstrated accumulation of liposomal ZnPC in tumors, the subsequent irradiation of which led to a significant reduction in tumor size [201]. A liposomal formulation of ZnPC (CGP-55847, Ciba-Geigy) was evaluated in a phase I/II clinical trial for the treatment of squamous cell carcinoma in the upper digestive tract [172]. However, the clinical trial with CGP-55847 was discontinued due to reasons not publicly disclosed.

An advantage of liposomal ZnPC, on top of the previously addressed benefits of liposomal encapsulation (Section 4.2), is that incorporation into a lipid bilayer does not negatively affect the photochemical properties of ZnPC (**Figs. 6F** and **7**). The electronic transition states of π-electrons are susceptible to changes in chemical environment (*e.g.*, solvent or polarity effects), which could impact the peak position of the absorption/excitation spectrum of a molecule as well as its singlet and triplet state quantum yield [251]. As shown in **Fig. 6F**, the main absorption bands of ZnPC in pyridine and liposomal ZnPC fully overlap, indicating that the Q-band electronic transition states are not influenced by the lipid bilayer. Moreover, the fluorescence excitation and emission spectra of ZnPC in pyridine are entirely superimposable on the spectra of liposomal ZnPC, attesting to the fact that the singlet state is not influenced by the lipid bilayer (**Fig. 7A**) [74]. **Fig. 7B** and **C** further show that liposomal ZnPC produces ROS upon PDT that oxidize small molecules (2',7'-dichlorodihydrofluorescein) and large biomolecules (albumin), respectively [74]. The generation of ROS proceeds in a PS:lipid molar ratio- (**Fig. 7B** and **C**) and irradiance-dependent manner (**Fig. 7D**) [74], and the extent of oxidation of extraliposomal compounds is hampered by the presence of antioxidants in the membrane, such as cholesterol [252], α-tocopherol [253], and (poly)unsaturated fatty acids [254]. Although the amount of ROS generation is linearly proportional to the amount of ZnPC in the membrane, there is an optimal PS:lipid molar ratio beyond which the extent of ROS generation plateaus and abandons linearity, despite an increased ZnPC bilayer density (**Fig. 7B** and **C**) [74]. At a PS:lipid molar ratio of >0.003, ZnPC starts forming aggregates [255] that, due to altered relaxation

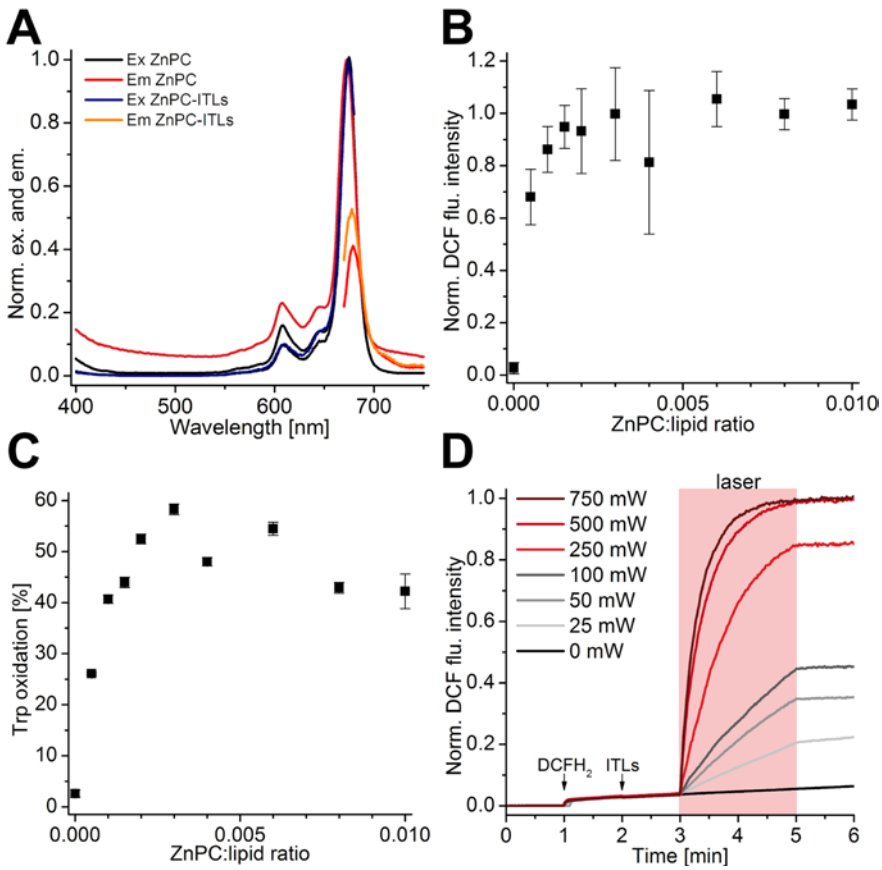

Fig. 7. (**A**) Normalized fluorescence emission (Em) and excitation (Ex) spectra of unencapsulated ZnPC and ZnPC-containing liposomes (ZnPC–ITLs) consisting of DPPC:cholesterol:DSPE-PEG (66:30:4 molar ratio) in physiological buffer. (**B**) ZnPC:lipid ratio-dependent ROS generation following PDT with ZnPC-ITLs. ROS production was assayed with 2',7'-dichlorodihydrofluorescein ($DCFH_2$). The protocol is described in [74]. (**C**) ZnPC:lipid ratio-dependent oxidation of tryptophan (Trp) residues in bovine serum albumin following PDT with ZnPC–ITLs. The protocol is described in [74]. (**D**) Laser power-dependent oxidation kinetics of $DCFH_2$ during PDT with ZnPC–ITLs. The protocol is described in [74].

mechanisms in excited PS dimers/multimers [219] and/or reduced oxygen availability in these aggregates [218], results in impaired $^1O_2$ generation. Similar effects have been described for AlPC [255].

The main implication of these findings is that ZnPC retains its photophysical and photochemical properties once it has entered a cell, where it will distribute to the cell- and subcellular membranes as elaborated in Section 2.2.2. PDT with liposomally delivered ZnPC will induce (per)oxidation of proximal cellular constituents (**Fig. 7B** and **C**), particularly membrane-embedded molecules and bilayer constituents. The (per)oxidation of intra/transmembrane molecules and unsaturated lipids causes membrane perturbation and leakage of intracellular content, which has been demonstrated with PDT-subjected cell phantoms containing ZnPC in the bilayer [74].

The biological consequences of membrane permeabilization have been addressed in Section 2.3 and ultimately result in cell death, as experimentally demonstrated in the following sections.

4.4. Targeting photosensitizer-encapsulating liposomes to solid tumors

4.4.1. Comprehensive tumor-targeting strategy

The microenvironment of solid cancers can essentially be classified into three pharmacologically relevant target areas: the tumor cells that make up the bulk of the cancer, the endothelial cells that line the intratumoral vasculature, and the interstitial space that is comprised of stromal proteins, fibroblasts, and immune cells (macrophages and dendritic cells). PS-encapsulating liposomes for systemic administration can be prepared that preferentially accumulate in one of the three target areas. The generic make-up of the liposomes is presented in **Fig. 8**, and each formulation, namely tumor-targeting liposomes (TTLs), tumor endothelium-targeting liposomes (ETLs), and interstitially-targeted liposomes (ITLs) is discussed separately in Sections 4.4.2 through 4.4.4.

Principally, each formulation can be employed individually for PDT, whereby the TTLs and ETLs have proven most effective *in vitro* in terms of tumor killing potential [256, 257]. However, the implementation of a combinatorial, multi-targeting modality for PDT as illustrated in **Fig. 9** is advocated for two important reasons. First, the generation of oxidative damage at multiple intratumoral locations will translate to more extensive interference with post-treatment biological and biochemical processes and hence exacerbate the degree of tumor cell death. For example, if only the tumor cells are targeted, which is usually the case, the PDT-induced activation of cell death mechanisms may be reverted due to co-activation of cell survival and stress response pathways [68], leading to increased cancer cell survival following PDT. When, however, the TTL-induced damage profile is complemented by concomitant ETL-mediated vascular shutdown and consequent intratumoral anoxia, the chances that partially viable cells survive as a result of survival and recovery programs will considerably diminish. Second, the induction of damage in a greater tumor volume (*i.e.*, tumor parenchyma + vasculature + stroma versus parenchyma only) is expected to trigger more extensive DAMP release with a broader spectrum of DAMP molecules, which will result in a more profound immune response. As addressed in **Fig. 1** and Section 2.4, the PDT-induced immune response is critical for tumor removal through immunogenic apoptosis and immunological processing of tumor cells.

4.4.2. Photosensitizer-encapsulating tumor cell-targeting liposomes

Tumor cells constitute a primary target for second-generation lipophilic PSs such as ZnPC because their high log *P* value (**Fig. 6E**) causes the PS to localize to

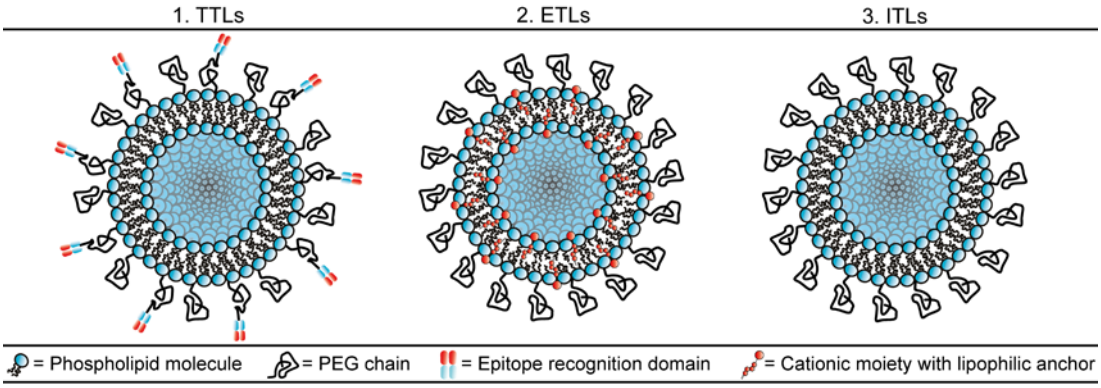

Fig. 8. (**1**) Tumor cell-targeting liposomes (TTLs) contain specific epitope recognition domains (*e.g.*, antibodies, Fab' fragments, nanobodies, or peptides) that are conjugated to an anchor molecule such as a lipid-conjugated, distally modified polyethylene glycol (PEG) chain. (**2**) Endothelial cell-targeting liposomes (ETLs) are typically cationic liposomes that exhibit a strong affinity for the negatively charged tumor endothelium. (**3**) Interstitially-targeted liposomes (ITLs) passively accumulate in the tumor interstitium by exploiting the enhanced permeability and retention (EPR) effect and poor lymphatic drainage in solid tumors. PEGylation of the liposomes imparts 'stealth' properties in that unspecific liposome uptake by the mononuclear phagocyte system is considerably forestalled.

the cell and organelle membranes, including those of mitochondria and the Golgi apparatus (ZnPC) [61, 258]. Consequently, PDT with PC-TTLs will induce oxidative damage at multiple critical sites, which will culminate in the execution of different cell death pathways as elaborated in Section 2.3.1. Extensive cell damage and death is not only imperative for optimal therapeutic efficacy, but also for minimizing the number of residual tumor cells that could mediate cancer recurrence, for optimally deterring the execution of cell survival pathways [68], and for maximally reducing post-treatment tumor sustenance through the processes related to the hallmarks of cancer [259, 260]. Moreover, tumor cells are the source of TAAs and DAMPs, which are released as a result of oxidation of membrane constituents or cell death signaling, that mediate the anti-tumor immune response (**Fig. 1**, Section 2.4) [96]. The extent to which these signaling molecules are liberated in the treated tissue, and hence the magnitude of the anti-tumor immune response, is proportional to the degree of induced damage. Accordingly, PDT with PC-TTLs is expected to induce widespread and pleiotropic oxidative damage that results in extensive cell death, a prolific anti-tumor immune response, and, in fully treated tumors, minimal probability of tumor recurrence.

TTLs (**Fig. 8**) are generally composed of phosphatidylcholines and a molar fraction of PEGylated lipids to which a ligand/epitope recognition molecule has been conjugated, such as an antibody, Fab' fragment, nanobody, or peptide (reviewed in [21, 217, 261]). The ligand/epitope recognition molecules typically bind to antigens that are abundantly expressed on the outer membrane of cancer cells but not or only minimally expressed by healthy cells. The different immunoliposome formulations and the ligand/epitope recognition molecules that have been investigated to date are summarized in **Table 3** and the ligands/epitopes that constitute viable targets for PS-containing

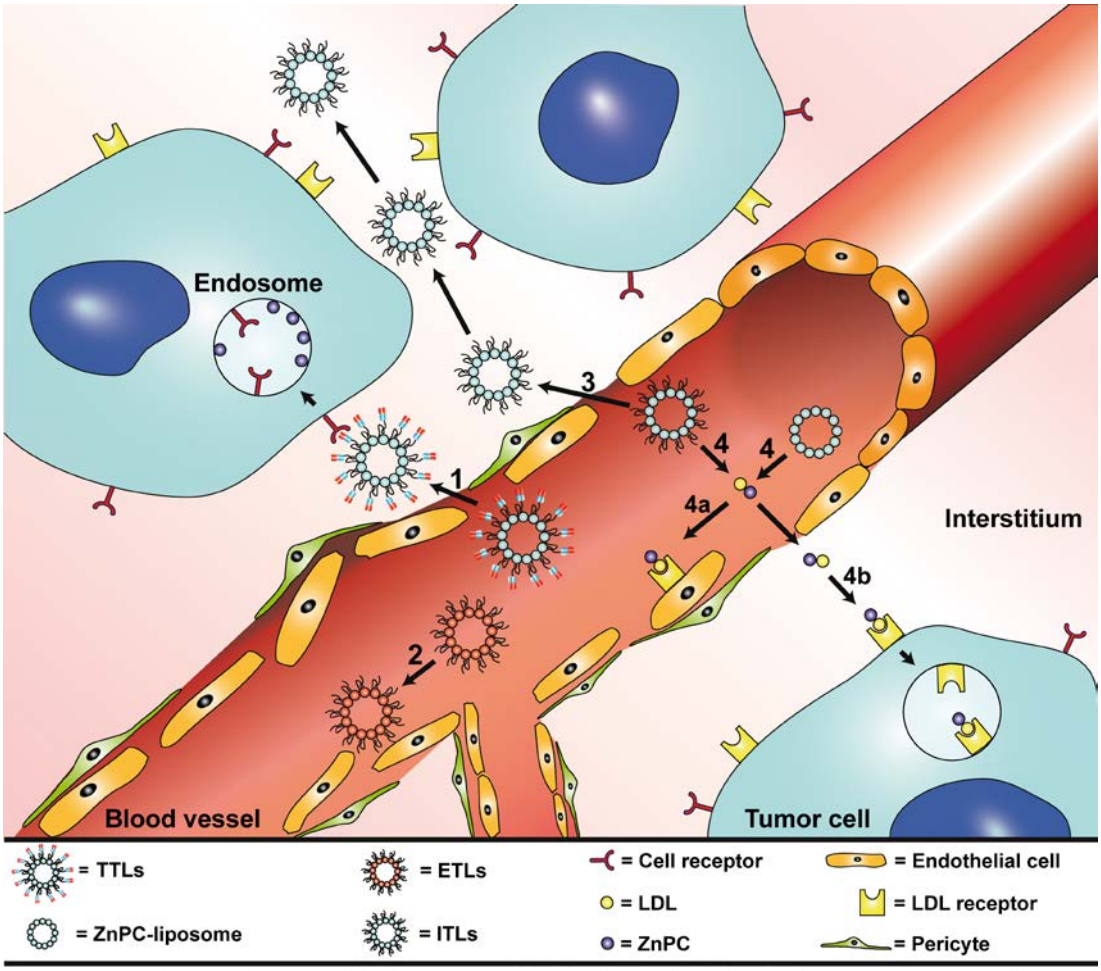

Fig. 9. *In vivo* pharmacokinetics of the liposomal PS-encapsulating formulations for tumor targeting (illustrated in **Fig. 8**). **Route 1** (Section 4.4.2): tumor-targeting liposomes (TTLs) extravasate and bind to the corresponding receptor on a tumor cell. **Route 2** (Section 4.4.3): cationic liposomes (ETLs) have a propensity to bind inflamed and angiogenic endothelium. **Route 3** (Section 4.4.4): sterically stabilized liposomes (ITLs) extravasate into the interstitium, enter the interstitial space, and accumulate due to the EPR effect. **Route 4** (Section 4.4.4): transfer of hydrophobic PSs from non-PEGylated liposomes to LDL particles. Consequently, the PS-LDL complexes (**4a**) bind to LDL receptors that are typically replete on endothelial cells lining the tumor vasculature or (**4b**) extravasate, bind to LDL receptors that are abundantly present on tumor cells, and enter the cells via endocytosis.

immunoliposomes specifically developed for the treatment of PDT-recalcitrant tumors (Section 1) are provided in **Table 4**.

The utility of immunoliposomes for the delivery of pharmacological agents has been demonstrated in numerous *in vitro* and *in vivo* studies. In mice, Song *et al.* [262] showed that systemically infused, sterically stabilized epidermal growth factor receptor (EGFR)-targeted liposomes were able to extravasate from the intratumoral microcirculation and specifically and efficiently bind to xenotransplanted EGFR-overexpressing human non-small cell lung carcinoma (H1299) cells, after which

Cancer type	Target ligand/epitope	Overexpression (OE) or positive staining (PS)	[Ref]
Superficial recurrent urothelial carcinoma	EGFR / HER-1	23.6% (OE)	[366]
	EGFR / HER-1	100% (PS)*	[367]
	HER-2	12.4% (OE)	[368]
	MUC-1	44.1% (OE)	[369]
Nasopharyngeal carcinoma	EGFR / HER-1	62.7% [43.2-83.3] (OE)	[370-373]
	HER-2	50.7% (PS)**	[371]
	IGF-1R	56% (OE)	[374]
Extrahepatic cholangiocarcinoma	EGFR / HER-1	33.7% [15.8-57.9] (OE)	[375-378]
	HER-2	23.2% [8.5-31.3] (OE)	[375-380]
	HER-2	80% (PS)***	[381]

Table 4. Potential targets of PDT-recalcitrant tumor types for immunoliposomes. An immunohistochemical expression score of ≥2 (scale 0–3) was considered overexpression. Positive staining was defined as followed: * staining index of ≥1.5 (staining intensity (0–3) × (number of positively stained cells/total number of cells counted)), ** staining in ≥10% of tumor cells, and *** >10% cytoplasm and membrane staining in all tumor cells. Abbreviations: EGFR, epidermal growth factor receptor; HER-1/2, human epidermal growth factor receptor 1/2; MUC-1, mucin 1, cell surface associated; IGF-1R, insulin-like growth factor 1 receptor.

the TTLs were internalized via an ATP-dependent process. Corroboratively, our group found that anti-EGFR nanobody-conjugated TTLs (1,2-dipalmitoyl-*sn*-glycero-3-phosphocholine (DPPC):cholesterol:1,2-distearoyl-*sn*-glycero-3-phosphoethanolamine-*N*-[methoxy(PEG)-2000] (DSPE-PEG), 66:30:4 molar ratio) extensively bound to and were taken up by human EGFR-transfected murine (HER14) fibroblasts (**Fig. 10A** and **B**) and A431 cells [21]. The *in vitro* and *in vivo* PDT efficacy of these TTLs will be published elsewhere [21, 263]. Mamot *et al*. [264] demonstrated that anti-EGFR TTLs exhibit a 6-fold higher uptake by EGFR-transfected human primary glioblastomas (U87) in mice versus non-targeted (anti-EGFR C225 Fab-lacking) liposomes. The TTLs were presumably internalized via receptor-mediated endocytosis. Park *et al*. [265] found that systemic administration of either sterically stabilized liposomes (comparable to ITLs, Section 4.4.4) or anti-human epidermal growth factor receptor 2 (HER-2)-conjugated TTLs resulted in equivalent levels of accumulation in xenografted breast cancer (BT-474, MDA-MB-453, MCF-7/HER2) tumors in mice, but the intratumoral distribution and internalization pattern clearly differed between the formulations. Whereas sterically stabilized liposomes accumulated extracellularly, the PEGylated anti-HER2 TTLs predominantly distributed in the cytoplasm of tumor cells. Of note, the conjugation of antibodies or fragments thereof to *e.g.*, PEG chains appear not to alter the size, surface charge, or pharmacokinetic properties of the liposomes compared to non-targeted, PEGylated liposomes [264, 266].

Due to the selective uptake of PS-TTLs, intracellular PS levels are generally higher than for their non-targeted counterparts, causing the TTLs to be more potent

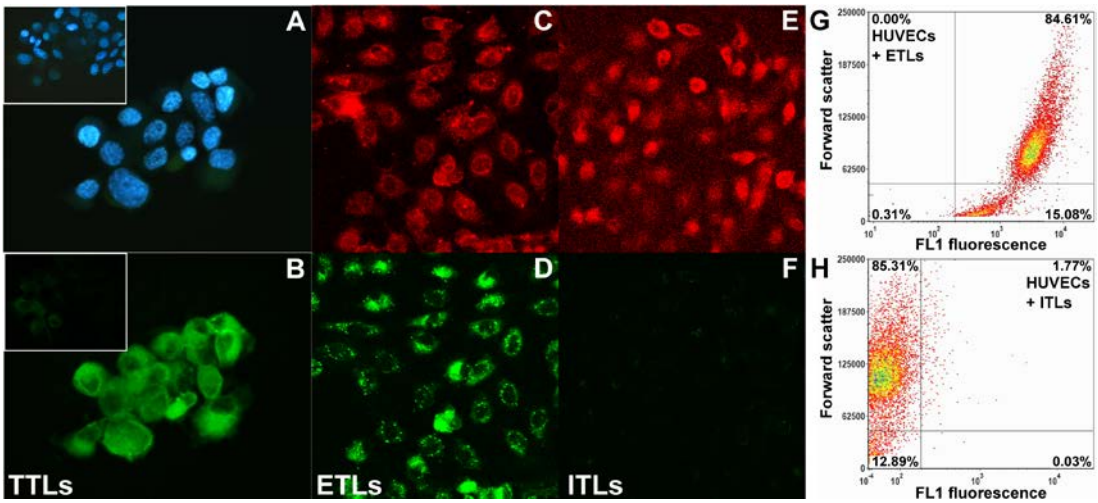

Fig. 10. Confocal images of DAPI-stained (in blue) EGFR-overexpressing HER14 cells (**A**) that have taken up anti-EGFR nanobody-conjugated TTLs (composed of DPPC:cholesterol:DSPE-PEG:NBD-PC (62:30:4:4 molar ratio)) fluorescently labeled with nitrobenzoxadiazole (NBD, green fluorescence) (**B**). The inserts in (**A**, **B**) are comparable images of HER14 cells incubated with fluorescently labeled control liposomes. Human umbilical vein endothelial cells (HUVECs) (isolated as described in [387]) were stained with ToPro3 (**C**, **E**) and incubated with NBD-labeled ETLs (composed of DPPC:DC-cholesterol:cholesterol:DSPE-PEG:NBD-DPPC (60:25:5:5:5 molar ratio)) (**D**) or ITLs (composed of DPPC:cholesterol:DSPE-PEG:NBD-DPPC (60:30:5:5 molar ratio)) (**F**). The uptake of NBD-labeled ETLs (**G**) and the lack of uptake of NBD-labeled ITLs (**H**) by HUVECs was confirmed by flow cytometry (protocol described in [74]). NBD fluorescence was measured in the FL1 fluorescence channel of the flow cytometer.

in terms of phototoxicity. Gijsens *et al.* [257] demonstrated that $AlPCS_4$-encapsulating transferrin-conjugated liposomes exhibit a 10-fold lower IC_{50} value than non-targeted liposomes in HeLa cells treated with PDT (0.63 μM versus 6.3 μM $AlPCS_4$, respectively). Moreover, the intracellular accumulation of transferrin-conjugated TTLs was significantly higher than free $AlPCS_4$ or non-targeted liposomes. García-Diaz *et al.* used folate-conjugated liposomes containing zinc tetraphenyl porphyrin (ZnTPP) to treat folate receptor-expressing HeLa cells [267]. At a concentration of 1 μM ZnTPP and a radiant exposure of 10 J/cm^2, the non-targeted liposomes induced cell death in 65% of HeLa cells, whereas folate-conjugated liposomes led to a 94% mortality rate 24 h post-PDT. In line with previous findings, human ovarian carcinoma (Ovcar-5) cells treated with verteporfin-containing anti-EGFR TTLs exhibited significantly lower cell viability than non-targeted liposomes [268].

The data presented in this section indicate that the overexpression of specific surface recognition domains (*e.g.*, transferrin receptor, EGFR) by tumor cells can be exploited for tumor cell targeting. High intracellular PS concentrations are subsequently achieved via endocytosis. Consequently, as has been determined in a variety of studies, this PDT strategy is expected to produce increased levels of phototoxicity compared to unencapsulated PSs or PS-encapsulating non-targeted liposomes.

4.4.3. Photosensitizer-encapsulating endothelial cell-targeting liposomes

It is widely accepted that intratumoral vasculature plays a pivotal role in tumor sustenance and progression, as it provides the tumor with oxygen and nutrients. Correspondingly, photodestruction of tumor vasculature is a decisive therapeutic outcome of PDT [249, 269-272]. It has been shown in mice that PDT with the systemically infused PS MV6401 resulted in acute vasoconstriction and thrombosis 3 h after PDT [273]. Fingar *et al.* [274] reported that verteporfin-mediated PDT of chondrosarcomas in rats resulted in selective destruction of tumor vasculature, which was associated with thrombus formation, hemostasis, and long-term tumor regression.

Blood vessels constitute an ideal target for PDT inasmuch as the relatively high local oxygen tension (in blood vessels and endothelium) as well as the physiologically abundant presence of the radical nitric oxide contribute to exacerbated ROS/RNS production upon PS excitation. Photochemical affliction of tumor microvasculature leads to acute tumor infarction, culminating in a local anoxic/hypoxic and malnourished environment that is associated with stalled tumor growth in case of sustained hemostasis [273]. Moreover, thrombi are potent chemoattractants for cells of the innate immune systems (neutrophils and monocytes/macrophages) that, when activated, propagate thrombus/vascular remodeling by releasing cytokines and chemokines to attract additional immune cells to the thrombostatic vasculature [275, 276]. Accordingly, PC-ETLs are potentially effective in PDT of particularly hypervascularized tumors by inducing cessation of oxygen and nutrient supply and corollary cell death [273, 277, 278], retarding tumor growth [273], and triggering pro-inflammatory signaling that leads to an anti-tumor immune response (Section 2.4) and removal of PDT-afflicted tissue (reviewed in [96]).

The uptake of PC-ETLs by intratumoral endothelial cells can be achieved by coating the liposomes with specific endothelium-recognizing epitopes or by imparting a positive surface charge on the liposomes. In case of the former, a variety of epitopes that are abundantly present on tumor cells can also be used to target the tumor endothelium, as elaborately described in [279] and summarized in **Table 3** and **Table 4**. These includes vascular cell adhesion molecule-1 (VCAM-1), membrane type-1-matrix metalloproteinase (MT1-MMP), integrins αvβ3, αvβ5, and α5β1 (*e.g.*, by employing arginine-glycine-aspartic acid (RGD)-peptides), and asparagine-glycine-arginine (NGR) peptides that target aminopeptidase N.

Alternatively, cationic liposomes have been employed to target the tumor vessels. Generally, cationic liposomes are partly composed of (phospho)lipids with a positively charged head group, frequently complemented by neutral lipids such as phosphatidylcholines and cholesterol (summarized in [280]). Alternatively, a non-to-minimally toxic cationic moiety with a lipophilic anchor, such as 3β-[N-(N',N'-dimethylaminoethane)-carbamoyl] cholesterol (DC-chol) [281], can be used in conjunction with neutral lipids. It is believed that cationic liposomes electrostatically

associate with the negatively charged glycocalyx of inflamed or angiogenic endothelial cells [282], as evidenced by their propensity to accumulate more extensively in tumor vessels (~25–28% of the total administered dose) than in normal vessels (~4% of the total administered dose) [283]. This binding specificity may be in part explained by the lethargic and irregular blood flow in the tumor environment, as a result of which a greater probability of ETL–glycocalyx interactions exists that in turn enables more profound accumulation of ETLs in the tumor vasculature. Another factor that may contribute to this phenomenon is the typical upregulation and overexpression of negatively charged surface glycoproteins (*e.g.*, sialic acid-rich glycoproteins) by tumor endothelium [284].

Presently, relatively limited *in vitro* and *in vivo* data is available on the utility of ETLs for PDT. The cationic ETLs are believed to be internalized by endothelial cells via endocytosis [282]; cationic PEGylated ZnPC–ETLs, but not their neutral controls (*i.e.*, ZnPC–ITLs, Section 4.4.4), are indeed taken up by cultured human umbilical vein endothelial cells (HUVECs) (**Fig. 10C–F**). Campbell *et al.* [283] showed that cationic ETLs (1,2-dioleoyl-3-trimethylammonium-propane (DOTAP)) specifically targeted to the vasculature of xenografted human colon carcinoma (LS174T) tumors in mice. The cationic ETLs exhibited heterogeneous vascular distribution and accumulated predominantly in vessel branches. In addition, Thurston *et al.* demonstrated that ETLs specifically accumulated in RIP-Tag2 tumor-bearing mice (**Fig. 11**) and that the degree of accumulation was associated with the developmental stage of the tumor [282]. In terms of *in vitro* efficacy, we have shown that ZnPC–ETLs (composed of DPPC:DC-chol:cholesterol:DSPE-PEG (66:25:5:4, molar ratio) and a ZnPC:lipid ratio of 0.003) exhibit no dark toxicity in HUVECs and respond to PDT in a PS concentration-dependent manner [285]. With respect to *in vivo* efficacy studies, Gross *et al.* [286] encapsulated verteporfin in ETLs (DOTAP) and performed PDT on laser-induced choroidal neovasculature in mice. The unencapsulated and ETL-encapsulated verteporfin were equally effective and significantly decreased the size of the choroidal neovessels, although the cationic ETLs demonstrated higher selectivity and reduced PS-associated side effects. However, choroidal neovessels are not equivalent to intratumoral vasculature, so the results are not *per se* extrapolatable to the responsiveness of solid tumors to ETL-mediated PDT. Nevertheless, the data collectively suggest that cationic ETLs can selectively deliver PSs to intratumoral vasculature and that PDT will result in vascular shutdown, tumor cell death, and retardation of tumor growth. Evidently, more *in vivo* studies are needed to establish pharmacokinetic-, pharmacodynamic-, and toxicological profiles of PC-containing ETLs.

4.4.4. Photosensitizer-encapsulating interstitially targeted liposomes

The interstitial compartment of a tumor contains tumor-associated fibroblasts and immune cells that continuously remodel the tumor extracellular matrix (stroma),

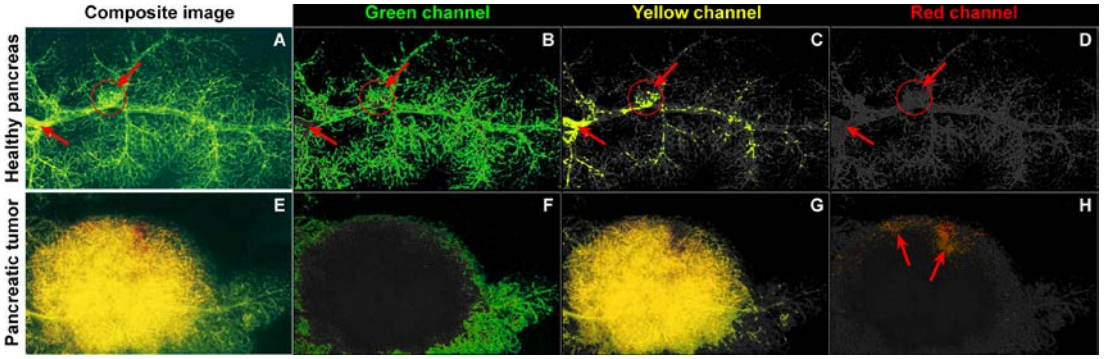

Fig. 11. *In vivo* proof-of-concept of cationic liposome targeting to intratumoral vasculature. Fluorescently labeled cationic liposomes (1,2-dioleoyl-3-trimethylammonium propane:cholesterol:Texas red-conjugated 1,2-dihexadecanoyl-*sn*-glycero-3-phosphoethanolamine, 55:45:0.2 molar ratio, in red) were systemically infused into wild-type mice (**A–D**) and RIP-Tag2 mice (**E–H**). The vasculature was stained with fluorescein-labeled lectin (in green) and yellow fluorescence indicates colocalization of cationic liposomes with (intratumoral) blood vessels (**C**, **G**). Images were modified from [282] and used with permission from Dr. Gavin Thurston.

which entails neovascularization, activation of extracellular matrix-bound growth factors, and tumor cell invasion following proteolytic degradation of extracellular matrix components. Stromal remodeling is also required for tumor metastasis (reviewed in [287-289]). Consequently, PS delivery to the tumor interstitium may constitute a useful means to inflict considerable damage to the tumor [290, 291]. The mechanisms that stand at the basis of PDT efficacy in the stromal environment include: (1) oxidation of cell membranes, either by primary ROS or by secondary or tertiary ROS (*e.g.*, $^{\bullet}OH$ [2]) that are formed from type I reactions in the tumor microenvironment, and (2) activation of immune cells by (a) direct oxidation of cellular constituents following PDT of PS-ITLs that have been taken up by the immune cells (*e.g.*, tumor-resident macrophages) and/or (b) by oxidized extracellular biomolecules [276] (*e.g.*, stromal proteins or glycocalyx degradation products [2]) that bind to immune receptors (*e.g.*, TLR-2, TLR-4, CD44) or are taken up by the immune cells following PDT [292].

The targeting of ITLs to the tumor interstitium and their retention proceeds passively via the EPR effect. For these purposes, liposomes are generally composed of neutral (zwitterionic) phospholipids (mostly phosphatidylcholines) and a molar fraction (4–6%) of PEGylated lipids for steric stabilization and to impart stealth properties [293]. Alternatively, ITLs may be sterically stabilized by other types of non-to-low immunogenic (block co-) polymers, including polyacrylamide (PAA), poly(vinylpyrrolidone) (PVP), and poly(acryloyl morpholine) (PAcM) (reviewed in [294]). Proper sizing is also important, as the ITLs must have a smaller diameter than the length of the inter-endothelial cell fenestrations in the tumor vasculature, *i.e.*, <200 nm [295], to extravasate. Moreover, particles <160 nm are profoundly taken up by the liver in rabbits, whereas particles >210 nm are avidly taken up by both the spleen and the liver [226]. Consequently, the diameter of ITLs should be between 160 and 210 nm. Steric stabilization in combination with proper sizing considerably prolongs the

circulation time, as a result of which the ITLs will have ample time to passively diffuse into the tumor interstitium. Accordingly, Wu *et al.* [296] demonstrated that, in rats, sterically stabilized liposomes rapidly accumulated in the interstitial compartment of xenografted rat breast adenocarcinomas (R3230Ac) following infusion, which was 3–4 fold more extensive than their non-PEGylated counterparts.

With respect to *in vitro* PDT studies, our group has demonstrated that ITLs encapsulating ZnPC exhibited no dark toxicity, but became cytotoxic upon irradiation of extrahepatic cholangiocarcinoma (Sk-Cha1) cells in a lipid concentration-dependent manner (at a constant ZnPC:lipid ratio of 0.003) [74]. The mode of cell death comprised both apoptosis and necrosis, whereby necrosis was the predominant mode of cell death, most likely because a small fraction of the ITLs was internalized by the cells [74]. Moreover, the ITLs were not taken up by HUVECs, which suggests that these liposomes will not be cleared by endothelial-like cells following intravenous infusion (**Fig. 10E**, **F**, and **H**). *In vivo* studies in mice bearing human fibrosarcoma (MS-2) tumors demonstrated that ZnPC-encapsulating non-PEGylated ITLs accumulated in the tumors at tumor:healthy tissue ratios of 7.5:1–9:1 24 h after systemic administration [190, 191], which is in agreement with the previously cited findings by Wu *et al.* [296] regarding interstitial ITL accumulation. Furthermore, Oku *et al.* [297] performed PDT with glucuronidated ITLs containing verteporfin and achieved a complete response rate in 80% of the Meth A sarcoma-bearing mice. In contrast, a 20% complete response rate was observed with free PS or verteporfin encapsulated in conventional anionic liposomes (DPPC:1-palmitoyl-2-oleoyl-*sn*-glycero-3-phosphocholine (POPC):cholesterol:1,2-dipalmitoyl-*sn*-glycero-3-phosphoglycerol (DPPG)). These data clearly indicate that the tumor interstitium comprises a viable target for PDT-mediated tumor eradication using PS-ITLs.

Alternatively, LDL can serve as an additional vehicle for the transfer of lipophilic PCs from the ITLs to blood-borne LDL and subsequently to tumor cells (**Fig. 9**). Various studies have found that ZnPC incorporated in non-PEGylated lipid-based delivery vehicles can transfer to plasma proteins, including LDL and high-density lipoprotein (HDL) [49, 298]. As demonstrated by Reddi *et al.* [201], intravenous infusion of *in vitro* prepared ZnPC–LDL complexes resulted in selective accumulation of these complexes in the tumor, as evidenced by a maximal tumor:healthy tissue ratio of 5.7, 24 h post-injection. None of the studies examined the effect of PEGylation on the transfer kinetics of ZnPC from ITLs to plasma proteins. Such studies have only been conducted with mTHPC [299, 300], showing that 42% of mTHPC was transferred from PEGylated ITLs to plasma proteins 30 minutes after incubation, which progressively increased to 74% after 24 h [300]. Inasmuch as mTHPC and metallated PCs are chemically comparable (**Fig. 2D** and **Fig. 6A–D**) and the PCs are typically encapsulated in lipid formulations that resemble the formulations used in [299, 300], it is expected that ZnPC will exhibit similar transfer behavior. Accordingly, the transfer of PC molecules

from (PEGylated) ITLs to LDL will lead to tumor-specific PC accumulation [301]. Based on *in vitro* results it appears that the ZnPC–LDL conjugates enter the cells via non-specific endocytosis [302]. The ZnPC–LDL complexes are not internalized via receptor-mediated endocytosis, since the association of PCs with LDL slightly distorts the molecular structure of apoprotein B [302] that is responsible for LDL receptor binding [303].

This section summarized the importance of targeting the stromal environment inasmuch as the tumor stroma is responsible for neovascularization and metastatic spread of tumor cells and contains oxidizable cellular and molecular constituents with immunogenic potential. PEGylated ITLs generally exhibit better pharmacokinetics, tumor-accumulating capacity, and hence therapeutic outcomes than their non-PEGylated equivalents. The transfer of ZnPC from ITLs to endogenous lipid-based nanocarriers such as LDL constitutes an alternative way to augment ZnPC accumulation in the tumor stroma.

4.5. Phototriggered release modalities for liposome-delivered anti-cancer agents

In addition to the delivery of PSs, liposomes may also be used for the delivery of water-soluble compounds to the tumor site rather than the tumor cells *per se*. With such modalities, the liposomal encapsulants may accumulate in the tumor interstitial space and undergo local release into the tumor microenvironment upon irradiation. Upon their release, these compounds essentially aid in the tumor eradication process.

The triggered release of the hydrophilic encapsulants can be integrated into the photodynamic process by the inclusion of photo-labile constituents such as photodegradable phospholipids. These constituents are chemically modified upon light irradiation, leading to a change in chemical properties or degradation, consequent perturbation/destabilization of the particle, and corollary release of the hydrophilic encapsulants. A complete overview of the phototriggered release mechanisms is provided in **Fig. 12**. Detailed reviews on these mechanisms are available elsewhere [304-306]. Unfortunately, a multitude of the photochemical triggering methods rely on UV light, which may have limited clinical applicability due to its low optical penetration depth and harmful effects. As such, novel methods or optimized methods are required that are compatible with wavelengths in the therapeutic window (**Fig. 3B**).

5. Concluding remarks

PDT is an attractive treatment modality for a variety of diseases, including anti-neoplastic treatment, has yielded promising clinical results at relatively low cost, and can be carried out in a non-invasive and patient-friendly manner. However, contemporary PDT strategies lack effectiveness in various solid cancer subtypes and are associated with a substantial amount of photosensitivity. To circumvent these

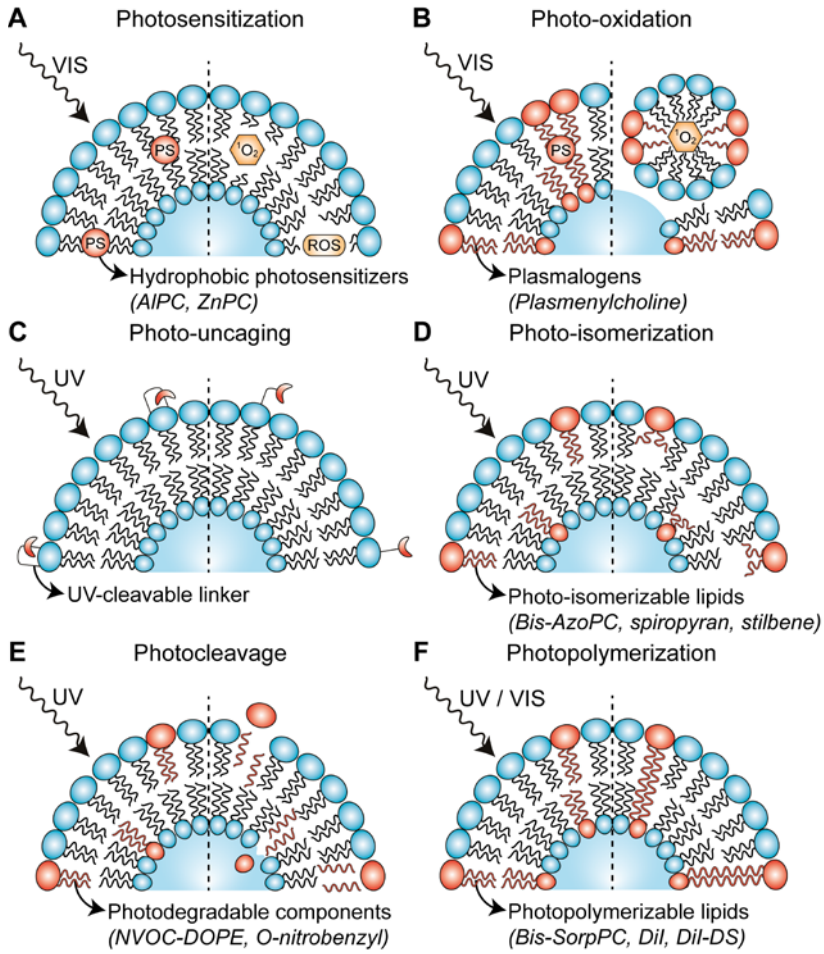

Fig. 12. Summary of methods for photochemically triggered drug release. Light-induced release of water-soluble compounds can be achieved by photosensitization (**A**), a process that involves ROS-mediated destabilization of the lipid bilayer, photo-oxidation of plasmalogens that drives micelle formation (**B**), photo-uncaging of recognition molecules that enable tumor cell uptake (**C**), photo-isomerization of lipids that switch from an extended form (*trans*) to a twisted form (*cis*) (**D**), light-induced degradation of lipid components (**E**), and light-induced cross-linking of photopolymerizable lipids (**F**). All processes, except for photo-uncaging, cause destabilization of the lipid bilayer that enables efflux of the liposomal cargo. Abbreviations: VIS, visible light; UV, ultraviolet light; bis-AzoPC, 1,2-bis[4-4(4-*n*-butylphenylazo)phenylbutyroyl] phosphatidylcholine; NVOC-DOPE, 6-nitroveratryloxycarbonylated 1,2-dioleoyl-*sn*-glycero-3-phosphoethanolamine; bis-SorpPC, 1,2-bis[10-(2',4'-hexadienoyloxy)-decanoyl]-*sn*-phosphatidylcholine; DiI, 1,1'-dioctadecyl-3,3,3',3'-tetramethylindocarbocyanine; DiI-DS, 1,1'-dioctadecyl-3,3,3,3'-tetramethylindocarbocyanine disulfonic acid.

issues, the application of diamagnetic PCs is expected to improve clinical outcome and lower the degree of photosensitivity and phototoxic reactions. The encapsulation of diamagnetic PCs into liposomes provides a sophisticated PS delivery platform for the targeting of pharmacologically important intratumoral sites, including the tumor interstitium, tumor endothelium, and tumor cells. Future *in vivo* and clinical research should determine whether this multi-faceted tumor targeting strategy improves

therapeutic efficacy in PDT-recalcitrant tumors while reducing side effects. Besides our proposed cancer treatment strategy, the versatility of this delivery platform offers researchers many new applications, varying from the delivery of contrast agents for tumor imaging to delivery of pharmaceutical agents for therapy.

Acknowledgements

The authors thank Dr. Gavin Thurston for his permission to publish the *in vivo* localization of cationic liposomes and Prof. Dr. Bing Tan for providing Foscan. This study was supported by grants from the Dutch Anti-Cancer Foundation (Stichting Nationaal Fonds Tegen Kanker, Amsterdam, the Netherlands), the Phospholipid Research Center (Heidelberg, Germany), and the Nijbakker-Morra Foundation (Leiden, the Netherlands) to MH.

References

1. K. Plaetzer, B. Krammer, J. Berlanda, F. Berr, T. Kiesslich, Photophysics and photochemistry of photodynamic therapy: fundamental aspects, Lasers Med. Sci. 24 (2009) 259–268.
2. R.F. van Golen, T.M. van Gulik, M. Heger, Mechanistic overview of reactive species-induced degradation of the endothelial glycocalyx during hepatic ischemia/reperfusion injury, Free Rad. Biol. Med. 52 (2012) 1382–1402.
3. B.W. Henderson, T.J. Dougherty, How does photodynamic therapy work? Photochem. Photobiol. 55 (1992) 145–157.
4. M. Triesscheijn, P. Baas, J.H. Schellens, F.A. Stewart, Photodynamic therapy in oncology, Oncologist 11 (2006) 1034–1044.
5. R.C. Benson, Jr., Laser photodynamic therapy for bladder cancer, Mayo Clin. Proc. 61 (1986) 859–864.
6. M.P. Copper, I.B. Tan, H. Oppelaar, M.C. Ruevekamp, F.A. Stewart, Meta-tetra (hydroxyphenyl) chlorin photodynamic therapy in early-stage squamous cell carcinoma of the head and neck, Arch. Otolaryngol. Head Neck Surg. 129 (2003) 709–711.
7. T.J. Dougherty, Photodynamic therapy (PDT) of malignant tumors, Crit. Rev. Oncol. Hematol. 2 (1984) 83–116.
8. A.C. Kubler, C.J. de, C. Hopper, A.G. Leonard, G. Putnam, Treatment of squamous cell carcinoma of the lip using Foscan-mediated photodynamic therapy, Int. J. Oral Maxillofac. Surg. 30 (2001) 504–509.
9. G.D. Mackenzie, J.M. Dunn, C.R. Selvasekar, C.A. Mosse, S.M. Thorpe, M.R. Novelli, S.G. Bown, L.B. Lovat, Optimal conditions for successful ablation of high-grade dysplasia in Barrett's oesophagus using aminolaevulinic acid photodynamic therapy, Lasers Med. Sci. 24 (2009) 729–734.
10. A. Morales, Treatment of superficial bladder cancer, Can. Med. Assoc. J. 122 (1980) 1133–1138.
11. C.A. Morton, C. Whitehurst, H. Moseley, J.H. McColl, J.V. Moore, R.M. Mackie, Comparison of photodynamic therapy with cryotherapy in the treatment of Bowen's disease, Br. J. Dermatol. 135 (1996) 766–771.
12. S.J. Rosenberg, R.D. Williams, Photodynamic therapy of bladder carcinoma, Urol. Clin. North Am. 13 (1986) 435–444.
13. A. Sibille, R. Lambert, J.C. Souquet, G. Sabben, F. Descos, Long-term survival after photodynamic therapy for esophageal cancer, Gastroenterology 108 (1995) 337–344.
14. N.C. Zeitouni, S. Shieh, A.R. Oseroff, Laser and photodynamic therapy in the management of cutaneous malignancies, Clin. Dermatol. 19 (2001) 328– 338.
15. U.O. Nseyo, B. Shumaker, E.A. Klein, K. Sutherland, Photodynamic therapy using porfimer sodium as an alternative to cystectomy in patients with refractory transitional cell carcinoma in situ of the bladder. Bladder Photofrin Study Group, J. Urol. 160 (1998) 39–44.
16. Z.Q. Sun, Photodynamic therapy of nasopharyngeal carcinoma by argon or dye laser—an analysis of 137 cases, Zhonghua Zhong Liu Za Zhi 14 (1992) 290–292.
17. F.L. Dumoulin, T. Gerhardt, S. Fuchs, C. Scheurlen, M. Neubrand, G. Layer, T. Sauerbruch, Phase II study of photodynamic therapy and metal stent as palliative treatment for nonresectable hilar cholangiocarcinoma, Gastrointest. Endosc. 57 (2003) 860–867.
18. M. Wiedmann, F. Berr, I. Schiefke, H. Witzigmann, K. Kohlhaw, J. Mossner, K. Caca, Photodynamic therapy in patients with non-resectable hilar cholangiocarcinoma: 5-year follow-up of a prospective phase II study, Gastrointest. Endosc. 60 (2004) 68–75.
19. E.A.J. Rauws, Photodynamic therapy and Klatskin tumour: an overview, Scand. J. Gastroenterol. 41 (2006) 135–138.
20. N. Oku, Y. Namba, S. Okada, Tumor accumulation of novel RES-avoiding liposomes, Biochim. Biophys. Acta 1126 (1992)

255–260.
21. R.T. van Kooten, W. Perini, L.G. Dijkstra, S.R. Veldkamp, A.K. Warps, E. van Elsäcker, M. Hafdi, Q. Hofsink, M. Kos, M. Broekgaarden, R. Weijer, R. van Vught, S. Oliveira, Y. Liu, Y. Nie, Z. Gu, J. Birkhoff, I.B. Tan, G. Storm, M. Heger, Lipid-based nanoparticulate drug delivery systems for photodynamic therapy of solid cancers: the utility of photosensitizer encapsulation. Manuscript in preparation (2015).
22. R.R. Allison, G.H. Downie, R. Cuenca, X.H. Hu, C.J. Childs, C.H. Sibata, Photosensitizers in clinical PDT, Photodiagn. Photodyn. Ther. 1 (2004) 27–42.
23. R.S. Wooten, K.C. Smith, D.A. Ahlquist, S.A. Muller, R.K. Balm, Prospective study of cutaneous phototoxicity after systemic hematoporphyrin derivative, Lasers Surg. Med. 8 (1988) 294–300.
24. A.R. Oseroff, L.R. Blumenson, B.D. Wilson, T.S. Mang, D.A. Bellnier, J.C. Parsons, N. Frawley, M. Cooper, N. Zeitouni, T.J. Dougherty, A dose ranging study, of photodynamic therapy with porfimer sodium (Photofrin) for treatment of basal cell carcinoma, Lasers Surg. Med. 38 (2006) 417–426.
25. J. Regula, A.J. MacRobert, A. Gorchein, G.A. Buonaccorsi, S.M. Thorpe, G.M. Spencer, A.R.W. Hatfield, S.G. Bown, Photosensitization and photodynamic therapy of esophageal, duodenal, and colorectal tumors using 5-aminolevulinic acid-induced protoporphyrin-IX—a pilot-study, Gut 36 (1995) 67–75.
26. G. Wagnieres, C. Hadjur, P. Grosjean, D. Braichotte, J.F. Savary, P. Monnier, H. van den Bergh, Clinical evaluation of the cutaneous phototoxicity of 5,10,15,20-tetra(m-hydroxyphenyl) chlorin, Photochem. Photobiol. 68 (1998) 382–387.
27. Q. Peng, J.M. Nesland, J. Moan, J.F. Evensen, M. Kongshaug, C. Rimington, Localization of fluorescent Photofrin-II and aluminum phthalocyanine tetrasulfonate in transplanted human malignant tumor LOX and normal tissues of nude mice using highly light-sensitive video intensification microscopy, Int. J. Cancer 45 (1990) 972–979.
28. D.G. Boyle, W.R. Potter, Photobleaching of Photofrin II as a means of eliminating skin photosensitivity, Photochem. Photobiol. 46 (1987) 997–1001.
29. S.L. Jacques, How tissue optics affect dosimetry of photodynamic therapy, J. Biomed. Opt. 15 (2010) 51608.
30. H. Maeda, The enhanced permeability and retention (EPR) effect in tumor vasculature: the key role of tumor-selective macromolecular drug targeting, Adv. Enzyme Regul. 41 (2001) 189–207.
31. D.A. Bellnier, Y.K. Ho, R.K. Pandey, J.R. Missert, T.J. Dougherty, Distribution and elimination of Photofrin II in mice, Photochem. Photobiol. 50 (1989) 221–228.
32. C.J. Gomer, A. Ferrario, Tissue distribution and photosensitizing properties of mono-L-aspartyl chlorin e6 in a mouse tumor model, Cancer Res. 50 (1990) 3985–3990.
33. W.S. Chan, J.F. Marshall, R. Svensen, J. Bedwell, I.R. Hart, Effect of sulfonation on the cell and tissue distribution of the photosensitizer aluminum phthalocyanine, Cancer Res. 50 (1990) 4533–4538.
34. M. Van de Putte, T. Roskams, G. Bormans, A. Verbruggen, P.A.M. de Witte, The impact of aggregation on the biodistribution of hypericin, Int. J. Oncol. 28 (2006) 655–660.
35. A. Barel, G. Jori, A. Perin, P. Romandini, A. Pagnan, S. Biffanti, Role of high-density, low-density and very low-density lipoproteins in the transport and tumor-delivery of hematoporphyrin in vivo, Cancer Lett. 32 (1986) 145–150.
36. M.A. Elfar, N.R. Pimstone, Tumor-localization of uroporphyrin isomer-I and isomer-III and their correlation to albumin and serum-protein binding, Cell Biochem. Funct. 1 (1983) 156–160.
37. I. Freitas, Lipid accumulation: the common feature to photosensitizer-retaining normal and malignant tissues, J. Photochem. Photobiol. B 7 (1990) 359–361.
38. P.J. Bugelski, C.W. Porter, T.J. Dougherty, Autoradiographic distribution of hematoporphyrin derivative in normal and tumor tissue of the mouse, Cancer Res. 41 (1981) 4606–4612.
39. Q. Peng, J. Moan, L.S. Cheng, The effect of glucose administration on the uptake of Photofrin-II in a human tumor xenograft, Cancer Lett. 58 (1991) 29–35.
40. M. Korbelik, G. Krosl, P.L. Olive, D.J. Chaplin, Distribution of Photofrin between tumor cells and tumor-associated macrophages, Br. J. Cancer 64 (1991) 508–512.
41. G. Jori, In vivo transport and pharmacokinetic behavior of tumour photosensitizers, Ciba Found. Symp. 146 (1989) 78–86.
42. M. Chopp, M.O. Dereski, L. Madigan, F. Jiang, B. Logie, Sensitivity of 9L gliosarcomas to photodynamic therapy, Radiat. Res. 146 (1996) 461–465.
43. B. Chen, B.W. Pogue, P.J. Hoopes, T. Hasan, Vascular and cellular targeting for photodynamic therapy, Crit. Rev. Eukaryot. Gene Expr. 16 (2006) 279–305.
44. K.C. Gatter, G. Brown, I.S. Trowbridge, R.E. Woolston, D.Y. Mason, Transferrin receptors in human tissues: their distribution and possible clinical relevance, J. Clin. Pathol. 36 (1983) 539–545.
45. S. Vitols, G. Gahrton, A. Ost, C. Peterson, Elevated low-density lipoprotein receptor activity in leukemic cells with monocytic differentiation, Blood 63 (1984) 1186–1193.
46. G. Stehle, H. Sinn, A. Wunder, H.H. Schrenk, J.C.M. Stewart, G. Hartung, W. MaierBorst, D.L. Heene, Plasma protein (albumin) catabolism by the tumor itself—implications for tumor metabolism and the genesis of cachexia, Crit. Rev. Oncol. Hematol. 26 (1997) 77–100.
47. S. Nakajima, T. Takemura, I. Sakata, Tumor-localizing activity of porphyrin and its affinity to LDL, transferrin, Cancer Lett. 92 (1995) 113–118.
48. D. Kessel, Porphyrin-lipoprotein association as a factor in porphyrin localization, Cancer Lett. 33 (1986) 183–188.
49. F. Ginevra, S. Biffanti, A. Pagnan, R. Biolo, E. Reddi, G. Jori, Delivery of the tumor photosensitizer zinc(II)-phthalocyanine

to serum proteins by different liposomes—studies in vitro and in vivo, Cancer Lett. 49 (1990) 59–65.
50. E. Alarcon, A.M. Edwards, A.M. Garcia, M. Munoz, A. Aspee, C.D. Borsarelli, E.A. Lissi, Photophysics and photochemistry of zinc phthalocyanine/bovine serum albumin adducts, Photochem. Photobiol. Sci. 8 (2009) 255–263.
51. H. Mojzisova, S. Bonneau, C. Vever-Bizet, D. Brault, Cellular uptake and subcellular distribution of chlorin e6 as functions of pH and interactions with membranes and lipoproteins, Biochim. Biophys. Acta 1768 (2007) 2748– 2756.
52. K.W. Woodburn, N.J. Vardaxis, J.S. Hill, A.H. Kaye, D.R. Phillips, Subcellular localization of porphyrins using confocal laser scanning microscopy, Photochem. Photobiol. 54 (1991) 725–732.
53. L.B. Chen, Mitochondrial-membrane potential in living cells, Ann. Rev. Cell Biol. 4 (1988) 155–181.
54. C.W. Lin, J.R. Shulok, S.D. Kirley, L. Cincotta, J.W. Foley, Lysosomal localization and mechanism of uptake of Nile Blue photosensitizers in tumor cells, Cancer Res. 51 (1991) 2710–2719.
55. J.M. Wessels, W. Strauss, H.K. Seidlitz, A. Ruck, H. Schneckenburger, Intracellular localization of meso-tetraphenylporphine tetrasulfonate probed by time-resolved and microscopic fluorescence spectroscopy, J. Photochem. Photobiol. B 12 (1992) 275–284.
56. J. Moan, K. Berg, S. H.B., W. T., M. K., Fluorescence and photodynamic effects of phthalocyanines and porphyrins in cells, in: B.W. Henderson, T.J. Dougherty (Eds.), Photodynamic Therapy. Basic Principles and Clinical Applications, Marcel-Dekker, New York, 1992, pp. 19–36.
57. B.C. Wilson, M. Olivo, G. Singh, Subcellular localization of Photofrin(R) and aminolevulinic acid and photodynamic cross-resistance in vitro in radiation-induced fibrosarcoma cells sensitive or resistant to Photofrin-mediated photodynamic therapy, Photochem. Photobiol. 65 (1997) 166–176.
58. J.R. Shulok, M.H. Wade, C.W. Lin, Subcellular localization of hematoporphyrin derivative in bladder tumor cells in culture, Photochem. Photobiol. 51 (1990) 451–457.
59. Y.J. Hsieh, C.C. Wu, C.J. Chang, J.S. Yu, Subcellular localization of Photofrin(R) determines the death phenotype of human epidermoid carcinoma A431 cells triggered by photodynamic therapy: when plasma membranes are the main targets, J. Cell. Physiol. 194 (2003) 363–375.
60. M.H. Teiten, L. Bezdetnaya, P. Morliere, R. Santus, F. Guillemin, Endoplasmic reticulum and Golgi apparatus are the preferential sites of Foscan((R)) localisation in cultured tumour cells, Br. J. Cancer 88 (2003) 146–152.
61. C. Fabris, G. Valduga, G. Miotto, L. Borsetto, G. Jori, S. Garbisa, E. Reddi, Photosensitization with zinc(II) phthalocyanine as a switch in the decision between apoptosis and necrosis, Cancer Res. 61 (2001) 7495–7500.
62. H.B. Ris, H.J. Altermatt, B. Nachbur, J.C.M. Stewart, Q. Wang, C.K. Lim, R. Bonnett, U. Althaus, Effect of drug-light interval on photodynamic therapy with meta-tetrahydroxyphenylchlorin in malignant mesothelioma, Int. J. Cancer 53 (1993) 141–146.
63. W.M. Sharman, C.M. Allen, J.E. van Lier, Role of activated oxygen species in photodynamic therapy, Methods Enzymol. 319 (2000) 376–400.
64. K.R. Weishaupt, C.J. Gomer, T.J. Dougherty, Identification of singlet oxygen as cytotoxic agent in photo-inactivation of a murine tumor, Cancer Res. 36 (1976) 2326–2329.
65. R.W. Redmond, I.E. Kochevar, Spatially resolved cellular responses to singlet oxygen, Photochem. Photobiol. 82 (2006) 1178–1186.
66. [66] M. Broekgaarden, R. Weijer, A.C. van Wijk, R.C. Cox, M.R. Egmond, R. Hoebe, T. M. van Gulik, M. Heger, Photodynamic therapy with liposomal zinc phtalocyanine and tirapazamine increases tumor cell death via DNA damage. Manuscript submitted, 2015.
67. S. Tada-Oikawa, S. Oikawa, J. Hirayama, K. Hirakawa, S. Kawanishi, DNA damage and apoptosis induced by photosensitization of 5,10,15,20-tetrakis (N-methyl-4-pyridyl)-21H,23H-porphyrin via singlet oxygen generation, Photochem. Photobiol. 85 (2009) 1391–1399.
68. M. Broekgaarden, R. Weijer, T.M. van Gulik, M.R. Hamblin, M. Heger, Tumor cell survival pathways activated by photodynamic therapy: a molecular framework for inhibition strategies, Cancer Metastasis Rev. (2015) (in press).
69. Z. Huang, H.P. Xu, A.D. Meyers, A.I. Musani, L.W. Wang, R. Tagg, A.B. Barqawi, Y.K. Chen, Photodynamic therapy for treatment of solid tumors—potential and technical challenges, Technol. Cancer Res. Treat. 7 (2008) 309–320.
70. A.P. Castano, T.N. Demidova, M.R. Hamblin, Mechanisms in photodynamic therapy: part one—photosensitizers, photochemistry and cellular localization, Photodiagn. Photodyn. Ther. 1 (2004) 279–293.
71. A.W. Girotti, Photodynamic lipid peroxidation in biological systems, Photochem. Photobiol. 51 (1990) 497–509.
72. E. Niki, Lipid peroxidation: physiological levels and dual biological effects, Free Rad. Biol. Med. 47 (2009) 469–484.
73. E. Tyrode, P. Niga, M. Johnson, M.W. Rutland, Molecular structure upon compression and stability toward oxidation of Langmuir films of unsaturated fatty acids: a vibrational sum frequency spectroscopy study, Langmuir 26 (2010) 14024–14031.
74. M. Broekgaarden, A.I. de Kroon, T.M. van Gulik, M. Heger, Development and in vitro proof-of-concept of interstitially targeted zinc-phthalocyanine liposomes for photodynamic therapy, Curr. Med. Chem. 21 (2013) 377–391.
75. K. Berg, K. Madslien, J.C. Bommer, R. Oftebro, J.W. Winkelman, J. Moan, Light-induced relocalization of sulfonated meso-tetraphenylporphines in Nhik 3025 cells and effects of dose fractionation, Photochem. Photobiol. 53 (1991) 203–210.
76. J. Moan, K. Berg, H. Anholt, K. Madslien, Sulfonated aluminum phthalocyanines as sensitizers for photochemotherapy—effects of small light doses on localization, dye fluorescence and photosensitivity in V79 cells, Int. J. Cancer 58 (1994) 865–870.

77. P.D. Wilson, R.A. Firestone, J. Lenard, The role of lysosomal enzymes in killing of mammalian cells by the lysosomotropic detergent N-dodecylimidazole, J. Cell Biol. 104 (1987) 1223–1229.
78. D. Kessel, M. Conley, M.G.H. Vicente, J.J. Reiners, Studies on the subcellular localization of the porphycene CPO, Photochem. Photobiol. 81 (2005) 569– 572.
79. E. Buytaert, G. Callewaert, N. Hendrickx, L. Scorrano, D. Hartmann, L. Missiaen, J.R. Vandenheede, I. Heirman, J. Grooten, P. Agostinis, Role of endoplasmic reticulum depletion and multidomain proapoptotic BAX and BAK proteins in shaping cell death after hypericin-mediated photodynamic therapy, FASEB J. 20 (2006) 756–758.
80. I. Moserova, J. Kralova, Role of ER stress response in photodynamic therapy: ROS generated in different subcellular compartments trigger diverse cell death pathways, Plos One 7 (2012) e32972.
81. J.M. Timmins, L. Ozcan, T.A. Seimon, G. Li, C. Malagelada, J. Backs, T. Backs, R. Bassel-Duby, E.N. Olson, M.E. Anderson, I. Tabas, Calcium/calmodulin-dependent protein kinase II links ER stress with Fas and mitochondrial apoptosis pathways, J. Clin. Invest. 119 (2009) 2925–2941.
82. J.J. Lemasters, A.L. Nieminen, T. Qian, L.C. Trost, S.P. Elmore, Y. Nishimura, R.A. Crowe, W.E. Cascio, C.A. Bradham, D.A. Brenner, B. Herman, The mitochondrial permeability transition in cell death: a common mechanism in necrosis, apoptosis and autophagy, Biochim. Biophys. Acta 1366 (1998) 177–196.
83. D. Kessel, Y. Luo, Y.Q. Deng, C.K. Chang, The role of subcellular localization in initiation of apoptosis by photodynamic therapy, Photochem. Photobiol. 65 (1997) 422–426.
84. D. Kessel, Y. Luo, Mitochondrial photodamage and PDT-induced apoptosis, J. Photochem. Photobiol. B 42 (1998) 89–95.
85. S.R. Chatterjee, H. Possel, T.S. Srivastava, J.P. Kamat, G. Wolf, T.P.A. Devasagayam, Photodynamic effects induced by meso-tetrakis[4-(carboxymethyleneoxy)phenyl]porphyrin on isolated Sarcoma 180 ascites mitochondria, J. Photochem. Photobiol. B 50 (1999) 79–87.
86. S.R. Chatterjee, T.S. Srivastava, J.P. Kamat, T.P.A. Devasagayam, Lipid peroxidation induced by a novel porphyrin plus light in isolated mitochondria: possible implications in photodynamic therapy, Mol. Cell. Biochem. 166 (1997) 25–33.
87. K. Plaetzer, T. Kiesslich, B. Krammer, P. Hammerl, Characterization of the cell death modes and the associated changes in cellular energy supply in response to AlPcS4-PDT, Photochem. Photobiol. Sci. 1 (2002) 172–177.
88. C. Soldani, M.G. Bottone, A.C. Croce, A. Fraschini, G. Bottiroli, C. Pellicciari, The Golgi apparatus is a primary site of intracellular damage after photosensitization with Rose Bengal acetate, Eur. J. Histochem. 48 (2004) 443–448.
89. S. Mukherjee, R. Chiu, S.M. Leung, D. Shields, Fragmentation of the Golgi apparatus: an early apoptotic event independent of the cytoskeleton, Traffic 8 (2007) 369–378.
90. R. Chin, L. Novikov, S. Mukherjee, D. Shields, A caspase cleavage fragment of p115 induces fragmentation of the Golgi apparatus and apoptosis, J. Cell Biol. 159 (2002) 637–648.
91. M. Ogata, O. Inanami, M. Nakajima, T. Nakajima, W. Hiraoka, M. Kuwabara, Ca (2+)-dependent and caspase-3-independent apoptosis caused by damage in golgi apparatus due to 2,4,5,7-tetrabromorhodamine 123 bromide-induced photodynamic effects, Photochem. Photobiol. 78 (2003) 241–247.
92. P. Agostinis, K. Berg, K.A. Cengel, T.H. Foster, A.W. Girotti, S.O. Gollnick, S.M. Hahn, M.R. Hamblin, A. Juzeniene, D. Kessel, M. Korbelik, J. Moan, P. Mroz, D. Nowis, J. Piette, B.C. Wilson, J. Golab, Photodynamic therapy of cancer: an update, CA Cancer J. Clin. 61 (2011) 250–281.
93. T.J. Dougherty, C.J. Gomer, B.W. Henderson, G. Jori, D. Kessel, M. Korbelik, J. Moan, Q. Peng, Photodynamic therapy, J. Natl. Cancer Inst. 90 (1998) 889–905.
94. M. Korbelik, Induction of tumor immunity by photodynamic therapy, J. Clin. Laser Med. Surg. 14 (1996) 329–334.
95. M. Korbelik, G. Krosl, J. Krosl, G.J. Dougherty, The role of host lymphoid populations in the response of mouse EMT6 tumor to photodynamic therapy, Cancer Res. 56 (1996) 5647–5652.
96. A.P. Castano, P. Mroz, M.R. Hamblin, Photodynamic therapy and anti-tumour immunity, Nat. Rev. Cancer 6 (2006) 535–545.
97. G.Y. Chen, G. Nunez, Sterile inflammation: sensing and reacting to damage, Nature Rev. Immunol. 10 (2010) 826–837.
98. P.M. Gallo, S. Gallucci, The dendritic cell response to classic, emerging, and homeostatic danger signals. Implications for autoimmunity, Front. Immunol. 4 (2013) 138.
99. A.D. Garg, D. Nowis, J. Golab, P. Agostinis, Photodynamic therapy: illuminating the road from cell death towards anti-tumour immunity, Apoptosis 15 (2010) 1050–1071.
100. A.D. Garg, D. Nowis, J. Golab, P. Vandenabeele, D.V. Krysko, P. Agostinis, Immunogenic cell death, DAMPs and anticancer therapeutics: an emerging amalgamation, Biochim. Biophys. Acta 1805 (2010) 53–71.
101. A.D. Garg, D.V. Krysko, P. Vandenabeele, P. Agostinis, DAMPs and PDT-mediated photo-oxidative stress: exploring the unknown, Photochem. Photobiol. Sci. 10 (2011) 670–680.
102. P. Srivastava, Roles of heat-shock proteins in innate and adaptive immunity, Nat. Rev. Immunol. 2 (2002) 185–194.
103. S. Basu, R.J. Binder, T. Ramalingam, P.K. Srivastava, CD91 is a common receptor for heat shock proteins gp96, hsp90, hsp70, and calreticulin, Immunity 14 (2001) 303–313.
104. M. Korbelik, Complement upregulation in photodynamic therapy-treated tumors: role of toll-like receptor pathway and NF kappa B, Cancer Lett. 281 (2009) 232–238.
105. B. Stott, M. Korbelik, Activation of complement C3, C5, and C9 genes in tumors treated by photodynamic therapy, Cancer Immunol. Immunother. 56 (2007) 649–658.
106. J.R. Theriault, H. Adachi, S.K. Calderwood, Role of scavenger receptors in the binding and internalization of heat shock protein 70, J. Immunol. 177 (2006) 8604–8611.

107. A.A. Beg, Endogenous ligands of Toll-like receptors: implications for regulating inflammatory and immune responses, Trends Immunol. 23 (2002) 509–512.
108. N. Fischer, M. Haug, W.W. Kwok, H. Kalbacher, D. Wernet, G.E. Dannecker, U. Holzer, Involvement of CD91 and scavenger receptors in Hsp70-facilitated activation of human antigen-specific CD4(+) memory T cells, Eur. J. Immunol. 40 (2010) 986–997.
109. A.D. Garg, D.V. Krysko, T. Verfaillie, A. Kaczmarek, G.B. Ferreira, T. Marysael, N. Rubio, M. Firczuk, C. Mathieu, A.J.M. Roebroek, W. Annaert, J. Golab, P. de Witte, P. Vandenabeele, P. Agostinis, A novel pathway combining calreticulin exposure and ATP secretion in immunogenic cancer cell death, EMBO J. 31 (2012) 1062–1079.
110. S. Pawaria, R.J. Binder, CD91-dependent programming of T-helper cell responses following heat shock protein immunization, Nat. Commun. 2 (2011) 521.
111. M. Korbelik, J.H. Sun, I. Cecic, Photodynamic therapy-induced cell surface expression and release of heat shock proteins: relevance for tumor response, Cancer Res. 65 (2005) 1018–1026.
112. F.F. Zhou, D. Xing, W.R. Chen, Regulation of HSP70 on activating macrophages using PDT-induced apoptotic cells, Int. J. Cancer 125 (2009) 1380–1389.
113. N. Etminan, C. Peters, D. Lakbir, E. Bunemann, V. Borger, M.C. Sabel, D. Hanggi, H.J. Steiger, W. Stummer, R.V. Sorg, Heat-shock protein 70-dependent dendritic cell activation by 5-aminolevulinic acid-mediated photodynamic treatment of human glioblastoma spheroids in vitro, Br. J. Cancer 105 (2011) 961–969.
114. S. Mitra, B.R. Giesselman, F.J. De Jesus-Andino, T.H. Foster, Tumor response to mTHPC-mediated photodynamic therapy exhibits strong correlation with extracellular release of HSP70, Lasers Surg. Med. 43 (2011) 632–643.
115. E. Panzarini, V. Inguscio, L. Dini, Immunogenic cell death: can it be exploited in photodynamic therapy for cancer? Biomed. Res. Int. (2013) 482160.
116. E.C. Tracy, M.J. Bowman, B.W. Henderson, H. Baumann, Interleukin-1 alpha is the major alarmin of lung epithelial cells released during photodynamic therapy to induce inflammatory mediators in fibroblasts, Br. J. Cancer 107 (2012) 1534–1546.
117. K.H. Krause, M. Michalak, Calreticulin, Cell 88 (1997) 439–443.
118. T.J. Ostwald, D.H. MacLennan, Isolation of a high affinity calcium-binding protein from sarcoplasmic reticulum, J. Biol. Chem. 249 (1974) 974–979.
119. S.J. Gardai, K.A. McPhillips, S.C. Frasch, W.J. Janssen, A. Starefeldt, J.E. Murphy-Ullrich, D.L. Bratton, P.A. Oldenborg, M. Michalak, P.M. Henson, Cell-surface calreticulin initiates clearance of viable or apoptotic cells through trans-activation of LRP on the phagocyte, Cell 123 (2005) 321–334.
120. D.V. Krysko, A.D. Garg, A. Kaczmarek, O. Krysko, P. Agostinis, P. Vandenabeele, Immunogenic cell death and DAMPs in cancer therapy, Nat. Rev. Cancer 12 (2012) 860–875.
121. M. Obeid, A. Tesniere, F. Ghiringhelli, G.M. Fimia, L. Apetoh, J.L. Perfettini, M. Castedo, G. Mignot, T. Panaretakis, N. Casares, D. Metivier, N. Larochette, P. van Endert, F. Ciccosanti, M. Piacentini, L. Zitvogel, G. Kroemer, Calreticulin exposure dictates the immunogenicity of cancer cell death, Nat. Med. 13 (2007) 54–61.
122. A.M. Dudek, A.D. Garg, D.V. Krysko, D. De Ruysscher, P. Agostinis, Inducers of immunogenic cancer cell death, Cytokine Growth Factor Rev. 24 (2013) 319–333.
123. A.D. Garg, D.V. Krysko, P. Vandenabeele, P. Agostinis, Hypericin-based photodynamic therapy induces surface exposure of damage-associated molecular patterns like HSP70 and calreticulin, Cancer Immunol. Immunother. 61 (2012) 215–221.
124. A.D. Garg, A.M. Dudek, G.B. Ferreira, T. Verfaillie, P. Vandenabeele, D.V. Krysko, C. Mathieu, P. Agostinis, ROS-induced autophagy in cancer cells assists in evasion from determinants of immunogenic cell death, Autophagy 9 (2013) 1292–1307.
125. J.O. Thomas, A.A. Travers, HMG1 and 2, and related 'architectural' DNA-binding proteins, Trends Biochem. Sci. 26 (2001) 167–174.
126. T. Bonaldi, F. Talamo, P. Scaffidi, D. Ferrera, A. Porto, A. Bachi, A. Rubartelli, A. Agresti, M.E. Bianchi, Monocytic cells hyperacetylate chromatin protein HMGB1 to redirect it towards secretion, EMBO J. 22 (2003) 5551– 5560.
127. S. Gardella, C. Andrei, D. Ferrera, L.V. Lotti, M.R. Torrisi, M.E. Bianchi, A. Rubartelli, The nuclear protein HMGB1 is secreted by monocytes via a non-classical, vesicle-mediated secretory pathway, EMBO Rep. 3 (2002) 995– 1001.
128. R. Palumbo, M. Sampaolesi, F. De Marchis, R. Tonlorenzi, S. Colombetti, A. Mondino, G. Cossu, M.E. Bianchi, Extracellular HMGB1 a signal of tissue damage, induces mesoangioblast migration and proliferation, J. Cell Biol. 164 (2004) 441–449.
129. P. Scaffidi, T. Misteli, M.E. Bianchi, Release of chromatin protein HMGB1 by necrotic cells triggers inflammation, Nature 418 (2002) 191–195.
130. U. Andersson, H.C. Wang, K. Palmblad, A.C. Aveberger, O. Bloom, H. Erlandsson-Harris, A. Janson, R. Kokkola, M.H. Zhang, H. Yang, K.J. Tracey, High mobility group 1 protein (HMG-1) stimulates proinflammatory cytokine synthesis in human monocytes, J. Exp. Med. 192 (2000) 565–570.
131. G.Q. Chen, M.F. Ward, A.E. Sama, H.C. Wang, Extracellular HMGB1 as a proinflammatory cytokine, J. Interferon Cytokine Res. 24 (2004) 329–333.
132. V.V. Orlova, E.Y. Choi, C.P. Xie, E. Chavakis, A. Bierhaus, E. Ihanus, C.M. Ballantyne, C.G. Gahmberg, M.E. Bianchi, P.P. Nawroth, T. Chavakis, A novel pathway of HMGB1-mediated inflammatory cell recruitment that requires Mac-1-integrin, EMBO J. 26 (2007) 1129–1139.
133. D. Yang, Q. Chen, H. Yang, K.J. Tracey, M. Bustin, J.J. Oppenheim, High mobility group box-1 protein induces the migration and activation of human dendritic cells and acts as an alarmin, J. Leukocyte Biol. 81 (2007) 59–66.
134. C.W. Bell, W.W. Jiang, C.F. Reich, D.S. Pisetsky, The extracellular release of HMGB1 during apoptotic cell death, Am. J.

Physiol. Cell Physiol. 291 (2006) C1318–C1325.
135. J. Thorburn, H. Horita, J. Redzic, K. Hansen, A.E. Frankel, A. Thorburn, Autophagy regulates selective HMGB1 release in tumor cells that are destined to die, Cell Death Differ. 16 (2009) 175–183.
136. M.E. Bianchi, HMGB1 loves company, J. Leukocyte Biol. 86 (2009) 573–576.
137. H. Yang, D.J. Antoine, U. Andersson, K.J. Tracey, The many faces of HMGB1: molecular structure-functional activity in inflammation, apoptosis, and chemotaxis, J. Leukocyte Biol. 93 (2013) 865–873.
138. M. Korbelik, W. Zhang, S. Merchant, Involvement of damage-associated molecular patterns in tumor response to photodynamic therapy: surface expression of calreticulin and high-mobility group box-1 release, Cancer Immunol. Immunother. 60 (2011) 1431–1437.
139. M.R. Elliott, F.B. Chekeni, P.C. Trampont, E.R. Lazarowski, A. Kadl, S.F. Walk, D. Park, R.I. Woodson, M. Ostankovich, P. Sharma, J.J. Lysiak, T.K. Harden, N. Leitinger, K.S. Ravichandran, Nucleotides released by apoptotic cells act as a find-me signal to promote phagocytic clearance, Nature 461 (2009) 282-U165.
140. F. Ghiringhelli, L. Apetoh, A. Tesniere, L. Aymeric, Y.T. Ma, C. Ortiz, K. Vermaelen, T. Panaretakis, G. Mignot, E. Ullrich, J.L. Perfettini, F. Schlemmer, E. Tasdemir, M. Uhl, P. Genin, A. Civas, B. Ryffel, J. Kanellopoulos, J. Tschopp, F. Andre, R. Lidereau, N.M. McLaughlin, N.M. Haynes, M.J. Smyth, G. Kroemer, L. Zitvogel, Activation of the NLRP3 inflammasome in dendritic cells induces IL-1 beta-dependent adaptive immunity against tumors, Nat. Med. 15 (2009) 1170–1171U1199.
141. L. Zitvogel, O. Kepp, L. Galluzzi, G. Kroemer, Inflammasomes in carcinogenesis and anticancer immune responses, Nat. Immunol. 13 (2012) 343–351.
142. P.A. Lang, D. Merkler, P. Funkner, N. Shaabani, A. Meryk, C. Krings, C. Barthuber, M. Recher, W. Bruck, D. Haussinger, P.S. Ohashi, K.S. Lang, Oxidized ATP inhibits T-cell-mediated autoimmunity, Eur. J. Immunol. 40 (2010) 2401– 2408.
143. C.M. Brackett, S.O. Gollnick, Photodynamic therapy enhancement of anti-tumor immunity, Photochem. Photobiol. Sci. 10 (2011) 649–652.
144. M. Firczuk, D. Nowis, J. Golab, PDT-induced inflammatory and host responses, Photochem. Photobiol. Sci. 10 (2011) 653–663.
145. P. Mroz, J.T. Hashmi, Y.Y. Huang, N. Lang, M.R. Hamblin, Stimulation of anti-tumor immunity by photodynamic therapy, Expert Rev. Clin. Immunol. 7 (2011) 75–91.
146. M. Korbelik, PDT-associated host response and its role in the therapy outcome, Lasers Surg. Med. 38 (2006) 500–508.
147. E.S. Trombetta, I. Mellman, Cell biology of antigen processing in vitro and in vivo, Annu. Rev. Immunol. 23 (2005) 975–1028.
148. G. Canti, D. Lattuada, A. Nicolin, P. Taroni, G. Valentini, R. Cubeddu, Antitumor immunity induced by photodynamic therapy with aluminum disulfonated phthalocyanines and laser-light, Anticancer Drugs 5 (1994) 443–447.
149. E. Kabingu, L. Vaughan, B. Owczarczak, K.D. Ramsey, S.O. Gollnick, CD8(+) T cell-mediated control of distant tumours following local photodynamic therapy is independent of CD4(+) T cells and dependent on natural killer cells, Br. J. Cancer 96 (2007) 1839–1848.
150. P.S.P. Thong, K.W. Ong, N.S.G. Goh, K.W. Kho, V. Manivasager, R. Bhuvaneswari, M. Oliva, K.C. Soo, Photodynamic-therapy-activated immune response against distant untreated tumours in recurrent angiosarcoma, Lancet Oncol. 8 (2007) 950–952.
151. E.S. Abdel-Hady, P. Martin-Hirsch, M. Duggan-Keen, P.L. Stern, J.V. Moore, G. Corbitt, H.C. Kitchener, I.N. Hampson, Immunological and viral factors associated with the response of vulval intraepithelial neoplasia to photodynamic therapy, Cancer Res. 61 (2001) 192–196.
152. E. Kabingu, A.R. Oseroff, G.E. Wilding, S.O. Gollnick, Enhanced systemic immune reactivity to a basal cell carcinoma associated antigen following photodynamic therapy, Clin. Cancer Res. 15 (2009) 4460–4466.
153. G. Dragieva, J. Hafner, R. Dummer, P. Schmid-Grendelmeier, M. Roos, B.M. Prinz, G. Burg, U. Binswanger, W. Kempf, Topical photodynamic therapy in the treatment of actinic keratoses and Bowen's disease in transplant recipients, Transplantation 77 (2004) 115–121.
154. A. Szokalska, M. Makowski, D. Nowis, G.M. Wilczynski, M. Kujawa, C. Wojcik, I. Mlynarczuk-Bialy, P. Salwa, J. Bil, S. Janowska, P. Agostinis, T. Verfaillie, M. Bugajski, J. Gietka, T. Issat, E. Glodkowska, P. Mrowka, T. Stoklosa, M.R. Hamblin, P. Mroz, M. Jakobisiak, J. Golab, Proteasome inhibition potentiates antitumor effects of photodynamic therapy in mice through induction of endoplasmic reticulum stress and unfolded protein response, Cancer Res. 69 (2009) 4235–4243.
155. J. Debnath, E.H. Baehrecke, G. Kroemer, Does autophagy contribute to cell death? Autophagy 1 (2005) 66–74.
156. D. Kessel, J.J. Reiners, Apoptosis and autophagy after mitochondrial or endoplasmic reticulum photodamage, Photochem. Photobiol. 83 (2007) 1024–1028.
157. H.R.C. Kim, Y. Luo, G.Y. Li, D. Kessel, Enhanced apoptotic response to photodynamic therapy after bcl-2 transfection, Cancer Res. 59 (1999) 3429– 3432.
158. L.Y. Xue, S.M. Chiu, N.L. Oleinick, Photochemical destruction of the Bcl-2 oncoprotein during photodynamic therapy with the phthalocyanine photosensitizer Pc 4, Oncogene 20 (2001) 3420–3427.
159. D. Kessel, M. Castelli, Evidence that bcl-2 is the target of three photosensitizers that induce a rapid apoptotic response, Photochem. Photobiol. 74 (2001) 318–322.
160. X.H. Liang, L.K. Kleeman, H.H. Jiang, G. Gordon, J.E. Goldman, G. Berry, B. Herman, B. Levine, Protection against fatal Sindbis virus encephalitis by Beclin, a novel Bcl-2-interacting protein, J. Virol. 72 (1998) 8586–8596.
161. S. Pattingre, A. Tassa, X.P. Qu, R. Garuti, X.H. Liang, N. Mizushima, M. Packer, M.D. Schneider, B. Levine, Bcl-2 antiapoptotic proteins inhibit Beclin 1-dependent autophagy, Cell 122 (2005) 927–939.

162. D. Kessel, A.S. Arroyo, Apoptotic and autophagic responses to Bcl-2 inhibition and photodamage, Photochem. Photobiol. Sci. 6 (2007) 1290–1295.
163. M. Andrzejak, M. Price, D.H. Kessel, Apoptotic and autophagic responses to photodynamic therapy in 1c1c7 murine hepatoma cells, Autophagy 7 (2011) 979–984.
164. P. Boya, R.A. Gonzalez-Polo, N. Casares, J.L. Perfettini, P. Dessen, N. Larochette, D. Metivier, D. Meley, S. Souquere, T. Yoshimori, G. Pierron, P. Codogno, G. Kroemer, Inhibition of macroautophagy triggers apoptosis, Mol. Cell. Biol. 25 (2005) 1025–1040.
165. C.H. Yan, Z.Q. Liang, Z.L. Gu, Y.P. Yang, P. Reid, Z.H. Qin, Contributions of autophagic and apoptotic mechanisms to CrTX-induced death of K562 cells, Toxicon 47 (2006) 521–530.
166. C.M. Allen, W.M. Sharman, J.E. Van Lier, Current status of phthalocyanines in the photodynamic therapy of cancer, J. Porphyrins Phthalocyanines 5 (2001) 161–169.
167. N. Brasseur, Sensitizers for PDT: phthalocyanines, in: T. Patrice (Ed.), Photodynamic Therapy, Royal Society of Chemistry, Cambridge, 2004, pp. 107–114.
168. J.E. van Lier, J.D. Spikes, The chemistry, photophysics and photosensitizing properties of phthalocyanines, Ciba Found. Symp. 146 (1989) 17–26.
169. J.R. Wagner, H. Ali, R. Langlois, N. Brasseur, J.E. Vanlier, Biological activities of phthalocyanines VI. Photooxidation of L-tryptophan by selectively sulfonated gallium phthalocyanines—singlet oxygen yields and effect of aggregation, Photochem. Photobiol. 45 (1987) 587–594.
170. J.R. Darwent, P. Douglas, A. Harriman, G. Porter, M.C. Richoux, Metal phthalocyanines and porphyrins as photosensitizers for reduction of water to hydrogen, Coord. Chem. Rev. 44 (1982) 83–126.
171. E. Ben-Hur, Basic photobiology and mechanisms of action of phthalocyanines, in: T.J. Dougherty, B.W. Henderson (Eds.), Photodynamic Therapy, Basic Principles and Clinical Applications, Marcel Dekker, New York, 1992, pp. 63–77.
172. M. Ochsner, Light scattering of human skin: a comparison between zinc(II)-phthalocyanine and Photofrin II, J. Photochem. Photobiol. B 32 (1996) 3–9.
173. E.D. Baron, C.L. Malbasa, D. Santo-Domingo, P.F. Fu, J.D. Miller, K.K. Hanneman, A.H. Hsia, N.L. Oleinick, V.C. Colussi, K.D. Cooper, Silicon phthalocyanine (Pc 4) photodynamic therapy is a safe modality for cutaneous neoplasms: results of a phase 1 clinical trial, Lasers Surg. Med. 42 (2010) 728–735.
174. M. Ochsner, Photophysical and photobiological processes in the photodynamic therapy of tumours, J. Photochem. Photobiol. B 39 (1997) 1– 18.
175. D.A. Bellnier, W.R. Greco, G.M. Loewen, H. Nava, A.R. Oseroff, T.J. Dougherty, Clinical pharmacokinetics of the PDT photosensitizers porfimer sodium (Photofrin), 2-[1-hexyloxyethyl]-2-devinyl pyropheophorbide-a (Photochlor) and 5-ALA-induced protoporphyrin IX, Lasers Surg. Med. 38 (2006) 439–444.
176. J. Berlanda, T. Kiesslich, V. Engelhardt, B. Krammer, K. Plaetzer, Comparative in vitro study on the characteristics of different photosensitizers employed in PDT, J. Photochem. Photobiol. B 100 (2010) 173–180.
177. R.M. Amin, C. Hauser, I. Kinzler, A. Rueck, C. Scalfi-Happ, Evaluation of photodynamic treatment using aluminum phthalocyanine tetrasulfonate chloride as a photosensitizer: new approach, Photochem. Photobiol. Sci. 11 (2012) 1156–1163.
178. E.C.C. Tapajos, J.P. Longo, A.R. Simioni, Z.G.M. Lacava, M.F.M.A. Santos, P.C. Morais, A.C. Tedesco, R.B. Azevedo, In vitro photodynamic therapy on human oral keratinocytes using chloroaluminum-phthalocyanine, Oral Oncol. 44 (2008) 1073–1079.
179. E. Ben-Hur, T. Fujihara, F. Suzuki, M.M. Elkind, Genetic toxicology of the photosensitization of Chinese hamster cells by phthalocyanines, Photochem. Photobiol. 45 (1987) 227–230.
180. K. Halkiotis, D. Yova, G. Pantelias, In vitro evaluation of the genotoxic and clastogenic potential of photodynamic therapy, Mutagenesis 14 (1999) 193– 198.
181. F.I. Mcnair, B. Marples, C.M.L. West, J.V. Moore, A comet assay of DNA damage and repair in K562 cells after photodynamic therapy using haematoporphyrin derivative, methylene blue and meso-tetrahydroxyphenylchlorin, Br. J. Cancer 75 (1997) 1721–1729.
182. C.M.N. Yow, N.K. Mak, S. Szeto, J.Y. Chen, Y.L. Lee, N.H. Cheung, D.P. Huang, A. W.N. Leung, Photocytotoxic and DNA damaging effect of Temoporfin (mTHPC) and merocyanine 540 (MC540) on nasopharyngeal carcinoma cell, Toxicol. Lett. 115 (2000) 53–61.
183. P. Duez, M. Hanocq, J. Dubois, Photodynamic DNA damage mediated by delta-aminolevulinic acid-induced porphyrins, Carcinogenesis 22 (2001) 771–778.
184. D.M. Fiedler, P.M. Eckl, B. Krammer, Does delta-aminolaevulinic acid induce genotoxic effects? J. Photochem. Photobiol. B 33 (1996) 39–44.
185. V.A. Bohr, T. Stevnsner, N.C. de Souza-Pinto, Mitochondrial DNA repair of oxidative damage in mammalian cells, Gene 286 (2002) 127–134.
186. T. Kiesslich, J. Berlanda, K. Plaetzer, B. Krammer, F. Berr, Comparative characterization of the efficiency and cellular pharmacokinetics of Foscan- (R) and Foslip (R)-based photodynamic treatment in human biliary tract cancer cell lines, Photochem. Photobiol. Sci. 6 (2007) 619–627.
187. M. Leunig, C. Richert, F. Gamarra, W. Lumper, E. Vogel, D. Jocham, A.E. Goetz, Tumor-localization kinetics of Photofrin and three synthetic prophyrinoids in an amelanotic melanoma of the hamster, Br. J. Cancer 68 (1993) 225–234.
188. S. Iinuma, R. Bachor, T. Flotte, T. Hasan, Biodistribution and phototoxicity of 5-aminolevulinic acid-induced PpIX in an

orthotopic rat bladder tumor model, J. Urol. 153 (1995) 802–806.
189. A.M. Ronn, M. Nouri, L.A. Lofgren, B.M. Steinberg, A. Westerborn, T. Windahl, M.J. Shikowitz, A.L. Abramson, Human tissue levels and plasma pharmacokinetics of temoporfin (Foscan(R), mTHPC), Lasers Med. Sci. 11 (1996) 267–272.
190. E. Reddi, G. Locastro, R. Biolo, G. Jori, Pharmacokinetic studies with zinc(II)-phthalocyanine in tumor-bearing mice, Br. J. Cancer 56 (1987) 597–600.
191. L. Polo, A. Segalla, G. Jori, G. Bocchiotti, G. Verna, R. Franceschini, R. Mosca, P. G. DeFilippi, Liposome-delivered I-131-labelled Zn(II)-phthalocyanine as a radiodiagnostic agent for tumours, Cancer Lett. 109 (1996) 57–61.
192. Q. Peng, J. Moan, M. Kongshaug, J.F. Evensen, H. Anholt, C. Rimington, Sensitizer for photodynamic therapy of cancer—a comparison of the tissue distribution of Photofrin II and aluminum phthalocyanine tetrasulfonate in nude mice bearing a human malignant tumor, Int. J. Cancer 48 (1991) 258– 264.
193. K.W. Woodburn, Q. Fan, D.R. Miles, D. Kessel, Y. Luo, S.W. Young, Localization and efficacy analysis of the phototherapeutic lutetium texaphyrin (PCI-0123) in the murine EMT6 sarcoma model, Photochem. Photobiol. 65 (1997) 410– 415.
194. J.F. Chiou, Y.H. Wang, M.J. Jou, T.Z. Liu, C.Y. Shiau, Verteporfin-photoinduced apoptosis in HepG2 cells mediated by reactive oxygen and nitrogen species intermediates, Free Rad. Res. 44 (2010) 155–170.
195. P.P. Deshpande, S. Biswas, V.P. Torchilin, Current trends in the use of liposomes for tumor targeting, Nanomedicine 8 (2013) 1509–1528.
196. A. Lukyanov, Z. Gao, L. Mazzola, V. Torchilin, Polyethylene glycol-diacyllipid micelles demonstrate increased accumulation in subcutaneous tumors in mice, Pharm. Res. 19 (2002) 1424–1429.
197. A. Fundarò, R. Cavalli, A. Bargoni, D. Vighetto, G.P. Zara, M.R. Gasco, Non-stealth and stealth solid lipid nanoparticles (SLN) carrying doxorubicin pharmacokinetics and tissue distribution after i.v. administration to rats, Pharmacol. Res. 42 (2000) 337–343.
198. P. Guo, S. Song, Z. Li, Y. Tian, J. Zheng, X. Yang, W. Pan, In vitro and in vivo evaluation of APRPG-modified angiogenic vessel targeting micelles for anticancer therapy, Int. J. Pharm. 486 (2015) 356–366.
199. Y.-C. Kuo, C.-Y. Shih-Huang, Solid lipid nanoparticles with surface antibody for targeting the brain and inhibiting lymphatic phagocytosis, J. Taiwan Inst. Chem. Eng. 45 (2014) 1154–1163.
200. M.R. Hamblin, E.L. Newman, Photosensitizer targeting in photodynamic therapy. II. Conjugates of haematoporphyrin with serum lipoproteins, J. Photochem. Photobiol. B 26 (1994) 147–157.
201. E. Reddi, C. Zhou, R. Biolo, E. Menegaldo, G. Jori, Liposome- or LDL-administered Zn(II)-phthalocyanine as a photodynamic agent for tumors I. Pharmacokinetic properties and phototherapeutic efficiency, Br. J. Cancer 61 (1990) 407–411.
202. G.I. Harisa, F.K. Alanazi, Low density lipoprotein bionanoparticles: from cholesterol transport to delivery of anti-cancer drugs, Saudi Pharm. J. 22 (2014) 504–515.
203. S. Svenson, D.A. Tomalia, Dendrimers in biomedical applications—reflections on the field, Adv. Drug Deliv. Rev. 64 (Suppl) (2012) 102–115.
204. K. Madaan, S. Kumar, N. Poonia, V. Lather, D. Pandita, Dendrimers in drug delivery and targeting: drug-dendrimer interactions and toxicity issues, J. Pharm. Bioallied Sci. 6 (2014) 139–150.
205. V.P. Torchilin, Micellar nanocarriers: pharmaceutical perspectives, Pharm. Res. 24 (2007) 1–16.
206. M. Yokoyama, Clinical applications of polymeric micelle carrier systems in chemotherapy and image diagnosis of solid tumors, J. Exp. Clin. Med. 3 (2011) 151–158.
207. S.A. Sibani, P.A. McCarron, A.D. Woolfson, R.F. Donnelly, Photosensitiser delivery for photodynamic therapy. Part 2: systemic carrier platforms, Expert Opin. Drug Deliv. 5 (2008) 1241–1254.
208. M.A. Manoukian, S.V. Ott, J. Rajadas, M. Inayathullah, Polymeric nanoparticles to combat squamous cell carcinomas in patients with dystrophic epidermolysis bullosa, Recent Pat. Nanomed. 4 (2014) 15–24.
209. A. Kumari, S.K. Yadav, S.C. Yadav, Biodegradable polymeric nanoparticles based drug delivery systems, Colloids Surf. B 75 (2010) 1–18.
210. E. Ricci-Júnior, J.M. Marchetti, Zinc(II) phthalocyanine loaded PLGA nanoparticles for photodynamic therapy use, Int. J. Pharm. 310 (2006) 187– 195.
211. E.S. Shibu, M. Hamada, N. Murase, V. Biju, Nanomaterials formulations for photothermal and photodynamic therapy of cancer, J. Photochem. Photobiol. C. 15 (2013) 53–72.
212. N.F. Gamaleia, I.O. Shton, Gold mining for PDT: Great expectations from tiny nanoparticles, Photodiagn. Photodyn. Ther. (2015), doi:http://dx.doi.org/ 10.1016/j.pdpdt.2015.03.002.
213. B.N. Khlebtsov, V.A. Khanadeev, I.L. Maksimova, G.S. Terentyuk, N.G. Khlebtsov, Silver nanocubes and gold nanocages: Fabrication and optical and photothermal properties, Nanotechnol. Russ. 5 (2010) 454–468.
214. L. Li, J.F. Zhao, N. Won, H. Jin, S. Kim, J.Y. Chen, Quantum dot-aluminum phthalocyanine conjugates perform photodynamic reactions to kill cancer cells via fluorescence resonance energy transfer, Nanoscale Res. Lett. 7 (2012) 386.
215. H.I. Chang, M.K. Yeh, Clinical development of liposome-based drugs: formulation, characterization, and therapeutic efficacy, Int. J. Nanomed. 7 (2012) 49–60.
216. M.L. Immordino, F. Dosio, L. Cattel, Stealth liposomes: review of the basic science, rationale, and clinical applications existing and potential, Int. J. Nanomed. 1 (2006) 297–315.
217. G. Aguilar, B. Choi, M. Broekgaarden, O.W. Yang, B. Yang, P. Ghasri, J.K. Chen, R. Bezemer, J.S. Nelson, A.M. van Drooge, A. Wolkerstorfer, K.M. Kelly, M. Heger, An overview of three promising mechanical, optical, and biochemical engineering approaches to improve selective photothermolysis of refractory port wine stains, Ann. Biomed. Eng. 40 (2012) 486–506.

218. X. Damoiseau, H.J. Schuitmaker, J.W.M. Lagerberg, M. Hoebeke, Increase of the photosensitizing efficiency of the bacteriochlorin a by liposome-incorporation, J. Photochem. Photobiol. B 60 (2001) 50–60.
219. S. Dhami, D. Phillips, Comparison of the photophysics of an aggregating and non-aggregating aluminium phthalocyanine system incorporated into unilamellar vesicles, J. Photochem. Photobiol. A 100 (1996) 77–84.
220. A.M. Garcia, E. Alarcon, M. Munoz, J.C. Scaiano, A.M. Edwards, E. Lissi, Photophysical behaviour and photodynamic activity of zinc phthalocyanines associated to liposomes, Photochem. Photobiol. Sci. 10 (2011) 507–514.
221. A.S.L. Derycke, P.A.M. de Witte, Liposomes for photodynamic therapy, Adv. Drug Deliv. Rev. 56 (2004) 17–30.
222. G. Jori, Factors controlling the selectivity and efficiency of tumour damage in photodynamic therapy, Lasers Med. Sci. 5 (1990) 115–120.
223. P.I. Campbell, Toxicity of some charged lipids used in liposome preparations, Cytobios 37 (1983) 21–26.
224. E. Mayhew, M. Ito, R. Lazo, Toxicity of non-drug containing liposomes for cultured human cells, Exp. Cell Res. 171 (1987) 195–202.
225. R. Banerjee, Liposomes: applications in medicine, J. Biomater. Appl. 16 (2001) 3–21.
226. V.D. Awasthi, D. Garcia, B.A. Goins, W.T. Phillips, Circulation and biodistribution profiles of long-circulating PEG-liposomes of various sizes in rabbits, Int. J. Pharm. 253 (2003) 121–132.
227. T.M. Allen, C. Hansen, F. Martin, C. Redemann, A. Yauyoung, Liposomes containing synthetic lipid derivatives of poly(ethylene glycol) show prolonged circulation half-lives in vivo, Biochim. Biophys. Acta 1066 (1991) 29–36.
228. A.L. Klibanov, K. Maruyama, V.P. Torchilin, L. Huang, Amphipathic polyethyleneglycols effectively prolong the circulation time of liposomes, FEBS Lett. 268 (1990) 235–237.
229. D. Papahadjopoulos, T.M. Allen, A. Gabizon, E. Mayhew, K. Matthay, S.K. Huang, K.D. Lee, M.C. Woodle, D.D. Lasic, C. Redemann, F.J. Martin, Sterically stabilized liposomes—improvements in pharmacokinetics and antitumor therapeutic efficacy, Proc. Natl. Acad. Sci. U. S. A. 88 (1991) 11460–11464.
230. J. Senior, C. Delgado, D. Fisher, C. Tilcock, G. Gregoriadis, Influence of surface hydrophilicity of liposomes on their interaction withp plasma protein and clearance from the circulation—studies with poly(ethylene glycol)-coated vesicles, Biochim. Biophys. Acta 1062 (1991) 77–82.
231. V.P. Torchilin, V.G. Omelyanenko, M.I. Papisov, A.A. Bogdanov, V.S. Trubetskoy, J.N. Herron, C.A. Gentry, Poly(ethylene glycol) on the liposome surface—on the mechanism of polymer-coated liposome longevity, Biochim. Biophys. Acta 1195 (1994) 11–20.
232. D. Needham, T.J. Mcintosh, D.D. Lasic, Repulsive interactions and mechanical stability of polymer-grafted lipid membranes, Biochim. Biophys. Acta 1108 (1992) 40–48.
233. A. Gabizon, D. Papahadjopoulos, The role of surface charge and hydrophilic groups on liposome clearance in vivo, Biochim. Biophys. Acta 1103 (1992) 94–100.
234. D.D. Lasic, F.J. Martin, A. Gabizon, S.K. Huang, D. Papahadjopoulos, Sterically stabilized liposomes—a hypothesis on the molecular origin of the extended circulation times, Biochim. Biophys. Acta 1070 (1991) 187–192.
235. J.A. Harding, C.M. Engbers, M.S. Newman, N.I. Goldstein, S. Zalipsky, Immunogenicity and pharmacokinetic attributes of poly(ethylene glycol)-grafted immunoliposomes, Biochim. Biophys. Acta 1327 (1997) 181–192.
236. M.J. Bovis, J.H. Woodhams, M. Loizidou, D. Scheglmann, S.G. Bown, A.J. MacRobert, Improved in vivo delivery of m-THPC via pegylated liposomes for use in photodynamic therapy, J. Control. Release 157 (2012) 196–205.
237. J. Buchholz, B. Kaser-Hotz, T. Khan, C.R. Bleyl, K. Melzer, R.A. Schwendener, M. Roos, H. Walt, Optimizing photodynamic therapy: in vivo pharmacokinetics of liposomal meta-(tetrahydroxyphenyl) chlorin in feline squamous cell carcinoma, Clin. Cancer Res. 11 (2005) 7538–7544.
238. C.B. Hansen, G.Y. Kao, E.H. Moase, S. Zalipsky, T.M. Allen, Attachment of antibodies to sterically stabilized liposomes—evaluation, comparison and optimization of coupling procedures, Biochim. Biophys. Acta 1239 (1995) 133–144.
239. S. Shahinian, J.R. Silvius, A novel strategy affords high-yield coupling of antibody Fab' fragments to liposomes, Biochim. Biophys. Acta 1239 (1995) 157–167.
240. V.P. Torchilin, A.L. Klibanov, L. Huang, S. Odonnell, N.D. Nossiff, B.A. Khaw, Targeted accumulation of polyethylene glycol-coated immunoliposomes in infarcted rabbit myocardium, FASEB J. 6 (1992) 2716–2719.
241. V.P. Torchilin, J. Narula, E. Halpern, B.A. Khaw, Poly(ethylene glycol)-coated anti-cardiac myosin immunoliposomes: factors influencing targeted accumulation in the infarcted myocardium, Biochim. Biophys. Acta 1279 (1996) 75–83.
242. J. Montanari, C. Maidana, M.I. Esteva, C. Salomon, M.J. Morilla, E.L. Romero, Sunlight triggered photodynamic ultradeformable liposomes against Leishmania braziliensis are also leishmanicidal in the dark, J. Control. Release 147 (2010) 368–376.
243. W.G. Love, S. Duk, R. Biolo, G. Jori, P.W. Taylor, Liposome-mediated delivery of photosensitizers: localization of zinc(II)-phthalocyanine within implanted tumors after intravenous administration, Photochem. Photobiol. 63 (1996) 656–661.
244. U. Isele, K. Schieweck, R. Kessler, P. Van Hoogevest, H.G. Capraro, Pharmacokinetics and body distribution of liposomal zinc phthalocyanine in tumor-bearing mice—influence of aggregation state, particle-size, and composition, J. Pharm. Sci. 84 (1995) 166–173.
245. A. Visona, G. Jori, Targeting of experimentally-induced atherosclerotic lesions by liposome-delivered Zn(II)-phthalocyanine, Atherosclerosis 100 (1993) 213–222.
246. C. Larroque, A. Pelegrin, J.E. Vanlier, Serum albumin as a vehicle for zinc phthalocyanine: photodynamic activities in solid tumour models, Br. J. Cancer 74 (1996) 1886–1890.

247. M. Fadel, K. Kassab, D.A. Fadeel, Zinc phthalocyanine-loaded PLGA biodegradable nanoparticles for photodynamic therapy in tumor-bearing mice, Lasers Med. Sci. 25 (2010) 283–292.
248. M.D. Soares, M.R. Oliveira, E.P. dos Santos, L.D. Gitirana, G.M. Barbosa, C.H. Quaresma, E. Ricci, Nanostructured delivery system for zinc phthalocyanine: preparation, characterization, and phototoxicity study against human lung adenocarcinoma A549 cells, Int. J. Nanomed. 6 (2011) 227–238.
249. H.L.L.M. Van Leengoed, V. Cuomo, A.A.C. Versteeg, N. Vanderveen, G. Jori, W. M. Star, In vivo fluorescence and photodynamic activity of zinc phthalocyanine administered in liposomes, Br. J. Cancer 69 (1994) 840–845.
250. E.R. da Silva, Z.M.F. de Freitas, L.D. Gitirana, E. Ricci, Improving the topical delivery of zinc phthalocyanine using oleic acid as a penetration enhancer: in vitro permeation and retention, Drug Dev. Ind. Pharm. 37 (2011) 569–575.
251. J.R. Lakowicz, Solvent and environmental effects, Principles of Fluorescence Spectroscopy, third ed., Springer, Baltimore, 2006, pp. 205–235.
252. K. Suwa, T. Kimura, A.P. Schaap, Reaction of singlet oxygen with cholesterol in liposomal membranes—effect of membrane fluidity on photooxidation of cholesterol, Photochem. Photobiol. 28 (1978) 469–473.
253. S.P. Stratton, D.C. Liebler, Determination of singlet oxygen-specific versus radical-mediated lipid peroxidation in photosensitized oxidation of lipid bilayers: effect of beta-carotene and alpha-tocopherol, Biochemistry 36 (1997) 12911–12920.
254. A.W. Girotti, Mechanisms of lipid peroxidation, Free Radic. Biol. Med.1 (1985) 87–95.
255. S.M.T. Nunes, F.S. Sguilla, A.C. Tedesco, Photophysical studies of zinc phthalocyanine and chloroaluminum phthalocyanine incorporated into liposomes in the presence of additives, Braz. J. Med. Biol. Res. 37 (2004) 273–284.
256. A. Molinari, M. Colone, A. Calcabrini, A. Stringaro, L. Toccacieli, G. Arancia, S. Mannino, A. Mangiola, G. Maira, C. Bombelli, G. Mancini, Cationic liposomes loaded with m-THPC, in photodynamic therapy for malignant glioma, Toxicol. In Vitro 21 (2007) 230–234.
257. A. Gijsens, L. Derycke, D. Missiaen, J. De Vos, E.A.P. Huwyler, Targeting of the photocytotoxic compound AlPcS4 to Hela cells by transferrin conjugated PEG-liposomes, Int. J. Cancer 101 (2002) 78–85.
258. A. Villanueva, J.C. Stockert, M. Canete, P. Acedo, A new protocol in photodynamic therapy: enhanced tumour cell death by combining two different photosensitizers, Photochem. Photobiol. Sci. 9 (2010) 295–297.
259. D. Hanahan, R.A. Weinberg, The hallmarks of cancer, Cell 100 (2000) 57–70.
260. D. Hanahan, R.A. Weinberg, Hallmarks of cancer: the next generation, Cell 144 (2011) 646–674.
261. A. Koshkaryev, R. Sawant, M. Deshpande, V. Torchilin, Immunoconjugates and long circulating systems: origins, current state of the art and future directions, Adv. Drug Deliv. Rev. 65 (2013) 24–35.
262. S.X. Song, D. Liu, J.L. Peng, Y. Sun, Z.H. Li, J.R. Gu, Y.H. Xu, Peptide ligand-mediated liposome distribution and targeting to EGFR expressing tumor in vivo, Int. J. Pharm. 363 (2008) 155–161.
263. M. Broekgaarden, R. van Vught, T.M. van Gulik, E. Breukink, M. Heger, Development of anti-epidermal growth factor receptor functionalized liposomes with zinc-phthalocyanine for photodynamic therapy. Manuscript in preparation, 2015.
264. C. Mamot, D.C. Drummond, C.O. Noble, V. Kallab, Z.X. Guo, K.L. Hong, D.B. Kirpotin, J.W. Park, Epidermal growth factor receptor-targeted immunoliposomes significantly enhance the efficacy of multiple anticancer drugs in vivo, Cancer Res. 65 (2005) 11631–11638.
265. J.W. Park, K.L. Hong, D.B. Kirpotin, G. Colbern, R. Shalaby, J. Baselga, Y. Shao, U. B. Nielsen, J.D. Marks, D. Moore, D. Papahadjopoulos, C.C. Benz, Anti-HER2 immunoliposomes: enhanced efficacy attributable to targeted delivery, Clin. Cancer Res. 8 (2002) 1172–1181.
266. K. Nishikawa, T. Asai, H. Shigematsu, K. Shimizu, H. Kato, Y. Asano, S. Takashima, E. Mekada, N. Oku, T. Minamino, Development of anti-HB-EGF immunoliposomes for the treatment of breast cancer, J. Control. Release 160 (2012) 274–280.
267. M. Garcia-Diaz, S. Nonell, A. Villanueva, J.C. Stockert, M. Canete, A. Casado, M. Mora, M.L. Sagrista, Do folate-receptor targeted liposomal photosensitizers enhance photodynamic therapy selectivity? Biochim. Biophys. Acta 1808 (2011) 1063–1071.
268. Y. Mir, S.A. Elrington, T. Hasan, A new nanoconstruct for epidermal growth factor receptor-targeted photo-immunotherapy of ovarian cancer, Nanomed. Nanotechnol. Biol. Med. 9 (2013) 1114–1122.
269. M. Triesscheijn, M. Ruevekamp, M. Aalders, P. Baas, F.A. Stewart, Outcome of mTHPC mediated photodynamic therapy is primarily determined by the vascular response, Photochem. Photobiol. 81 (2005) 1161–1167.
270. V.H. Fingar, K.A. Siegel, T.J. Wieman, K.W. Doak, The effects of thromboxane inhibitors on the microvascular and tumor response to photodynamic therapy, Photochem. Photobiol. 58 (1993) 393–399.
271. P. Cramers, M. Ruevekamp, H. Oppelaar, O. Dalesio, P. Baas, F.A. Stewart, Foscan(R) uptake and tissue distribution in relation to photodynamic efficacy, Br. J. Cancer 88 (2003) 283–290.
272. B. Chen, P.A. de Witte, Photodynamic therapy efficacy and tissue distribution of hypericin in a mouse P388 lymphoma tumor model, Cancer Lett. 150 (2000) 111–117.
273. D.E.J.G. Dolmans, A. Kadambi, J.S. Hill, C.A. Waters, B.C. Robinson, J.P. Walker, D. Fukumura, R.K. Jain, Vascular accumulation of a novel photosensitizer MV6401, causes selective thrombosis in tumor vessels after photodynamic therapy, Cancer Res. 62 (2002) 2151–2156.
274. V.H. Fingar, P.K. Kik, P.S. Haydon, P.B. Cerrito, M. Tseng, E. Abang, T.J. Wieman, Analysis of acute vascular damage after photodynamic therapy using benzoporphyrin derivative (BPD), Br. J. Cancer 79 (1999) 1702–1708.
275. M. Heger, J.F. Beek, N.I. Moldovan, C.M.A.M. van der Horst, M.J.C. van Gemert, Towards optimization of selective

photothermolysis: prothrombotic pharmaceutical agents as potential adjuvants in laser treatment of port wine stains—a theoretical study, Thromb. Haemost. 93 (2005) 242–256.
276. M. Heger, R.F. van Golen, M. Broekgaarden, R.R. van den Bos, H.A.M. Neumann, T.M. van Gulik, M.J.C. van Gemert, Endovascular laser-tissue interactions and biological responses in relation to endovenous laser therapy, Lasers Med. Sci. 29 (2014) 405–422.
277. J. Zilberstein, S. Schreiber, M.C.W.M. Bloemers, P. Bendel, M. Neeman, E. Schechtman, F. Kohen, A. Scherz, Y. Salomon, Antivascular treatment of solid melanoma tumors with bacteriochlorophyll-serine-based photodynamic therapy, Photochem. Photobiol. 73 (2001) 257–266.
278. N. Madar-Balakirski, C. Tempel-Brami, V. Kalchenko, O. Brenner, D. Varon, A. Scherz, Y. Salomon, Permanent occlusion of feeding arteries and draining veins in solid mouse tumors by vascular targeted photodynamic therapy (VTP) with Tookad, Plos One 5 (2010).
279. G. Zhao, B.L. Rodriguez, Molecular targeting of liposomal nanoparticles to tumor microenvironment, Int. J. Nanomed. 8 (2013) 61–71.
280. C. Lonez, M. Vandenbranden, J.M. Ruysschaert, Cationic lipids activate intracellular signaling pathways, Adv. Drug Deliv. Rev. 64 (2012) 1749–1758.
281. W.J. Choi, J.K. Kim, S.H. Choi, J.S. Park, W.S. Ahn, C.K. Kim, Low toxicity of cationic lipid-based emulsion for gene transfer, Biomaterials 25 (2004) 5893–5903.
282. G. Thurston, J.W. Mclean, M. Rizen, P. Baluk, A. Haskell, T.J. Murphy, D. Hanahan, D.M. McDonald, Cationic liposomes target angiogenic endothelial cells in tumors and chronic inflammation in mice, J. Clin. Invest. 101 (1998) 1401–1413.
283. R.B. Campbell, D. Fukumura, E.B. Brown, L.M. Mazzola, Y. Izumi, R.K. Jain, V.P. Torchilin, L.L. Munn, Cationic charge determines the distribution of liposomes between the vascular and extravascular compartments of tumors, Cancer Res. 62 (2002) 6831–6836.
284. S.L. Diaz, V. Padler-Karavani, D. Ghaderi, N. Hurtado-Ziola, H. Yu, X. Chen, E.C. M. Brinkman-Van der Linden, A. Varki, N.M. Varki, Sensitive and specific detection of the non-human sialic acid N-glycolylneuraminic acid in human tissues and biotherapeutic products, PloS One 4 (2009).
285. M. Broekgaarden, R. Weijer, A.I. de Kroon, T.M. van Gulik, M. Heger, Liposomal delivery of Zn(II)-phthalocyanine towards tumor vascular endothelial cells increases efficacy of photodynamic therapy. Manuscript in preparation, 2015.
286. N. Gross, M. Ranjbar, C. Evers, J. Hua, G. Martin, B. Schulze, U. Michaelis, L.L. Hansen, H.T. Agostini, Choroidal neovascularization reduced by targeted drug delivery with cationic liposome-encapsulated paclitaxel or targeted photodynamic therapy with verteporfin encapsulated in cationic liposomes, Mol. Vision 19 (2013) 54–61.
287. L.M. Coussens, Z. Werb, Inflammation and cancer, Nature 420 (2002) 860– 867.
288. M.M. Mueller, N.E. Fusenig, Friends or foes—bipolar effects of the tumour stroma in cancer, Nat. Rev. Cancer 4 (2004) 839–849.
289. J.W. Pollard, Tumour-educated macrophages promote tumour progression and metastasis, Nat. Rev. Cancer 4 (2004) 71–78.
290. C.J. Gomer, A. Ferrario, M. Luna, N. Rucker, S. Wong, Photodynamic therapy: combined modality approaches targeting the tumor microenvironment, Lasers Surg. Med. 38 (2006) 516–521.
291. M.D.C. Pazos, H.B. Nader, Effect of photodynamic therapy on the extracellular matrix and associated components, Braz. J. Med. Biol. Res. 40 (2007) 1025– 1035.
292. R.F. van Golen, T.M. van Gulik, M. Heger, The sterile immune response during hepatic ischemia/reperfusion, Cytokine Growth Factor Rev. 23 (2012) 69–84.
293. Z. Amoozgar, Y. Yeo, Recent advances in stealth coating of nanoparticle drug delivery systems, Wiley Interdiscip. Rev. Nanomed. Nanobiotechnol. 4 (2012) 219–233.
294. V.P. Torchilin, V.S. Trubetskoy, Which polymers can make nanoparticulate drug carriers long-circulating? Adv. Drug Deliv. Rev. 16 (1995) 141–155.
295. S.K. Hobbs, W.L. Monsky, F. Yuan, W.G. Roberts, L. Griffith, V.P. Torchilin, R.K. Jain, Regulation of transport pathways in tumor vessels: role of tumor type and microenvironment, Proc. Natl. Acad. Sci. U. S. A. 95 (1998) 4607– 4612.
296. N.Z. Wu, D. Da, T.L. Rudoll, D. Needham, A.R. Whorton, M.W. Dewhirst, Increased microvascular permeability contributes to preferential accumulation of stealth liposomes in tumor tissue, Cancer Res. 53 (1993) 3765–3770.
297. N. Oku, N. Saito, Y. Namba, H. Tsukada, D. Dolphin, S. Okada, Application of long-circulating liposomes to cancer photodynamic therapy, Biol. Pharm. Bull. 20 (1997) 670–673.
298. L. Polo, G. Bianco, E. Reddi, G. Jori, The effect of different liposomal formulations on the interaction of Zn(II)-phthalocyanine with isolated low and high-density lipoproteins, Int. J. Biochem. Cell Biol. 27 (1995) 1249–1255.
299. C. Decker, F. Steiniger, A. Fahr, Transfer of a lipophilic drug (temoporfin) between small unilamellar liposomes and human plasma proteins: influence of membrane composition on vesicle integrity and release characteristics, J. Liposome Res. 23 (2013) 154–165.
300. V. Reshetov, V. Zorin, A. Siupa, M.A. D'Hallewin, F. Guillemin, L. Bezdetnaya, Interaction of liposomal formulations of meta-tetra(hydroxyphenyl) chlorin (temoporfin) with serum proteins: protein binding and liposome destruction, Photochem. Photobiol. 88 (2012) 1256–1264.
301. E. Reddi, S. Cernuschi, R. Biolo, G. Jori, Liposome- or LDL-administered Zn(II)-phthalocyanine as a photodynamic agent for tumours III. Effect of cholesterol on pharmacokinetic and phototherapeutic properties, Lasers Med. Sci. 5 (1990) 339–343.

302. L. Polo, G. Valduga, G. Jori, E. Reddi, Low-density lipoprotein receptors in the uptake of tumour photosensitizers by human and rat transformed fibroblasts, Int. J. Biochem. Cell Biol. 34 (2002) 10–23.
303. J.L. Goldstein, M.S. Brown, Low-density lipoprotein pathway and its relation to atherosclerosis, Ann. Rev. Biochem. 46 (1977) 897–930.
304. P. Shum, J.-M. Kim, D.H. Thompson, Phototriggering of liposomal drug delivery systems, Adv. Drug Deliv. Rev. 53 (2001) 273–284.
305. N. Fomina, J. Sankaranarayanan, A. Almutairi, Photochemical mechanisms of light-triggered release from nanocarriers, Adv. Drug Deliv. Rev. 64 (2012) 1005–1020.
306. S.J. Leung, M. Romanowski, Light-activated content release from liposomes, Theranostics 2 (2012) 1020–1036.
307. A. Andreoni, R. Cubeddu, S. Desilvestri, P. Laporta, G. Jori, E. Reddi, Hematoporphyrin derivative—experimental evidence for aggregated species, Chem. Phys. Lett. 88 (1982) 33–36.
308. A. Maier, F. Tomaselli, V. Matzi, P. Rehak, H. Pinter, F.M. Smolle-Juttner, Photosensitization with hematoporphyrin derivative compared to 5-aminolaevulinic acid for photodynamic therapy of esophageal carcinoma, Ann. Thorac. Surg. 72 (2001) 1136–1140.
309. P. Zimcik, M. Miletin, Photodynamic therapy, in: A.R. Lang (Ed.), Dyes and Pigments: New Reserach, Nova Science Publishers Inc., New York, 2009, pp.1–62.
310. M. Oertel, S.I. Schastak, A. Tannapfel, R. Hermann, U. Sack, J. Mossner, F. Berr, Novel bacteriochlorine for high tissue-penetration: photodynamic properties in human biliary tract cancer cells in vitro and in a mouse tumour model, J. Photochem. Photobiol. B 71 (2003) 1–10.
311. S.P. Pereira, L. Ayaru, R. Ackroyd, D. Mitton, G. Fullarton, M. Zammit, Z. Grzebieniak, H. Messmann, M.A. Ortner, L. Gao, M.M. Trinh, J. Spenard, The pharmacokinetics and safety of porfimer after repeated administration 30– 45 days apart to patients undergoing photodynamic therapy, Aliment. Pharmacol. Ther. 32 (2010) 821–827.
312. T.J. Dougherty, M.T. Cooper, T.S. Mang, Cutaneous phototoxic occurrences in patients receiving Photofrin, Lasers Surg. Med. 10 (1990) 485–488.
313. J.A. Woods, N.J. Traynor, L. Brancaleon, H. Moseley, The effect of Photofrin on DNA strand breaks and base oxidation in HaCaT keratinocytes: a comet assay study, Photochem. Photobiol. 79 (2004) 105–113.
314. J.T. Dalton, C.R. Yates, D.H. Yin, A. Straughn, S.L. Marcus, A.L. Golub, M.C. Meyer, Clinical pharmacokinetics of 5-aminolevulinic acid in healthy volunteers and patients at high risk for recurrent bladder cancer, J. Pharmacol. Exp. Ther. 301 (2002) 507–512.
315. J. Webber, D. Kessel, D. Fromm, Plasma levels of protoporphyrin IX in humans after oral administration of 5-aminolevulinic acid, J. Photochem. Photobiol. B 37 (1997) 151–153.
316. G. Ackermann, C. Abels, W. Baumler, S. Langer, M. Landthaler, E.W. Lang, R.M. Szeimies, Simulations on the selectivity of 5-aminolaevulinic acid-induced fluorescence in vivo, J. Photochem. Photobiol. B 47 (1998) 121–128.
317. H.B. Ris, H.J. Altermatt, R. Inderbitzi, R. Hess, B. Nachbur, J.C.M. Stewart, Q. Wang, C.K. Lim, R. Bonnett, M.C. Berenbaum, U. Althaus, Photodynamic therapy with chlorins for diffuse malignant mesothelioma—initial clinical results, Br. J. Cancer 64 (1991) 1116–1120.
318. E. Ricci-Junior, J.M. Marchetti, Zinc(II) phthalocyanine loaded PLGA nanoparticles for photodynamic therapy use, Int. J. Pharm. 310 (2006) 187– 195.
319. Z. Chen, S.Y. Zhou, J.C. Chen, Y.C. Deng, Z.P. Luo, H.W. Chen, M.R. Hamblin, M.D. Huang, Pentalysine beta-carbonylphthalocyanine zinc: an effective tumor-targeting photosensitizer for photodynamic therapy, Chem. Med. Chem. 5 (2010) 890–898.
320. J. Taillefer, M.C. Jones, N. Brasseur, J.E. van Lier, J.C. Leroux, Preparation and characterization of pH-responsive polymeric micelles for the delivery of photosensitizing anticancer drugs, J. Pharm. Sci. 89 (2000) 52–62.
321. Y.P. Fang, P.C. Wu, Y.H. Tsai, Y.B. Huang, Physicochemical and safety evaluation of 5-aminolevulinic acid in novel liposomes as carrier for skin delivery, J. Liposome Res. 18 (2008) 31–45.
322. Y. Sadzuka, K. Tokutomi, F. Iwasaki, I. Sugiyama, T. Hirano, H. Konno, N. Oku, T. Sonobe, The phototoxicity of Photofrin was enhanced by PEGylated liposome in vitro, Cancer Lett. 241 (2006) 42–48.
323. J. Soriano, M. Garcia-Diaz, M. Mora, M.L. Sagrista, S. Nonell, A. Villanueva, J.C. Stockert, M. Canete, Liposomal temocene (m-THPPo) photodynamic treatment induces cell death by mitochondria-independent apoptosis, Biochim. Biophys. Acta 1830 (2013) 4611–4620.
324. [324] G. Sharma, S. Anabousi, C. Ehrhardt, M.N.V. Ravi Kumar, Liposomes as targeted drug delivery systems in the treatment of breast cancer, J. Drug Target. 14 (2006) 301–310.
325. [325] D.E. Marotta, W. Cao, E.P. Wileyto, H. Li, I. Corbin, E. Rickter, J.D. Glickson, B. Chance, G. Zheng, T.M. Busch, Evaluation of bacteriochlorophyll-reconstituted low-density lipoprotein nanoparticles for photodynamic therapy efficacy in vivo, Nanomedicine (London England) 6 (2011) 475–487.
326. [326] H. Li, D.E. Marotta, S. Kim, T.M. Busch, E.P. Wileyto, G. Zheng, High payload delivery of optical imaging and photodynamic therapy agents to tumors using phthalocyanine-reconstituted low-density lipoprotein nanoparticles, J. Biomed. Opt. 10 (2005) 41203.
327. R. Decreau, M.J. Richard, P. Verrando, M. Chanon, M. Julliard, Photodynamic activities of silicon phthalocyanines against achromic M6 melanoma cells and healthy human melanocytes and keratinocytes, J. Photochem. Photobiol. B 48 (1999) 48–56.

328. M. Garcia-Diaz, M. Kawakubo, P. Mroz, M.L. Sagrista, M. Mora, S. Nonell, M.R. Hamblin, Cellular and vascular effects of the photodynamic agent temocene are modulated by the delivery vehicle, J. Control. Release 162 (2012) 355–363.
329. J. Shao, Y. Dai, W. Zhao, J. Xie, J. Xue, J. Ye, L. Jia, Intracellular distribution and mechanisms of actions of photosensitizer Zinc(II)-phthalocyanine solubilized in Cremophor EL against human hepatocellular carcinoma HepG2 cells, Cancer Lett. 330 (2013) 49–56.
330. R.P. Bagwe, J.R. Kanicky, B.J. Palla, P.K. Patanjali, D.O. Shah, Improved drug delivery using microemulsions: rationale, recent progress, and new horizons, Crit. Rev. Ther. Drug Carrier Syst. 18 (2001) 77–140.
331. A.M. Lima, C.D. Pizzol, F.B. Monteiro, T.B. Creczynski-Pasa, G.P. Andrade, A.O. Ribeiro, J.R. Perussi, Hypericin encapsulated in solid lipid nanoparticles: phototoxicity and photodynamic efficiency, J. Photochem. Photobiol. B 125 (2013) 146–154.
332. F.P. Navarro, G. Creusat, C. Frochot, A. Moussaron, M. Verhille, R. Vanderesse, J. S. Thomann, P. Boisseau, I. Texier, A.C. Couffin, M. Barberi-Heyob, Preparation and characterization of mTHPC-loaded solid lipid nanoparticles for photodynamic therapy, J. Photochem. Photobiol. B 130 (2014) 161–169.
333. C. Pardeshi, P. Rajput, V. Belgamwar, A. Tekade, G. Patil, K. Chaudhary, A. Sonje, Solid lipid based nanocarriers: an overview, Acta Pharm. (Zagreb, Croatia) 62 (2012) 433–472.
334. S.H. Battah, C.E. Chee, H. Nakanishi, S. Gerscher, A.J. MacRobert, C. Edwards, Synthesis and biological studies of 5-aminolevulinic acid-containing dendrimers for photodynamic therapy, Bioconjugate Chem. 12 (2001) 980–988.
335. O. Taratula, C. Schumann, M.A. Naleway, A.J. Pang, K.J. Chon, O. Taratula, A multifunctional theranostic platform based on phthalocyanine-loaded dendrimer for image-guided drug delivery and photodynamic therapy, Mol. Pharm. 10 (2013) 3946–3958.
336. Z. Mohammadi, A. Sazgarnia, O. Rajabi, S. Soudmand, H. Esmaily, H.R. Sadeghi, An in vitro study on the photosensitivity of 5-aminolevulinic acid conjugated gold nanoparticles, Photodiagn. Photodyn. Ther. 10 (2013) 382–388.
337. H. Eshghi, A. Sazgarnia, M. Rahimizadeh, N. Attaran, M. Bakavoli, S. Soudmand, Protoporphyrin IX-gold nanoparticle conjugates as an efficient photosensitizer in cervical cancer therapy, Photodiagn. Photodyn. Ther. 10 (2013) 304–312.
338. T. Stuchinskaya, M. Moreno, M.J. Cook, D.R. Edwards, D.A. Russell, Targeted photodynamic therapy of breast cancer cells using antibody-phthalocyanine-gold nanoparticle conjugates, Photochem. Photobiol. Sci. 10 (2011) 822–831.
339. R. Arvizo, R. Bhattacharya, P. Mukherjee, Gold nanoparticles: opportunities and challenges in nanomedicine, Expert Opin. Drug Deliv. 7 (2010) 753–763.
340. J.W. Hofman, M.G. Carstens, F. van Zeeland, C. Helwig, F.M. Flesch, W.E. Hennink, C.F. van Nostrum, Photocytotoxicity of mTHPC (temoporfin) loaded polymeric micelles mediated by lipase catalyzed degradation, Pharm. Res. 25 (2008) 2065–2073.
341. A.M. Master, M.E. Rodriguez, M.E. Kenney, N.L. Oleinick, A.S. Gupta, Delivery of the photosensitizer Pc 4 in PEG-PCL micelles for in vitro PDT studies, J Pharm Sci. 99 (2010) 2386–2398.
342. L. Lamch, U. Bazylinska, J. Kulbacka, J. Pietkiewicz, K. Biezunska-Kusiak, K.A. Wilk, Polymeric micelles for enhanced Photofrin II (R) delivery, cytotoxicity and pro-apoptotic activity in human breast and ovarian cancer cells, Photodiagn. Photodyn. Ther. 11 (2014) 570–585.
343. M.N. Sibata, A.C. Tedesco, J.M. Marchetti, Photophysicals and photochemicals studies of zinc(II) phthalocyanine in long time circulation micelles for photodynamic therapy use, Eur. J. Pharm. Sci. 23 (2004) 131–138.
344. M. Yokoyama, Polymeric micelles as a new drug carrier system and their required considerations for clinical trials, Expert Opin. Drug Deliv. 7 (2010) 145–158.
345. L. Shi, X. Wang, F. Zhao, H. Luan, Q. Tu, Z. Huang, H. Wang, H. Wang, In vitro evaluation of 5-aminolevulinic acid (ALA) loaded PLGA nanoparticles, Int. J. Nanomed. 8 (2013) 2669–2676.
346. A. Vaidya, Y. Sun, Y. Feng, L. Emerson, E.K. Jeong, Z.R. Lu, Contrast-enhanced MRI-guided photodynamic cancer therapy with a pegylated bifunctional polymer conjugate, Pharm. Res. 25 (2008) 2002–2011.
347. I.V. Martynenko, V.A. Kuznetsova, A.O. Orlova, P.A. Kanaev, V.G. Maslov, A. Loudon, V. Zaharov, P. Parfenov, Y.K. Gun'ko, A.V. Baranov, A.V. Fedorov, Chlorin e6-ZnSe/ZnS quantum dots based system as reagent for photodynamic therapy, Nanotechnology 26 (2015) 55102.
348. C. Fowley, N. Nomikou, A.P. McHale, B. McCaughan, J.F. Callan, Extending the tissue penetration capability of conventional photosensitisers: a carbon quantum dot-protoporphyrin IX conjugate for use in two-photon excited photodynamic therapy, Chem. Commun. (Cambridge, England) 49 (2013) 8934–8936.
349. J.M. Tsay, M. Trzoss, L. Shi, X. Kong, M. Selke, M.E. Jung, S. Weiss, Singlet oxygen production by peptide-coated quantum dot-photosensitizer conjugates, J. Am. Chem. Soc. 129 (2007) 6865–6871.
350. J. Drbohlavova, V. Adam, R. Kizek, J. Hubalek, Quantum dots— characterization, preparation and usage in biological systems, Int. J. Mol. Sci. 10 (2009) 656–673.
351. P. Sapra, T.M. Allen, Internalizing antibodies are necessary for improved therapeutic efficacy of antibody-targeted liposomal drugs, Cancer Res. 62 (2002) 7190–7194.
352. P. Sapra, E.H. Moase, J. Ma, T.M. Allen, Improved therapeutic responses in a xenograft model of human B lymphoma (Namalwa) for liposomal vincristine versus liposomal doxorubicin targeted via anti-CD19 IgG2a or Fab' fragments, Clin. Cancer Res. 10 (2004) 1100–1111.
353. C. Mamot, R. Ritschard, W. Kung, J.W. Park, R. Herrmann, C.F. Rochlitz, EGFR-targeted immunoliposomes derived from the monoclonal antibody EMD72000 mediate specific and efficient drug delivery to a variety of colorectal cancer cells, J. Drug Target. 14 (2006) 215–223.

354. I.Y. Kim, Y.S. Kang, D.S. Lee, H.J. Park, E.K. Choi, Y.K. Oh, H.J. Son, J.S. Kim, Antitumor activity of EGFR targeted pH-sensitive immunoliposomes encapsulating gemcitabine in A549 xenograft nude mice, J. Control. Release 140 (2009) 55–60.
355. J.H. Mortensen, M. Jeppesen, L. Pilgaard, R. Agger, M. Duroux, V. Zachar, T. Moos, Targeted antiepidermal growth factor receptor (cetuximab) immunoliposomes enhance cellular uptake in vitro and exhibit increased accumulation in an intracranial model of glioblastoma multiforme, J. Drug Deliv. 2013 (2013) 209205.
356. J. Lehtinen, M. Raki, K.A. Bergstrom, P. Uutela, K. Lehtinen, A. Hiltunen, J. Pikkarainen, H.M. Liang, S. Pitkanen, A.M. Maatta, R.A. Ketola, M. Yliperttula, T. Wirth, A. Urtti, Pre-targeting and direct immunotargeting of liposomal drug carriers to ovarian carcinoma, Plos One 7 (2012) e41410.
357. F. Pastorino, C. Brignole, D. Marimpietri, P. Sapra, E.H. Moase, T.M. Allen, M. Ponzoni, Doxorubicin-loaded Fab' fragments of anti-disialoganglioside immunoliposomes selectively inhibit the growth and dissemination of human neuroblastoma in nude mice, Cancer Res. 63 (2003) 86–92.
358. U.B. Nielsen, D.B. Kirpotin, E.M. Pickering, K.L. Hong, J.W. Park, M.R. Shalaby, Y. Shao, C.C. Benz, J.D. Marks, Therapeutic efficacy of anti-ErbB2 immunoliposomes targeted by a phage antibody selected for cellular endocytosis, Biochim. Biophys. Acta. 1591 (2002) 109–118.
359. J. Gao, W. Zhong, J.Q. He, H.M. Li, H. Zhang, G.C. Zhou, B.H. Li, Y. Lu, H. Zou, G. Kou, D.P. Zhang, H. Wang, Y.J. Guo, Y.Q. Zhong, Tumor-targeted PE38KDEL delivery via PEGylated anti-HER2 immunoliposomes, Int. J. Pharm. 374 (2009) 145–152.
360. D. Kirpotin, J.W. Park, K. Hong, S. Zalipsky, W.L. Li, P. Carter, C.C. Benz, D. Papahadjopoulos, Sterically stabilized anti-HER2 immunoliposomes: design and targeting to human breast cancer cells in vitro, Biochemistry 36 (1997) 66–75.
361. C. Hantel, F. Lewrick, S. Schneider, O. Zwermann, A. Perren, M. Reincke, R. Suss, F. Beuschlein, Anti insulin-like growth factor I receptor immunoliposomes: a single formulation combining two anticancer treatments with enhanced therapeutic efficiency, J. Clin. Endocrinol. Metab. 95 (2010) 943–952.
362. H. Hatakeyama, H. Akita, E. Ishida, K. Hashimoto, H. Kobayashi, T. Aoki, J. Yasuda, K. Obata, H. Kikuchi, T. Ishida, H. Kiwada, H. Harashima, Tumor targeting of doxorubicin by anti-MT1-MMP antibody-modified PEG liposomes, Int. J. Pharm. 342 (2007) 194–200.
363. S. Gosk, T. Moos, C. Gottstein, G. Bendas, VCAM-1 directed immunoliposomes selectively target tumor vasculature in vivo, Biochim. Biophys. Acta 1778 (2008) 854–863.
364. P. Roth, C. Hammer, A.C. Piguet, M. Ledermann, J.F. Dufour, E. Waelti, Effects on hepatocellular carcinoma of doxorubicin-loaded immunoliposomes designed to target the VEGFR-2, J. Drug Target. 15 (2007) 623–631.
365. A. Wicki, C. Rochlitz, A. Orleth, R. Ritschard, I. Albrecht, R. Herrmann, G. Christofori, C. Mamot, Targeting tumor-associated endothelial cells: anti-VEGFR2 immunoliposomes mediate tumor vessel disruption and inhibit tumor growth, Clin. Cancer Res. 18 (2012) 454–464.
366. P. Lipponen, M. Eskelinen, Expression of epidermal growth factor receptor in bladder cancer as related to established prognostic factors, oncoprotein (c-erbB-2, p53) expression and long-term prognosis, Br. J. Cancer 69 (1994) 1120–1125.
367. L.N. Turkeri, M.L. Erton, I. Cevik, A. Akdas, Impact of the expression of epidermal growth factor, transforming growth factor alpha, and epidermal growth factor receptor on the prognosis of superficial bladder cancer, Urology 51 (1998) 645–649.
368. H. Olsson, I.M. Fyhr, P. Hultman, S. Jahnson, HER2 status in primary stage T1 urothelial cell carcinoma of the urinary bladder, Scand. J. Urol. Nephrol. 46 (2012) 102–107.
369. T.A. Abd Elazeez, A. El-Balshy, M.M. Khalil, M.M. El-Tabye, H. Abdul-Halim, Prognostic significance of P27 (Kip 1) and MUC1 in papillary transitional cell carcinoma of the urinary bladder, Urol. Ann. 1 (2011) 8–13.
370. X.J. Cao, J.F. Hao, X.H. Yang, P. Xie, L.P. Liu, C.P. Yao, J. Xu, Prognostic value of expression of EGFR and nm23 for locoregionally advanced nasopharyngeal carcinoma, Med. Oncol. 29 (2012) 263–271.
371. T.J. Kim, Y.S. Lee, J.H. Kang, Y.S. Kim, C.S. Kang, Prognostic significance of expression of VEGF and Cox-2 in nasopharyngeal carcinoma and its association with expression of C-erbB2 and EGFR, J. Surg. Oncol. 103 (2011) 46–52.
372. J.J. Pan, L. Kong, S.N. Lin, G. Chen, Q. Chen, J.J. Lu, The clinical significance of coexpression of cyclooxygenases-2, vascular endothelial growth factors, and epidermal growth factor receptor in nasopharyngeal carcinoma, Laryngoscope 118 (2008) 1970–1975.
373. R. Soo, T. Putti, Q. Tao, B.C. Goh, K.H. Lee, L. Kwok-Seng, L. Tan, W.S. Hsieh, Overexpression of cyclooxygenase-2 in nasopharyngeal carcinoma and association with epidermal growth factor receptor expression, Arch. Otolaryngol. Head Neck Surg. 131 (2005) 147–152.
374. Y.L. Yuan, X.H. Zhou, J. Song, X.P. Qiu, J. Li, L.F. Ye, X.P. Meng, D. Xia, Expression and clinical significance of epidermal growth factor receptor and type 1 insulin-like growth factor receptor in nasopharyngeal carcinoma, Ann. Otol. Rhinol. Laryngol. 117 (2008) 192–200.
375. J. Harder, O. Waiz, F. Otto, M. Geissler, M. Olschewski, B. Weinhold, H.E. Blum, A. Schmitt-Graeff, O.G. Opitz, EGFR and HER2 expression in advanced biliary tract cancer, World J. Gastroenterol. 15 (2009) 4511–4517.
376. Y. Pignochino, I. Sarotto, C. Peraldo-Neia, J.Y. Penachioni, G. Cavalloni, G. Migliardi, L. Casorzo, G. Chiorino, M. Risio, A. Bardelli, M. Aglietta, F. Leone, Targeting EGFR/HER2 pathways enhances the antiproliferative effect of gemcitabine in biliary tract and gallbladder carcinomas, BMC Cancer 10 (2010) 631.
377. M. Wiedmann, J. Feisthammel, T. Bluthner, A. Tannapfel, T. Kamenz, A. Kluge, J. Mossner, K. Caca, Novel targeted approaches to treating biliary tract cancer: the dual epidermal growth factor receptor and ErbB-2 tyrosine kinase inhibitor NVP-AEE788 is more efficient than the epidermal growth factor receptor inhibitors gefitinib and erlotinib, Anticancer

Drugs 17 (2006) 783–795.
378. D. Yoshikawa, H. Ojima, M. Iwasaki, N. Hiraoka, T. Kosuge, S. Kasai, S. Hirohashi, T. Shibata, Clinicopathological and prognostic significance of EGFR, VEGF, and HER2 expression in cholangiocarcinoma, Br. J. Cancer 98 (2008) 418–425.
379. T. Kawamoto, S. Krishnamurthy, E. Tarco, S. Trivedi, I.I. Wistuba, D. Li, I. Roa, J. C. Roa, M.B. Thomas, HER receptor family: novel candidate for targeted therapy for gallbladder and extrahepatic bile duct cancer, Gastrointest. Cancer Res. 6 (2007) 221–227.
380. H.J. Kim, T.W. Yoo, D.I. Park, J.H. Park, Y.K. Cho, C.I. Sohn, W.K. Jeon, B.I. Kim, M. K. Kim, S.W. Chae, J.H. Sohn, Gene amplification and protein overexpression of HER-2/neu in human extrahepatic cholangiocarcinoma as detected by chromogenic in situ hybridization and immunohistochemistry: its prognostic implication in node-positive patients, Ann. Oncol. 18 (2007) 892–897.
381. J. Zheng, Y.M. Zhu, Expression of c-erbB-2 proto-oncogene in extrahepatic cholangiocarcinoma and its clinical significance, Hepatobiliary Pancreat. Dis. Int. 6 (2007) 412–415.
382. VCCLAB, Virtual Computational Chemistry Laboratory, http://www.vcclab. org, 2005.
383. S. Jacques, Optical absorption of melanin, Oregon Medical Laser Center, http://omlc.ogi.edu/spectra/melanin/, 2012.
384. S. Prahl, Optical absorption of hemoglobin, Oregon Medical Laser Center, http://omlc.ogi.edu/spectra/hemoglobin/, 2012.
385. R. Kang, K.M. Livesey, H.J. Zeh, M.T. Lotze, D.L. Tang, HMGB1 A novel Beclin 1-binding protein active in autophagy, Autophagy 6 (2010) 1209–1211.
386. J.J. Kloek, X. Marechal, J. Roelofsen, R.H. Houtkooper, A.B.P. van Kuilenburg, W. Kulik, R. Bezemer, R. Neviere, T.M. van Gulik, M. Heger, Cholestasis is associated with hepatic microvascular dysfunction and aberrant energy metabolism before and during ischemia-reperfusion, Antioxid. Redox Signaling 17 (2012) 1109–1123.
387. I.C.J.H. Post, W.M.I. de Boon, M. Heger, A.C.W.A. van Wijk, J. Kroon, J.D. van Buul, T.M. van Gulik, Endothelial cell preservation at hypothermic to normothermic conditions using clinical and experimental organ preservation solutions, Exp. Cell Res. 319 (2013) 2501–2513.

Chapter 3

Low-power photodynamic therapy induces survival signaling in perihilar cholangiocarcinoma cells

BMC Cancer (2015)

RUUD WEIJER
MANS BROEKGAARDEN
ROWAN F. VAN GOLEN
ESTHER BULLE
ESTHER NIEUWENHUIS
ALDO JONGEJAN
PERRY D. MOERLAND
ANTOINE H. VAN KAMPEN
THOMAS M. VAN GULIK
MICHAL HEGER

Abstract

Photodynamic therapy (PDT) of solid cancers comprises the administration of a photosensitizer followed by illumination of the photosensitizer-replete tumor with laser light. This induces a state of local oxidative stress, culminating in the destruction of tumor tissue and microvasculature and induction of an anti-tumor immune response. However, some tumor types, including perihilar cholangiocarcinoma, are relatively refractory to PDT, which may be attributable to the activation of survival pathways in tumor cells following PDT (*i.e.*, activator protein 1 (AP-1)-, nuclear factor of kappa light polypeptide gene enhancer in B-cells (NF-κB)-, hypoxia-inducible factor 1-alpha (HIF-1α)-, nuclear factor (erythroid-derived 2)-like 2 (NFE2L2)-, and unfolded protein response-mediated pathways).

To assess the activation of survival pathways after PDT, human perihilar cholangiocarcinoma (SK-ChA-1) cells were subjected to PDT with zinc phthalocyanine (ZnPC)-encapsulating liposomes. Following 30-minute incubation with liposomes, the cells were either left untreated or treated at low (50 mW) or high (500 mW) laser power (cumulative light dose of 15 J/cm^2). Cells were harvested 90 min post-PDT and whole genome expression analysis was performed using Illumina HumanHT-12 v4 expression beadchips. The data were interpreted in the context of the survival pathways. In addition, the safety of ZnPC-encapsulating liposomes was tested both *in vitro* and *in vivo*.

PDT-treated SK-ChA-1 cells exhibited activation of the hypoxia-induced stress response via HIF-1α and initiation of the pro-inflammatory response via NF-κB. PDT at low laser power in particular caused extensive survival signaling, as evidenced by the significant upregulation of HIF-1- ($P < 0.001$) and NF-κB-related ($P < 0.001$) genes. Low-power PDT was less lethal to SK-ChA-1 cells 90 min post-PDT, confirmed by annexin V/propidium iodide staining. *In vitro* toxicogenomics and toxicological testing in chicken embryos and mice revealed that the ZnPC-encapsulating liposomes are non-toxic.

PDT-treated perihilar cholangiocarcinoma cells exhibit extensive survival signaling that may translate to a suboptimal therapeutic response and possibly tumor recurrence. These findings encourage the development of photosensitizer delivery systems with co-encapsulated inhibitors of survival pathways.

Keywords
Drug delivery system, metallated phthalocyanines, non-resectable perihilar cholangiocarcinoma, therapeutic recalcitrance, tumor targeting

Background

Photodynamic therapy (PDT) is a non-to-minimally invasive treatment modality that is used for the curative or palliative treatment of early-stage and late-stage solid cancers, respectively. The therapy relies on the accumulation of a non-toxic photosensitizer in the tumor following topical or systemic administration. Subsequently, the tumor is light-irradiated locally at a wavelength that corresponds to the red absorption peak of the photosensitizer. This leads to photosensitizer activation and generation of cytotoxic reactive oxygen species (ROS) via type I (superoxide anion) and/or type II (singlet oxygen) photochemical reactions. Extensive intratumoral ROS production initiates several key processes that culminate in the removal of the tumor, including: (1) induction of different forms of tumor cell death, (2) destruction of tumor microvasculature, (3) blood flow stasis and consequent tumor hypoxia/anoxia, and (4) induction of an anti-tumor immune response (reviewed in [1–3]).

Although PDT is highly effective in some cancer types (*e.g.*, basal cell carcinoma, early-stage esophageal carcinoma) [4–7], other solid cancers are relatively unresponsive to PDT (*e.g.*, nasopharyngeal carcinoma [8], perihilar cholangiocarcinoma [9]). This therapeutic recalcitrance may be explained by three key factors. First, the route of photosensitizer administration may be suboptimal for a specific tumor type, thereby deterring optimal photosensitizer accumulation in the tumor. Second, the approved first-generation photosensitizers (*i.e.*, hematoporphyrin derivatives and 5-aminolevulinic acid) exhibit poor photophysical and physicochemical properties, leading to insufficient and/or heterogeneous ROS production throughout the tumor bulk. Third, activation of survival pathways by tumor cells as a result of PDT may lead to insufficient tumor cell death following PDT [10].

To resolve these issues, a novel PDT modality was proposed based on the encapsulation of the photosensitizer zinc phthalocyanine (ZnPC) into polyethylene glycol (PEG)-coated liposomes [11]. Accordingly, three distinct ZnPC-containing nanoparticulate formulations were developed that are either targeted to tumor cells (tumor cell-targeting liposomes), tumor endothelium (endothelium-targeting liposomes), or tumor interstitium (interstitially-targeted liposomes (ITLs)) [11]. This comprehensive tumor-targeting strategy is expected to augment therapeutic efficacy and minimize photosensitivity and phototoxicity that are observed in patients treated with currently approved PDT modalities.

The aims of this study were to evaluate whether ZnPC-encapsulating ITLs (ZnPC-ITLs) are safe for future clinical application using toxicogenomics [12], chicken embryos, and mice as toxicological test models and to study the PDT-induced activation of survival pathways in human perihilar cholangiocarcinoma cells – *i.e.*, cells derived from a cancer that is recalcitrant to PDT. For the latter aim, whole genome gene expression profiles were determined in the early phase (90 min) after PDT in

accordance with literature [13] and the data were analyzed in the context of the five major PDT-induced survival pathways [10] (**Fig. 1**).

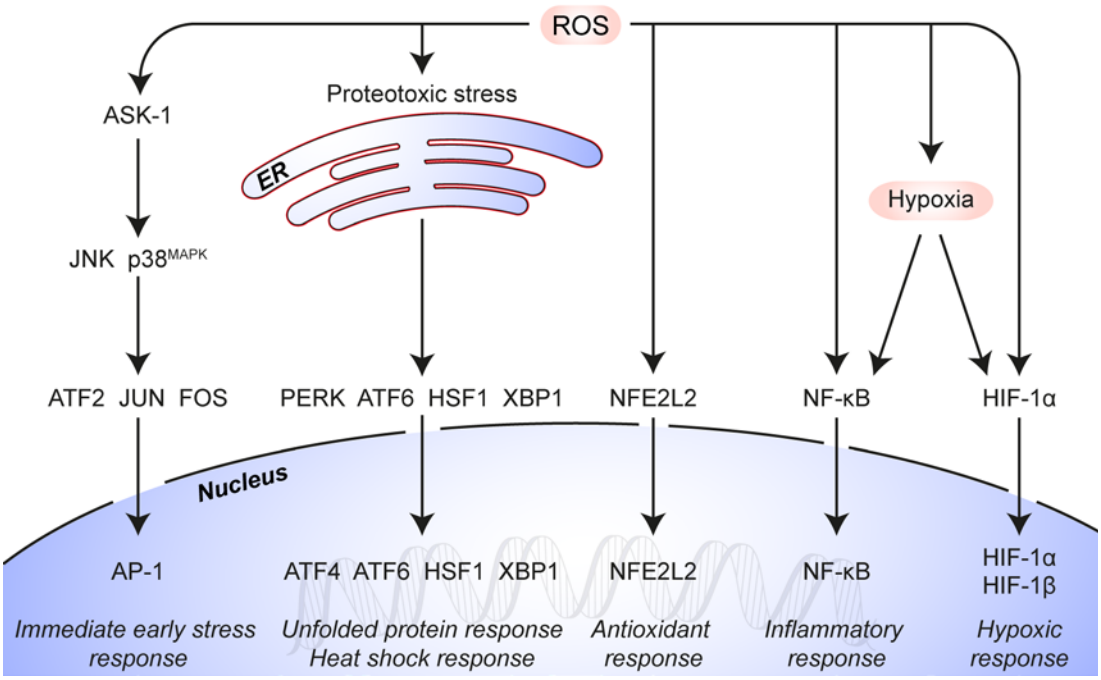

Fig. 1. Induction of survival signaling after PDT. PDT-mediated ROS production results in activation of (**1**) the immediate early gene response via activator protein 1 (AP-1), (**2**) the unfolded protein response in reaction to endoplasmic reticulum (ER) stress, (**3**) the antioxidant response via nuclear factor (erythroid-derived 2)-like 2 (NFE2L2), (**4**) the inflammatory response via activation of nuclear factor of kappa light polypeptide gene enhancer in B-cells (NF-κB), and (**5**) the hypoxia-induced stress response via hypoxia-inducible factor 1-alpha (HIF-1α). Data and figure adapted from [10]

The main findings were, first, that ZnPC-ITLs are not toxic *in vitro* and *in vivo* up to a 500-μM and 2.5-mM final lipid concentration, respectively, at a ZnPC:lipid molar ratio of 0.003. Second, irradiation of cells at low laser power (50 mW, 15 J/cm^2) caused considerable survival signaling after PDT via activation of hypoxia-inducible factor 1 (HIF-1) and nuclear factor of kappa light polypeptide gene enhancer in B-cells (NF-κB), which was associated with limited photokilling capacity. Irradiation of cells at high laser power (500 mW, 15 J/cm^2) was associated with less extensive survival signaling and resulted in more profound cell death.

Results

PDT efficacy

The *in vitro* proof-of-concept regarding ZnPC-ITLs as part of a novel multi-targeting strategy for PDT was provided previously [14]. However, this study did not examine the effect of laser power on post-PDT viability. It was hypothesized that low

laser power (*i.e.*, low degree of ROS production per unit time) would allow cells to cope with ROS-induced damage, whereas high laser power would be more toxic to cells. To investigate the influence of laser power on PDT efficacy, SK-ChA-1 cells were incubated with ZnPC-ITLs and either not irradiated (dark toxicity, designated as 'ITL') or irradiated at high laser power (500 mW, designated as 'ITL 500') or low laser power (50 mW, designated as 'ITL 50') with a cumulative radiant exposure of 15 J/cm^2. As shown in **Fig. 2A**, cells in the ITL group exhibited slightly higher metabolic activity than the control cells 24 h after treatment, whereas metabolic activity was completely abrogated in the treated cells. Cell death was assessed with the SRB protein assay, which revealed that cell viability had decreased to 47.6 % and 51.4 % (normalized to the control group) in the ITL 50 and ITL 500 groups, respectively (**Fig. 2B**).

In addition, SK-ChA-1 cells were stained with annexin V and PI 90 min (**Fig. 2C**) and 24 h (**Fig. 2D**) after PDT to evaluate the mode of cell death by flow cytometry. After 90 min, the ITL group paralleled the control group with a cell viability of approximately 90 %, whereas 43.6 % and 27.2 % of cells were viable in the ITL 50 and ITL 500 groups, respectively (**Fig. 2C**). The difference in cell viability between the treatment groups was abolished 24 h after PDT (**Fig. 2D**), suggesting that execution of cell death programs had not yet completed 90 min after low light dose PDT and that laser power therefore dictates the rate at which cell death programs are executed.

In vitro and in vivo toxicity

Next to efficacy, the safety of a new liposomal formulation is a critical parameter in the preclinical development trajectory. Therefore, *in vivo* toxicity was evaluated in two different animal models, namely in chicken embryos and in C57BL/6 mice. The chicken embryo model was chosen to assess acute toxicity, as it is a cheap and suitable substitute for mammalian models [15]. Alternatively, a mouse model was used to study long-term toxicity. As shown in **Fig. S1**, systemically administered ZnPC-ITLs did not exhibit any toxicity. In addition, whole genome microarray-based toxicogenomics is considered a valuable tool for evaluating the toxicity of xenobiotics [12, 16]. Therefore, as a complementary method to the *in vivo* toxicity testing, the *in vitro* toxicity of ZnPC-ITLs was analyzed in SK-ChA-1 cells by microarray analysis. SK-ChA-1 control cells and cells that were incubated with ZnPC-ITLs in the dark (ITL) exhibited similar transcriptional responses (**Fig. 3A**). None of the genes were differentially expressed when comparing the ITL group to the control group, corroborating the *in vivo* data at a molecular level.

Gross transcriptional response to PDT

In addition to the toxicogenomic profile of ZnPC-ITLs, the transcriptomic data was used to gain insight in the immediate early gene response [13] and explain the differences in cell viability that were observed 90 min post-PDT (**Fig. 2C**). As depicted

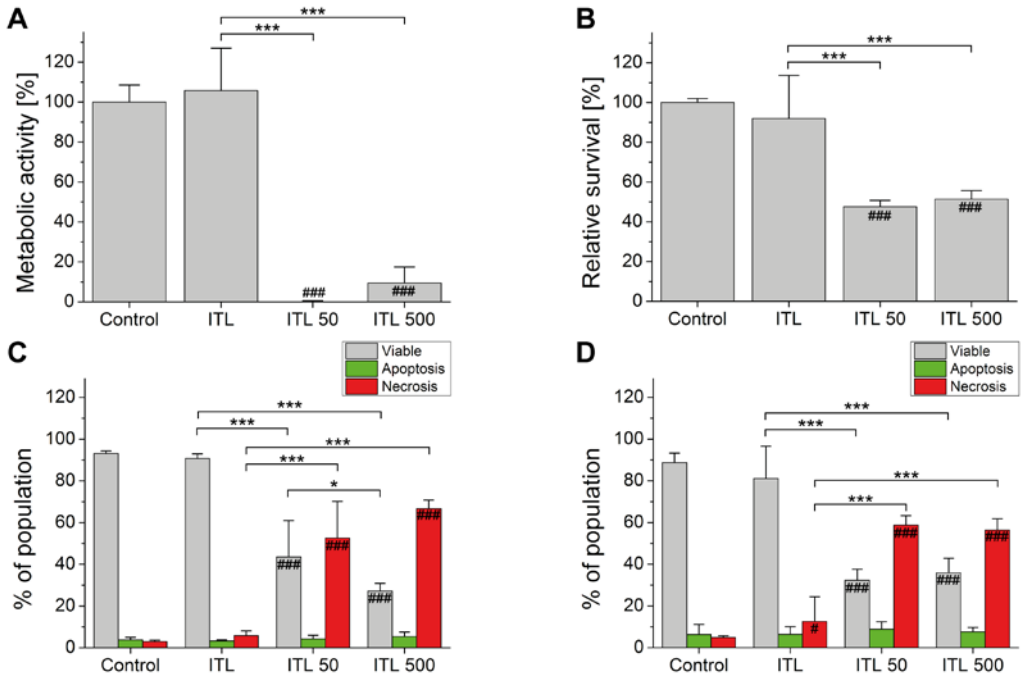

Fig. 2. Viability of SK-ChA-1 cells after ZnPC-ITL-PDT. SK-ChA-1 cells were incubated with 500 µM ZnPC-ITLs (final lipid concentration) and kept in the dark (ITL) or were irradiated with 50-mW (ITL 50) or 500-mW (ITL 500) laser light at a cumulative radiant exposure of 15 J/cm^2. Metabolic activity and the extent of cell death were assessed after 24 hours with a WST-1 assay (**A**) and SRB assay (**B**), respectively. Data were normalized to control cells that were set at 100 %. Alternatively, the mode of cell death was assessed 90 minutes (**C**) or 24 hours (**D**) post-PDT by flow cytometry. For this purpose, cells were stained with Alexa Fluor 488-conjugated annexin V and propidium iodide (PI). Necrotic cells are represented in red (PI-positive), apoptotic cells are shown in green (PI-negative, annexin V-positive), and healthy cells are represented in white (PI-negative, annexin V-negative). Values are presented as mean + SD for n = 6 per group. Readers are referred to section Statistical analysis for the significance of the statistical symbols.

in **Fig. 3A**, the global molecular response of the ITL 50 and ITL 500 groups were not associated and both groups showed a distinct response relative to the control group. The ITL 500 modality resulted in the upregulation of 213 genes and downregulation of 375 genes (588 total) compared to the control regimen (**Fig. 3B**). The number of differentially expressed genes in the ITL 50 group relative to control was ~10-fold greater (*i.e.*, 5,598) versus the ITL 500 group. Cells in the ITL 50 and the ITL 500 group exhibited some overlap in differentially expressed genes, namely 154 upregulated genes and 218 downregulated genes.

Differential gene regulation in response to PDT

To gain insight in the key processes that are initiated by PDT at the molecular level, the top increased and decreased genes were ranked based on the $\log_2$ fold-change (**Fig. 4**, with more detailed information in **Tables 1** and **2**). Compared to the control group, the ITL 50 group exhibited more profound changes in gene expression than the

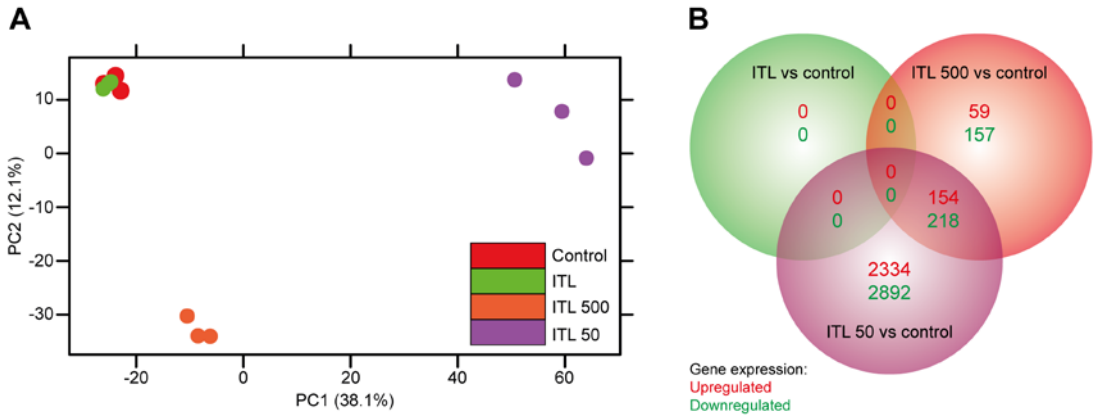

Fig. 3. (**A**) Principal component analysis of SK-ChA-1 cells that were either untreated (in red), incubated with 500 µM ZnPC-ITLs (final lipid concentration) and kept in the dark (ITL, in green), or treated with 500-mW (ITL 500, in orange) or 50-mW (ITL 50, in purple) laser light. The extent to which a principal component (PC) accounts for the variability in the data is indicated in parentheses. (**B**) Venn diagram showing the number of non-overlapping upregulated and downregulated genes per group (in-circle values) and the number of overlapping upregulated and downregulated genes (values in the respective overlapping region) between the various treatment groups compared to the control group. The total number of genes that were up- and downregulated per group comprises the sum of all regions in a given circle.

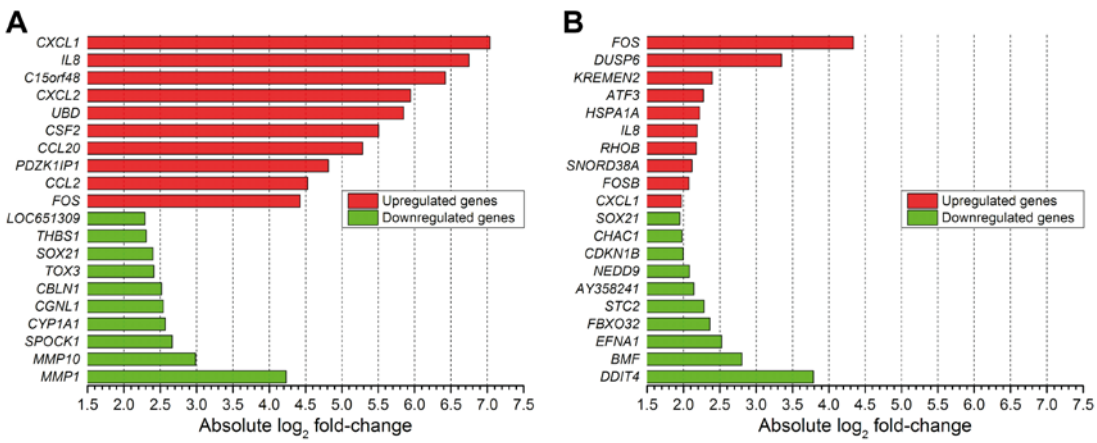

Fig. 4. Top upregulated and downregulated PDT-induced genes as expressed by the $\log_2$ fold-change in gene expression in the ITL 50 (**A**) and ITL 500 group (**B**) compared to the control group. Genes were ordered by decreasing absolute $\log_2$ fold-change. Values are presented as the mean of $n = 3$ per group.

ITL 500 group. Of note, the microarray expression data were validated by determining the transcript levels of specific genes by qRT-PCR, which revealed a strong correlation (**Fig. S2**).

As shown in **Table 1**, the top upregulated genes in the ITL 50 group are involved in chemotaxis (chemokine (C-X-C motif) ligand 1 (*CXCL1*) and *CXCL2*), inflammation (interleukin 8 (*IL8*), FBJ murine osteosarcoma viral oncogene homolog (*FOS*)), and the immune response (colony stimulating factor 2 (*CSF2*)), whereas downregulated genes are associated with cell adhesion (thrombospondin 1 (*THBS1*)) and the extracellular

matrix (matrix metallopeptidase 1 (*MMP1*), *MMP10*). In contrast, treatment of SK-ChA-1 cells at 500-mW laser power activated transcripts related to mitogen-activated protein (MAP) kinase (MAPK) signaling (dual specificity phosphatase 6 (*DUSP6*)), the stress response (activating transcription factor 3 (*ATF3*)), and response to ROS and unfolded proteins (*FOS*, heat shock 70 kDa protein 1A (*HSPA1A*)) (**Table 2**). High-power irradiation also resulted in downregulation of genes involved in cell cycle arrest (cyclin-dependent kinase inhibitor 1B (*CDKN1B*)) and apoptosis initiation (Bcl2 modifying factor (*BMF*)).

Gene	Full name	Function
CXCL1	chemokine (C-X-C motif) ligand 1	Cell proliferation, chemotaxis, inflammation
IL8	interleukin 8	Angiogenesis, chemotaxis, inflammation
C15orf48	chromosome 15 open reading frame 48	
CXCL2	chemokine (C-X-C motif) ligand 2	Chemotaxis, inflammation
UBD	ubiquitin D	Protein ubiquitination, aggresome formation, myeloid DC differentiation
CSF2	colony stimulating factor 2	Macrophage activation, DC differentiation, immune response
CCL20	chemokine (C-C motif) ligand 20	Chemotaxis, inflammation
PDZK1IP1	PDZK1 interacting protein 1	
CCL2	chemokine (C-C motif) ligand 2	Chemotaxis, inflammation
FOS	FBJ murine osteosarcoma viral oncogene homolog	Inflammation, cellular response to ROS, DNA methylation
LOC651309		
THBS1	thrombospondin 1	Cell adhesion, extracellular matrix organization,
SOX21	SRY (sex determining region Y)-box 21	Transcription from RNA polymerase II promoter, SC differentiation
TOX3	TOX high mobility group box family member 3	DNA-dependent transcription
CBLN1	cerebellin 1 precursor	Positive regulation of synapse assembly
CGNL1	cingulin-like 1	Motor activity
CYP1A1	cytochrome P450, family 1, subfamily A, polypeptide 1	Xenobiotic metabolic processes, drug metabolic processes
SPOCK1	testican 1	Neuron migration, neurogenesis
MMP10	matrix metallopeptidase 10	Proteolysis, extracellular matrix disassembly
MMP1	matrix metallopeptidase 1	Proteolysis, extracellular matrix disassembly

Table 1. Top 10 most up- and downregulated genes induced by the 50-mW PDT regimen. Gene functions were obtained from The Gene Ontology Consortium (http://www.geneontology.org/).

In addition, gene ontology analysis was performed using the DAVID Bioinformatics Resources 6.7 database to gain insight in the upregulated genes (absolute $\log_2$ fold-change of >1, corrected *P*-value of <0.05 (section Data analysis and processing)) in the ITL 50 and ITL 500 group in terms of biological processes. Overrepresented gene ontology (GO) terms were evaluated and are presented in **Table**

Gene	Full name	Function
FOS	FBJ murine osteosarcoma viral oncogene homolog	Inflammation, cellular response to ROS, DNA methylation
DUSP6	dual specificity phosphatase 6	Inactivation of MAPK activity
KREMEN2	kringle containing transmembrane protein 2	Wnt receptor signaling pathway
ATF3	activating transcription factor 3	Response to stress
HSPA1A	heat shock 70kDa protein 1A	Response to unfolded protein, ubiquitin protein ligase binding
IL8	interleukin 8	Angiogenesis, chemotaxis, inflammation
RHOB	ras homolog family member B	GTP binding, apoptotic process, cellular response to H_2O_2
SNORD38A	small nucleolar RNA, C/D box 38A	
FOSB	FBJ murine osteosarcoma viral oncogene homolog B	Transcription factor binding
CXCL1	chemokine (C-X-C motif) ligand 1	Cell proliferation, chemotaxis, inflammation
SOX21	SRY (sex determining region Y)-box 21	Transcription from RNA polymerase II promoter, stem cell differentiation
CHAC1	ChaC, cation transport regulator homolog 1	Intrinsic apoptotic signaling pathway in response to ER stress, negative regulator of Notch signaling pathway
CDKN1B	cyclin-dependent kinase inhibitor 1B	Cell cycle arrest
NEDD9	neural precursor cell expressed, developmentally down-regulated 9	Cell adhesion, cell division, cytoskeleton organization
AY358241		
STC2	stanniocalcin 2	Cellular calcium ion homeostasis
FBXO32	F-box protein 32	Protein ubiquitination, response to denervation involved in regulation of muscle adaptation
EFNA1	ephrin-A1	Activation of MAPK activity, cell migration, aortic valve morphogenesis
BMF	Bcl2 modifying factor	Positive regulation of intrinsic apoptotic signaling pathway
DDIT4	DNA-damage-inducible transcript 4	Response to hypoxia, intrinsic apoptotic signaling pathway in response to DNA damage by p53 class mediator, negative regulation of TOR signaling cascade

Table 2. Top 10 most up- and downregulated genes induced by the 500-mW PDT regimen. Gene functions were obtained from The Gene Ontology Consortium (http://www.geneontology.org/).

3. Characterization of the top 8 overrepresented GO terms revealed that the GO term "response to stress" applied to both the ITL 50 (involving 92 genes) and the ITL 500 (involving 16 genes) group. In the ITL 50 group, genes annotated with the GO terms "response to biotic stimulus" and "apoptosis" were overrepresented, as reflected by a *P*-value of 1.2×10^{-17} and 2.0×10^{-7}, respectively. In contrast, the GO terms "MAP kinase phosphatase" and "regulation of cellular process" were overrepresented in the ITL 500 group. In summary, the main processes that were initiated following PDT include oxidative stress, cell death, and inflammation.

ITL50

Cluster [ES]	GO term	Count	*P*-value (FDR)
1 [12.96]	Response to biotic stimulus	45	1.2E-17
2 [11.83]	Response to stress	92	6.2E-13
3 [5.89]	Apoptosis	39	2.0E-7
4 [5.77]	Response to cytokine stimulus	14	9.8E-8
5 [5.13]	Regulation of apoptosis	47	2.4E-7
6 [4.92]	Regulation of response to stress	25	1.3E-7
7 [4.38]	Chemotaxis	19	1.3E-7
8 [4.18]	bZIP transcription factor	10	5.7E-6

ITL500

Cluster [ES]	GO term	Count	*P*-value (FDR)
1 [3.97]	Response to stress	16	2.4E-5
2 [3.55]	MAP kinase phosphatase	4	1.8E-6
3 [3.15]	Regulation of cellular process	32	7.2E-5
4 [2.68]	Response to chemical stimulus	12	6.1E-4
5 [2.41]	Angiogenesis	6	5.7E-5
6 [2.33]	Fos transforming protein	4	8.5E-7
7 [2.08]	Regulation of cell proliferation	8	6.1E-3
8 [1.89]	Regulation of catalytic activity	9	2.2E-3

Table 3. Overrepresented GO terms in the ITL 50 and ITL 500 group. Gene ontology (GO) analysis was performed using the DAVID Bioinformatics Resources 6.7 database (https://david.ncifcrf.gov/). Significantly upregulated genes were loaded into DAVID and the HumanHT-12_V3_0_R2_11283641_A was selected as a background reference. An EASE score of 0.1 was used in the analysis and FDR-corrected *P*-values are presented.

Activation of survival pathways following PDT

Based on the survival pathways depicted in **Fig. 1** and described in [10], survival signaling pathways were constructed in PathVisio to investigate whether and to what extent the PDT modalities initiated survival signaling in SK-ChA-1 cells (**Figs. 5** and **6**).

Activation of ASK-1 and consequent JNK and p38 MAPK signaling

Apoptosis signal regulating kinase 1 (ASK-1) can be activated in two distinct ways: (1) as a result of ROS production and (2) via tumor necrosis factor (TNF) production and subsequent tumor necrosis factor receptor-associated factor 2 (TRAF2), TRAF5, and TRAF6 signaling, all of which associate with ASK-1 and stimulate autophosphorylation and activation of ASK1 [17]. As depicted in **Fig. 5A**, activator protein 1 (*AP-1*, consisting of JUN and FOS, amongst others) was upregulated in both the ITL 50 and ITL 500 groups. Relative to the control group, numerous downstream genes of AP-1 signaling that exert pro-inflammatory and proliferative functions were more highly expressed in the ITL 50 group, including *TNF*, cyclin D1 (*CCND1*), heparin-binding EGF-like growth factor (*HBEGF*), B-cell CLL/lymphoma 3 (*BCL3*),

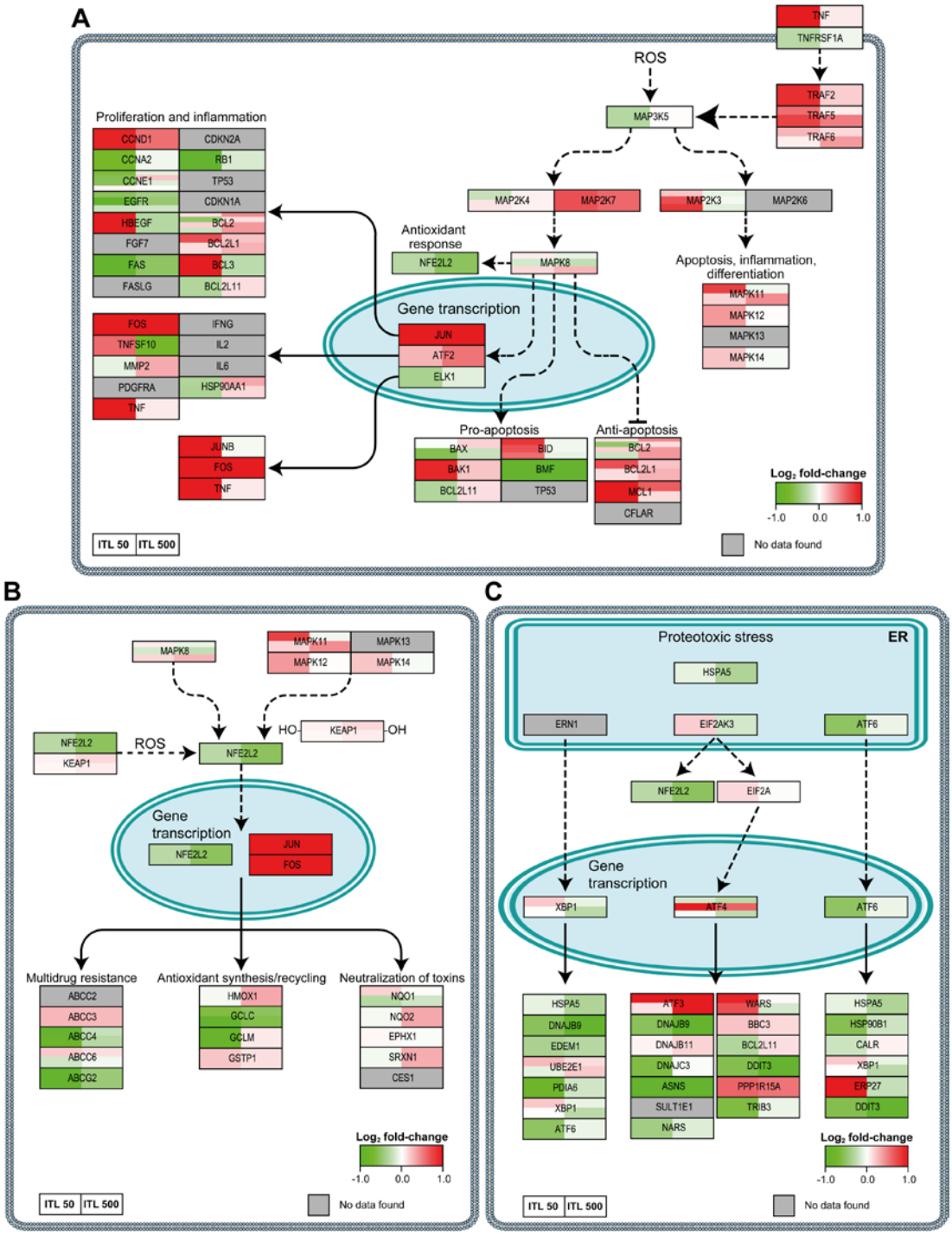

Fig. 5. PDT-induced survival signaling. Genes are mapped that are involved in MAP3K5 (also known as ASK-1) signaling (**A**), NFE2L2 signaling (**B**), and the unfolded protein response following PDT (**C**). The color and intensity of the box indicates the direction and extent of the $\log_2$ fold-change for the indicated gene, respectively (lower right corner of each panel). Grey boxes signify probes that exhibited poor quality or were not included in the gene

expression analysis. Each gene box, which typically comprises multiple probes as indicated by vertical splits, is horizontally divided in two halves corresponding to the PDT regimens (legend lower left). All comparisons were made between the PDT-treated groups versus the control group. Dashed lines indicate interactions that are not directly transcriptionally regulated. The molecular pathways were adapted from [10].

and jun B proto-oncogene (*JUNB*) compared to the ITL 500 group.

NFE2L2 signaling following PDT

Nuclear factor (erythroid-derived 2)-like 2 (NFE2L2) is a transcription factor that is ubiquitously expressed in the cytoplasm and degraded via kelch-like ECH-associated protein 1 (KEAP1) under non-stressed conditions. During oxidative stress the redox-sensitive KEAP1 is oxidized, causing dissociation of KEAP1 from NFE2L2 [18]. In turn, NFE2L2 dimerizes with small Maf, JUN, and FOS proteins, which then translocate to the nucleus to bind to the antioxidant responsive element (ARE) [19, 20]. This binding initiates transcription of a plethora of antioxidant-responsive genes. An overview of the effects of ZnPC-ITL-PDT treatment on the NFE2L2-mediated pathway is shown in **Fig. 5B**. PDT resulted in modest downregulation of *NFE2L2* transcription levels, although cells in both the ITL 50 and ITL 500 groups upregulated NFE2L2 binding partners (*JUN*, *JUNB*, *FOS*). Despite the fact that *NFE2L2* was downregulated in the ITL 500 group, several NFE2L2 target genes were upregulated (*e.g.*, heme oxygenase 1 (*HMOX1*), NAD(P)H dehydrogenase, quinone 2 (*NQO2*), sulfiredoxin 1 (*SRXN1*)). Furthermore, expression of various genes involved in glutathione and redox cycling (glutamate-cysteine ligase, catalytic subunit (*GCLC*), glutamate-cysteine ligase, modifier subunit (*GCLM*), glutathione reductase (*GSR*)) were decreased in the ITL 50 group. Overall, there was no unequivocal induction of NFE2L2-related antioxidant-responsive genes 90 min after PDT in either group (**Table 4**).

Unfolded protein response following PDT

The unfolded protein response (UPR) is a process that is initiated upon ER stress. In response to the accumulation of unfolded and misfolded proteins in the ER, protein translation is stalled, unfolded and misfolded proteins are degraded, and molecular players involved in protein folding are upregulated (reviewed in [21]). However, apoptotic cell death is triggered when the amount of unfolded and misfolded proteins exceeds a certain threshold [21, 22]. During UPR signaling, HSPA5 binds unfolded and misfolded proteins in the ER lumen, which causes activation of endoplasmic reticulum to nucleus signaling 1 (ERN1), eukaryotic translation initiation factor 2-alpha kinase 3 (EIF2AK3), and ATF6 (**Fig. 5C**). Activation of these proteins in turn triggers the release of various transcription factors, which include X-box binding protein 1 (XBP1), ATF4, and ATF6. As shown in **Fig. 5C**, both the ITL 50 and ITL 500 groups did not clearly induce these transcription factors. In fact, various downstream genes of XBP1, ATF4, and ATF6 were downregulated rather than upregulated (*e.g.*, ER degradation enhancer, mannosidase alpha-like 1 (*EDEM1*), heat shock protein 90 kDa beta (*HSP90B1*)) in

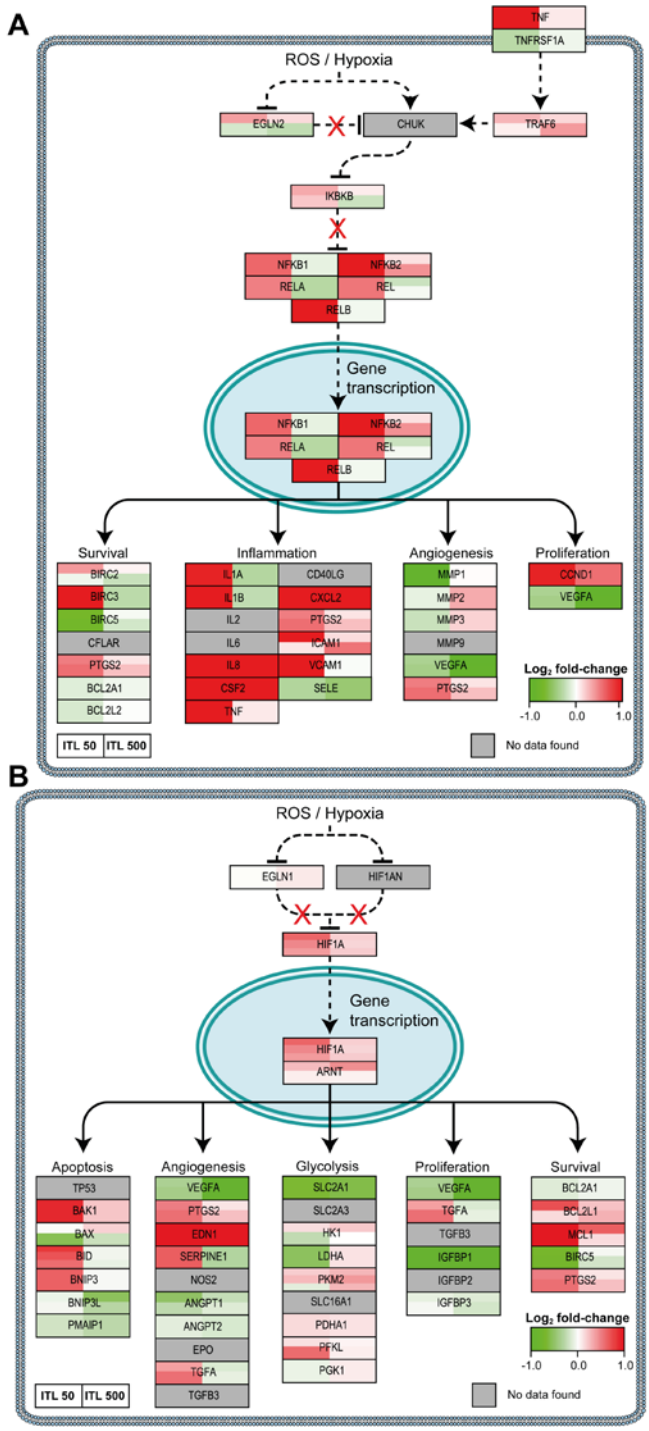

Fig. 6. PDT-induced survival signaling. Genes are mapped that are involved in NF-κB signaling (**A**) and HIF-1 signaling (**B**) following PDT. The color and intensity of the box indicates the direction and extent of the $\log_2$ fold-change for the indicated gene, respectively (lower right corner of each panel). Grey boxes signify probes that exhibited poor quality or were not included in the gene expression analysis. Each gene box, which typically

comprises multiple probes as indicated by vertical splits, is horizontally divided in two halves corresponding to the PDT regimens (legend lower left). All comparisons were made between the PDT-treated groups versus the control group. Dashed lines indicate interactions that are not directly transcriptionally regulated. The molecular pathways were adapted from [10].

both groups 90 min after PDT, altogether attesting to the disinvolvement of the UPR survival pathway in ZnPC-ITL-PDT.

Activation of pro-inflammatory signaling via NF-κB

NF-κB consists of a subfamily of proteins that include NF-κB1, NF-κB2, v-rel avian reticuloendotheliosis viral oncogene homolog (REL), RELA, and RELB. Activation of NF-κB following PDT can occur by various pathways as shown in **Fig. 6A**. First, NF-κB can be activated via direct activation of conserved helix-loop-helix ubiquitous kinase (CHUK) during hypoxic conditions, which inhibits inhibitor of kappa light polypeptide gene enhancer in B-cells, kinase beta (IKBKB) [23]. Second, NF-κB activation occurs via inhibition of oxygen-dependent egl-9 family hypoxia-inducible factor 2 (EGLN2) that leads to CHUK activation and consequently IKBKB inhibition [23]. Third, NF-κB can be activated via tumor necrosis factor receptor superfamily, member 1A (TNFRSF1A) signaling, leading to TRAF6 activation and NF-κB induction [24]. The activation of NF-κB promotes various pathways directly and indirectly related to cell survival, including proliferation, inflammation, and survival.

As presented in **Fig. 6A**, treatment of SK-ChA-1 cells at low laser power resulted in upregulation of all members of the NF-κB subfamily. Strikingly, this response was not observed in the ITL 500 group, suggesting that the acute damage induced by the high-dose irradiation favored cell death signaling rather than cell salvage signaling. Furthermore, the ITL 50 group exhibited upregulated expression of NF-κB downstream genes (**Table 4**), including *CSF2*, *CXCL2*, and vascular cell adhesion molecule (*VCAM*). In addition, cells in the ITL 50 group also upregulated various pro-inflammatory cytokines, including IL1 alpha (*IL1A*), IL1 beta (*IL1B*), and *IL8*, with a $\log_2$ fold-change of 0.93, 1.48, and 6.75, respectively.

		ITL50		ITL500	
Geneset	**Genes**	**Direction**	***P*-value (FDR)**	**Direction**	***P*-value (FDR)**
AP-1	18	▲	0.102	▼	0.927
NFE2L2	13	▼	<0.001	▲	0.927
UPR	22	▼	0.141	▼	0.164
HIF-1	28	▲	<0.001	▼	0.059
NF-κB	21	▲	<0.001	▲	0.059

Table 4. A ROAST gene set test was performed to evaluate whether a specific survival pathway was either up- (▲) or downregulated (▼). The gene sets are based on the specific survival pathways as presented in **Figs. 5** and **6**. FDR-corrected *P*-values are presented.

Activation of HIF-1 following PDT

Under normoxic conditions, HIF1A is hydroxylated by EGLN1 and hypoxia inducible factor 1, alpha subunit inhibitor (HIF1AN), which mediates recognition of HIF1A by von Hippel-Lindau tumor suppressor, E3 ubiquitin protein ligase (VHL) that targets HIF1A for ubiquitin-mediated proteasomal degradation. However, during oxidative stress and hypoxia, the oxygen sensors EGLN1 and HIF1AN are inhibited and thereby prevent degradation of HIF1A (reviewed in [25]). Downstream HIF-1 target genes then promote glycolysis, angiogenesis, and proliferation, all of which support cell survival. As shown in **Fig. 6B**, upregulation of HIF-1-induced genes was observed 90 min post-PDT in the ITL 50 group (**Table 4**). ZnPC-ITL-PDT led to upregulation of endothelin 1 (*EDN1*), a gene that is downstream of HIF1A and a known vasoconstrictor, in both groups after PDT. Unexpectedly, downregulation of vascular endothelial growth factor A (*VEGFA*), solute carrier family 2 (facilitated glucose transporter), member 1 (*SLC2A1*), and insulin-like growth factor binding protein 1 (*IGFBP1*) was observed in both groups.

Discussion

Perihilar cholangiocarcinoma is a rare but highly lethal cancer that is typically diagnosed at an advanced tumor stage, accounting for the fact that the tumor cannot be resected in approximately 70–80 % of the patients [26]. It was demonstrated in a cohort of non-resectable patients that, when standard intervention (stenting) was combined with PDT, the median survival could be prolonged from 6 to 9 months to 21 months post-diagnosis (summarized in [27]). However, the management of non-resectable perihilar cholangiocarcinoma remains palliative. Inasmuch as PDT is a promising treatment strategy for perihilar cholangiocarcinoma, novel routes have been explored to increase therapeutic efficacy and to develop a more patient-friendly PDT strategy [11]. For those purposes, ZnPC-encapsulating liposomes (ITLs), which are part of a novel multi-targeted liposomal delivery platform for PDT [11, 14], were evaluated for toxicity and for the potential use in PDT of perihilar cholangiocarcinoma. The experiments demonstrated that (1) ZnPC-ITLs are not toxic *in vitro* and *in vivo* at high lipid concentrations, (2) irradiation of SK-ChA-1 cells at high laser power (500 mW, 15 J/cm^2) resulted in more profound acute cell death than PDT at low laser power (50 mW, 15 J/cm^2), and (3) irradiation of SK-ChA-1 cells at low laser power caused considerable survival signaling after PDT via activation of mainly HIF-1 and NF-κB.

The response of SK-ChA-1 cells to PDT at low (50 mW) or high laser power (500 mW) was compared. Since PDT treatment at low laser power causes moderate ROS production over an extended period of time [14], cells likely had the opportunity to activate an antioxidant (possibly via NFE2L2) and survival response to remediate the acute effects of ROS and cope with the ROS-induced damage more effectively than

cells that were severely damaged by the 500-mW laser irradiation. This postulation is supported by the viability data, which demonstrated that cells irradiated at 50 mW were more viable at 90 min post-PDT than cells irradiated at 500 mW. The difference in cell viability at 90 min post-PDT was, however, abolished 24 h after PDT. A possible explanation is that, when cells are unable to cope with the PDT-inflicted damage, the execution of cell death programs via either apoptosis, (programmed) necrosis, and/or autophagy is ultimately completed. The time required to complete the activated cell death programs is apparently longer for moderately damaged cells than for highly damaged cells. Both PDT regimens also entirely abrogated metabolic activity 24 h post-PDT, which may be explained by the intracellular localization of ZnPC. ZnPC is largely confined to mitochondria upon cell entry [11], which is the source of electrons for the WST-1-based metabolic activity assay [28]. PDT-induced mitochondrial damage debilitates electron production and leakage from the electron transport chain, thereby hampering the reduction of WST-1 to the formazan chromophore. Metabolic perturbations (measured by WST-1) occur chronologically before cell death-mediated fragmentation and detachment from the wells plate (measured by the SRB assay), as a result of which the WST-1 data reflects more profound cell damage than the total protein assay at 24 h post-PDT.

To understand the molecular events that are triggered directly after PDT, whole genome expression profiles were established of PDT-treated SK-ChA-1 cells in the early phase (90 min) after PDT in line with previous reports [13]. Since the cellular redox state of a cell changes during PDT as a result of the production of ROS and reactive nitrogen species (*e.g.*, peroxynitrite) [29], PDT causes activation of a variety of redox-sensitive proteins and transcription factors [10]. ASK-1, also known as mitogen-activated protein kinase kinase kinase 5 (MAP3K5)) is associated with thioredoxin under physiological conditions and thereby kept inactive. However, during oxidative stress thioredoxin is oxidized and dissociates from ASK-1, leading to its activation [17]. Consequently, JUN N-terminal kinase (JNK, also designated as MAPK8) and protein 38 (p38) MAPK signaling is induced, leading to the immediate-early gene response via AP-1 [30]. Furthermore, UPR signaling and redox-sensitive transcription factors NFE2L2, NF-κB, and HIF1A are activated under oxidative stress and are able to initiate a plethora of processes (reviewed in [10]), including cell proliferation, inflammation, and angiogenesis.

When the PDT-treated groups were compared to the control group, SK-ChA-1 cells subjected to low-power PDT displayed a different response than cells treated using high-power PDT. Moreover, the number of up- and downregulated genes was considerably greater in the ITL 50 group than in the ITL 500 group. These data indicate that SK-ChA-1 cells treated by low-power PDT attempt to survive, as evidenced by the significant upregulation of HIF-1- ($P < 0.001$) and NF-κB-mediated ($P < 0.001$) pathways. It should be noted, however, that the experiments were carried out under normoxic

conditions. Since HIF-1A is rapidly degraded under normoxia [31], the effects that were observed in terms of HIF-1 activation are probably an underestimation. Nevertheless, in line with the results of this study, Liu *et al.* observed significant upregulation of various proinflammatory genes, including *FOS*, *FOSB*, *IL8*, and tumor necrosis factor, alpha-induced protein 3 (*TNFAIP3*) in 5-aminolevulinic acid (5-ALA)-treated human gingival (Ca9-22) cells [32]. In our study, SK-ChA-1 cells treated with low-power PDT also demonstrated extensive upregulation of *FOS*, *FOSB*, *IL8*, and *TNFAIP3* ($\log_2$ fold-changes of 4.42, 2.13, 6.75, and 2.75, respectively). Moreover, Kammerer and co-workers observed significant upregulation of inflammation-related genes, including *CXCL2*, *CXCL3*, *IL1A*, and IL6 receptor (*IL6R*)) after non-lethal 5-ALA-PDT in a panel of prostate and glioblastoma cell lines [33]. Cells in the ITL 50 group also significantly upregulated *CXCL2* and *IL1A*, whereas *IL6R* remained unaffected. Contrary to expectations, cells in the ITL 50 group downregulated the NFE2L2-mediated pathway ($P < 0.001$); an effect that was absent in the ITL 500 group. This response could be due to the crosstalk between the NF-κB and NFE2L2 pathways. It has been proposed that RELA, a subunit of NF-κB, interferes with NFE2L2 activation through deprivation of CREB binding protein (CREBBP) and activation of histone deacetylase 3 (HDAC3) [34]. Thus, a strong induction of the NF-κB pathway, as observed in the ITL 50 group, may impede NFE2L2 signaling. Lastly, the UPR did not seem to be important in the early phase after PDT in SK-ChA-1 cells, which could be explained by the localization of ZnPC at the time of PDT. Since ZnPC translocates from the plasma membrane to intracellular organelles in a time-dependent manner [35], it is likely that the ZnPC concentration in the ER is low, as a result of which ER stress and the UPR were probably less important under these experimental conditions.

The data in this study as well as in previously published studies plead for the development and use of fourth-generation photosensitizers (*i.e.*, second-generation photosensitizer encapsulated in a nanoparticulate delivery system (making it a third-generation photosensitizer) with co-encapsulated small-molecular inhibitors of survival pathways) in PDT. In that respect, the HIF-1- and NF-κB-mediated survival responses that were induced by PDT in mainly the ITL 50 group comprise potential target sites for pharmacological intervention. Corroboratively, HIF-1 induction with cobalt chloride in human esophageal carcinoma (Het-1a) cells reduced the extent of cell death and abrogated apoptosis after 5-ALA-PDT [36]. This pro-survival response was blocked following HIF-1 silencing with siRNA, which augmented PDT efficacy in the Het-1a cells [36]. Chen *et al.* revealed that nanoparticulate delivery of HIF-1 siRNAs to head-and-neck carcinoma (SSC4) xenografts significantly enhanced photosan-PDT efficacy in mice [37], leading to 40 % tumor regression within 10 days post-PDT. Similarly, the combination treatment with ALA-PDT and celecoxib, an anti-inflammatory drug that inhibits prostaglandin-endoperoxide synthase 2 (PTGS2) (a downstream target of HIF-1 and NF-κB), yielded an additional 40 % reduction in tumor growth compared

to ALA-PDT alone in human cholangiocarcinoma (HuCC-T1)-bearing mice [38]. Although the authors stated that increased ROS generation was mainly responsible for the increased response, it is likely that the inhibition of prostaglandin synthesis (reviewed in [39]), which is normally initiated by PTGS2 to promote survival, also contributed to therapeutic efficacy. Lastly, it was demonstrated that inhibition of HIF-1α with acriflavine, a small molecule that prevents the dimerization of HIF-1α with HIF-1β and thus its activation [40], potentiated PDT efficacy in human epidermoid carcinoma (A431) cells and SK-ChA-1 cells using liposomal ZnPC Broekgaarden *et al.*, Inhibition of hypoxia inducible factor 1 with acriflavine sensitizes tumor cells to photodynamic therapy with zinc phthalocyanine-encapsulating cationic liposomes, in preparation [41].

Comparable results were obtained in studies where other survival pathways were inhibited before PDT. Coupienne *et al.* inhibited NF-κB with BAY 11–7082 (an inhibitor of IKK) prior to 5-ALA-PDT of glioblastoma cells [42], achieving increased therapeutic efficacy as a result of an impaired autophagic response, which otherwise mediates survival. Moreover, verteporfin-PDT induced epidermal growth factor receptor (EGFR) and signal transducer and activator of transcription 3 (STAT-3) signaling in ovarian carcinoma (OVCAR-5) and non-small cell lung cancer (H460) cells [43]. Activation of the STAT-3 pathway results in the transcription of both HIF-1- and NF-κB target genes [44, 45]. Accordingly, siRNA-mediated knockdown of either EGFR or STAT-3 increased PDT efficacy.

At this stage, combination treatments with respect to PDT and inhibitors in the clinical setting are limited to the treatment of macular degeneration, in which case VEGF inhibitors are employed to deter neovascularization. Nevertheless, the data that have become available to date indicate that the combined use of PDT and inhibitors of survival pathways in the form of fourth-generation photosensitizers may be an attractive approach to improve therapeutic efficacy.

Conclusions

In summary, ZnPC-encapsulating liposomes are non-toxic in various *in vivo* models in the absence of irradiation but become highly cytotoxic upon PDT *in vitro*. Low-power PDT-treated perihilar cholangiocarcinoma cells activate extensive survival signaling *in vitro*, which is characterized by the induction of HIF-1- and NF-κB-related genes. Induction of these genes concurred with higher viability 90 min after PDT. Such post-PDT survival signaling may translate to a suboptimal therapeutic response in the clinical setting and possibly tumor recurrence. These findings encourage the development of photosensitizer delivery systems with co-encapsulated inhibitors of survival pathways, or so-called fourth-generation photosensitizers.

Methods

Chemicals

1,2-dipalmitoyl-*sn*-glycero-3-phosphocholine (DPPC) was obtained from Avanti Polar Lipids (Alabaster, AL). 1,2-distearoyl-*sn*-glycero-3-phosphoethanolamine-polyethylene glycol (DSPE-PEG, average PEG molecular mass of 2,000 amu), ZnPC (97 % purity), HEPES (4-(2-hydroxyethyl)-1-piperazineethanesulfonic acid), pyridine, and sulforhodamine B (SRB) were acquired from Sigma-Aldrich (St. Louis, MO). Acetic acid (glacial), ethidium bromide, ethylenediaminetetraacetic acid (EDTA), formaldehyde solution (36.5–38 % in water), sodium chloride, and tris(hydroxymethyl) aminomethane (Tris) were obtained from Merck KGaA (Darmstadt, Germany). Agarose was purchased from Gibco-BRL (Paisley, UK) and ethanol was from J.T. Baker (Deventer, the Netherlands).

All lipids were dissolved in chloroform and ZnPC was dissolved in pyridine at a 178-μM concentration. All dissolved lipids were stored under a nitrogen atmosphere at −20 °C.

Cell culture

Human perihilar cholangiocarcinoma (SK-ChA-1) cells were maintained at standard culture conditions (37 °C, 5 % CO_2 and 95 % air). SK-ChA-1 cells were cultured in Roswell Park Memorial Institute (RPMI) 1640 culture medium supplemented with 10 % fetal bovine serum (FBS) (v/v) (Gibco, Invitrogen, Carlsbad, CA), 1 % penicillin/streptomycin (v/v), 1 % L-glutamine (v/v) (both from Lonza, Walkersville, MD), and 1×10^{-5} % β-mercaptoethanol (v/v) (Sigma-Aldrich). The cells were passaged weekly at a 1:10 ratio.

Preparation of ZnPC-ITLs

ZnPC-ITLs were prepared by the lipid film hydration technique as described previously [14]. Briefly, ZnPC-ITLs were composed of DPPC and DSPE-PEG (96:4, molar ratio). ZnPC was incorporated at a ZnPC-to-phospholipid ratio of 0.003. The liposomes were sized with a bath sonicator and characterized for size and polydispersity by photon correlation spectroscopy [14]. Liposome suspensions were purged with nitrogen gas and stored for a maximum of 3 days at 4 °C in the dark.

PDT protocol

Cells were harvested using Accutase (Innovative Cell Technologies, San Diego, CA) and seeded in 6-wells culture plates (Corning Life Sciences, Tewksbury, MA) at a density of 0.5×10^6 cells/well. After reaching confluence, cells were washed with PBS and incubated with ZnPC-ITLs (500 μM final lipid concentration) in serum-free RPMI 1640 medium (1.5 mL final volume per well) for 30 min at 37 °C in the dark. Control

cells received an equal volume of PBS. In case of PDT, cells were irradiated with a 671-nm diode laser (CNI, Changchun, China) at a laser power of either 50 or 500 mW until a cumulative light dose of 15 J/cm^2 was reached. PDT was performed in the dark while the cells were maintained at 37 °C using a hotplate (cat. no. 97042–616, VWR, Radnor, PA).

Cell function and death assays

Mitochondrial metabolism was assessed using WST-1 reagent (Roche). Twenty-four hours post-PDT, the culture medium was removed and 1,500 µL of WST-1-containing RPMI medium (at a 1:25 volume ratio, serum- and phenol red-free) was added to the wells. After 30 min of incubation under standard culture conditions, 300-µL aliquots were transferred to 24-wells plates and the absorbance was read at 450 nm using 600 nm as a reference wavelength (BioTek Synergy HT multi-well plate reader, Winooski, VT). Data were normalized to the mean absorbance of the control cells.

In addition, cell death was determined 24 h post-PDT using the SRB total protein assay as described by Vichai *et al.* [46]. SRB absorbance was read at 564 nm using 690 nm as a reference wavelength (BioTek Synergy HT multi-well plate reader). Data were normalized to the mean absorbance of the control cells.

Determination of mode of cell death

The mode of cell death following PDT was analyzed by flow cytometry using the Alexa Fluor 488 annexin V/dead cell apoptosis kit (Life Technologies, Carlsbad, CA). Cells were cultured in 6-wells plates as described in section "Cell culture" and irradiated as described in section "PDT protocol". Samples were prepared as described previously [14] and assayed on a FACSCanto II (Becton Dickinson, Franklin Lakes, NJ). Ten thousand events were recorded in the gated region and data were analyzed using FlowJo software (Treestar, Ashland, OR). Healthy cells were defined as annexin V-negative/propidium iodide (PI)-negative, apoptotic cells were defined as annexin V-positive/PI-negative, and necrotic cells were defined as PI-positive.

ZnPC-ITL acute toxicity in chicken embryos

Fertilized chicken eggs (White Leghorn) were ordered from Drost Loosdrecht (Loosdrecht, the Netherlands), placed on paper towel in an egg incubator (Ova-Easy 190 Advance, Brinsea, Weston-super-Mare, UK), and maintained under dark conditions at 37.5 °C, 60 % humidity, and a 90° turn interval of 60 min. After 72 h, 2–3 mL of albumin was removed with a syringe to create empty volume in the superior portion of the egg. Next, surgical tape (Transpore White, 3M, St. Paul, MN) was fastened on the upper part of the eggshell and a small window (1.5 × 3.0 cm) was cut in the tape-covered eggshell that was immediately sealed with a second strip of surgical tape, after which the egg was placed back in the incubator. Previously opened eggs were incubated as

described above but without the turn cycles. On embryonic development day 12, 50 µL of ZnPC-ITLs (final lipid concentration of 0.3, 0.5, or 0.7 mM in blood; blood volumes were derived from [47]) in 0.75 % NaCl (*i.e.*, iso-osmolar relative to embryonic blood) or 50 µL of 0.75 % NaCl (control) was intravenously injected into a large-sized blood vessel in the chorioallantoic membrane using a 30-gauge needle and a 1-mL syringe (Becton Dickinson). All surgical procedures were performed as fast as possible under sterile conditions in a LAF hood. Acute toxicity was defined as embryonic death within 24 h after systemic administration.

ZnPC-ITL long term toxicity in mice

The animal experiments were approved by the animal ethics committee of the Academic Medical Center under BEX103077 and performed in accordance with the NIH Guide for the Care and Use of Laboratory Animals. Six-to-eight week old male C57BL/6 mice were purchased from Charles River (Leiden, the Netherlands). All mice were acclimated for 1 week and were provided with water and standard chow (Harlan Teklad, Harlan, Madison, WI) *ad libitum*. Mice were housed under green light at all times (Philips TL-D 36 W/17, Philips, Eindhoven, the Netherlands) with standard dark/light cycles to prevent activation of the photosensitizer. At the start of the experiment, mice were randomly assigned to the ZnPC-ITL or control group ($n = 8$ per group). A dose of 2.5 mM ZnPC-ITLs (final lipid concentration in blood, corresponding to an administered lipid dosage of 200 µmol/kg) was intravenously administered via the penile vein, whereas control mice received the same volume of buffer (0.88 % NaCl, 10 mM HEPES, pH = 7.4, 0.292 osmol/kg). Systemic lipid concentration was determined using a total blood volume of 80 mL/kg [48, 49]. Subsequently, all mice were inspected daily and were weighed every 4 days as part of toxicological vigilance. After 28 days, mice were anesthetized and blood was collected via cardiac puncture in heparin- or EDTA-anticoagulated microtainers (BD, Franklin Lakes, NJ). Biochemical and hematological parameters were determined by routine clinical chemistry (Department of Clinical Chemistry, Academic Medical Center). Lung, liver, and spleen tissue was loafed and fixed in FAA (47.5 % (v/v) ethanol, 5 % (v/v) acetic acid, 3.7 % (v/v) formaldehyde) at 4 °C, dehydrated in graded concentrations of ethanol and xylene, embedded in paraffin, cut to 5 µm-thick sections, and stained with hematoxylin and eosin as described in [50].

Illumina HumanHT-12 array

SK-ChA-1 cells received either PBS ('control') or 500 µM ZnPC-ITLs (final lipid concentration) and were kept in the dark ('ITL'), or were treated with 500-mW ('ITL 500') or 50-mW ('ITL 50') laser light ($n = 3$ per group). Ninety minutes after PDT, total cellular RNA was extracted from SK-ChA-1 cells using 1 mL of TRIzol (Life Technologies) according to the manufacturer's protocol. RNA samples were purified

using the RNeasy mini kit (Qiagen, Venlo, the Netherlands) and eluted in 30 μL RNAse-free H_2O. The quality control, RNA labeling, hybridization, and data extraction were outsourced to ServiceXS (Leiden, the Netherlands). The RNA concentration was measured using a Nanodrop ND-1000 spectrophotometer (Nanodrop Technologies, Wilmington, DE) and the RNA quality and integrity was determined using Lab-on-Chip analysis on the Agilent BioAnalyzer (Agilent Technologies, Santa Clara, CA). Biotinylated cRNA was prepared using the Illumina TotalPrep RNA amplification kit (Ambion, Austin, TX) according to the manufacturer's specifications with an input of 200 ng total RNA. Per sample, 750 ng of the obtained biotinylated cRNA samples was hybridized onto the Illumina HumanHT-12 v4 beadchip (Illumina, San Diego, CA). Hybridization and washing were performed according to the Illumina Manual "Direct Hybridization Assay Guide" and the scanning procedure was performed on the Illumina iScan (Illumina). Image analysis and extraction of raw expression data was performed with Illumina GenomeStudio v2011.1 Gene Expression software with default settings (no background subtraction and no normalization).

Microarray preprocessing and data analysis

Analyses were carried out with Bioconductor packages using the statistical software package R (version 3.0.0). Raw data normalization was performed on the Illumina sample and control probe profiles by a normexp-by-control background correction, quantile normalization, and $\log_2$ transformation using the limma package (version 3.16.5). The arrayQualityMetrics package (version 3.16.0) was used to confirm that the microarray data was of good quality. Probes with a detection *P*-value of > 0.05 (non-expressed) on all arrays (17,521 of 47,231 probes) were filtered out. Principal component analysis was performed on unscaled data (function prcomp). Differential expression between the experimental conditions was assessed with a moderated t-test using the linear model framework from the limma package. Resulting *P*-values were corrected for multiple testing using the Benjamini-Hochberg false discovery rate. Corrected *P*-values of ≤ 0.05 were considered as statistically significant. Probes were reannotated using the Bioconductor package IlluminaHumanv4.db package (version 1.18.0). The microarray data have been deposited in NCBI Gene Expression Omnibus in a MIAME compliant format and are accessible under GEO series accession number GSE68292. In addition, a ROAST gene set test [51] was performed on the selected survival pathways (**Table S1**) to statistically determine whether a survival pathway was upregulated or downregulated using 10,000 rotations with Benjamini-Hochberg-based multiple testing correction. If multiple probes were mapped to the same Entrez Gene identifier according to the illuminaHumanv4.db package, the probe with the highest standard deviation was chosen. Survival pathways were visualized using PathVisio 3.1.3. [52] on the basis of [10].

Quantitative reverse transcription polymerase chain reaction (qRT-PCR)

The experiment as described in section "Illumina HumanHT-12 array" was repeated, RNA was extracted (section "Illumina HumanHT-12 array"), and cDNA was prepared using the oligo-dT-based Transcriptor first strand cDNA synthesis kit (Roche Diagnostics, Basel, Switzerland) with an input of 500 ng total RNA. In addition, 2 µM ribosomal protein S18 (*RPS18*) reverse transcriptase primer (GCATCGCCGGTCGGCATCG) was added to each reaction mix. cDNA was synthesized according to the manufacturer's instructions and diluted in RNAse-free H_2O to obtain a final concentration of 5 ng/µL.

For amplification reactions, 5 µL of 2× SensiFAST SYBR No-ROX master mix (Bioline, London, UK), 1 µL of forward and reverse primer mix (5 µM) (primer sequences can be found in **Fig. S2**), 2 µL of nuclease-free H_2O, and 2 µL of cDNA template (10 ng) were mixed. The qRT-PCR reaction was carried out using a LightCycler 480 II instrument (Roche). The qRT-PCR program consisted of 3 min at 95 °C, 45 cycles of 1 s at 94 °C, 7 s at 65 °C, and 10 s at 72 °C, followed by melting curve analysis (65–97 °C, with a temperature increase of 0.11 °C/s). Subsequently, the quantitative analysis of the qRT-PCR data was performed according to Ruijter *et al.* [53] to calculate the starting concentration (N_0) of each cDNA template. Gene expression levels of the target genes were normalized to the expression level of the reference gene *RPS18* and $\log_2$ fold-changes of the target genes were calculated based on the mean values of the control group.

To assure product specificity, all qRT-PCR amplification products were separated by gel electrophoresis using 2 % agarose in 0.5 × TAE buffer (40 mM Tris, 20 mM acetic acid, 1 mM EDTA) in the presence of 0.5 µg/mL ethidium bromide (**Fig. S3**). Subsequently, the ethidium bromide-stained qRT-PCR products were analyzed under UV using an ImageQuant LAS4000 imager (GE Healthcare Life Sciences, Piscataway, NJ). The O'GeneRuler DNA Ladder Mix (#SM1173, Thermo Scientific, Waltham, MA) was used as a reference to estimate the size of the qRT-PCR products. In addition, all qRT-PCR products were validated by sequencing. Therefore, qRT-PCR products were purified using the QIAquick PCR purification kit (Qiagen) and sequencing was performed using the BigDye Terminator Cycle sequencing kit (Thermo Scientific) according to the manufacturer's instructions with an input of 5 ng DNA. Samples were sequenced on a Lifetech 3130xl genetic analyzer (Applied Biosystems, Waltham, MA) and data analysis was performed using NCBI BLAST (http://blast.ncbi.nlm.nih.gov/Blast.cgi). Sequencing results can be found in **Table S2**.

Statistical analysis

Statistical analysis was performed in GraphPad Prism 5 (GraphPad Software, La Jolla, CA). Normality was tested with the D'Agostino Pearson omnibus test. Differences between normally distributed variables were analyzed with an unpaired t-test or one-

way ANOVA with Bonferroni post-hoc test and not normally distributed variables were analyzed with a Mann–Whitney U test. The Bonferroni method was applied to adjust the *P*-value in case of multiple testing (**Fig. S1**). Intergroup differences groups were indicated with (*) and differences between the treated groups and the control group were indicated with (#). A single, double, and triple sign indicate a *P*-value of ≤ 0.05, ≤ 0.01, and ≤ 0.001, respectively. Data are presented as mean ± SD throughout the manuscript.

Acknowledgements

This work was financed with grants from the Phospholipid Research Center in Heidelberg (RW, MH), the Dutch Anticancer Foundation in Amsterdam (Stichting Nationaal Fonds Tegen Kanker) (RW, MB, MH), and the Nijbakker Morra Foundation (MH). The SK-ChA-1 cells were a kind gift from Alexander Knuth and Claudia Matter from the University Hospital Zurich, Switzerland. We are grateful to Dr. Maurice van den Hoff (AMC Department of Anatomy, Embryology, and Physiology) for critical insights into chicken embryology and physiology.

References

1. Agostinis P, Berg K, Cengel KA, Foster TH, Girotti AW, Gollnick SO, *et al*. Photodynamic therapy of cancer: An update. CA Cancer J Clin. 2011;61(4):250–81.
2. Castano AP, Mroz P, Hamblin MR. Photodynamic therapy and anti-tumour immunity. Nat Rev Cancer. 2006;6(7):535–45.
3. Triesscheijn M, Baas P, Schellens JH, Stewart FA. Photodynamic therapy in oncology. Oncologist. 2006;11(9):1034–44.
4. Copper MP, Tan IB, Oppelaar H, Ruevekamp MC, Stewart FA. Meta-tetra(hydroxyphenyl)chlorin photodynamic therapy in early-stage squamous cell carcinoma of the head and neck. Arch Otolaryngol Head Neck Surg. 2003;129(7):709–11.
5. Mackenzie GD, Dunn JM, Selvasekar CR, Mosse CA, Thorpe SM, Novelli MR, *et al*. Optimal conditions for successful ablation of high-grade dysplasia in Barrett's oesophagus using aminolaevulinic acid photodynamic therapy. Lasers Med Sci. 2009;24(5):729–34.
6. Sibille A, Lambert R, Souquet JC, Sabben G, Descos F. Long-term survival after photodynamic therapy for esophageal cancer. Gastroenterology. 1995;108(2):337–44.
7. Zeitouni NC, Shieh S, Oseroff AR. Laser and photodynamic therapy in the management of cutaneous malignancies. Clin Dermatol. 2001;19(3):328–38.
8. Sun ZQ. Photodynamic therapy of nasopharyngeal carcinoma by argon or dye laser- an analysis of 137 cases. Zhonghua Zhong Liu Za Zhi. 1992;14(4):290–2.
9. Dumoulin FL, Gerhardt T, Fuchs S, Scheurlen C, Neubrand M, Layer G, *et al*. Phase II study of photo dynamic therapy and metal stent as palliative treatment for nonresectable hilar cholangiocarcinoma. Gastrointest Endosc. 2003;57(7):860–7.
10. Broekgaarden M, Weijer R, van Gulik TM, Hamblin MR, Heger M. Tumor cell survival pathways activated by photodynamic therapy: a molecular framework for inhibition strategies. Cancer Metastasis Rev. 2015;34(4):643–90.
11. Weijer R, Broekgaarden M, Kos M, van Vught R, Rauws EA, Breukink E, *et al*. Enhancing photodynamic therapy of refractory solid cancers: combining second-generation photosensitizers with multi-targeted liposomal delivery. J Photochem Photobiol C: Photochem Rev. 2015;23:103–31.
12. Lee TL, Chan WY, Rennert OM. Assessing the safety of nanomaterials by genomic approach could be another alternative. ACS Nano. 2009;3(12):3830.
13. Luna MC, Wong S, Gomer CJ. Photodynamic therapy mediated induction of early response genes. Cancer Res. 1994;54(5):1374–80.
14. Broekgaarden M, de Kroon AIPM, van Gulik TM, Heger M. Development and in vitro proof-of-concept of interstitially targeted zinc-phthalocyanine liposomes for photodynamic therapy. Curr Med Chem. 2014;21(3):377–91.
15. Valdes TI, Kreutzer D, Moussy F. The chick chorioallantoic membrane as a novel in vivo model for the testing of biomaterials.

J Biomed Mater Res. 2002;62(2):273–82.
16. Watanabe H. Toxicogenomics as a tool for evaluation of chemical effects. Yakugaku Zasshi. 2007;127(12):1967–74.
17. Saitoh M, Nishitoh H, Fujii M, Takeda K, Tobiume K, Sawada Y, *et al.* Mammalian thioredoxin is a direct inhibitor of apoptosis signal-regulating kinase (ASK) 1. EMBO J. 1998;17(9):2596–606.
18. Itoh K, Wakabayashi N, Katoh Y, Ishii T, Igarashi K, Engel JD, *et al.* Keap1 represses nuclear activation of antioxidant responsive elements by Nrf2 through binding to the amino-terminal Neh2 domain. Genes Dev. 1999;13(1):76–86.
19. Itoh K, Chiba T, Takahashi S, Ishii T, Igarashi K, Katoh Y, *et al.* An Nrf2/small Maf heterodimer mediates the induction of phase II detoxifying enzyme genes through antioxidant response elements. Biochem Biophys Res Commun. 1997;236(2):313–22.
20. Venugopal R, Jaiswal AK. Nrf2 and Nrf1 in association with Jun proteins regulate antioxidant response element-mediated expression and coordinated induction of genes encoding detoxifying enzymes. Oncogene. 1998;17(24):3145–56.
21. Dufey E, Sepulveda D, Rojas-Rivera D, Hetz C. Cellular mechanisms of endoplasmic reticulum stress signaling in health and disease. 1. An overview. Am J Physiol Cell Physiol. 2014;307(7):C582–94.
22. Kim R, Emi M, Tanabe K, Murakami S. Role of the unfolded protein response in cell death. Apoptosis. 2006;11(1):5–13.
23. Cummins EP, Berra E, Comerford KM, Ginouves A, Fitzgerald KT, Seeballuck F, *et al.* Prolyl hydroxylase-1 negatively regulates I kappa B kinase-beta, giving insight into hypoxia-induced NF kappa B activity. Proc Natl Acad Sci U S A. 2006;103(48):18154–9.
24. Aggarwal BB. Signalling pathways of the TNF superfamily: A double-edged sword. Nat Rev Immunol. 2003;3(9):745–56.
25. Schofield CJ, Ratcliffe PJ. Oxygen sensing by HIF hydroxylases. Nat Rev Mol Cell Biol. 2004;5(5):343–54.
26. Ruys AT, van Haelst S, Busch OR, Rauws EA, Gouma DJ, van Gulik TM. Long-term survival in hilar cholangiocarcinoma also possible in unresectable patients. World J Surg. 2012;36(9):2179–86.
27. Lee TY, Cheon YK, Shim CS. Current status of photodynamic therapy for bile duct cancer. Clin Endosc. 2013;46(1):38–44.
28. Berridge MV, Herst PM, Tan AS. Tetrazolium dyes as tools in cell biology: new insights into their cellular reduction. Biotechnol Annu Rev. 2005;11:127–52.
29. Frank J, Lambert C, Biesalski HK, Thews O, Vaupel P, Kelleher DK. Intensified oxidative and nitrosative stress following combined ALA-based photodynamic therapy and local hyperthermia in rat tumors. Int J Cancer. 2003;107(6):941–8.
30. Ichijo H, Nishida E, Irie K, ten Dijke P, Saitoh M, Moriguchi T, *et al.* Induction of apoptosis by ASK1, a mammalian MAPKKK that activates SAPK/JNK and p38 signaling pathways. Science. 1997;275(5296):90–4.
31. Jewell UR, Kvietikova I, Scheid A, Bauer C, Wenger RH, Gassmann M. Induction of HIF-1alpha in response to hypoxia is instantaneous. FASEB J. 2001;15(7):1312–4.
32. Liu KH, Wang CP, Chang MF, Chung YW, Lou PJ, Lin JH. Molecular characterization of photosensitizer-mediated photodynamic therapy by gene expression profiling. Hum Exp Toxicol. 2013;33(6):629–37.
33. Kammerer R, Buchner A, Palluch P, Pongratz T, Oboukhovskij K, Beyer W, *et al.* Induction of immune mediators in glioma and prostate cancer cells by non-lethal photodynamic therapy. PLoS One. 2011;6(6):e21834.
34. Liu GH, Qu J, Shen X. NF-kappaB/p65 antagonizes Nrf2-ARE pathway by depriving CBP from Nrf2 and facilitating recruitment of HDAC3 to MafK. Biochim Biophys Acta. 2008;1783(5):713–27.
35. Fabris C, Valduga G, Miotto G, Borsetto L, Jori G, Garbisa S, *et al.* Photosensitization with zinc (II) phthalocyanine as a switch in the decision between apoptosis and necrosis. Cancer Res. 2001;61(20):7495–500.
36. Ji Z, Yang G, Shahzidi S, Tkacz-Stachowska K, Suo Z, Nesland JM, *et al.* Induction of hypoxia-inducible factor-1alpha overexpression by cobalt chloride enhances cellular resistance to photodynamic therapy. Cancer Lett. 2006;244(2):182–9.
37. Chen W-H, Lecaros RLG, Tseng Y-C, Huang L, Hsu Y-C. Nanoparticle delivery of HIF1α siRNA combined with photodynamic therapy as a potential treatment strategy for head-and-neck cancer. Cancer Lett. 2015;359(1):65–74.
38. Kim CH, Chung CW, Lee HM, Kim do H, Kwak TW, Jeong YI, *et al.* Synergistic effects of 5-aminolevulinic acid based photodynamic therapy and celecoxib via oxidative stress in human cholangiocarcinoma cells. Int J Nanomedicine. 2013;8:2173–86.
39. Vosooghi M, Amini M. The discovery and development of cyclooxygenase-2 inhibitors as potential anticancer therapies. Expert Opin Drug Discov. 2014;9(3):255–67.
40. Lee K, Zhang H, Qian DZ, Rey S, Liu JO, Semenza GL. Acriflavine inhibits HIF-1 dimerization, tumor growth, and vascularization. Proc Natl Acad Sci U S A. 2009;106(42):17910–5.
41. Weijer R, Broekgaarden M, Krekorian M, Alles LK, van Wijk AC, Mackaaij C, *et al.* Inhibition of hypoxia inducible factor 1 with acriflavine sensitizes perihilar cholangiocarcinomas to photodynamic therapy. Oncotarget. in press.
42. Coupienne I, Bontems S, Dewaele M, Rubio N, Habraken Y, Fulda S, *et al.* NF-kappaB inhibition improves the sensitivity of human glioblastoma cells to 5-aminolevulinic acid-based photodynamic therapy. Biochem Pharmacol. 2011;81(5):606–16.
43. Edmonds C, Hagan S, Gallagher-Colombo SM, Busch TM, Cengel KA. Photodynamic therapy activated signaling from epidermal growth factor receptor and STAT3: Targeting survival pathways to increase PDT efficacy in ovarian and lung cancer. Cancer Biol Ther. 2012;13(14):1463–70.
44. Pawlus MR, Wang L, Hu CJ. STAT3 and HIF1alpha cooperatively activate HIF1 target genes in MDA-MB-231 and RCC4 cells. Oncogene. 2014;33(13):1670–9.
45. Fan Y, Mao R, Yang J. NF-κB and STAT3 signaling pathways collaboratively link inflammation to cancer. Protein Cell. 2013;4(3):176–85.
46. Vichai V, Kirtikara K. Sulforhodamine B colorimetric assay for cytotoxicity screening. Nat Protoc. 2006;1(3):1112–6.

47. Kind C. The development of the circulating blood volume of the chick embryo. Anat Embryol. 1975;147(2):127–32.
48. Riches AC, Sharp JG, Thomas DB, Smith SV. Blood volume determination in the mouse. J Physiol. 1973;228(2):279–84.
49. Vacha J. Blood volume in inbred strain BALB/c, CBA/J and C57BL/10 mice determined by means of 59Fe-labelled red cells and 59Fe bound to transferrin. Physiol Bohemoslov. 1975;24(5):413–9.
50. van Golen RF, Reiniers MJ, Verheij J, Heger M. Solutions to the discrepancies in liver damage profiles following ischemia/reperfusion in standardized mouse models. J Hepatol. 2015;62(4):975–7.
51. Wu D, Lim E, Vaillant F, Asselin-Labat ML, Visvader JE, Smyth GK. ROAST: rotation gene set tests for complex microarray experiments. Bioinformatics. 2010;26(17):2176–82.
52. Kutmon M, van Iersel MP, Bohler A, Kelder T, Nunes N, Pico AR, *et al*. PathVisio 3: An extendable pathway analysis toolbox. PLoS Comput Biol. 2015;11(2):e1004085.
53. Ruijter JM, Ramakers C, Hoogaars WM, Karlen Y, Bakker O, van den Hoff MJ, *et al*. Amplification efficiency: linking baseline and bias in the analysis of quantitative PCR data. Nucleic Acids Res. 2009;37(6):e45.

Supplementary information

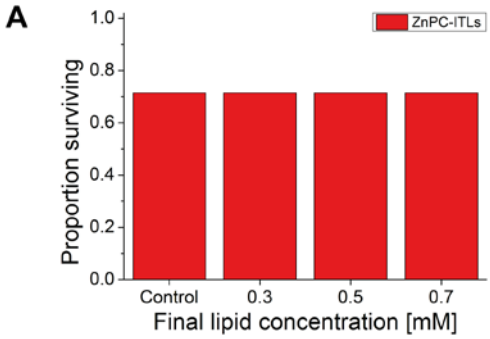

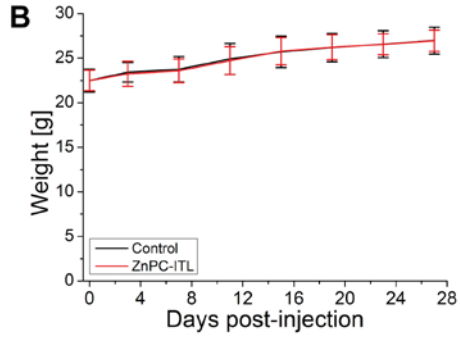

C

	Control	ZnPC-ITL	*P*-value
Biochemical parameters			
ALT [U/L]	37.0 ± 3.1	33.6 ± 8.1	0.30
Amylase [U/L]	4639.2 ± 509.3	4796.1 ± 633.8	0.59
AST [U/L]	76.1 ± 14.9	76.3 ± 12.8	0.98
Creatinin [µmol/L]	**10.2 ± 0.8**	**7.5 ± 1.1**	**<0.001**
CK-MB [µg/L]	0.3 ± 0.0	0.3 ± 0.0	1.00
CPK [U/L]	310.3 ± 146.0	277.0 ± 121.9	0.63
Free fatty acids [mmol/L]	1.2 ± 0.2	1.1 ± 0.2	0.17
Glucose [mmol/L]	15.8 ± 2.2	15.3 ± 1.8	0.63
LDH [U/L]	208.5 ± 16.6	218.0 ± 47.9	0.88
Hematological parameters			
Erythrocytes [x10^{12}/L]	9.2 ± 0.4	9.1 ± 0.3	0.96
Hemoglobin [mmol/L]	8.6 ± 0.4	8.4 ± 0.2	0.32
Leukocytes [x10^{9}/L]	5.3 ± 0.9	7.9 ± 3.1	0.04
Thrombocytes [x10^{9}/L]	573.5 ± 37.6	570.7 ± 52.7	0.91

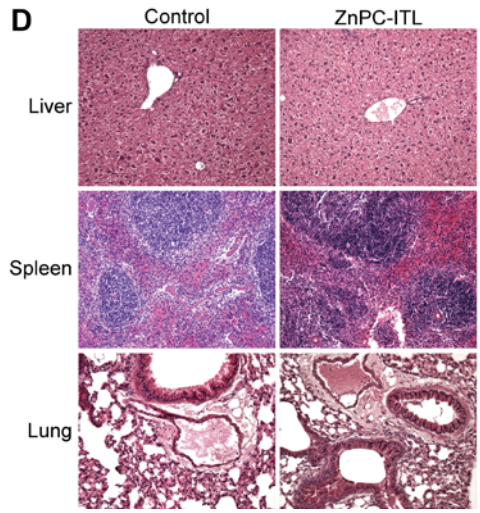

Fig. S1. *In vivo* toxicity evaluation of ZnPC-ITLs. (**A**) Chicken embryos were intravenously injected on embryonic development day 12 with different concentrations of ZnPC-ITLs (n = 7 per group). The concentrations indicate the final lipid concentration in blood. Control embryos were intravenously injected with an equal volume of 0.75% NaCl. (**B**) C57BL/6 mice were intravenously injected with ZnPC-ITLs (2.5 mM, final lipid concentration in blood, red line) or physiological buffer (black line). Mice were weighed every four days until day 28 post-injection. Data is presented as mean ± SD with n = 8 per group. (**C**) Biochemical and hematological parameters assessed in C57BL/6 mice 28 days after systemic administration of ZnPC-ITLs. Data is presented as mean ± SD with n = 8 per group. Statistical analysis was performed as described in section 5.12. Abbreviations: ALT, alanine transaminase; AST, aspartate transaminase; CK-MB, creatine kinase M and B; CPK, creatine phosphokinase; LDH, lactate dehydrogenase. (**D**) Histology of liver, spleen, and lung of C57BL/6 mice 28 days after systemic administration of ZnPC-ITLs or physiological buffer (control). Hematoxylin and eosin staining, magnification 20×.

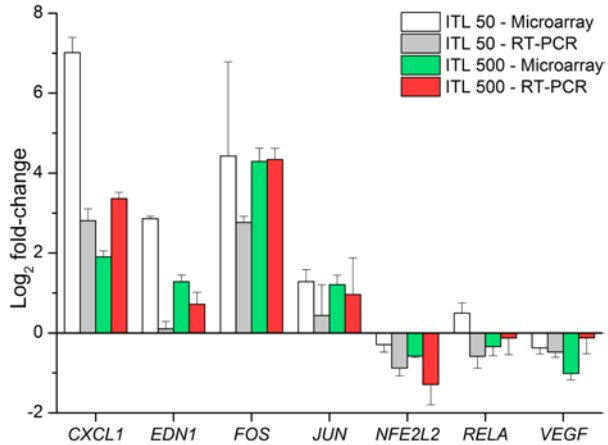

Fig. S2. Validation of absolute $\log_2$ fold-changes as obtained by microarray with qRT-PCR. Microarray-derived transcript levels of a panel of genes are depicted for the ITL 50 and ITL 500 group in white and green, respectively. The corresponding qRT-PCR levels of these genes are depicted for the ITL 50 group in grey and the ITL 500 group in red. Gene expression is depicted as the $\log_2$ fold-change between treated and untreated cells. The microarray and qRT-PCR data were normalized to the expression level of the reference gene *RPS18*.

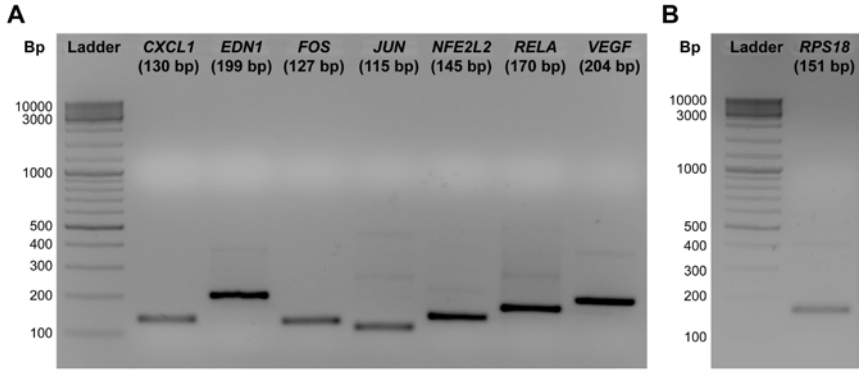

Fig. S3. Analysis of qRT-PCR products by gel electrophoresis. (**A**) Lane 1 contains a ladder and lanes 2 – 8 show the specific qRT-PCR products of the genes that are listed on top of each lane. (**B**) Lane 1 contains a ladder and lane 2 shows the reference gene *RPS18*. The amplicon size of a specific gene product is noted in parentheses below each gene name.

AP-1		UPR		NFE2L2		NF-κB		HIF-1α	
HGNC	Gene ID	HGNC	Gene ID	HGNC	Gene ID	HGNC	Gene ID	HGNC	Gene ID
BCL2	596	*ASNS*	440	*ABCC2*	1244	*BCL2A1*	597	*ANGPT1*	284
BCL2L1	598	*ATF3*	467	*ABCC3*	8714	*BCL2L1*	598	*ANGPT2*	285
BCL2L11	10018	*ATF6*	22926	*ABCC4*	10257	*BIRC2*	329	*BAK1*	578
BCL3	602	*BBC3*	27113	*ABCC6*	368	*BIRC3*	330	*BAX*	581
CCNA2	890	*BC2L11*	10018	*ABCG2*	9429	*BIRC5*	332	*BCL2A1*	597
CCND1	595	*CALR*	811	*CES1*	1066	*CCND1*	595	*BCL2L1*	598
CCNE1	898	*DDIT3*	1649	*EPHX1*	2052	*CD40LG*	959	*BID*	637
CDKN1A	1026	*DNAJB11*	51726	*GCLC*	2729	*CFLAR*	8837	*BIRC5*	332
CDKN2A	1029	*DNAJB9*	4189	*GCLM*	2730	*CSF2*	1437	*BNIP3*	664
EGFR	1956	*DNAJC3*	5611	*GSTP1*	2950	*CXCL2*	2920	*BNIP3L*	665
FAS	355	*EDEM1*	9695	*HMOX1*	3162	*CXCL8*	3576	*EDN1*	1906
FASLG	356	*ERP27*	121506	*NQO1*	1728	*ICAM1*	3383	*EPO*	2056
FGF7	2252	*HSP90B1*	7184	*NQO2*	4835	*IL1A*	3552	*HK1*	3098
FOS	2353	*HSPA5*	3309	*SRXN1*	140809	*IL1B*	3553	*IGFBP1*	3484
HBEGF	1839	*NARS*	4677			*IL2*	3558	*IGFBP2*	3485
HSP90AA1	3320	*PDIA6*	10130			*IL6*	3569	*IGFBP3*	3486
IFNG	3458	*PPP1R15A*	23645			*MMP1*	4312	*LDHA*	3939
IL2	3558	*SULT1E1*	6783			*MMP2*	4313	*MCL1*	4170
IL6	3569	*TRIB3*	57761			*MMP3*	4314	*NOS2*	4843
JUNB	3726	*UBE2E1*	7324			*MMP9*	4318	*PDHA1*	5160
MMP2	4313	*WARS*	7453			*PTGS2*	5743	*PFKL*	5211
PDGFRA	5156	*XBP1*	7494			*SELE*	6401	*PGK1*	5230
RB1	5925					*TNF*	7124	*PKM*	5315
TNF	7124					*VCAM1*	7412	*PMAIP1*	5366
TNFSF10	8743					*VEGFA*	7422	*PTGS2*	5743
TP53	7157							*SERPINE1*	5054
								SLC16A1	6566
								SLC2A1	6513
								SLC2A3	6515
								TGFA	7039
								TGFB3	7043
								TP53	7157
								VEGFA	7422

Table S1. Overview of transcriptional targets of the five survival pathways. Official gene names are listed that were derived from the Hugo Gene Nomenclature Committee (HGNC) along with their Genbank accession numbers (Gene ID).

Gene	Forward primer	Reverse primer	Amplicon size (bp)	Design	Nucleotide sequence as determined with sequencing
CXCL1	AGGGAATTCACCCCAAGAAC	ACTATGGGGGATGCAGGATT	130	RTPrimerDB	GACGCTTTCGCCATTCTTGATGTGGCTTGACTTCGGTTTGGGCG-CAGTGGGGTCCGGGGGACTTCACGTTCACACTTTGGATGTTCTT-GGGGTGAATTCCCTTGA
EDN1	GGGCTGAAGGATCGCTTTGA	GCGCCTAAGACTGCTGTTTTC	199	NCBI primer blast	GATCTGCAGCCAAAGCAGATGAATCTGAGCAAATAATCCTTCT-GAAAAAAGGGATCAAAAACCTCCCGTTCAAACTGAACCCAAAG-GAAAACGAAGAAAAACAGCTTCAGGTCCCTCAAAGCGCTGCGG-GTTCCTCAGATCTCAAAGCGATCCTTCAGCCCTA
FOS	GTGACCGTGGGAATGAAGTT	CCGGGGATAGCCTCTCTTAC	127	qPrimerDepot	TCCGCGCTCCTTCTCCGCATGGGCTCGCCTGTCACGCGCAGG-ACTTCTGCACGGACCTGGCCGTCTCCAGAGCCAACTTCATTCCCA-CGGTCACTA
JUN	GTCCTTCTTCTCTTGCGTGG	GGAGACAAGTGGCAGAGTCC	115	qPrimerDepot	GGCGACGTTGCGCCTTTCCTGCGTCTTAGGCTTCTCCGGCGGG-TAAAGACCGAAGGCGGCGGGAGAGCCACGCAAGAGAAGAAGGA-CAC
NFE2L2	GCTCATACTCTTTCCGTCGC	ATCATGATGGACTTGGAGCTG	145	qPrimerDepot	GCACGCATCCGTCCAGCAGGAATGGATTTGATTGACATACTTTG-GAGGCAAGATATAGATCTTGGAGTAAGTCGAGAAGTATTTGACTT-CAGTCAGCGACGGAAAGAGTATGAGCC
RELA	TCCGCGGGCAGCATCCC	CCATCCCGGCAGTCCTTTCCTAC	170	NCBI primer blast	AAAAGTGCGGGTGAGGCCGGTGAGGAGGTCCTTGGTGACCGG-GAGATGCGCACTGTCCCTGGTCCTGTGTAGCCTTGATCTTGATG-GTGGGGTGGGTCTTGGTGGTATCTGTCGCTCCTCTCGCCTGGGAT-GCTGCCCGCGGA
VEGF	CCACACCATCACCATCGACA	CTAATCTTCCGGGCTCGGTG	204	NCBI primer blast	TGCAGCATATGATGGCGAATCAATTCAAGAGGACCGTGCTGGGT-CCCCGCCCGGGAATGCTTCCGCCGGAGTCTCGCCCTCCGGACC-CAAAGTGCTCTGCGCAGAGTCTCCCTCTTCCTTCATTTCAGGTT-TCTGGATTAAGGACTGTTCTGTCGATGGTGATGGTGTGG
RPS18	TTCGGAACTGAGGCCATGAT	CGAACCTCCGACTTTCGTTCT	151	NCBI primer blast	GCATGAATTCTTGGCAATGCTTTCGCTCTGGTCCGTCTTGCGCCG-GTCCAAGAATTTCACCTCTAGCGGCGCAATACGAATGCCCCCGG-CCGTCCCTCTTAATCTGGCCTCAGTTCCGAAA

Table S2. Overview of primer sequences and resulting amplicon sizes (in bp) that were used for the validation of microarray expression levels using qRT-PCR. The primers are listed in the 5' to 3' direction.

Chapter 4

Multi-OMIC profiling of survival and metabolic signaling networks in cells subjected to photodynamic therapy

Cellular and Molecular Life Sciences (2016)

RUUD WEIJER
SÉVERINE CLAVIER*
ESTHER A. ZAAL*
MAUD M.E. PIJLS*
ROBERT T. VAN KOOTEN*
KLAAS VERMAAS
RENÉ LEEN
ALDO JONGEJAN
PERRY D. MOERLAND
ANTOINE H.C. VAN KAMPEN
ANDRÉ B.P. VAN KUILENBURG
CELIA R. BERKERS[$]
SIMONE LEMEER[$]
MICHAL HEGER[$]

*authors contributed equally
[$]shared senior authorship

Abstract

Photodynamic therapy (PDT) is an established palliative treatment for perihilar cholangiocarcinoma that is clinically promising. However, tumors tend to regrow after PDT, which may result from the PDT-induced activation of survival pathways in sublethally afflicted tumor cells. In this study, tumor-comprising cells (*i.e.*, vascular endothelial cells, macrophages, perihilar cholangiocarcinoma cells, and EGFR-overexpressing epidermoid cancer cells) were treated with the photosensitizer zinc phthalocyanine that was encapsulated in cationic liposomes (ZPCLs). The post-PDT survival pathways and metabolism were studied following sublethal (LC_{50}) and supralethal (LC_{90}) PDT.

Sublethal PDT induced survival signaling in perihilar cholangiocarcinoma (SK-ChA-1) cells via mainly HIF-1-, NF-κB-, AP-1-, and heat shock factor (HSF)-mediated pathways. In contrast, supralethal PDT damage was associated with a dampened survival response. PDT-subjected SK-ChA-1 cells downregulated proteins associated with EGFR signaling, particularly at LC_{90}. PDT also affected various components of glycolysis and the tricarboxylic acid cycle as well as metabolites involved in redox signaling.

In conclusion, sublethal PDT activates multiple pathways in tumor-associated cell types that transcriptionally regulate cell survival, proliferation, energy metabolism, detoxification, inflammation/angiogenesis, and metastasis. Accordingly, tumor cells sublethally afflicted by PDT are a major therapeutic culprit. Our multi-omic analysis further unveiled multiple druggable targets for pharmacological co-intervention.

Keywords

Cancer therapy, metallated phthalocyanines, non-resectable perihilar cholangiocarcinoma, reactive oxygen species, therapeutic recalcitrance, tumor targeting

Introduction

Photodynamic therapy (PDT) is a non-to-minimally invasive treatment modality for solid cancers that entails the photosensitization of a tumor using light-sensitive compounds called photosensitizers. After the photosensitizer molecules have sufficiently accumulated in the target tissue, the tumor is illuminated with light to activate the photosensitizer molecules [1]. Activated photosensitizers interact with molecular oxygen through energy or electron transfer, leading to the photochemical production of singlet oxygen and superoxide anion, respectively. These reactive oxygen species (ROS) subsequently attack biomolecules in the vicinity of their production site and induce a state of hyperoxidative stress in the illuminated tumor cells in case of an optimal PDT regimen. The oxidative damage in turn results in tumor cell death, microvascular shutdown and corollary tumor hypoxia and hyponutrition, and induction of an anti-tumor immune response (reviewed in [2]), altogether culminating in tumor destruction and removal.

Some types of cancers respond well to PDT and are associated with excellent cure rates, including esophageal carcinoma [3] and basal cell carcinoma [4]. In contrast, the cure rates for nasopharyngeal carcinoma [5] and superficial recurrent urothelial carcinoma HCl [6, 7] are suboptimal with respect to PDT and warrant improvement. Moreover, non-resectable perihilar cholangiocarcinomas respond better to PDT than to any other last-line treatment such as chemotherapy [8], but all available treatments (including PDT) are currently palliative and not curative. The recalcitrant nature of these tumor types to PDT is believed to stem from the use of photosensitizers with suboptimal spectral properties and poor pharmacokinetics as well as the activation of cell survival pathways by tumor cells following PDT [2, 9].

To resolve these issues with a single therapeutic modality, we have developed a 4th-generation photosensitizer-based PDT platform that aims to target pharmacologically relevant locations in the tumor, namely the tumor cells [10], the tumor endothelium [11–13], and the tumor interstitium [14]. The platform employs a 2nd-generation photosensitizer (zinc phthalocyanine, ZnPC) encapsulated in targeted liposomes (making it a 3rd-generation photosensitizer, which was employed in this study) with co-encapsulated molecular inhibitors of survival pathways (making it a 4th-generation photosensitizer) [2, 9–14]. Previously, we demonstrated that PDT of human skin and bile duct cancer cells with liposomal ZnPC and acriflavine, an inhibitor of hypoxia-inducible factor 1α (HIF-1α) [15], increases therapeutic efficacy by downmodulation of HIF-1α-driven survival signaling following PDT [11, 13]. In light of this combined therapy and the broader scope of applicability of the PDT platform technology, it is imperative to map post-PDT survival pathways [9] for every liposomal formulation so as to identify druggable targets beyond those already tested [9]. So far we have mapped PDT-activated survival pathways with respect to the interstitially targeted ZnPC-

liposomes [16], but not yet for the endothelium- and tumor cell-targeting liposomes.

Of the three different liposomal formulations that were developed, the most promising is the tumor endothelium-targeting ZnPC formulation. These liposomes, which are cationic and PEGylated, are taken up by cultured endothelial cells [14], macrophages (manuscript in preparation), and tumor cells [11, 13, 14], enabling multi-targeted delivery of the photosensitizer to key locations. Moreover, the liposomes are relatively non-toxic in the absence of light (this study), but become highly toxic to cultured cells upon illumination in the low nanomolar photosensitizer concentration range [11, 13]. Finally, ZnPC distributes to multiple intracellular loci after uptake of the liposomes [17, 18], from which different cell death pathways but also cell survival pathways are activated [2]. In preliminary experiments it was discovered that epidermal growth factor receptor (EGFR), a receptor overexpressed in a multitude of cancers [19] including perihilar cholangiocarcinoma [20, 21], was afflicted by PDT with ZnPC-liposomes. EGFR constitutes an important druggable target in cancer therapy, as evidenced by the approval status of the monoclonal antibodies cetuximab and panitumumab, as well as the kinase inhibitors gefitinib and erlotinib [22].

This study therefore examined the cell survival pathways induced by ZnPC-encapsulating PEGylated cationic liposomes (ZPCLs) in tumor parenchymal and non-parenchymal cell types using a multi-omics approach: transcriptomics, (phospho)proteomics, and metabolomics. The cells that were employed are human umbilical vein endothelial cells (HUVECs) as a model for vascular endothelium; RAW 264.7 murine macrophages as a model for tumor-resident macrophages; human biliary adenocarcinoma (SK-ChA-1) cells as model for PDT-recalcitrant perihilar cholangiocarcinomas; and EGFR-overexpressing human epidermoid carcinoma (A431) cells to further elaborate on the preliminary experimental results. The studies were performed at supralethal light dose (90% lethal concentration, LC_{90}), reflective of cells fully affected by PDT, and at sublethal light dose (LC_{50}), representative of cells in the distant and peripheral portions of the illuminated tumor, where the fluence rates are insufficient due to light absorption and scattering [23]. Therapeutically, the low-fluence sites are the most important tumor regions because survival signaling is expected to predominate, which may negatively impact therapeutic outcome and facilitate tumor recurrence as has been observed in PDT-treated patients [24].

The most important results of the study were that (1) ZPCLs were not toxic *in vitro*, which is key for clinical translation, (2) sublethal PDT was associated with extensive survival signaling, which is detrimental to therapeutic outcome, (3) PDT resulted in downregulation of proteins involved in EGFR signaling and cell adhesion, in particular after optimal PDT, and (4) sublethal and optimal PDT both downregulated metabolic pathways involved in energy production, including glycolysis and the tricarboxylic acid (TCA) cycle. The latter two findings are chiefly advantageous for therapeutic efficacy.

Materials and methods

Chemicals

1,2-Dipalmitoyl-*sn*-glycero-3-phosphocholine (DPPC) and 3β-[N-(N',N'-dimethylaminoethane)-carbimoyl]cholesterol (DC-cholesterol) were purchased from Avanti Polar Lipids (Alabaster, AL, USA). β-Mercaptoethanol, cholesterol, chloroform, 1,2-distearoyl-*sn*-glycero-3-phosphoethanolamine-polyethylene glycol (DSPE-PEG, average PEG molecular mass of 2000 amu), ZnPC (97% purity), acetonitrile, 4-(2-hydroxyethyl)-1-piperazineethanesulfonic acid (HEPES), potassium carbonate (K2CO3), pyridine, sodium chloride (NaCl), sodium deoxycholate, sodium fluoride, sodium orthovanadate, sulforhodamine B (SRB), tris(hydroxymethyl)aminomethane (Tris), and Triton X-100 were obtained from Sigma-Aldrich (St. Louis, MO, USA). Glycerol was purchased from Fisher Scientific (Hampton, NH, USA), and sodium dodecyl sulfate (SDS) and bromophenol blue were obtained from Bio-Rad Laboratories (Hercules, CA, USA). Methanol, perchloric acid (O_4), and sodium hydroxide (NaOH) were from Merck (Darmstadt, Germany).

All lipids were dissolved in chloroform and stored under a nitrogen atmosphere at −20 °C. ZnPC was dissolved in pyridine at a 178-μM concentration and stored under nitrogen at room temperature (RT) in the dark.

Cell culture

Human epidermoid carcinoma (A431) cells and murine macrophages (RAW 264.7) were cultured in Dulbecco's modified Eagle's medium (DMEM, Lonza, Walkersville, MD, USA) supplemented with 10% fetal bovine serum (FBS) (Bodinco, Alkmaar, the Netherlands), 100 U/mL penicillin, 100 μg/mL streptomycin, and 2 mM L-glutamine (all from Lonza). Human umbilical vein endothelial cells (HUVECs) were isolated as described in [25] and maintained in EndoGro-LS complete culture medium (Merck Millipore, Billerica, MA, USA). HUVECs were grown in Primaria cell culture flasks (Corning Life Sciences, Tewksbury, MA, USA). Human perihilar cholangiocarcinoma (SK-ChA-1) cells were cultured in Roswell Park Memorial Institute (RPMI) 1640 culture medium (Lonza) supplemented with 10% FBS, 100 U/mL penicillin, 100 μg/mL streptomycin, 2 mM L-glutamine, and 143 μM β-mercaptoethanol. All cells were maintained at standard culture conditions (37 °C, 5% CO_2, 95% air, humidified atmosphere).

Preparation of ZPCLs

ZPCLs were composed of DPPC, DC-cholesterol, cholesterol, and DSPE-PEG (66:25:5:4, molar ratio) and prepared by the lipid film hydration technique as described previously [13, 16]. Physiological buffer composed of 10 mM HEPES, 0.88% (w/v) NaCl, pH = 7.4, 0.293 osmol/kg [14] was used as hydration solution. ZnPC

was incorporated in the liposomal formulation at a ZnPC:lipid molar ratio of 0.003. Liposomal formulations were purged with nitrogen gas and stored at 4 °C in the dark. Under these conditions the liposomal ZnPC remains stable for at least 56 days [13].

PDT protocol

Cells were seeded in either 6-well (2 mL per well) or 24-well (0.5 mL medium per well) culture plates (Corning Life Sciences) as specified in the corresponding subsections and grown under standard culture conditions. HUVEC, RAW 264.7, SK-ChA-1, and A431 cells were seeded at a density of 0.5×10^5 cells/mL, 0.5×10^6 cells/mL, 0.25×10^6 cells/mL, and 0.5×10^6 cells/mL, respectively, and cultured until confluence in 24 h (48 h for SK-ChA-1 cells). HUVECs were cultured in Primaria culture plates (Corning Life Sciences) throughout the study. After reaching confluence, cells were washed with PBS and incubated with ZPCLs in serum-free supplemented phenol red-free medium for 1 h (drug-light interval) at 37 °C under standard culture conditions. Control cells received an equal volume of physiological buffer. The concentrations of ZPCLs that were used for the different cell types are specified in **Table S1**. Next, cells were washed with PBS and fresh fully supplemented phenol red-free medium was added. Cells were either returned to the incubator (control and dark toxicity) or irradiated with a 671-nm diode laser (CNI, Changchun, China) at a laser power of 500 mW with a fluence of 15 J/cm^2. The spot size was set to the exact dimensions of the well (6-wells plate: 9.5 cm^2, 24-wells plate: 1.9 cm^2). During the application of PDT, cells were maintained at 37 °C using a hotplate (Cat. No. 97042-616, VWR, Radnor, PA, USA).

Cell metabolic activity and viability assays

Cell metabolic activity was assessed using the water-soluble tetrazolium salt (WST-1) reagent (Roche Diagnostics, Basel, Switzerland). Cells were seeded in 24-wells plates and cultured until confluence. After a predetermined time interval following PDT, the culture medium was removed and 300 µL of WST-1-containing serum-free and phenol red-free medium (at a 1:25 volume ratio) was added to the wells. After 30 min of incubation under standard culture conditions, the absorbance was read at 450 nm using 600 nm as a reference wavelength (BioTek Synergy HT multi-well plate reader, Winooski, VT, USA). Data were normalized to the average value of the control cells that was set at a metabolic activity of 100%.

After the measurement, the wells were washed with PBS and the protein content was determined with the SRB total protein assay as described by Vichai *et al.* [26]. SRB absorbance was read at 564 nm using 690 nm as a reference wavelength (BioTek Synergy HT). Data were normalized to the average value of the control cells that was set at a viability of 100%.

Whole genome expression analysis

Cells were seeded in 6-wells plates and cultured until confluence. Cells were treated using the PDT protocol as described in "PDT protocol" ($n = 3$ per group). Total cellular RNA was extracted using 1 mL of TRIzol (Life Technologies, Carlsbad, CA, USA) according to the manufacturer's protocol. RNA samples were purified using the NucleoSpin RNA kit (Machery-Nagel, Düren, Germany) and eluted in 30 µL RNAse-free water. The quality control, RNA labeling, hybridization, and data extraction were performed at ServiceXS (Leiden, the Netherlands). The procedure can be found in [16]. Samples for human cell lines were randomly assigned to three Human-HT12 v4 arrays. For the RAW 264.7 cell line, MouseWG-6 v2 arrays were used with control and vehicle samples on one chip and LC_{50} and LC_{90} samples on a second chip.

Microarray data preprocessing and analysis

Microarray data preprocessing and analysis were performed as described previously [16]. In short, each cell line was analyzed separately with Bioconductor packages (version 2.13) using the statistical software package R (version 3.1.0). Normalization was performed starting from the Illumina sample and control probe profiles by a normexp-by-control background correction, quantile normalization, and log2 transformation (limma package). Probes with a detection *P* value of >0.05 (non-expressed) on all arrays for the cell line under study were filtered out. Differential expression between the experimental conditions was assessed with a moderated *t* test using the linear model framework (limma package). Resulting *P* values were corrected for multiple testing using the Benjamini-Hochberg false discovery rate. Corrected *P* values ≤0.05 were considered statistically significant. Probes were reannotated using the Bioconductor IlluminaHumanv4.db and lluminaMousev2.db packages. The microarray data have been deposited in NCBI Gene Expression Omnibus in a MIAME compliant format and are accessible under GEO series accession number GSE84758. Microarray data were confirmed using quantitative reverse transcription polymerase chain reaction (qRT-PCR) since the qRT-PCR data were in agreement with the microarray data (**Fig. S1**). This also strongly suggests that, for the RAW 264.7 cells, potentially confounding effects due to systematic differences between chips and biological effects of interest (comparison of LC_{50}/LC_{90} versus control/vehicle) are limited. In addition, a ROAST gene set test [27] was performed on the downstream targets of each survival pathway (**Table S2**) to statistically determine whether a survival pathway was either upregulated or downregulated using 10,000 rotations with Benjamini-Hochberg-based multiple testing correction of the mid *P* values.

qRT-PCR

RNA was extracted as described in "Whole genome expression analysis". cDNA synthesis and qRT-PCR reactions were performed as described previously [16]. Primer

sequences can be found in **Table S3**. The quantitative analysis of the qRT-PCR data was performed according to Ruijter et al. [28] to calculate the starting concentration (N_0) of each cDNA template. Gene expression levels were normalized to the expression level of the reference gene ribosomal protein S18 (*RPS18*). Log_2 fold-changes of the target genes were calculated based on the mean values of the control group.

Proteomics

Harvesting

SK-ChA-1 cells were seeded in 6-wells plates and cultured until confluence. Cells were treated using the PDT protocol as described in "PDT protocol" (n = 12 per group). Ninety minutes post-PDT, cells were washed three times with 2 mL PBS and 150 µL of lysis buffer [8 M urea, 0.5% sodium deoxycholate, 50 mM NH_4HCO_3, supplemented with cOmplete Mini protease inhibitor cocktail and phosSTOP (both from Roche)] was added to each well that was ensued by 30-min incubation on ice. Lysates were scraped, collected, pooled (to yield n = 4 per treatment group), and centrifuged for 15 min at 20,000×*g*. The supernatant was stored at −80 °C for further analysis. Protein concentrations were determined with the bicinchoninic acid (BCA) assay (Thermo Fisher Scientific, Waltham, MA, USA).

Affinity purification and digestion

For each sample, 400 µg of proteins was reduced by incubating with 2 µL of 1 M DTT at 56 °C for 25 min, alkylated by adding 4 µL of 200 mM IAA for 30 min at RT in the dark, and digested by Lys-C (enzyme:protein ratio of 1:75) for 4 h at 37 °C. Samples were then diluted four times with 50 mM NH_4HCO_3 and digested overnight at 37 °C with trypsin (enzyme:protein ratio of 3:100). Next, 100 µL of acetic acid was added to each sample to precipitate sodium deoxycholate, after which the samples were centrifuged for 15 min at 20,000×*g*. The obtained digests were desalted using 1 cc Sep-Pak C18 cartridges. Phosphoenrichment was performed with Ti-IMAC microcolumns with 250 µg of digests following the protocol previously described in detail [29], while the rest of the digests was kept for proteome analysis.

NanoLC–MS/MS analysis

Phosphoproteome and proteome were analyzed by NanoLC-MS/MS using an Agilent 1100 HPLC system (Agilent Technologies, Santa Clara, CA, USA) coupled to a Q Exactive Plus Orbitrap (Thermo Scientific) mass spectrometer. Peptides were trapped at 5 µL/min in 100% solvent A (0.1 M acetic acid in water) on an in-house packed 20 mm × 100 µm ID trapping column (ReproSil-Pur C18-AQ, 3 µm, Dr. Maisch, Ammerbuch, Germany) and then transferred to an in-house packed 50-cm × 50-µm ID analytical column (Poroshell 120 EC-C18, 2.7 µm, Agilent Technologies) maintained at 40 °C. The gradient used for proteome analysis ranged from 10% to 40% solvent B

[0.1 M acetic acid in 8:2 (v/v) acetonitrile/water] in 180 min at ~100 nL/min, whereas the gradient for phosphopeptides ranged from 4% to 40% in 120 min. The eluent was sprayed via distal coated emitter tips (New Objective, Woburn, MA, USA) connected to the analytical column. The Q Exactive Plus was operated in data-dependent mode, automatically switching between MS and MS/MS. Full-scan MS spectra (from m/z 350 to 1500) were acquired in the Orbitrap with a resolution of 60,000 at m/z 400 (after accumulation to a target value of 500,000). The 20 most intense ions at a threshold above m/z 500 were successively selected and fragmented in HCD cells at normalized collision energy of 35% after accumulation to a target value of 10,000.

Protein quantification and identification

Data analysis was performed using MaxQuant (version 1.5.2.8) [30] and the integrated search engine Andromeda [31]. For peptide and protein identification, raw files were searched against the human Swissprot database (20,201 entries) with carbamidomethylated cysteine as fixed modification and phosphorylation of serine, threonine, and tyrosine and oxidation of methionine as variable modifications. Trypsin/P was set as the proteolytic enzyme for which up to two missed cleavage sites were allowed. Precursor tolerance was set to 4.5 ppm and fragment ion tolerance to 0.05 Da. Peptide identifications required a minimal length of 7 amino acids and all data sets were adjusted to 1% PSM FDR. For label-free quantification (LFQ), match between runs was selected with a maximum shift time window of 3 min and the intensities of razor and unique peptides were summed up. Resulting protein intensities were then normalized to obtain LFQ intensities. To facilitate further data analysis, the results were imported into Perseus (version 1.5.2.4). Replicates were grouped per condition, and proteins or phosphopeptides identified in less than 3 out of 4 replicates were discarded. A two-tailed t-test was used to assess statistical significance. Phosphopeptide and protein *P* values were corrected by permutation-based FDR correction (FDR 5%). Phosphopeptides were filtered for a localization probability of >0.75 (class 1 sites). Regulated proteins were analyzed using Reactome within the Cytoscape environment and regulated phosphorylation sites were analyzed by Phosphopath [32] within Cytoscape. The mass spectrometry proteomics data have been deposited to the ProteomeXchange Consortium via the PRIDE partner repository with the dataset identifier PXD004320.

Western blotting

Western Blotting was performed to validate the (phospho)proteomic data (**Fig. S2**). For these purposes, SK-ChA-1 cells were seeded in 6-wells plates, cultured until confluence, and treated by PDT as described in "PDT protocol" (n = 3 per group). Ninety minutes after PDT, cells were washed twice with ice-cold PBS, placed on ice, and lysed in ice-cold RIPA buffer (50 mM Tris, 150 mM NaCl, 1% Triton X-100, 0.5%

sodium deoxycholate, 1% SDS) supplemented with cOmplete Mini protease inhibitor cocktail, 10 mM sodium fluoride, and 1 mM sodium orthovanadate. The samples were centrifuged for 15 min at 14,000×*g* (4 °C) and the supernatant was stored for further analysis. Protein lysates were mixed with 4 × SDS sample buffer (200 mM Tris (pH = 6.8), 8% SDS, 40% glycerol, 0.02% bromophenol blue) and boiled for 5 min at 95 °C. Next, samples (20–30 µg) were loaded on a TGX 10% precast gel (Bio-Rad Laboratories) and electrophoresis was performed at 150 V. The gels were blotted onto Amersham Hybond P 0.45 PVDF membranes (GE Healthcare, Little Chalfont, UK) for 2 h at 250 mA at 4 °C. The membranes were blocked for 1 h with 5% BSA (Sigma-Aldrich) in 0.1% Tween 20 Tris-buffered saline (TBST, 20 mM Tris, 150 mM NaCl, pH = 7.6), after which the membranes were incubated overnight with the primary antibody at 4 °C on a rocker. The primary antibodies used were (dilution factor, catalogue number, company): EGFR [1:1000, #4267, Cell Signaling (Danvers, MA, USA)], phospho-ERK (1:1000, #4370, Cell Signaling), phospho-p38 MAPK (1:500, #9216, Cell Signaling), p38 MAPK (1:1000, #9228, Cell Signaling), COX IV (1:1000, #4844, Cell Signaling), and ERK [1:1000, sc-2711270, Santa Cruz Biotechnology (Dallas, TX, USA)]. All primary antibodies were diluted with 5% BSA in TBST. Next, the membranes were washed three times in TBST and incubated with an HRP-conjugated secondary antibody [1:2000, Dako Cytomation (Glostrup, Denmark)] for 1 h at RT. Subsequently, membranes were washed three times with TBST. The enhanced chemiluminescence (ECL) kit (Thermo Scientific) was used as substrate and protein bands were visualized on an ImageQuant LAS 4000 luminometer (GE Healthcare).

Metabolomics

SK-ChA-1 cells were seeded in 6-wells plates and cultured until confluence. Cells were treated using the PDT protocol as described in "PDT protocol" (n = 3 per group). After 90 min, the cells were washed with 1 mL cold PBS and the cells were lysed in 1 mL lysis buffer (40% acetonitrile, 40% methanol, 20% water). The cells were scraped and transferred to 2-mL centrifuge tubes that were shaken for 10 min at 4 °C. Next, the samples were centrifuged for 15 min at 20,000×*g* (4 °C), after which the supernatant was aspirated and stored at −80 °C. LC-MS analysis was performed on an Exactive mass spectrometer (Thermo Scientific) coupled to a Dionex Ultimate 3000 autosampler and pump (Thermo Scientific). The MS operated in polarity-switching mode with spray voltages of 4.5 and −3.5 kV. Metabolites were separated using a Sequant ZIC-pHILIC column [2.1 × 150 mm, 5 µm, guard column 2.1 × 20 mm, 5 µm (Merck)] using a linear gradient of acetonitrile and eluent A (20 mM $(NH_4)_2CO_3$, 0.1% NH_4OH in ULC/MS grade water [Biosolve, Valkenswaard, the Netherlands)]. The flow rate was set to 150 µL/min. Metabolites were identified and quantified using LCquan software (Thermo Scientific) on the basis of exact mass within 5 ppm and further validated in accordance with the retention times of standards. Peak intensities

were normalized based on total ion count.

Nucleotide profiles

SK-ChA-1 cells were seeded in 6-wells plates and cultured until confluence. Cells were treated using the PDT protocol as described in "PDT protocol" (n = 3 per group). After 90 min, the cells were washed twice with PBS, placed on ice, and nucleotides were extracted using 200 µL of ice-cold 0.4 M $HClO_4$. After 10-min incubation on ice, the samples were centrifuged for 5 min at 10,000×g (4 °C) and the nucleotide-containing supernatant was neutralized using 7.5 µL of 5 M K_2CO_3. The wells were washed twice with 150 µL 0.2 M NaOH to remove residual proteins, which was added to the protein-containing dry pellet as obtained in the previous centrifugation step. In addition, 300 µL of 0.8 M $HClO_4$ was added to the protein fraction. After mixing thoroughly, the samples were centrifuged for 5 min at 10,000×g (4 °C) and the protein-containing pellet was dissolved in 200 µL of 0.2 M NaOH. Protein content was determined using the bicinchoninic acid assay protein kit (Thermo Scientific).

Nucleotide extracts were analyzed by high-performance liquid chromatography (HPLC) using a Partisphere 5-µm SAX cartridge column (Cat. No. 4621-0505, Hichrom, Reading, United Kingdom). Nucleotides were eluted with a gradient from 100% buffer A (100-fold dilution of buffer B) to 70% buffer B (0.75 M $NaH_2PO_4^-$, pH = 4.55) in 50 min at a flow rate of 1 mL/min.

Statistical analysis

Statistical analysis was performed in GraphPad Prism 6 (GraphPad Software, La Jolla, CA, USA). Normality was tested with the D'Agostino Pearson omnibus test. Differences between normally distributed variables were analyzed with a one-way ANOVA with Bonferroni post hoc test. Intergroup differences were indicated with (*) and differences between the treated groups and the control group at the same time point were indicated with (#). Differences between a condition and the previous condition at the same time point are, when relevant, indicated with ($) (pertains only to **Fig. 1**). A single, double, and triple sign indicate a P value of ≤ 0.05, ≤ 0.01, and ≤ 0.001, respectively. Data are presented as mean ± SD throughout the manuscript.

Results

PDT induces photosensitizer concentration- and time-dependent cell death

To correlate the transcriptomic-, (phospho)proteomic-, and metabolomic responses to the extent of PDT-induced cell death, the viability of HUVEC, RAW 264.7, SK-ChA-1, and A431 cells was determined first as a function of time after PDT at previously calculated LC_{50} and LC_{90} concentrations (details can be found in **Table S1**). The effect of PDT on cells was assessed with the WST-1 and SRB assays. WST-1 is a

measure of mitochondrial metabolic activity [33] and therefore represents a parameter of early onset cell demise. In contrast, SRB stains total protein and is therefore used as a parameter of late, fully executed cell death.

The ZPCLs exhibited no deleterious effect on metabolic activity (**Fig. 1a–d**) or cell viability (**Fig. 1e–h**) in any of the cell types in the absence of laser irradiation, indicating that the ZPCLs imparted no dark toxicity. The loss of metabolic activity (**Fig. 1a–d**) and extent of cell death (**Fig. 1e–h**) were more pronounced in the LC_{90} group versus the LC_{50} group and occurred in a time-dependent manner. The loss of metabolic activity is in line with the localization of ZnPC to mitochondrial membranes [2] and the post-PDT induction of mitochondrial permeability transition [12]. Typically, cells were most afflicted at the longest incubation time, underscoring that metabolic perturbations and execution of cell death pathways are progressive during at least 24 h after PDT. Unexpectedly, the LC_{90} HUVECs showed significantly higher cell viability 24 h after PDT compared to 2 h post-PDT (**Fig. 1e**). HUVECs in the LC_{90} group were also more resilient to treatment 24 h following PDT than HUVECs in the LC_{50} group (**Fig. 1e**).

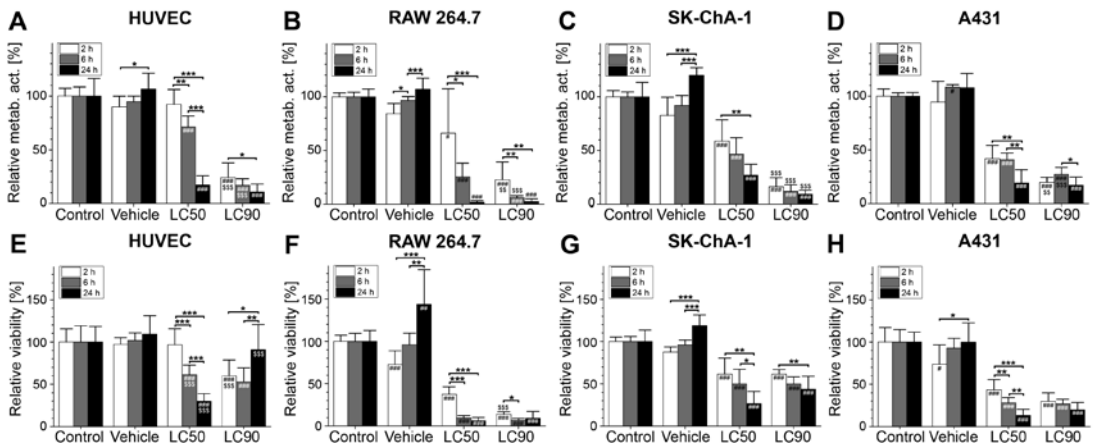

Fig. 1. Cell viability after ZPCL-PDT. (**A-H**) HUVEC, RAW 264.7, SK-ChA-1, and A431 cells were incubated with ZPCLs (concentrations can be found in **Table S1**) and treated with PDT. Two hours (white bar), 6 hours (light grey bar), and 24 hours (dark grey bar) after PDT, cell viability was determined using the (**A-D**) WST-1 and (**E-H**) SRB assay (n = 8 per group). Readers are referred to the experimental section for the significance of the statistical symbols. Abbreviation: Metab. act., metabolic activity.

PDT at LC_{90} has greater transcriptional effects than at LC_{50}, but the effect size is cell type-dependent

To gain insight in the early transcriptomic response after PDT with ZPCLs, non-illuminated and PDT-treated cells were harvested 90 min after (control) treatment and the transcriptome was analyzed by whole genome microarray, summarized in **Fig. 2**, and correlated to cell viability. This toxicogenomics approach corroborated the absence of dark toxicity of ZPCLs (**Fig. 2**, vehicle vs control), given that of all screened genes,

none were dysregulated compared to control. The same had been observed previously with the ZnPC-encapsulating interstitially targeted liposomes [16], which differ from the ZPCLs in that they lack DC-cholesterol in the membrane and therefore bear a neutral surface charge rather than a cationic charge.

In case of the interstitially targeted liposomes, the milder PDT protocol (irradiation of cells at 50 mW) induced more profound transcriptional dysregulation than the severe PDT regimen (500 mW laser irradiation) [16]. In contrast, the extent of mRNA dysregulation following PDT with ZPCLs was most pronounced in the LC_{90} groups compared to the LC_{50} groups (**Fig. 2**). The overlap between genes dysregulated in both the LC_{90} and LC_{50} groups was also cell type-specific. The highest number of commonly afflicted genes was observed in RAW 264.7 cells (3363), followed by A431 (790), SK-ChA-1 (638), and HUVEC (134) cells.

PDT-mediated induction of survival signaling

The basis of therapeutic recalcitrance towards PDT may partly originate from the induction of survival signaling after PDT [16]. PDT activates six major pathways that encompass a nuclear factor of kappa light polypeptide gene enhancer in B cells (NF-κB)-mediated inflammatory response, a proteotoxic stress response via the unfolded protein response (UPR) and heat shock transcription factor (HSF)-mediated response, an activator protein 1 (AP-1)-mediated immediate early gene response, a HIF-1-mediated hypoxia-induced stress response, and a nuclear factor (erythroid-derived 2)-like (NFE2L2)-mediated antioxidant response [9]. The pathways have been described in detail in [16, 34]. The microarray expression data were superimposed on these pathways [**Fig. S3** (with pathways and transcriptional targets) and **Fig. 3** (transcriptional targets only)].

The downstream targets of the survival pathways were analyzed with a ROAST gene test to determine whether a pathway was differentially regulated in response to PDT. All cell types upregulated the NF-κB, AP-1, and HSF survival pathways at LC_{50} and LC_{90}, whereas only the LC_{50} groups exhibited upregulation of HIF-1-mediated signaling (**Table S4**). Importantly, HIF-1-, UPR-, AP-1-, and NF-κB-associated genes were less extensively dysregulated in the LC_{90} group of the tumor-derived cell lines (A431, SK-ChA-1) compared to the LC_{50} group. In contrast, the LC_{90} group of the non-tumor derived cells (RAW 264.7, HUVEC) displayed more HSF-mediated signaling than the LC_{50} group. Altogether, these findings indicate that PDT induced extensive survival signaling in all cell types tested, whereby survival signaling was more prominent in cells treated by sublethal PDT.

NF-κB-mediated inflammatory response

NF-κB mediates an inflammatory response following PDT [35, 36]. As shown in **Fig. 3**, the transcription of various pro-inflammatory cytokines that are under the

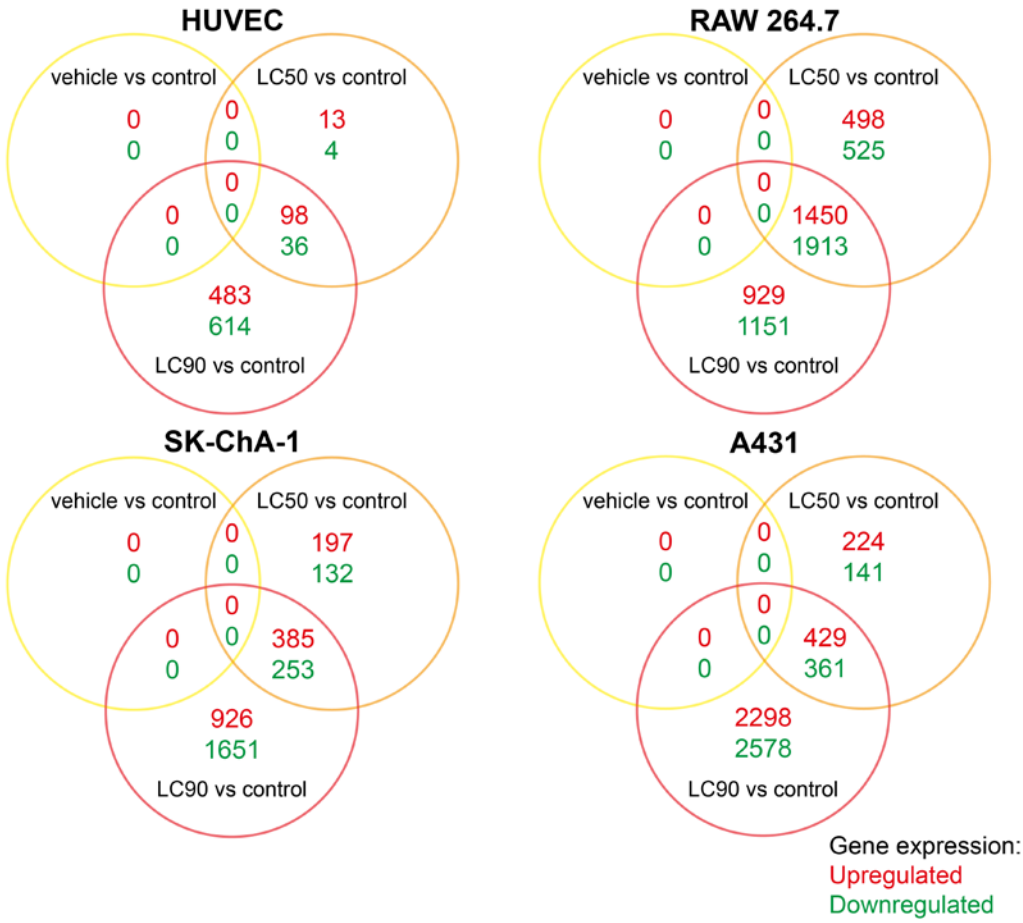

Fig. 2. Gross transcriptional response 90 minutes after ZPCL-PDT. The Venn diagrams show the number of upregulated (red) and downregulated (green) genes compared to the control group (FDR < 0.05), as well as the overlapping genes between the vehicle (dark toxicity), LC_{50}, and LC_{90} groups ($n = 3$ per group). The total number of upregulated and downregulated genes per PDT regimen (full circle) equals the sum of all values enveloped by the respective circle.

control of NF-κB, including interleukin 1A (*IL1A*), *IL1B*, *IL6*, and chemokine (C-X-C motif) ligand 8 (*CXCL8*), increased following PDT in the human cell types. Murine *Il1b* and *Cxcl2* were also considerably induced following PDT in RAW 264.7 cells. Sublethal PDT resulted in upregulation of vascular endothelial growth factor (*VEGF*) in SK-ChA-1 and A431 cells, which was downregulated in HUVEC cells. The pro-inflammatory factor prostaglandin-endoperoxide synthase 2 (*PTGS2*, *Ptgs2*) was also highly upregulated following PDT in HUVEC, RAW 264.7, and A431 cells.

Proteotoxic stress response

The proteotoxic stress response can be induced by ROS-mediated endoplasmic reticulum (ER) stress that leads to the accumulation of misfolded and unfolded

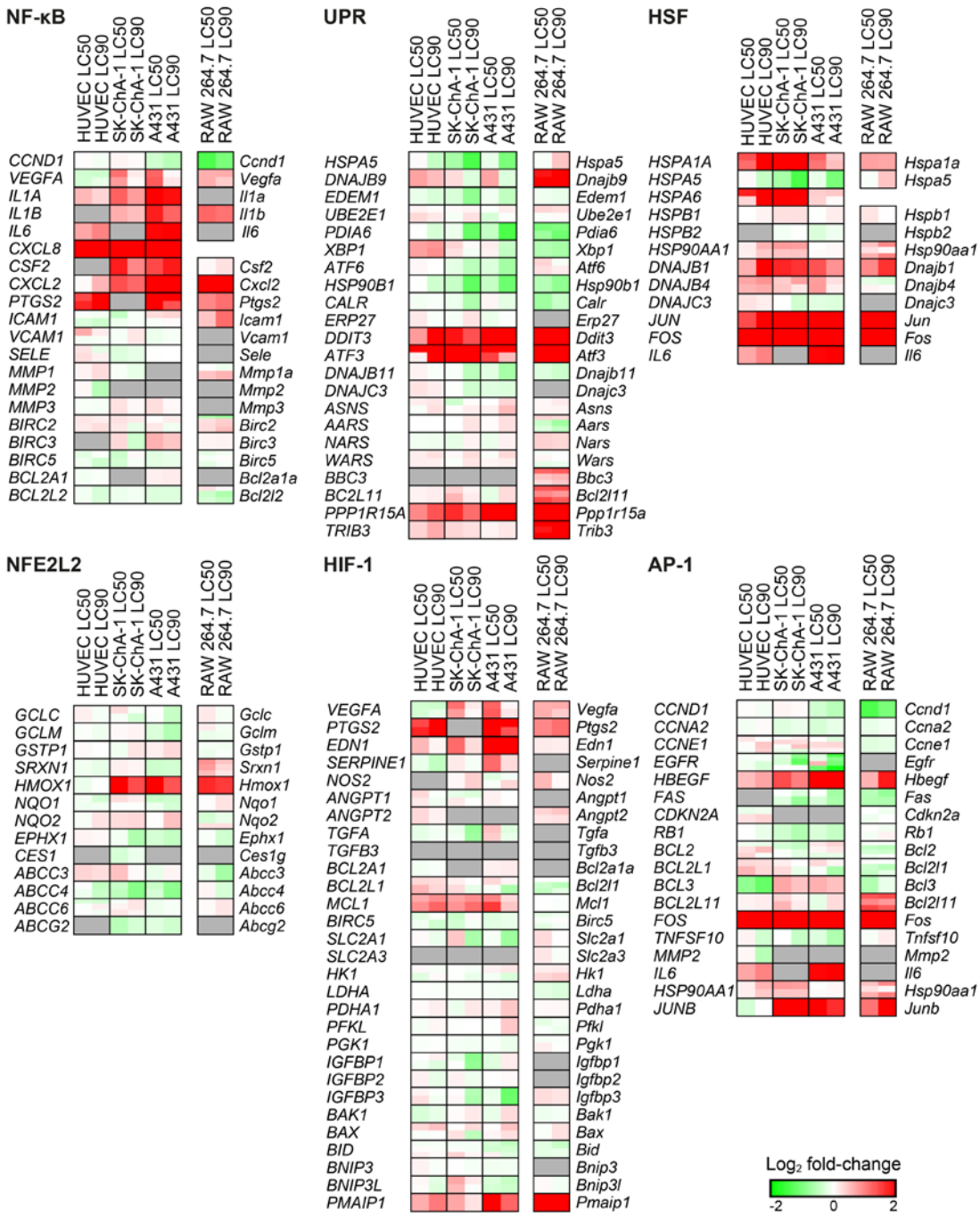

Fig. 3. Transcriptional response following ZPCL-PDT. Expression analysis of genes that are involved in NF-κB, UPR, HSF, NFE2L2, HIF-1, and AP-1 signaling as shown by the log2 fold-change (lower right corner). All comparisons were made between the PDT-treated groups versus the control group (n = 3 per group). A gene may correspond to multiple probes as indicated by horizontal splits. Each gene is divided in two halves corresponding to the LC_{50} (left) and LC_{90} (right) group. Grey boxes signify probes that exhibited poor quality or were not included in the gene expression analysis.

proteins in the ER [37]. As a result, the UPR is initiated together with the activation of HSF1 [38]. ZPCL-PDT at both regimens induced upregulation of the UPR-associated genes DNA-damage-inducible transcript 3 (*DDIT3*, *Ddit3*), activating transcription factor 3 (*ATF3*, *Atf3*), protein phosphatase 1, and regulatory subunit 15A (*PPP1R15A*, *Ppp1r15a*) in all cell types (**Fig. 3**). PDT at LC_{50} triggered upregulation of DnaJ (Hsp40) homolog, subfamily B, member 9 (*DNAJB9*) in all cell types, of which the protein product protects cells from apoptosis [39]. With respect to HSF signaling, all cell types exhibited elevated *DNAJB1* (*Dnajb1*) and heat shock 70 kDa protein 1A (*HSPA1A*, *Hspa1a*) mRNA levels following PDT (**Fig. 3**). In contrast to RAW 264.7, SK-ChA-1, and A431 cells, HUVECs revealed a dose-dependent effect on the transcript levels of *HSPA1A*, *DNAJB1*, *JUN*, and *FOS*, where PDT at LC_{90} caused the most pronounced upregulation of these genes.

AP-1-mediated immediate early gene response

In response to various extracellular and intracellular (*e.g.*, ROS) stimuli, the immediate early response is activated via apoptosis signal-regulating kinase 1 (ASK-1) that enables AP-1-mediated transcription [40]. The AP-1 transcription factors FBJ murine osteosarcoma viral oncogene homolog (*FOS*, *Fos*) and jun B proto-oncogene (*JUNB*, *Junb*) were upregulated in RAW 264.7, SK-ChA-1, and A431 cells in both the LC_{50} and LC_{90} groups (**Fig. 3**). Furthermore, the survival factor heparin-binding EGF-like growth factor (*HGEGF*, *Hbegf*) was strongly upregulated in all cell types following both PDT regimens. *EGFR* was downregulated in HUVEC, SK-ChA-1, and A431 cells, particularly in the LC_{90} group.

In addition, the effect of PDT on EGFR signaling in EGFR-overexpressing A431 cells versus SK-ChA-1 cells is shown in more detail in **Fig. S4**. This subanalysis revealed that PDT had an inhibitory effect on the various ErbB isoforms, which was observed in both cell lines, although *EGFR* (*ERBB1*) was mostly afflicted. Also, known downstream targets of EGFR [41] appeared to be more inhibited in A431 cells compared to SK-ChA-1 cells after supralethal PDT (**Fig. S4**).

HIF-1-mediated hypoxia-induced stress response

HIF-1 is a transcription factor that is induced by ROS and hypoxia [42], which promotes the transcription of genes involved in cell survival and angiogenesis [43]. ZPCL-PDT caused upregulation of various HIF-1-associated genes, including *VEGFA* (not in HUVECs), *PTGS2*, endothelin 1 (*EDN1*), myeloid cell leukemia 1 (*MCL1*), and phorbol-12-myristate-13-acetate-induced protein 1 (*PMAIP1*) (**Fig. 3**). The effects were more pronounced after sublethal PDT. PDT also upregulated several HIF-1-associated genes in RAW 264.7 cells, including *Vegfa*, *Ptgs2*, *Edn1*, and *Pmaip1* but not *Mcl1*. However, RAW 264.7 cells did not exhibit any dose-dependent differences as observed in the human cell types.

NFE2L2-mediated antioxidant response

The NFE2L2-mediated antioxidant response is activated by oxidative stress and serves to restore the cellular redox balance. As shown in **Fig. 3**, the NFE2L2 pathway was largely unaffected. In fact, PDT reduced the expression of genes involved in detoxification [*e.g.*, ATP binding cassette subfamily C member 4 (*ABCC4*, *Abcc4*), ATP binding cassette subfamily G member 2 (*ABCG2*, *Abcg2*)] and antioxidant activity [*e.g.*, epoxide hydrolase 1 (*EPHX1*, *Ephx1*)]. Heme oxygenase 1 (*HMOX1*, *Hmox1*) is linked to cell survival following PDT [44]. In addition to NFE2L2, HIF-1 ("HIF-1-mediated hypoxia-induced stress response") is also able to mediate transcription of *HMOX1* [45]. Its gene expression after PDT was higher in RAW 264.7, SK-ChA-1, and A431 cells but not in HUVEC cells. This effect was more pronounced in the LC_{50} cells compared to the LC_{90} cells as evidenced by the $\log_2$ fold-changes in *HMOX1*/*Hmox1* gene expression: A431 (2.1 versus 1.3, respectively), SK-ChA-1 (2.1 versus 1.4, respectively), and RAW 264.7 cells (1.7 versus 1.5) respectively.

PDT upregulates transcription-related proteins and downregulates proteins linked to EGFR signaling

To explore the cellular response in a cell line derived from a tumor that is refractory towards PDT [24], SK-ChA-1 cells were subjected to more in-depth analysis using an untargeted (phospho)proteomic-based approach 90 min after PDT. The EGFR-overexpressing A431 cell line was excluded from the (phospho)proteomic analysis to eliminate redundancy, given that SK-ChA-1 cells also express high basal levels of EGFR [46]. The differentially expressed phosphorylated and non-phosphorylated proteins (compared to non-treated cells) are presented in **Table S5**. A no-liposome, irradiation-only group was excluded because we have shown previously that red light irradiation has no effect on cells [14].

The proteome data revealed a dose-dependent response in the number of differentially expressed proteins (**Fig. S5**). To gain more insight in the affected molecular pathways, the data were analyzed with Reactome [47, 48] (**Fig. 4**). Based on the proteomics data, PDT caused downregulation of various proteins involved in endocytosis in the LC_{50} group, but more predominantly in the LC_{90} group [AP-2 complex subunit alpha-1 (AP2A1), AP2M1, AP2B1, AP3B1]. Furthermore, SK-ChA-1 cells that had been treated at LC_{90} upregulated proteins involved in pre-RNA splicing (serine/arginine-rich splicing factor 4 (SRSF4), SRSF6) and epigenetic control of transcription [protein dpy-30 homolog (DPY30), WD repeat-containing protein 5 (WDR5)] (**Fig. 4**).

Phosphoproteomic data were analyzed with the Phosphopath plugin in Cytoscape [32] and only phosphosites which were differentially regulated in either LC_{50} or LC_{90} groups were analyzed. PDT of SK-ChA-1 cells induced phosphorylation of heat shock protein beta-1 (HSPB1) (**Fig. 5**), which is involved in the defense against

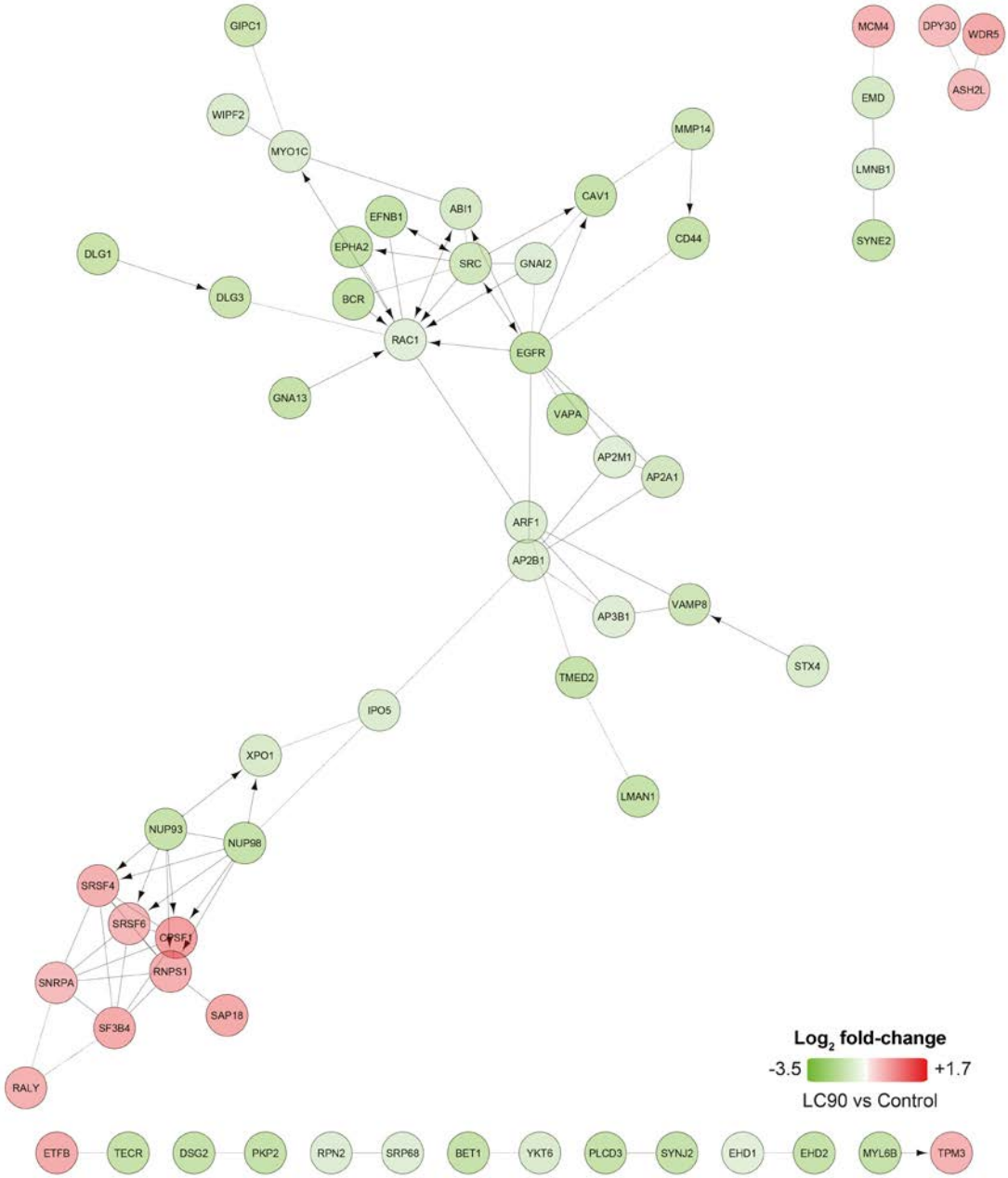

Fig. 4. Differentially expressed proteins observed after ZPCL-PDT of SK-ChA-1 cells in the LC_{90} group. Up- (in red) and downregulated (in green) proteins between the PDT-treated groups and control group (n = 4 per group) were analyzed using Reactome to assess functional interactions [38, 39]. Arrows indicate activating/catalyzing reactions, whereas straight and dashed lines indicate functional and predicted functional interactions, respectively. Proteins without functional interactions are not displayed in the figure.

oxidative stress [49, 50]. Furthermore, PDT decreased phosphorylation of proteins involved in EGFR signaling, such as mitogen-activated protein kinase 1 (MAPK1), son of sevenless homolog 1 (SOS1), and catenin delta-1 (CTNND1). This effect was more evident at LC_{90} inasmuch as these cells downregulated the EGFR-associated proteins EGFR (confirmed by Western blotting, **Fig. S2**), proto-oncogene tyrosine-protein kinase Src (SRC), caveolin-1 (CAV1), and phosphorylated proteins SOS1, related RAS viral (r-ras) oncogene homolog 2 (RRAS2), MAPK1, and MAPK3. Altogether, it seems that PDT induced the expression of transcription-related proteins and downregulated proteins involved in EGFR signaling.

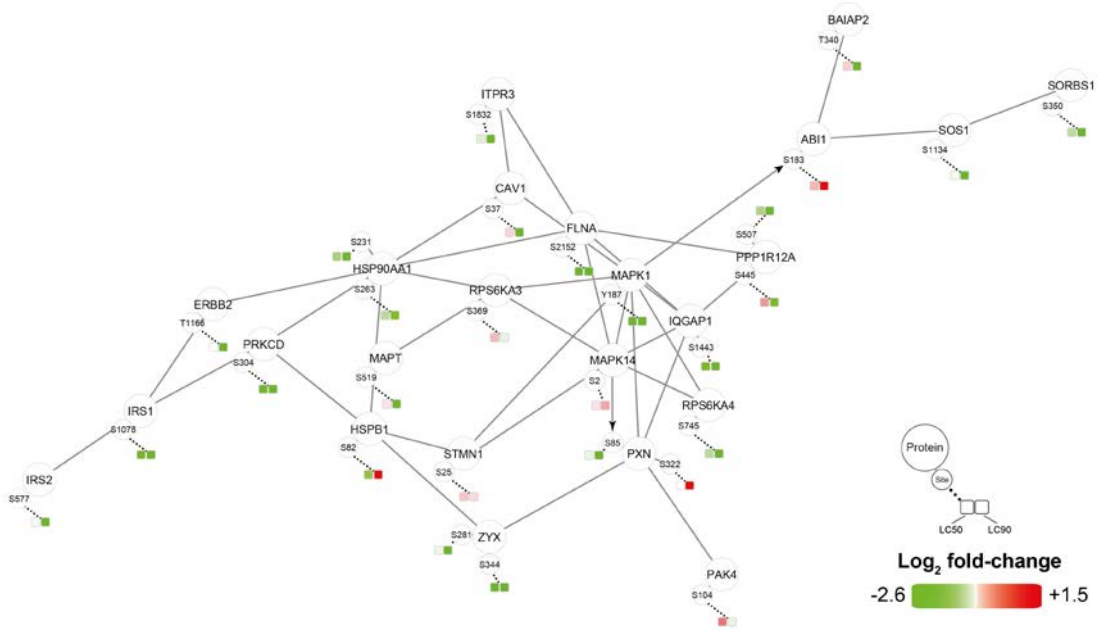

Fig. 5. Phosphoproteomic analysis of SK-ChA-1 cells after ZPCL-PDT. The data (n = 4 per group) were analyzed with the Phosphopath plugin in Cytoscape [40] and increased and decreased phosphorylation of proteins in the PDT-treated groups versus the control group are indicated in red and green, respectively. Straight lines and arrows indicate protein interactions (derived from the Biogrid database [77]) and kinase-substrate interactions (imported from PhosphoSitePlus [78]), respectively. Wikipathways was used for pathway analysis [79], where the dataset was queried against this database to identify pathways. For this figure, EGF, VEGF, insulin, FAK, and MAPK signaling pathways were selected.

PDT affects metabolites that are involved in energy production and redox signaling

Finally, PDT-treated SK-ChA-1 cells were investigated in terms of metabolomics at 90 min post-PDT. Incubation of cells with ZPCLs in the absence of light only marginally affected the metabolomic profile (**Fig. 6a**, **Table S6**), again confirming the *in vitro* safety of the ZPCLs.

PDT highly influenced almost all studied metabolites, whereby the effects observed in the LC_{50} group were essentially exacerbated in the LC_{90} group. PDT-subjected SK-ChA-1 cells upregulated multiple amino acid levels as well as metabolites

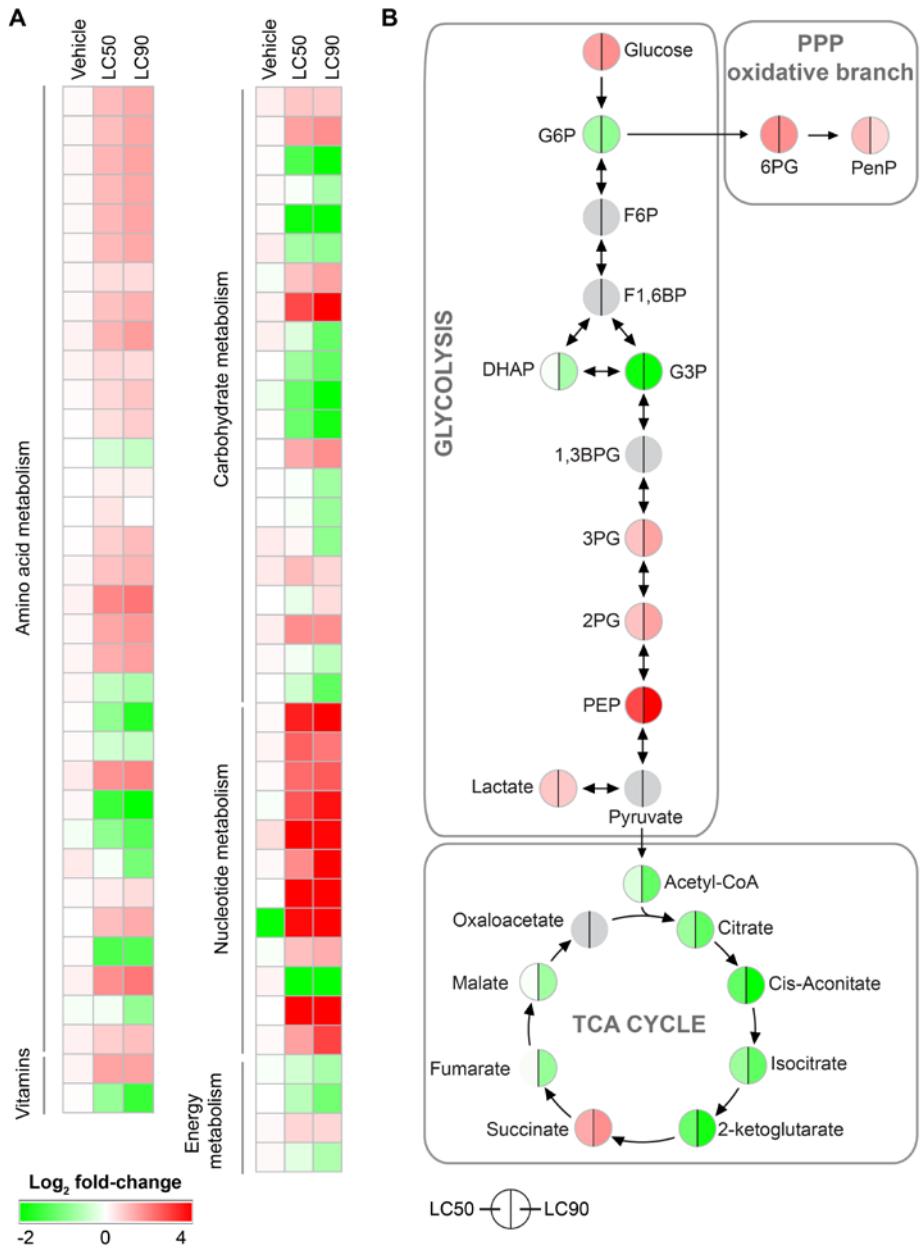

Fig. 6. Metabolomic analysis of SK-ChA-1 cells after ZPCL-PDT. (**A**) Metabolites were classified into pathways and metabolite expression is depicted as the $\log_2$ fold-change (bottom left corner) between treated and control cells (n = 3 per group). Numerical values can be found in **Table S6**. (**B**) $\log_2$ fold-change of metabolites in the category carbohydrate metabolism grouped per pathway. Changes in LC_{50}- (left) and LC_{90}-treated (right) SK-ChA-1 cells compared to control cells are depicted. Identical $\log_2$ fold-change values are plotted for 3PG and 2PG and for citrate and isocitrate, as these metabolites could not be resolved. Metabolites indicated in grey could not be quantified. Abbreviations: TCA cycle, tricarboxylic acid cycle; PPP, pentose phosphate pathway; G6P, glucose-6-phosphate; F6P, fructose-6-phosphate; F1,6BP, fructose-1,6-bisphosphate; DHAP, dihydroxyacetone phosphate; G3P, glyceraldehyde-3-phosphate; 1,3 BPG, 1,3-bisphosphoglycerate; 3PG, 3-phosphoglycerate; 2PG, 2-phosphoglycerate; PEP, phosphoenolpyruvate; 6pG, 6-phosphogluconate; PenP, pentose-phosphate.

involved in nucleotide metabolism. In contrast, metabolites involved in the TCA cycle and urea cycle were downregulated, reflecting perturbations in anaerobic energy production as evidenced by the lactate and succinate accumulation. Moreover, PDT also affected metabolites that modulate the redox balance (**Fig. 6b**). Glutathione and oxidized glutathione (GSSG) were downregulated, while nicotinamide adenine dinucleotide phosphate (NADP+) was upregulated. Possibly as a consequence of the pro-oxidative state, metabolites in the oxidative branch of the pentose phosphate pathway were upregulated (**Table S6**). Lastly, the nucleotide profile was also determined in PDT-treated cells, which showed slightly lower uridine triphosphate (UTP), cytidine triphosphate (CTP), and guanosine triphosphate (GTP) levels in the LC_{50} group (**Fig. S6**). The lower ATP:ADP ratio in PDT-treated cells may be indicative of dying cells (**Fig. S6**).

Discussion

Clinical PDT may be enhanced by pharmacologically interfering in molecular pathways that mediate resistance to therapy [2]. During PDT, light intensity attenuates in the tumor tissue as a result of absorption and scattering, creating a gradient of cumulative light dose (fluence) across the tumor. Since PDT-mediated ROS production is proportional to the fluence [14], tumor cells that are more distal from the light source, or tumor cells that are insufficiently oxygenated, may experience less oxidative stress than fully exposed and oxygenated cells [23], allowing the sublethally afflicted cells to activate survival pathways. Inasmuch as tumor cell survival may ultimately enable recurrence and metastasis, it is critical that the tumor bulk is completely eradicated in a single PDT session.

One potential strategy to optimize PDT is using pharmacological adjuvants that inhibit post-PDT survival signaling, which may be co-administered with the photosensitizer [11–13]. This study was conducted to determine which pathways are activated and hence eligible for pharmacological targeting. The response of tumor parenchymal and non-parenchymal cells subjected to sublethal (LC_{50}) and supralethal PDT (LC_{90}) was therefore investigated in the acute phase of PDT—a time point where the transcriptome and acute phase proteins were expected to be dysregulated. SK-ChA-1 and A431 cells were used because the former are derived from a tumor known to be refractory to PDT [51, 52] and because both overexpress EGFR, which was shown to be profoundly affected by PDT. It is critical to underscore that the post-PDT environment temporally evolves in a dynamic manner at the level of the transcriptome, lipidome, proteome, and metabolome [53]. In support of this, the extent of PDT-induced cell death progressively increased at 2, 4, and 24 h after PDT and transcriptomic and (phospho) proteomic analysis revealed that mRNA and protein expression was discordant at 90 min post-PDT (**Fig. S7**). First, mRNA and protein expression profiles may be more

in sync at later time points, *i.e.*, when the mRNA has been translated to functional proteins. Second, the transcriptome and proteome are also expected to change over time, potentially necessitating an acclimating pharmacological inhibition strategy after PDT. Because the transcriptomic-, (phospho)proteomic-, and metabolomic temporal changes are vital to therapeutic outcome, studies in our labs are underway to establish post-PDT molecular signatures across the 24-hour time span.

In the acute phase, transcriptomic analysis revealed that PDT-treated tumor cells (SK-ChA-1, A431) were afflicted at multiple physiological and biochemical junctions and activated extensive survival signaling via HIF-1, NF-κB, AP-1, and HSF. Survival signaling was most pronounced in the low-dose PDT group, which is detrimental to the desired clinical outcome. Second, PDT-treated SK-ChA-1 cells downregulated proteins involved in EGFR signaling. Third, metabolomic analysis of PDT-treated SK-ChA-1 cells pointed to downregulation of metabolites involved in energy metabolism (glycolysis, TCA cycle), altered cellular redox state, and upregulation of metabolites involved in nucleotide metabolism and the pentose phosphate pathway. These latter two findings are expected to be beneficial for PDT outcome, as EGFR downregulation and perturbed energy metabolism negatively affect cell viability and proliferation and hence offset the survival signaling.

The ROAST gene set analysis supports our hypothesis that suboptimally treated tumor cells (LC_{50}) engage in more extensive survival signaling in response to PDT. Especially the HIF-1- and NF-κB-mediated pathways may be attractive for therapeutic interventions. PDT of SK-ChA-1 and A431 cells upregulated genes downstream of HIF-1 and NF-κB (*IL1A*, *IL1B*, *IL6*, *CXCL8*, *VEGFA*, *HMOX1*) that mediate inflammation, survival, and angiogenesis [54, 55]. These findings have been echoed in literature (**Table 1**). Whereas overexpression of HIF-1 was associated with therapeutic resistance in 5-aminolevulinic acid (5-ALA)-PDT-treated human esophageal carcinoma cells [56], combination therapy of siRNA-mediated knockdown of HIF-1 with Photosan-PDT significantly improved therapeutic efficacy in human head-and-neck cancer (SCC4, SAS) tumor-bearing mice [57]. Corroboratively, treatment of A431 and SK-ChA-1 cells with the HIF-1 inhibitor acriflavine significantly improved PDT efficacy [11, 13]. Similarly, it was shown in various studies that combined treatment comprising NF-κB inhibitors and PDT augmented therapeutic efficacy [35, 58, 59].

In addition to the tumor-derived cell lines, murine macrophages (RAW 264.7) responded fervently to PDT, inasmuch as these cells significantly upregulated all survival pathways (except for NFE2L2 in the LC_{90} group). This hyperactive state may in part have been caused by the fact that macrophages become activated upon exposure to dying cells and cell debris [60], including post-PDT [35]. The same pattern was observed for HUVEC cells, but in contrast to the tumor cell lines, only few differences were observed between the LC_{50} and LC_{90} groups. Unexpectedly, after PDT the endothelial cells slightly downregulated VEGF, which is a growth factor for (tumor)

	Identified target	Druggable target	General function	Inhibitor	PDT efficacy	Ref.
Transcriptomics	▲ HMOX1	HMOX1	Cytoprotective, antoxidative properties	SnPPIX	▲	[75]
				ZnPPiX	▲	[44, 76]
	▲ AP-1 pathway	AP-1	Proliferation, inflammation, apoptosis	-	n.d.	[9]
	▲ HIF-1 pathway	HIF-1	Survival, angiogenesis, glycolysis	Acriflavine	▲	[11, 13]
				HIF-1α siRNA	▲	[57]
	▲ HSF pathway	HSF1	Proteostasis, survival	-	n.d.	[9]
	▲ NF-κB pathway	NF-κB	Inflammation, proliferation, anti-apoptosis	NF-κB siRNA	▲	[35]
				Dihydroartemisinin	▲	[58]
				BAY 11-7082	▲	[59]
Proteomics	▲ HSPB1	HSPB1	Anti-apoptosis, cell invasion	-	▲ ▼	[50, 77]
Metabolomics	▲ Succinate	SUCNR1	Inflammation, HIF-1 stabilization	-	n.d.	[73]

Table 1. Potential druggable targets that were identified in this study. For all the molecular targets, its general function is listed, as well as whether inhibition improves (indicated with ▲) or hampers (indicated with ▼) PDT efficacy. Abbreviations: SnPPIX, tin protoporphyrin; ZnPPIX, zinc protoporphyrin; siRNA, small interfering RNA; n.d., not determined; SUCNR1, succinate receptor 1.

endothelium that stimulates angiogenesis. Zhang *et al.* also observed downregulated VEGF protein levels after hypericin-PDT in HUVECs [61], which may indicate that PDT is able to induce growth inhibition of tumor endothelium.

SK-ChA-1 cells were also subjected to (phospho)proteomic and metabolomic analysis, of which the main results are summarized in **Fig. 7**. At the proteomic level, PDT-mediated phosphorylation of HSPB1, which is a stress protein that acts as a chaperone to stimulate survival under stress conditions [50]. PDT at LC_{90} downregulated proteins involved in focal adhesion [CAV1, integrin alpha-2 (ITA2)], adherens junctions (CTNND1, EpCAM), and tight junctions (phosphorylated ZO1 and ZO3). As reported in [62–64], PDT may oxidatively damage proteins involved in cell–cell adhesion, cytoskeletal structure, and focal adhesion, which appears to be dependent on cell type, photosensitizer concentration, and light dose. However, it may also contribute to a higher metastatic potential after PDT, inasmuch as loss of adhesion proteins is associated with invasion [62]. Further research is warranted to establish whether PDT enhances the metastatic potential of cancer cells, as activation of both survival and metastasis pathways by PDT may hamper clinical safety of the procedure.

Supralethal PDT also downregulated various proteins involved in EGFR signaling, which is an important therapeutic target as it is overexpressed in numerous cancer types [19]. Previous studies have shown that SK-ChA-1 and A431 cells in the absence of PDT are sensitive to EGFR inhibitors, as these compounds inhibited cell growth [46, 65]. ZPCL-PDT of SK-ChA-1 cells at LC_{90} revealed downregulation of EGFR on both the transcriptomic and proteomic level. Both SK-ChA-1 and A431 cells exhibited a reduction in EGFR mRNA levels after PDT and this effect was enhanced

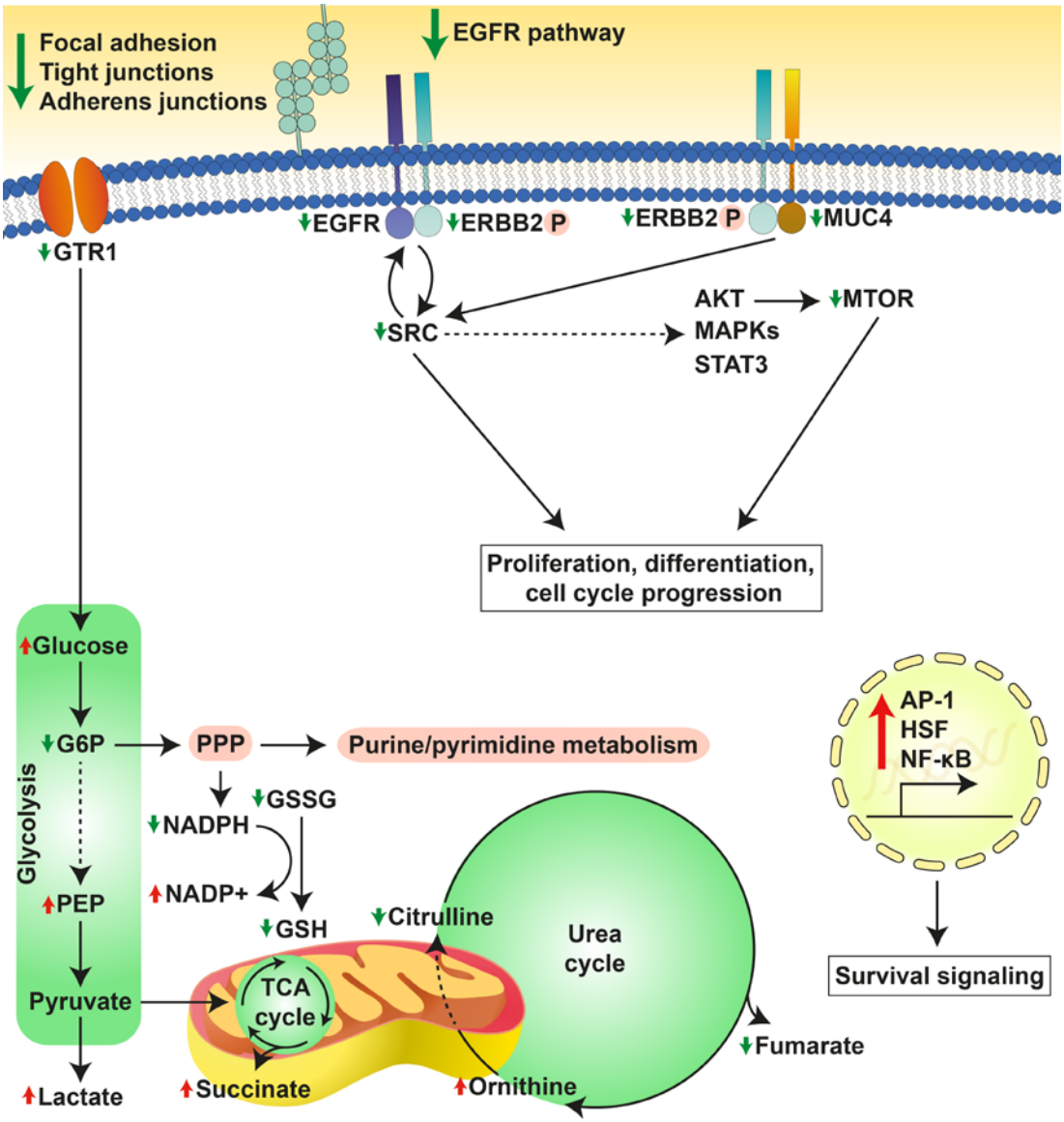

Fig. 7. Overview of the cellular response of SK-ChA-1 cells to supralethal (LC_{90}) PDT. In response to PDT, SK-ChA-1 cells downregulate proteins involved in focal adhesion, tight and adherens junctions, and EGFR signaling. Metabolic processes that are dependent on mitochondria (TCA cycle, urea cycle) appear to be downmodulated, whereas the antioxidant response was activated. On the transcriptomic level, SK-ChA-1 cells demonstrated an upregulation of AP-1-, HSF-, and NF-κB-mediated signaling that may contribute to cell survival.

in the LC_{90} group. Although the exact mechanism is still unknown, the general trend is that PDT is able to inhibit and/or degrade EGFR, thereby deterring tumor growth and inducing apoptosis [66]. However, exceptions do exist. For instance, Edmonds and co-workers showed that human ovarian carcinoma (OVCAR-5) and non-small cell lung cancer (H460) cell lines upregulated EGFR after PDT with verteporfin (log P =

3.74) [67, 68]. Inhibition of EGFR with erlotinib increased PDT efficacy and resulted in apoptotic cell death [67], linking pharmacological EGFR inhibition to cell demise. Also, a more recent study demonstrated that erlotinib treatment prior to PDT induced higher complete response rates in NSCLC (H460, A549)-xenografted mice [69]. Interestingly, treatment of various cancer cell lines with the photosensitizer Photofrin (porfimer sodium, log P = 8.5 [2]) alone downregulated EGFR protein expression, which was enhanced upon PDT, indicating that Photofrin alone is able to downmodulate EGFR expression [70]. ZnPC is a highly lipophilic photosensitizer (log P = 8.5 [2]) that intercalates into biomembranes [13]. Given that EGFR is a transmembrane protein, ZnPC is expected to reside in the direct vicinity of the transmembrane domain of EGFR, where it can subsequently cause oxidative modification of EGFR's transmembrane structures and impede its functional properties. The same applies to verteporfin and Photofrin. However, apparently the site of ROS generation is not ubiquitously linked to protein dysfunctionalization. Instead, EGFR expression after PDT is photosensitizer-dependent, whereby inhibition of EGFR by PDT may contribute to an anti-cancer effect when photosensitizers are employed that induce its downregulation, such as ZnPC, by an as yet undefined mechanism.

The metabolomics data of PDT-treated SK-ChA-1 cells showed similar trends between the LC_{50} and LC_{90} groups, although the effects were more pronounced in the LC_{90} group. PDT-treated cells exhibited increased glucose whereas a number of glycolysis-associated metabolites were reduced, suggesting that glucose is shuttled into pathways that branch off glycolysis, such as the pentose phosphate pathway. Also, the TCA cycle appeared to be downregulated following PDT, as evidenced by downregulation of acetyl-CoA, citrate, α-ketoglutarate, and malate. As a result of ROS production during PDT, the redox status of a cell may be seriously affected. This is also observed in PDT-treated SK-ChA-1 cells, as regulators of the redox response differed (*e.g.*, reduction of glutathione and GSSG, increase in $NADP^+$). The post-PDT pro-oxidative state may also explain the upregulation of the pentose phosphate pathway (**Fig. 6b**), as the pentose phosphate pathway contributes to the production of NADPH—a major player in the antioxidant response [71]. Another important factor that was increased in PDT-treated SK-ChA-1 cells is succinate. Mitochondria are a known target of ZnPC-based PDT [2, 17], after which mitochondria-localized succinate may be released into the cytoplasm [72]. Succinate has been shown to mediate ATP generation in mitochondria, activation of HIF-1, and pro-inflammatory signaling (reviewed in [73]). Pharmacological strategies that limit succinate production could therefore serve as a strategy to augment PDT efficacy, although succinate build-up in mitochondria is also a precursor condition for latent oxidative stress [74] that in turn may promote tumor cell death.

To our knowledge, this is the first study that explored the PDT response in such detail at the cellular and molecular level. Therefore, it may provide novel

information that could be valuable to design new therapeutic strategies, possibly based on therapeutic targets that were found in this study (**Table 1**). Consistent with earlier reports, the combined use of PDT and inhibitors of survival pathways may be an attractive approach to improve therapeutic efficacy in the aforementioned clinically recalcitrant cancer types.

Acknowledgements

MH has received grants from Stichting Technologische Wetenschap (STW 12064), the Phospholipid Research Center in Heidelberg, the Dutch Anticancer Foundation in Amsterdam (Stichting Nationaal Fonds Tegen Kanker), and the Nijbakker Morra Foundation. SL and SC were supported by the Netherlands Organization for Scientific Research (NWO) through a VIDI Grant (Project 723.013.008). CRB was supported by NWO through a VENI Grant (Project 722.013.009). The A431 cell line was a kind a gift from Gerben Koning (Erasmus Medical Center, the Netherlands). The SK-ChA-1 cell line was a kind gift from Alexander Knuth and Claudia Matter (University Hospital Zurich, Switzerland). The RAW 264.7 cell line was a kind gift from Joan Kwakkel (Academic Medical Center, the Netherlands).

References

1. Plaetzer K, Krammer B, Berlanda J, Berr F, Kiesslich T (2009) Photophysics and photochemistry of photodynamic therapy: fundamental aspects. Lasers Med Sci 24(2):259–268. doi:10.1007/s10103-008-0539-1
2. Weijer R, Broekgaarden M, Kos M, van Vught R, Rauws EAJ, Breukink E, van Gulik TM, Storm G, Heger M (2015) Enhancing photodynamic therapy of refractory solid cancers: Combining second-generation photosensitizers with multi-targeted liposomal delivery. J Photochem Photobiol C Photochem Rev 23:103–131. doi:10.1016/j.jphotochemrev.2015.05.002
3. Sibille A, Lambert R, Souquet JC, Sabben G, Descos F (1995) Long-term survival after photodynamic therapy for esophageal cancer. Gastroenterology 108(2):337–344
4. Zeitouni NC, Shieh S, Oseroff AR (2001) Laser and photodynamic therapy in the management of cutaneous malignancies. Clin Dermatol 19(3):328–338
5. Sun ZQ (1992) Photodynamic therapy of nasopharyngeal carcinoma by argon or dye laser—an analysis of 137 cases. Zhonghua Zhong Liu Za Zhi 14(4):290–292
6. Benson RC Jr (1986) Laser photodynamic therapy for bladder cancer. Mayo Clin Proc 61(11):859–864
7. Nseyo UO, Dougherty TJ, Boyle DG, Potter WR, Wolf R, Huben R, Pontes JE (1985) Whole bladder photodynamic therapy for transitional cell carcinoma of bladder. Urology 26(3):274–280
8. Quyn AJ, Ziyaie D, Polignano FM, Tait IS (2009) Photodynamic therapy is associated with an improvement in survival in patients with irresectable hilar cholangiocarcinoma. HPB (Oxford) 11(7):570–577. doi:10.1111/j.1477-2574.2009.00102.x
9. Broekgaarden M, Weijer R, van Gulik TM, Hamblin MR, Heger M (2015) Tumor cell survival pathways activated by photodynamic therapy: a molecular framework for inhibition strategies. Cancer Metastasis Rev:1–48
10. Broekgaarden M, van Vught R, Oliveira S, Roovers RC, van Bergen en Henegouwen PM, Pieters RJ, van Gulik TM, Breukink E, Heger M (2016) Site-specific conjugation of single domain antibodies to liposomes enhances photosensitizer uptake and photodynamic therapy efficacy. Nanoscale 8(12):6490–6494
11. Weijer R, Broekgaarden M, Krekorian M, Alles LK, van Wijk AC, Mackaaij C, Verheij J, van der Wal AC, van Gulik TM, Storm G, Heger M (2016) Inhibition of hypoxia inducible factor 1 and topoisomerase with acriflavine sensitizes perihilar cholangiocarcinomas to photodynamic therapy. Oncotarget 7(3):3341–3356. doi:10.18632/oncotarget.6490
12. Broekgaarden M, Weijer R, van Wijk AC, Cox RC, Egmond MR, Hoebe R, van Gulik TM, Heger M (2016) Photodynamic therapy with liposomal zinc phthalocyanine and tirapazamine increases tumor cell death via DNA damage. J Biomed Nanotechnol 12:1–16
13. Broekgaarden M, Weijer R, Krekorian M, van den IJssel B, Kos M, Alles LK, van Wijk AC, Bikadi Z, Hazai E, van Gulik TM, Heger M (2016) Inhibition of hypoxia-inducible factor 1 with acriflavine sensitizes hypoxic tumor cells to photodynamic

therapy with zinc phthalocyanine-encapsulating cationic liposomes. Nano Res 9(6):1639–1662
14. Broekgaarden M, de Kroon AI, Gulik TM, Heger M (2014) Development and in vitro proof-of-concept of interstitially targeted zinc-phthalocyanine liposomes for photodynamic therapy. Curr Med Chem 21(3):377–391
15. Lee K, Zhang H, Qian DZ, Rey S, Liu JO, Semenza GL (2009) Acriflavine inhibits HIF-1 dimerization, tumor growth, and vascularization. Proc Natl Acad Sci U S A 106(42):17910–17915. doi:10.1073/pnas.0909353106
16. Weijer R, Broekgaarden M, van Golen RF, Bulle E, Nieuwenhuis E, Jongejan A, Moerland PD, van Kampen AH, van Gulik TM, Heger M (2015) Low-power photodynamic therapy induces survival signaling in perihilar cholangiocarcinoma cells. BMC Cancer 15(1):1014. doi:10.1186/s12885-015-1994-2
17. Alexandratou E, Yova D, Loukas S (2005) A confocal microscopy study of the very early cellular response to oxidative stress induced by zinc phthalocyanine sensitization. Free Radic Biol Med 39(9):1119–1127. doi:10.1016/j.freeradbiomed.2005.06.006
18. Fabris C, Valduga G, Miotto G, Borsetto L, Jori G, Garbisa S, Reddi E (2001) Photosensitization with zinc (II) phthalocyanine as a switch in the decision between apoptosis and necrosis. Cancer Res 61(20):7495–7500
19. Herbst RS, Shin DM (2002) Monoclonal antibodies to target epidermal growth factor receptor-positive tumors: a new paradigm for cancer therapy. Cancer 94(5):1593–1611
20. Harder J, Waiz O, Otto F, Geissler M, Olschewski M, Weinhold B, Blum HE, Schmitt-Graeff A, Opitz OG (2009) EGFR and HER2 expression in advanced biliary tract cancer. World J Gastroenterol 15(36):4511–4517
21. Yang X, Wang W, Wang C, Wang L, Yang M, Qi M, Su H, Sun X, Liu Z, Zhang J, Qin X, Han B (2014) Characterization of EGFR family gene aberrations in cholangiocarcinoma. Oncol Rep 32(2):700–708. doi:10.3892/or.2014.3261
22. Joseph SO, Wu J, Muggia FM (2012) Targeted therapy: its status and promise in selected solid tumors. Part II: Impact on selected tumor subsets, and areas of evolving integration. Oncology (Williston Park) 26 (11):1021–1030, 1035
23. Postiglione I, Chiaviello A, Palumbo G (2011) Enhancing photodynamic therapy efficacy by combination therapy: current and oncoming strategies. Cancers (Basel) 3(2):2597–2629
24. Shim CS, Cheon YK, Cha SW, Bhandari S, Moon JH, Cho YD, Kim YS, Lee LS, Lee MS, Kim BS (2005) Prospective study of the effectiveness of percutaneous transhepatic photodynamic therapy for advanced bile duct cancer and the role of intraductal ultrasonography in response assessment. Endoscopy 37(5):425–433. doi:10.1055/s-2005-861294
25. Post IC, de Boon WM, Heger M, van Wijk AC, Kroon J, van Buul JD, van Gulik TM (2013) Endothelial cell preservation at hypothermic to normothermic conditions using clinical and experimental organ preservation solutions. Exp Cell Res 319(17):2501–2513. doi:10.1016/j.yexcr.2013.05.011
26. Vichai V, Kirtikara K (2006) Sulforhodamine B colorimetric assay for cytotoxicity screening. Nat Protoc 1(3):1112–1116. doi:10.1038/nprot.2006.179
27. Wu D, Lim E, Vaillant F, Asselin-Labat ML, Visvader JE, Smyth GK (2010) ROAST: rotation gene set tests for complex microarray experiments. Bioinformatics 26(17):2176–2182. doi:10.1093/bioinformatics/btq401
28. Ruijter JM, Ramakers C, Hoogaars WM, Karlen Y, Bakker O, van den Hoff MJ, Moorman AF (2009) Amplification efficiency: linking baseline and bias in the analysis of quantitative PCR data. Nucleic Acids Res 37(6):e45. doi:10.1093/nar/gkp045
29. Zhou H, Ye M, Dong J, Corradini E, Cristobal A, Heck AJ, Zou H, Mohammed S (2013) Robust phosphoproteome enrichment using monodisperse microsphere-based immobilized titanium (IV) ion affinity chromatography. Nat Protoc 8(3):461–480. doi:10.1038/nprot.2013.010
30. Cox J, Mann M (2008) MaxQuant enables high peptide identification rates, individualized p.p.b.-range mass accuracies and proteome-wide protein quantification. Nat Biotechnol 26(12):1367–1372. doi:10.1038/nbt.1511
31. Cox J, Neuhauser N, Michalski A, Scheltema RA, Olsen JV, Mann M (2011) Andromeda: a peptide search engine integrated into the MaxQuant environment. J Proteome Res 10(4):1794–1805. doi:10.1021/pr101065j
32. Raaijmakers LM, Giansanti P, Possik PA, Mueller J, Peeper DS, Heck AJ, Altelaar AF (2015) PhosphoPath: Visualization of phosphositecentric dynamics in temporal molecular networks. J Proteome Res 14(10):4332–4341. doi:10.1021/acs.jproteome.5b00529
33. Berridge MV, Herst PM, Tan AS (2005) Tetrazolium dyes as tools in cell biology: new insights into their cellular reduction. Biotechnol Annu Rev 11:127–152. doi:10.1016/s1387-2656(05)11004-7
34. Kutmon M, Riutta A, Nunes N, Hanspers K, Willighagen EL, Bohler A, Melius J, Waagmeester A, Sinha SR, Miller R, Coort SL, Cirillo E, Smeets B, Evelo CT, Pico AR (2016) WikiPathways: capturing the full diversity of pathway knowledge. Nucleic Acids Res 44(D1):D488–D494. doi:10.1093/nar/gkv1024
35. Broekgaarden M, Kos M, Jurg FA, van Beek AA, van Gulik TM, Heger M (2015) Inhibition of NF-kappaB in tumor cells exacerbates immune cell activation following photodynamic therapy. Int J Mol Sci 16(8):19960–19977. doi:10.3390/ijms160819960
36. Karin M, Cao Y, Greten FR, Li ZW (2002) NF-kappaB in cancer: from innocent bystander to major culprit. Nat Rev Cancer 2(4):301–310. doi:10.1038/nrc780
37. Iurlaro R, Munoz-Pinedo C (2015) Cell death induced by endoplasmic reticulum stress. The FEBS journal. doi:10.1111/febs.13598
38. Fujimoto M, Nakai A (2010) The heat shock factor family and adaptation to proteotoxic stress. The FEBS journal 277(20):4112–4125
39. Lee HJ, Kim JM, Kim KH, Heo JI, Kwak SJ, Han JA (2015) Genotoxic stress/p53-induced DNAJB9 inhibits the pro-apoptotic function of p53. Cell Death Differ 22(1):86–95. doi:10.1038/cdd.2014.116
40. Nishitoh H, Saitoh M, Mochida Y, Takeda K, Nakano H, Rothe M, Miyazono K, Ichijo H (1998) ASK1 is essential for JNK/

SAPK activation by TRAF2. Mol Cell 2(3):389–395. doi:10.1016/S1097-2765(00)80283-X
41. Brand TM, Iida M, Li C, Wheeler DL (2011) The nuclear epidermal growth factor receptor signaling network and its role in cancer. Discov Med 12(66):419–432
42. Movafagh S, Crook S, Vo K (2015) Regulation of hypoxia-inducible factor-1a by reactive oxygen species: new developments in an old debate. J Cell Biochem 116(5):696–703. doi:10.1002/jcb.25074
43. Carmeliet P, Dor Y, Herbert JM, Fukumura D, Brusselmans K, Dewerchin M, Neeman M, Bono F, Abramovitch R, Maxwell P, Koch CJ, Ratcliffe P, Moons L, Jain RK, Collen D, Keshert E (1998) Role of HIF-1alpha in hypoxia-mediated apoptosis, cell proliferation and tumour angiogenesis. Nature 394(6692):485–490. doi:10.1038/28867
44. Grimm S, Mvondo D, Grune T, Breusing N (2011) The outcome of 5-ALA-mediated photodynamic treatment in melanoma cells is influenced by vitamin C and heme oxygenase-1. BioFactors 37(1):17–24. doi:10.1002/biof.129
45. Ockaili R, Natarajan R, Salloum F, Fisher BJ, Jones D, Kukreja RC (2005) HIF-1 activation attenuates postischemic myocardial injury: role for heme oxygenase-1 in modulating microvascular chemokine generation. Am J Physiol Heart Circ Physiol 289(2):H542–H548
46. Wiedmann M, Feisthammel J, Bluthner T, Tannapfel A, Kamenz T, Kluge A, Mossner J, Caca K (2006) Novel targeted approaches to treating biliary tract cancer: the dual epidermal growth factor receptor and ErbB-2 tyrosine kinase inhibitor NVP-AEE788 is more efficient than the epidermal growth factor receptor inhibitors gefitinib and erlotinib. Anticancer Drugs 17(7):783–795. doi:10.1097/01.cad.0000217433.48870.37
47. Fabregat A, Sidiropoulos K, Garapati P, Gillespie M, Hausmann K, Haw R, Jassal B, Jupe S, Korninger F, McKay S, Matthews L, May B, Milacic M, Rothfels K, Shamovsky V, Webber M, Weiser J, Williams M, Wu G, Stein L, Hermjakob H, D'Eustachio P (2016) The Reactome pathway knowledgebase. Nucleic Acids Res 44(D1):D481–D487. doi:10.1093/nar/gkv1351
48. Croft D, Mundo AF, Haw R, Milacic M, Weiser J, Wu G, Caudy M, Garapati P, Gillespie M, Kamdar MR, Jassal B, Jupe S, Matthews L, May B, Palatnik S, Rothfels K, Shamovsky V, Song H, Williams M, Birney E, Hermjakob H, Stein L, D'Eustachio P (2014) The Reactome pathway knowledgebase. Nucleic Acids Res 42 (Database issue):D472-477. doi:10.1093/nar/gkt1102
49. Zhang J, Zhang Y, Liu S, Zhang Q, Wang Y, Tong L, Chen X, Ji Y, Shang Q, Xu B, Chu M, Wei L (2013) Metadherin confers chemoresistance of cervical cancer cells by inducing autophagy and activating ERK/NF-kappaB pathway. Tumour Biol 34(4):2433–2440. doi:10.1007/s13277-013-0794-z
50. Wang HP, Hanlon JG, Rainbow AJ, Espiritu M, Singh G (2002) Up-regulation of Hsp27 plays a role in the resistance of human colon carcinoma HT29 cells to photooxidative stress. Photochem Photobiol 76(1):98–104
51. Wagner A, Wiedmann M, Tannapfel A, Mayr C, Kiesslich T, Wolkersdorfer GW, Berr F, Hauss J, Witzigmann H (2015) Neoadjuvant down-sizing of hilar cholangiocarcinoma with photodynamic therapy: long-term outcome of a phase II pilot study. Int J Mol Sci 16(11):26619–26628. doi:10.3390/ijms161125978
52. Zoepf T, Jakobs R, Arnold JC, Apel D, Riemann JF (2005) Palliation of nonresectable bile duct cancer: improved survival after photodynamic therapy. Am J Gastroenterol 100(11):2426–2430. doi:10.1111/j.1572-0241.2005.00318.x
53. Buescher JM, Driggers EM (2016) Integration of omics: more than the sum of its parts. Cancer & metabolism 4:4. doi:10.1186/s40170-016-0143-y
54. Masoud GN, Li W (2015) HIF-1alpha pathway: role, regulation and intervention for cancer therapy. Acta Pharm Sin B 5(5):378–389. doi:10.1016/j.apsb.2015.05.007
55. DiDonato JA, Mercurio F, Karin M (2012) NF-kappaB and the link between inflammation and cancer. Immunol Rev 246(1):379–400. doi:10.1111/j.1600-065X.2012.01099.x
56. Ji Z, Yang G, Shahzidi S, Tkacz-Stachowska K, Suo Z, Nesland JM, Peng Q (2006) Induction of hypoxia-inducible factor-1alpha overexpression by cobalt chloride enhances cellular resistance to photodynamic therapy. Cancer Lett 244(2):182–189. doi:10.1016/j.canlet.2005.12.010
57. Chen WH, Lecaros RL, Tseng YC, Huang L, Hsu YC (2015) Nanoparticle delivery of HIF1a siRNA combined with photodynamic therapy as a potential treatment strategy for head-andneck cancer. Cancer Lett 359(1):65–74. doi:10.1016/j.canlet.2014.12.052
58. Li YJ, Zhou JH, Du XX, de Jia X, Wu CL, Huang P, Han Y, Sui H, Wei XL, Liu L, Yuan HH, Zhang TT, Zhang WJ, Xie R, Lang XH, Liu T, Jiang CL, Wang LY, Bai YX (2014) Dihydroartemisinin accentuates the anti-tumor effects of photodynamic therapy via inactivation of NF-kappaB in Eca109 and Ec9706 esophageal cancer cells. Cell Physiol Biochem 33(5):1527–1536. doi:10.1159/000358716
59. Coupienne I, Bontems S, Dewaele M, Rubio N, Habraken Y, Fulda S, Agostinis P, Piette J (2011) NF-kappaB inhibition improves the sensitivity of human glioblastoma cells to 5-aminolevulinic acid-based photodynamic therapy. Biochem Pharmacol 81(5):606–616. doi:10.1016/j.bcp.2010.12.015
60. Porta C, Riboldi E, Ippolito A, Sica A (2015) Molecular and epigenetic basis of macrophage polarized activation. Semin Immunol 27(4):237–248. doi:10.1016/j.smim.2015.10.003
61. Zhang Q, Li ZH, Li YY, Shi SJ, Zhou SW, Fu YY, Zhang Q, Yang X, Fu RQ, Lu LC (2015) Hypericin-photodynamic therapy induces human umbilical vein endothelial cell apoptosis. Sci Rep 5:18398. doi:10.1038/srep18398
62. Di Venosa G, Perotti C, Batlle A, Casas A (2015) The role of cytoskeleton and adhesion proteins in the resistance to photodynamic therapy. Possible therapeutic interventions. Photochem Photobiol Sci 14(8):1451–1464. doi:10.1039/c4pp00445k
63. Acedo P, Stockert JC, Canete M, Villanueva A (2014) Two combined photosensitizers: a goal for more effective photodynamic therapy of cancer. Cell Death Dis 5:e1122. doi:10.1038/cddis.2014.77

64. Galaz S, Espada J, Stockert JC, Pacheco M, Sanz-Rodriguez F, Arranz R, Rello S, Canete M, Villanueva A, Esteller M, Juarranz A (2005) Loss of E-cadherin mediated cell-cell adhesion as an early trigger of apoptosis induced by photodynamic treatment. J Cell Physiol 205(1):86–96. doi:10.1002/jcp.20374
65. Gendreau SB, Ventura R, Keast P, Laird AD, Yakes FM, Zhang W, Bentzien F, Cancilla B, Lutman J, Chu F, Jackman L, Shi Y, Yu P, Wang J, Aftab DT, Jaeger CT, Meyer SM, De Costa A, Engell K, Chen J, Martini JF, Joly AH (2007) Inhibition of the T790 M gatekeeper mutant of the epidermal growth factor receptor by EXEL-7647. Clin Cancer Res 13(12):3713–3723. doi:10.1158/1078-0432.ccr-06-2590
66. Martinez-Carpio PA, Trelles MA (2010) The role of epidermal growth factor receptor in photodynamic therapy: a review of the literature and proposal for future investigation. Lasers Med Sci 25(6):767–771. doi:10.1007/s10103-010-0790-0
67. Edmonds C, Hagan S, Gallagher-Colombo SM, Busch TM, Cengel KA (2012) Photodynamic therapy activated signaling from epidermal growth factor receptor and STAT3: Targeting survival pathways to increase PDT efficacy in ovarian and lung cancer. Cancer Biol Ther 13(14):1463–1470. doi:10.4161/cbt.22256
68. Kawczyk-Krupka A, Bugaj AM, Potempa M, Wasilewska K, Latos W, Sieron A (2015) Vascular-targeted photodynamic therapy in the treatment of neovascular age-related macular degeneration: clinical perspectives. Photodiagnosis Photodyn Ther 12(2):161–175. doi:10.1016/j.pdpdt.2015.03.007
69. Gallagher-Colombo SM, Miller J, Cengel KA, Putt ME, Vinogradov SA, Busch TM (2015) Erlotinib pretreatment improves photodynamic therapy of non-small cell lung carcinoma xenografts via multiple mechanisms. Cancer Res 75(15):3118–3126. doi:10.1158/0008-5472.can-14-3304
70. Yang PW, Hung MC, Hsieh CY, Tung EC, Wang YH, Tsai JC, Lee JM (2013) The effects of Photofrin-mediated photodynamic therapy on the modulation of EGFR in esophageal squamous cell carcinoma cells. Lasers Med Sci 28(2):605–614. doi:10.1007/s10103-012-1119-y
71. Tomanek L (2015) Proteomic responses to environmentally induced oxidative stress. J Exp Biol 218(Pt 12):1867–1879. doi:10.1242/jeb.116475
72. Ariza AC, Deen PM, Robben JH (2012) The succinate receptor as a novel therapeutic target for oxidative and metabolic stress-related conditions. Front Endocrinol 3:22. doi:10.3389/fendo.2012. 00022
73. Mills E, O'Neill LA (2014) Succinate: a metabolic signal in inflammation. Trends Cell Biol 24(5):313–320. doi:10.1016/j.tcb.2013.11.008
74. Chouchani ET, Pell VR, Gaude E, Aksentijevic D, Sundier SY, Robb EL, Logan A, Nadtochiy SM, Ord EN, Smith AC, Eyassu F, Shirley R, Hu CH, Dare AJ, James AM, Rogatti S, Hartley RC, Eaton S, Costa AS, Brookes PS, Davidson SM, Duchen MR, Saeb-Parsy K, Shattock MJ, Robinson AJ, Work LM, Frezza C, Krieg T, Murphy MP (2014) Ischaemic accumulation of succinate controls reperfusion injury through mitochondrial ROS. Nature 515(7527):431–435. doi:10.1038/nature13909
75. Frank J, Lornejad-Schafer MR, Schoffl H, Flaccus A, Lambert C, Biesalski HK (2007) Inhibition of heme oxygenase-1 increases responsiveness of melanoma cells to ALA-based photodynamic therapy. Int J Oncol 31(6):1539–1545
76. Nowis D, Legat M, Grzela T, Niderla J, Wilczek E, Wilczynski GM, Glodkowska E, Mrowka P, Issat T, Dulak J, Jozkowicz A, Was H, Adamek M, Wrzosek A, Nazarewski S, Makowski M, Stoklosa T, Jakobisiak M, Golab J (2006) Heme oxygenase-1 protects tumor cells against photodynamic therapy-mediated cytotoxicity. Oncogene 25(24):3365–3374. doi:10.1038/sj.onc.1209378
77. Kim J, Lim H, Kim S, Cho H, Kim Y, Li X, Choi H, Kim O (2016) Effects of HSP27 downregulation on PDT resistance through PDT-induced autophagy in head and neck cancer cells. Oncol Rep 35(4):2237–2245. doi:10.3892/or.2016.4597
78. Chatr-Aryamontri A, Breitkreutz BJ, Heinicke S, Boucher L, Winter A, Stark C, Nixon J, Ramage L, Kolas N, O'Donnell L, Reguly T, Breitkreutz A, Sellam A, Chen D, Chang C, Rust J, Livstone M, Oughtred R, Dolinski K, Tyers M (2013) The BioGRID interaction database: 2013 update. Nucleic Acids Res 41 (Database issue):D816–D823. doi:10.1093/nar/gks1158
79. Hornbeck PV, Kornhauser JM, Tkachev S, Zhang B, Skrzypek E, Murray B, Latham V, Sullivan M (2012) PhosphoSitePlus: a comprehensive resource for investigating the structure and function of experimentally determined post-translational modifications in man and mouse. Nucleic Acids Res 40 (Database issue):D261–D270. doi:10.1093/nar/gkr1122
80. Kelder T, van Iersel MP, Hanspers K, Kutmon M, Conklin BR, Evelo CT, Pico AR (2012) WikiPathways: building research communities on biological pathways. Nucleic Acids Res 40 (Database issue):D1301–D1307. doi:10.1093/nar/gkr1074

Supplemental information

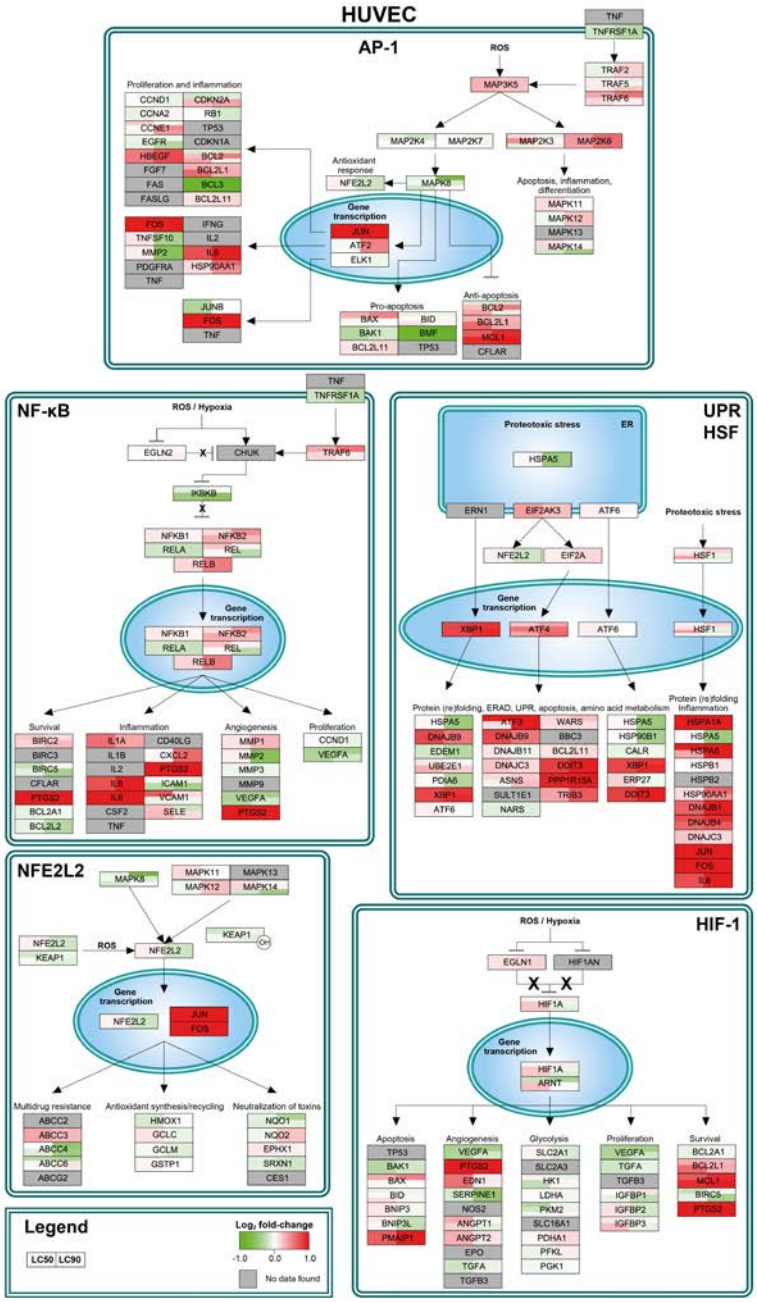

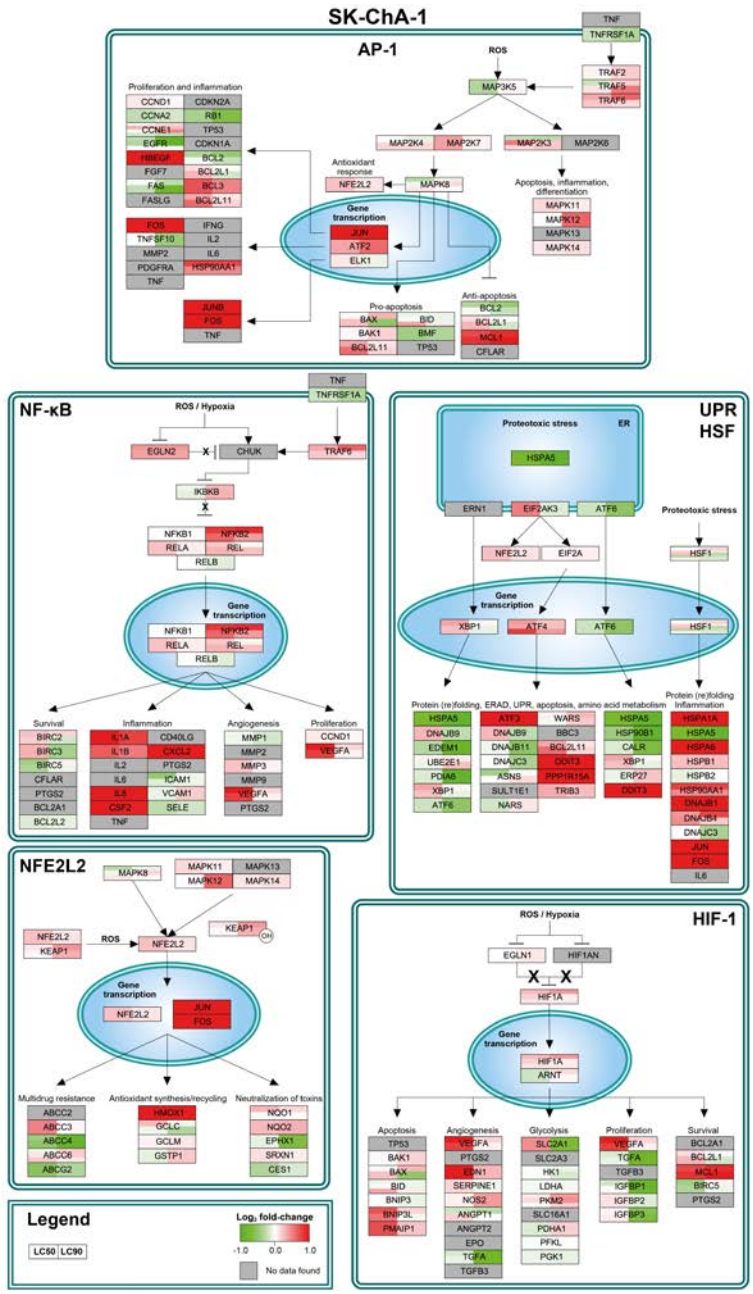
SK-ChA-1
AP-1
TNF
TNFRSF1A
ROS
TRAF2
TRAF5
TRAF6
MAP3K5
MAP2K4
MAP2K7
MAP2K3
MAP2K6
MAPK8
NFE2L2
Antioxidant response
Apoptosis, inflammation, differentiation
MAPK11
MAPK12
MAPK13
MAPK14
Proliferation and inflammation
CCND1
CDK2A
CCNA2
RB1
CCNE1
TP53
EGFR
CDKN1A
HBEGF
BCL2
FGF7
BCL2L1
FAS
BCL3
FASLG
BCL2L11
FOS
IFNG
TNFSF10
IL2
MMP2
IL6
PDGFRA
HSP90AA1
TNF
JUNB
FOS
TNF
Gene transcription
JUN
ATF2
ELK1
Pro-apoptosis
BAX
BID
BAK1
BMF
BCL2L11
TP53
Anti-apoptosis
BCL2
BCL2L1
MCL1
CFLAR
NF-κB
ROS / Hypoxia
TNF
TNFRSF1A
EGLN2
CHUK
TRAF6
IKBKB
NFKB1
NFKB2
RELA
REL
RELB
Gene transcription
Survival
BIRC2
BIRC3
BIRC5
CFLAR
PTGS2
BCL2A1
BCL2L2
Inflammation
IL1A
CD40LG
IL1B
CXCL2
IL2
PTGS2
IL6
ICAM1
IL8
VCAM1
CSF2
SELE
TNF
Angiogenesis
MMP1
MMP2
MMP3
MMP9
VEGFA
PTGS2
Proliferation
CCND1
VEGFA
UPR
HSF
Proteotoxic stress
ER
HSPA5
ERN1
EIF2AK3
ATF6
NFE2L2
EIF2A
HSF1
Gene transcription
XBP1
ATF4
ATF6
HSF1
Protein (re)folding, ERAD, UPR, apoptosis, amino acid metabolism
Protein (re)folding
Inflammation
HSPA5
DNAJB9
EDEM1
UBE2E1
PDIA6
XBP1
ATF6
ATF3
DNAJB9
DNAJB11
DNAJC3
ASNS
SULT1E1
NARS
WARS
BBC3
BCL2L11
DDIT3
PPP1R15A
TRIB3
HSPA5
HSP90B1
CALR
XBP1
ERP27
DDIT3
HSPA1A
HSPA5
HSPA6
HSPB1
HSPB2
HSP90AA1
DNAJB1
DNAJB4
DNAJC3
JUN
FOS
IL6
NFE2L2
MAPK8
MAPK11
MAPK12
MAPK13
MAPK14
NFE2L2
KEAP1
ROS
NFE2L2
KEAP1
OH
Gene transcription
NFE2L2
JUN
FOS
Multidrug resistance
ABCC2
ABCC3
ABCC4
ABCC6
ABCG2
Antioxidant synthesis/recycling
HMOX1
GCLC
GCLM
GSTP1
Neutralization of toxins
NQO1
NQO2
EPHX1
SRXN1
CES1
HIF-1
ROS / Hypoxia
EGLN1
HIF1AN
HIF1A
Gene transcription
HIF1A
ARNT
Apoptosis
TP53
BAK1
BAX
BID
BNIP3
BNIP3L
PMAIP1
Angiogenesis
VEGFA
PTGS2
EDN1
SERPINE1
NOS2
ANGPT1
ANGPT2
EPO
TGFA
TGFB3
Glycolysis
SLC2A1
SLC2A3
HK1
LDHA
PKM2
SLC16A1
PDHA1
PFKL
PGK1
Proliferation
VEGFA
TGFA
TGFB3
IGFBP1
IGFBP2
IGFBP3
Survival
BCL2A1
BCL2L1
MCL1
BIRC5
PTGS2
Legend
LC50 LC90
Log2 fold-change
-1.0 0.0 1.0
No data found

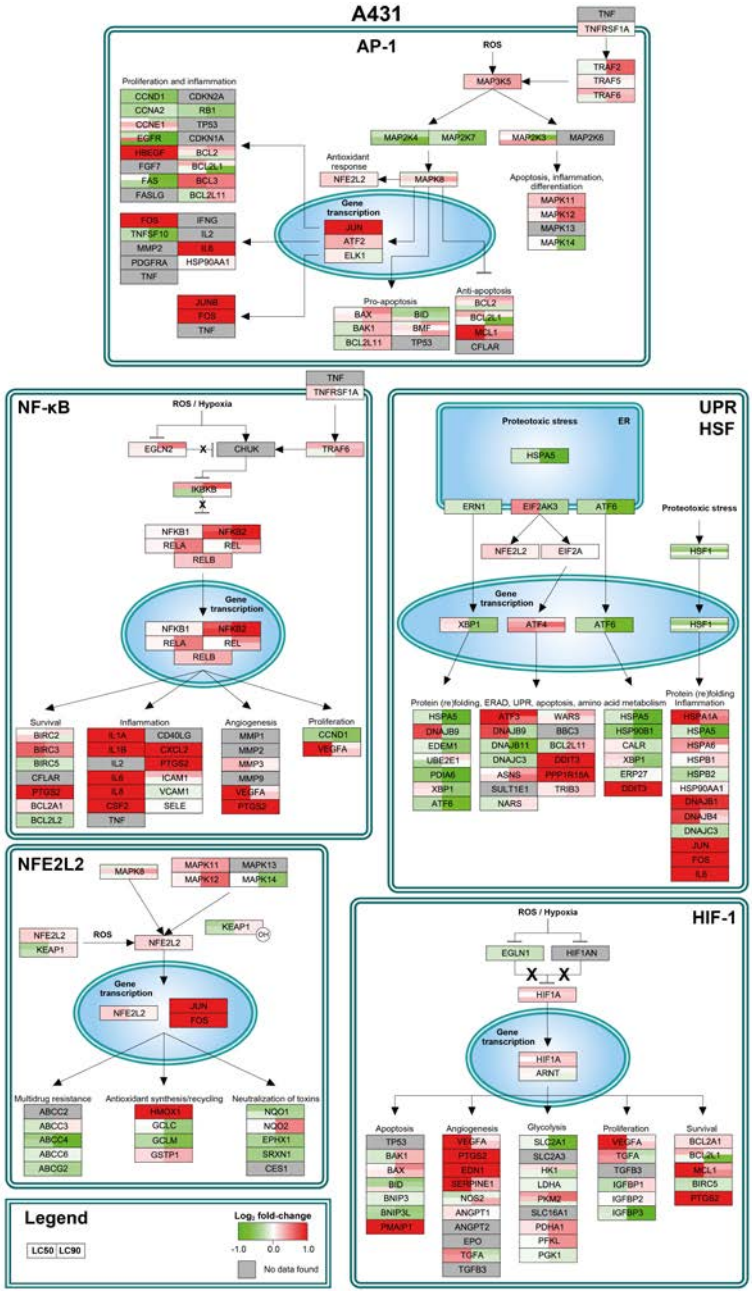
A431
AP-1
TNF
TNFRSF1A
ROS
MAP3K5
TRAF2
TRAF5
TRAF6
Proliferation and inflammation
CCND1
CDKN2A
CCNA2
RB1
CCNE1
TP53
EGFR
CDKN1A
HBEGF
BCL2
FGF7
BCL2L1
FAS
BCL3
FASLG
BCL2L11
FOS
IFNG
TNFSF10
IL2
MMP2
IL8
PDGFRA
HSP90AA1
TNF
JUNB
FOS
TNF
MAP2K4
MAP2K7
MAP2K3
MAP2K6
Antioxidant response
NFE2L2
MAPK8
Apoptosis, inflammation, differentiation
MAPK11
MAPK12
MAPK13
MAPK14
Gene transcription
JUN
ATF2
ELK1
Pro-apoptosis
BAX
BID
BAK1
BMF
BCL2L11
TP53
Anti-apoptosis
BCL2
BCL2L1
MCL1
CFLAR
NF-κB
TNF
TNFRSF1A
ROS / Hypoxia
EGLN2
CHUK
TRAF6
IKBKB
NFKB1
NFKB2
RELA
REL
RELB
Gene transcription
Survival
BIRC2
BIRC3
BIRC5
CFLAR
PTGS2
BCL2A1
BCL2L2
Inflammation
IL1A
CD40LG
IL1B
CXCL2
IL2
PTGS2
IL6
ICAM1
IL8
VCAM1
CSF2
SELE
TNF
Angiogenesis
MMP1
MMP2
MMP3
MMP9
VEGFA
PTGS2
Proliferation
CCND1
VEGFA
UPR
HSF
Proteotoxic stress
ER
HSPA5
ERN1
EIF2AK3
ATF6
Proteotoxic stress
NFE2L2
EIF2A
HSF1
Gene transcription
XBP1
ATF4
ATF6
HSF1
Protein (re)folding, ERAD, UPR, apoptosis, amino acid metabolism
HSPA5
DNAJB9
EDEM1
UBE2E1
PDIA6
XBP1
ATF6
ATF3
DNAJB9
DNAJB11
DNAJC3
ASNS
SULT1E1
NARS
WARS
BBC3
BCL2L11
DDIT3
PPP1R15A
TRIB3
HSPA5
HSP90B1
CALR
XBP1
ERP27
DDIT3
Protein (re)folding Inflammation
HSPA1A
HSPA5
HSPA6
HSPB1
HSPB2
HSP90AA1
DNAJB1
DNAJB4
DNAJC3
JUN
FOS
IL6
NFE2L2
MAPK8
MAPK11
MAPK12
MAPK13
MAPK14
NFE2L2
KEAP1
ROS
NFE2L2
KEAP1
Gene transcription
NFE2L2
JUN
FOS
Multidrug resistance
ABCC2
ABCC3
ABCC4
ABCC6
ABCG2
Antioxidant synthesis/recycling
HMOX1
GCLC
GCLM
GSTP1
Neutralization of toxins
NQO1
NQO2
EPHX1
SRXN1
CES1
HIF-1
ROS / Hypoxia
EGLN1
HIF1AN
HIF1A
Gene transcription
HIF1A
ARNT
Apoptosis
TP53
BAK1
BAX
BID
BNIP3
BNIP3L
PMAIP1
Angiogenesis
VEGFA
PTGS2
EDN1
SERPINE1
NOS2
ANGPT1
ANGPT2
EPO
TGFA
TGFB3
Glycolysis
SLC2A1
SLC2A3
HK1
LDHA
PKM2
SLC16A1
PDHA1
PFKL
PGK1
Proliferation
VEGFA
TGFA
TGFB3
IGFBP1
IGFBP2
IGFBP3
Survival
BCL2A1
BCL2L1
MCL1
BIRC5
PTGS2
Legend
LC50 LC90
Log2 fold-change
-1.0 0.0 1.0
No data found

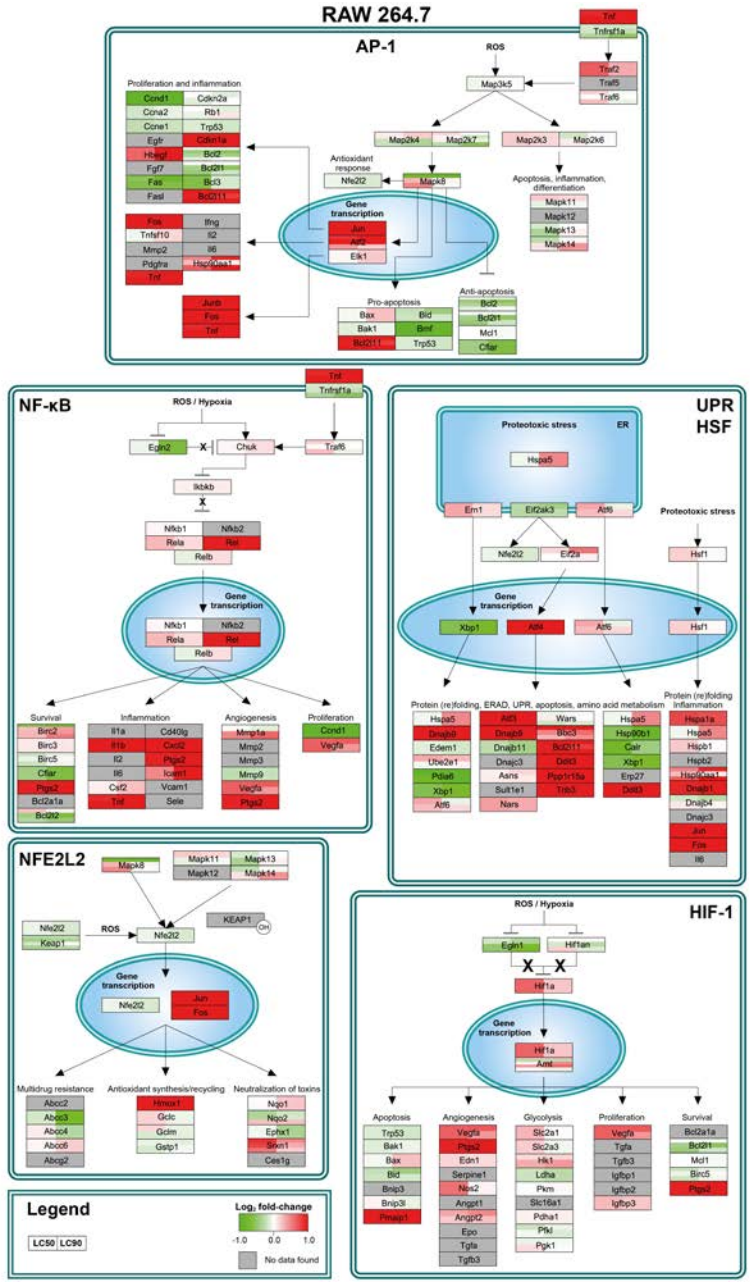

Fig. S1. Cell type-dependent PDT-induced survival signaling. Transcriptomic response of HUVEC, RAW 264.7, SK-ChA-1, and A431 cells following ZPCL-PDT at the LC_{50} and LC_{90} concentrations. Gene expression data were mapped onto AP-1- (top), NF-κB- (middle left), UPR- (middle right), NFE2L2- (bottom left), and HIF-1α-mediated pathways (bottom right), irrespective of *P*-value. The color and intensity of the box indicates the direction and extent of the log_2 fold-change (versus the control group) for the indicated gene, respectively (legend lower left). Grey boxes signify probes that exhibited poor quality or were not included in the gene expression analysis. Each gene box, which may comprise multiple probes as indicated by horizontal splits, is vertically divided in two halves corresponding to the LC_{50} and LC_{90} groups (legend lower left). Abbreviations: ER, endoplasmic reticulum; ERAD, ER-associated degradation.

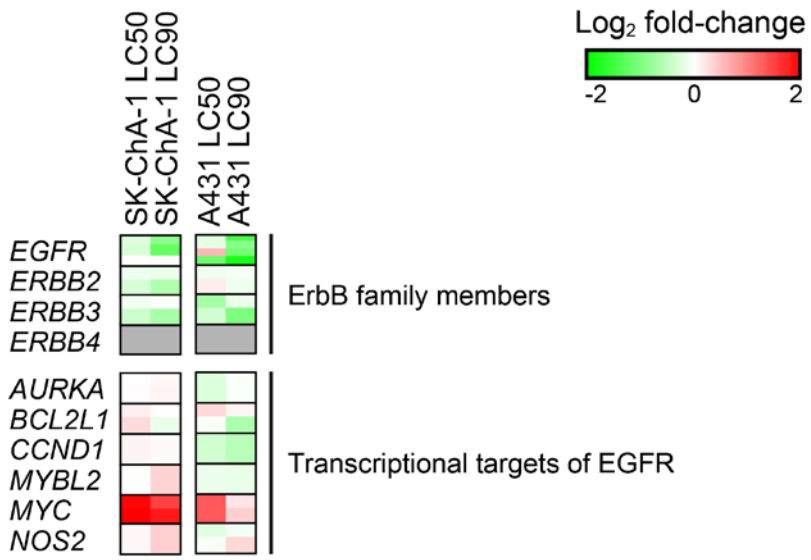

Fig. S2. Analysis of EGFR signaling after ZPCL-PDT. Gene expression is depicted as the $\log_2$ fold-change (upper right corner) between the PDT-treated groups versus the control group (n = 3 per group). A gene may consist of multiple probes as indicated by horizontal splits. Grey boxes signify probes that exhibited poor quality or were not included in the gene expression analysis.

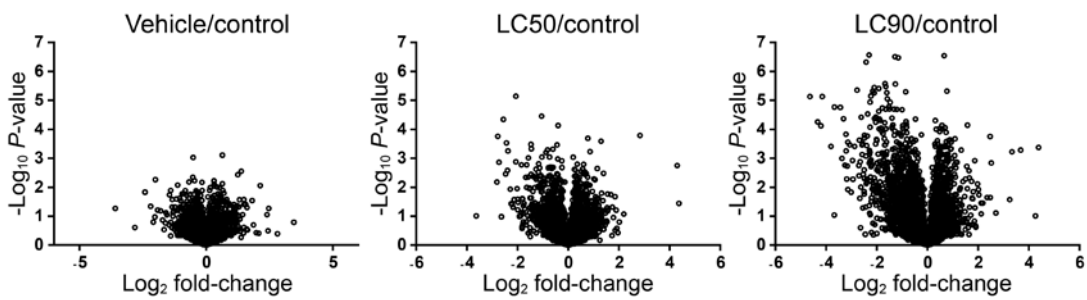

Fig. S3. Differentially expressed proteins as visualized by volcano plots. The group comparisons show $\log_2$ fold-changes of proteins and corresponding P-values observed in SK-ChA-1 cells in response to ZPCL-PDT.

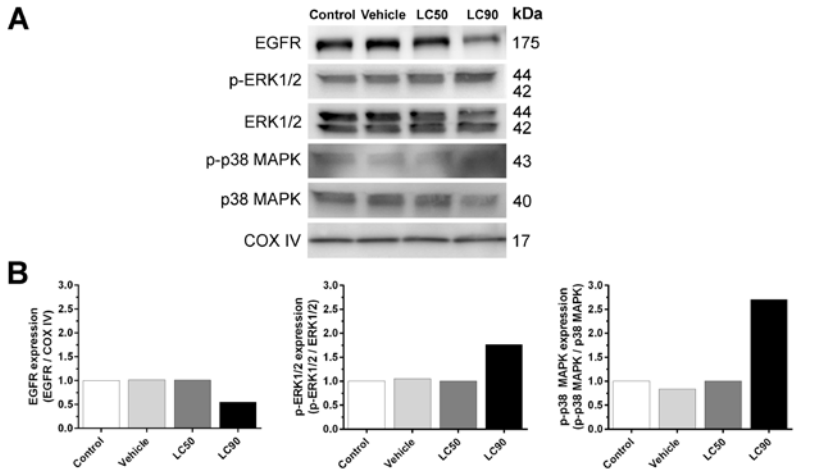

Fig. S4. Western Blot analysis of SK-ChA-1 cells after ZPCL-PDT. (**A**) Western Blot analysis of a panel of proteins that were differentially expressed after (phospho)proteomics. Western Blot analysis revealed similar trends for EGFR and p-p38 MAPK as obtained by (phospho)proteomics. While p-ERK1 (MAPK3) was detected by Western Blot, SK-ChA-1 cells did not reveal any detectable p-ERK2 (MAPK1) levels. (**B**) Protein bands were quantified using ImageJ software and normalized to total protein (COX IV for EGFR, and total ERK and total p38 MAPK for their corresponding phosphorylated forms).

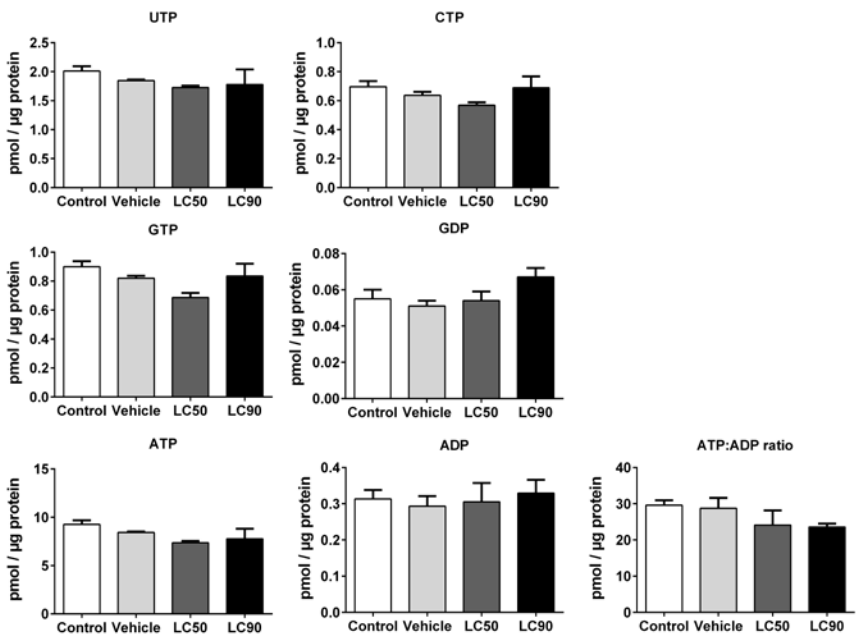

Fig. S5. Nucleotide analysis of SK-ChA-1 cells after ZPCL-PDT. Nucleotides were quantified using HPLC and depicted as pmol / µg protein (n = 3 per group).

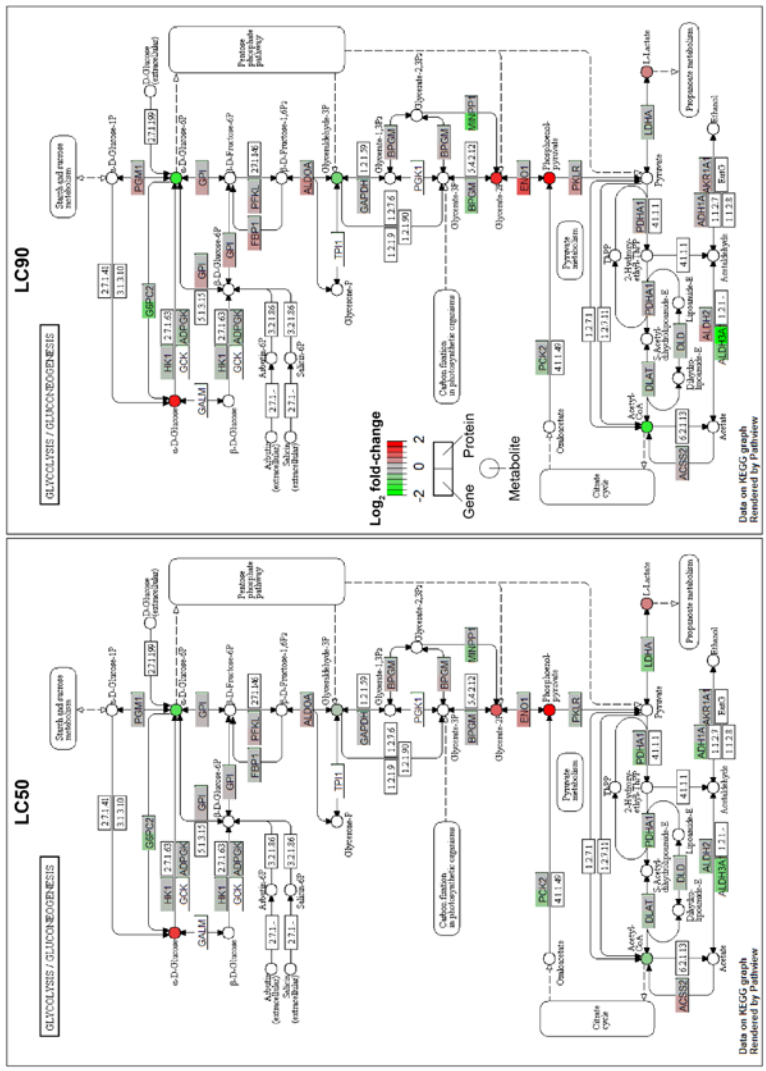

A

Fig. S6. Integration of transcriptomics, proteomics, and metabolomics data of SK-ChA-1 cells after ZPCL-PDT. Data was integrated for (**A**) the glycolysis/gluconeogenesis pathway, (**B**) tricarboxylic acid (TCA) cycle, and (**C**) the pentose phosphate pathway. Metabolites are indicated in circles and genes (left half of the square) and proteins (right half of the square) are indicated in squares. The left part of each pathway corresponds to the LC_{50} group, whereas the right part of each pathway corresponds to the LC_{90} group. Expression is depicted as the log_2 fold-change between the treated groups versus the control group, where green and red represent down- and upregulation, respectively.

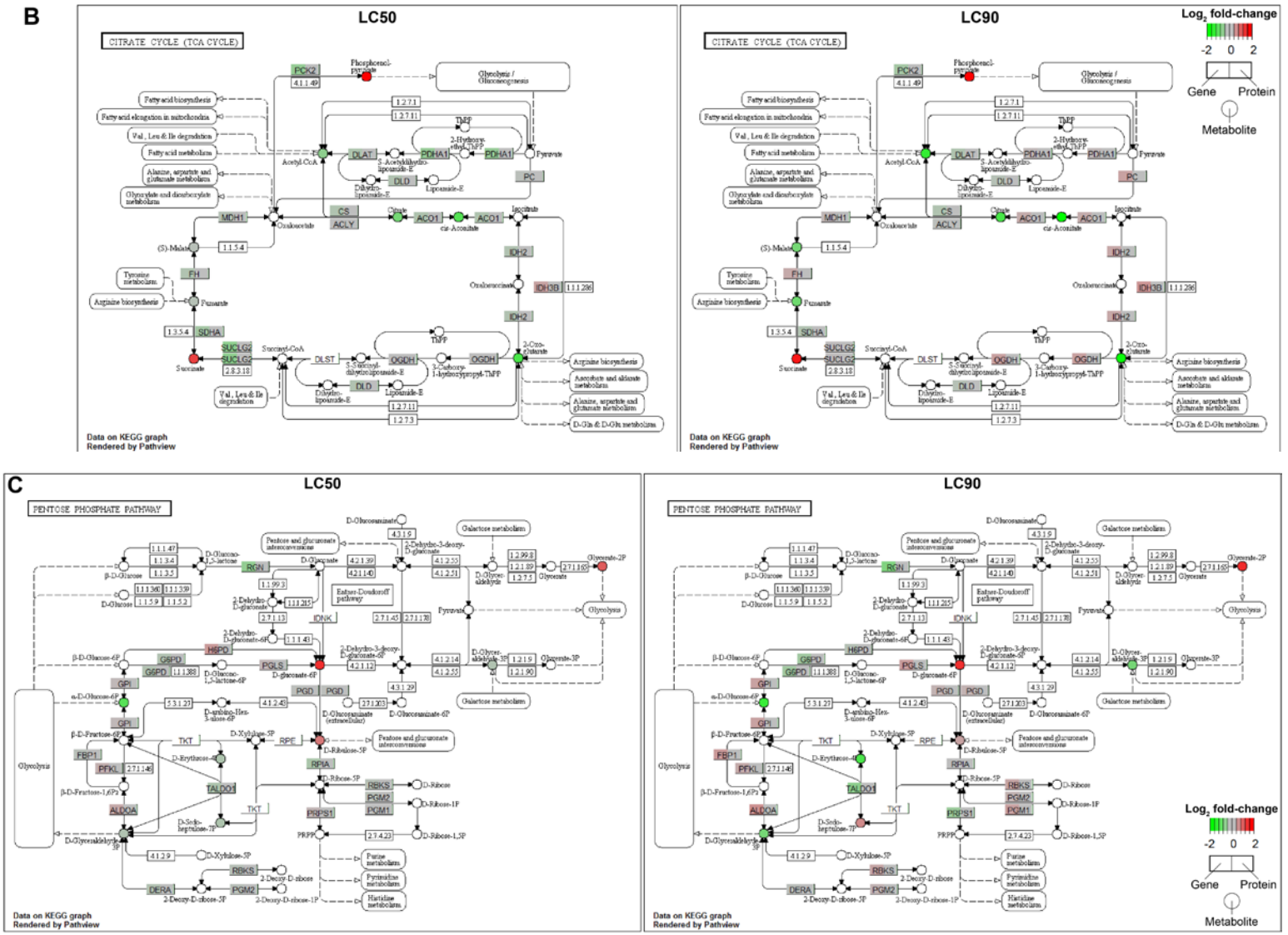
B
LC50
LC90
CITRATE CYCLE (TCA CYCLE)
Log2 fold-change
-2 0 2
Gene
Protein
Metabolite
Data on KEGG graph
Rendered by Pathview
C
LC50
LC90
PENTOSE PHOSPHATE PATHWAY
Log2 fold-change
-2 0 2
Gene
Protein
Metabolite
Data on KEGG graph
Rendered by Pathview

4

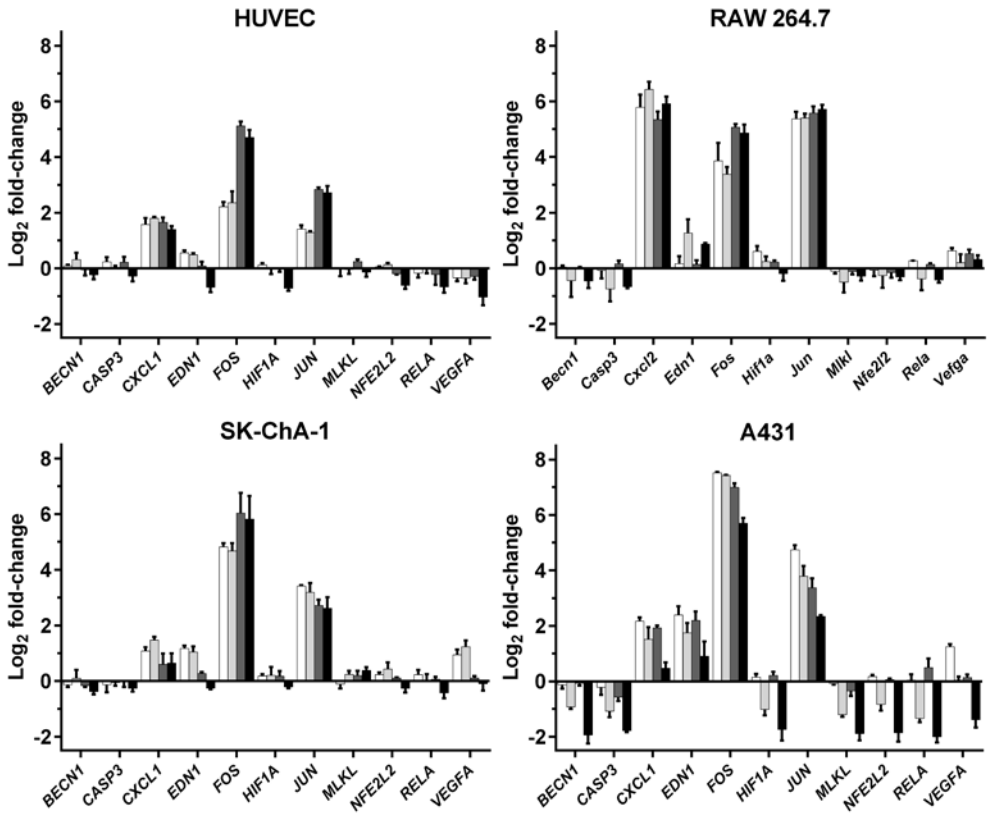

Fig. S7. Microarray validation by qRT-PCR. The expression levels of a panel of genes for both the LC_{50} (white bars) and LC_{90} group (dark grey bars bars) as assessed by microarray were validated by qRT-PCR. The corresponding qRT-PCR data are depicted for the LC_{50} group in light grey and the LC_{90} group in black. Gene expression is depicted as the $\log_2$ fold-change between PDT-treated and control cells. qRT-PCR data were normalized to the expression level of the reference gene RPS18.

	Control	Vehicle	LC50	LC90
HUVEC	Buffer	10	10	50
RAW 264.7	Buffer	30	30	75
SK-ChA-1	Buffer	25	25	80
A431	Buffer	65	65	250

Table S1. The concentrations of ZPCLs that were used for the different cell types. Concentrations indicate μM ZPCLs (final lipid concentration) and were calculated based on previously obtained cell viability data 4 hours post-PDT as measured by the WST-1 method. Cells in the vehicle group were incubated with ZPCLs, but were not irradiated.

Table S2 can be accessed at https://static-content.springer.com/esm/art%3A10.1007%2Fs00018-016-2401-0/MediaObjects/18_2016_2401_MOESM3_ESM.xlsx.

Species	Gene	Forward primer	Reverse primer	Amplicon size (bp)
Human	*BECN1*	ATCTGCGAGAGACACCATCC	TGTCACCATCCAGGAACTCA	137
Human	*CASP3*	TGGTTTGAGCCTGAGCAGAG	TGGCAGCATCATCCACACAT	122
Human	*CXCL1*	AGGGAATTCACCCCAAGAAC	ACTATGGGGGATGCAGGATT	130
Human	*EDN1*	GGGCTGAAGGATCGCTTTGA	GCGCCTAAGACTGCTGTTTC	199
Human	*FOS*	GTGACCGTGGGAATGAAGTT	CCGGGGATAGCCTCTCTTAC	127
Human	*HIF1A*	GCGCGAACGACAAGAAAAAGA	CCAGAAGTTTCCTCACACGC	204
Human	*JUN*	GTCCTTCTTCTCTTGCGTGG	GGAGACAAGTGGCAGAGTCC	115
Human	*MLKL*	TACGCAGGATGTTGGGAGAT	AGAGCTCCAGTGGCCATAAA	124
Human	*NFE2L2*	GCTCATACTCTTTCCGTCGC	ATCATGATGGACTTGGAGCTG	145
Human	*RELA*	TCCGCGGGCAGCATCCC	CCATCCCGGCAGTCCTTTCCTAC	170
Human / Mouse	*RPS18*	TTCGGAACTGAGGCCATGAT	CGAACCTCCGACTTTCGTTCT	151
Human	*VEGFA*	CCACACCATCACCATCGACA	CTAATCTTCCGGGCTCGGTG	204
Mouse	*Becn1*	CATCCTGGCGAGTTTCAATAA	TCACCATCCAGGAACTCACA	117
Mouse	*Casp3*	TGAATCCACTGAGGTTTTGTTG	TGCTGGTGGGATCAAAGC	93
Mouse	*Cxcl2*	GTGCCATCAGAGCAGTCTGT	GCACCCAAACCGAAGTCATA	148
Mouse	*Edn1*	ACTCCATTCTCAGCTCCGGT	TCCCGTGATCTTCTCTCTGC	96
Mouse	*Fos*	ACGGAGGAGACCAGAGTGG	ATGGGCTCTCCTGTCAACAC	137
Mouse	*Hif1a*	TGACGGCGACATGGTTTACA	AATATGGCCCGTGCAGTGAA	280
Mouse	*Jun*	TGAAAGCTGTGTCCCCTGTC	ATCACAGCACATGCCACTTC	220
Mouse	*Mlkl*	AGGAACCAGTGGGTCAGGAT	CAAGATTCCGTCCACAGAGGG	101
Mouse	*Nfe2l2*	TCTATGTCTTGCCTCCAAAGG	CTCAGCATGATGGACTTGGA	92
Mouse	*Rela*	GAACCTGGGGATCCAGTGTG	AGTTCCGGTTTACTCGGCAG	266
Mouse	*Vegfa*	GGAGATCCTTCGAGGAGCACTT	GGCGATTTAGCAGCAGATATAAGAA	130

Table S3. Overview of primers that were used for qRT-PCR.

HUVEC

LC50 vs CTRL

Pathway	NGenes	PropDown	PropUp	Direction	PValue	FDR	PValue.Mixed	FDR.Mixed
HIF1	30	0.10	0.37	Up	1.00E-04	7.50E-05	1.00E-04	7.50E-05
UPR	23	0.04	0.30	Up	1.00E-04	7.50E-05	1.00E-04	7.50E-05
NF-κB	17	0.06	0.29	Up	1.00E-04	7.50E-05	1.00E-04	7.50E-05
HSF	11	0.00	0.64	Up	1.00E-04	7.50E-05	1.00E-04	7.50E-05
AP-1	17	0.12	0.24	Up	0.0037	0.00438	4.00E-04	0.00042
NFE2L2	11	0.00	0.09	Up	0.9373	0.93725	0.718	0.71795

LC90 vs CTRL

Pathway	NGenes	PropDown	PropUp	Direction	PValue	FDR	PValue.Mixed	FDR.Mixed
UPR	23	0.26	0.30	Up	1.00E-04	1.00E-04	1.00E-04	6.00E-05
NF-κB	17	0.24	0.41	Up	1.00E-04	1.00E-04	1.00E-04	6.00E-05
HSF	11	0.09	0.82	Up	1.00E-04	1.00E-04	1.00E-04	6.00E-05
HIF1	30	0.13	0.23	Up	0.001	0.001425	1.00E-04	6.00E-05
AP-1	17	0.18	0.35	Up	0.0025	0.00294	1.00E-04	6.00E-05
NFE2L2	11	0.18	0.09	Down	0.2058	0.20575	0.0239	0.02385

LC90 vs LC50

Pathway	NGenes	PropDown	PropUp	Direction	PValue	FDR	PValue.Mixed	FDR.Mixed
HSF	11	0.09	0.64	Up	1.00E-04	3.00E-04	1.00E-04	1.00E-04
HIF1	30	0.27	0.10	Down	0.1141	0.259575	2.00E-04	0.000225
AP-1	17	0.24	0.35	Up	0.1561	0.259575	1.00E-04	1.00E-04
NFE2L2	11	0.18	0.09	Down	0.1731	0.259575	0.0269	0.02685
NF-κB	17	0.24	0.29	Up	0.6789	0.81462	3.00E-04	3.00E-04
UPR	23	0.22	0.22	Up	0.8639	0.86385	1.00E-04	1.00E-04

RAW 264.7

LC50 vs CTRL

Pathway	NGenes	PropDown	PropUp	Direction	PValue	FDR	PValue.Mixed	FDR.Mixed
UPR	21	0.29	0.43	Up	1.00E-04	1.00E-04	1.00E-04	6.00E-05
NF-κB	15	0.27	0.53	Up	1.00E-04	1.00E-04	1.00E-04	6.00E-05
HSF	8	0.00	0.63	Up	1.00E-04	1.00E-04	1.00E-04	6.00E-05
HIF1	23	0.13	0.35	Up	0.0013	0.001875	1.00E-04	6.00E-05
NFE2L2	11	0.09	0.27	Up	0.007	0.00834	0.0031	0.00305
AP-1	19	0.32	0.42	Up	0.0095	0.00945	1.00E-04	6.00E-05

LC90 vs CTRL

Pathway	NGenes	PropDown	PropUp	Direction	PValue	FDR	PValue.Mixed	FDR.Mixed
UPR	21	0.33	0.52	Up	1.00E-04	7.50E-05	1.00E-04	7.50E-05
AP-1	19	0.32	0.42	Up	1.00E-04	7.50E-05	1.00E-04	7.50E-05
NF-κB	15	0.20	0.60	Up	1.00E-04	7.50E-05	1.00E-04	7.50E-05
HSF	8	0.00	0.75	Up	1.00E-04	7.50E-05	1.00E-04	7.50E-05
HIF1	23	0.17	0.26	Up	0.0138	0.0165	2.00E-04	0.00018
NFE2L2	11	0.18	0.18	Up	0.7325	0.73245	8.00E-04	0.00075

LC90 vs LC50

Pathway	NGenes	PropDown	PropUp	Direction	PValue	FDR	PValue.Mixed	FDR.Mixed
AP-1	19	0.11	0.42	Up	0.003	0.01695	1.00E-04	3.00E-04
NF-κB	15	0.13	0.33	Up	0.0057	0.01695	0.004	0.0079
HSF	8	0.00	0.50	Up	0.0103	0.0205	0.0059	0.008775
NFE2L2	11	0.36	0.00	Down	0.0378	0.056625	0.0233	0.0279
UPR	21	0.14	0.29	Up	0.2092	0.25098	0.0025	0.00735
HIF1	23	0.13	0.09	Down	0.3754	0.37535	0.0446	0.04455

SK-ChA-1

LC50 vs CTRL

Pathway	NGenes	PropDown	PropUp	Direction	PValue	FDR	PValue.Mixed	FDR.Mixed
HIF1	25	0.08	0.32	Up	1.00E-04	7.50E-05	1.00E-04	6.00E-05
NF-κB	16	0.19	0.38	Up	1.00E-04	7.50E-05	1.00E-04	6.00E-05
AP-1	15	0.33	0.47	Up	1.00E-04	7.50E-05	1.00E-04	6.00E-05
HSF	10	0.10	0.80	Up	1.00E-04	7.50E-05	1.00E-04	6.00E-05
UPR	23	0.30	0.35	Up	0.1493	0.1791	1.00E-04	6.00E-05
NFE2L2	13	0.23	0.31	Up	0.3278	0.32775	3.00E-04	0.00025

LC90 vs CTRL

Pathway	NGenes	PropDown	PropUp	Direction	PValue	FDR	PValue.Mixed	FDR.Mixed
AP-1	15	0.33	0.40	Up	1.00E-04	0.00015	1.00E-04	6.00E-05
HSF	10	0.20	0.80	Up	1.00E-04	0.00015	1.00E-04	6.00E-05
NF-κB	16	0.06	0.31	Up	8.00E-04	0.0015	2.00E-04	0.00015
UPR	23	0.48	0.35	Down	0.0016	0.002325	1.00E-04	6.00E-05
HIF1	25	0.16	0.20	Down	0.5088	0.6105	1.00E-04	6.00E-05
NFE2L2	13	0.23	0.23	Down	0.9279	0.92785	1.00E-04	6.00E-05

LC90 vs LC50

Pathway	NGenes	PropDown	PropUp	Direction	PValue	FDR	PValue.Mixed	FDR.Mixed
HIF1	25	0.32	0.08	Down	1.00E-04	0.00015	1.00E-04	6.00E-05
UPR	23	0.70	0.26	Down	1.00E-04	0.00015	1.00E-04	6.00E-05
AP-1	15	0.60	0.13	Down	3.00E-04	5.00E-04	1.00E-04	6.00E-05
NF-κB	16	0.31	0.06	Down	0.0041	0.006075	0.0012	0.00115
NFE2L2	13	0.31	0.15	Down	0.077	0.09234	1.00E-04	6.00E-05
HSF	10	0.40	0.30	Down	0.219	0.21895	1.00E-04	6.00E-05

A431

LC50 vs CTRL

Pathway	NGenes	PropDown	PropUp	Direction	PValue	FDR	PValue.Mixed	FDR.Mixed
HIF1	28	0.00	0.36	Up	1.00E-04	7.50E-05	1.00E-04	5.00E-05
NF-κB	18	0.11	0.50	Up	1.00E-04	7.50E-05	1.00E-04	5.00E-05
AP-1	16	0.25	0.38	Up	1.00E-04	7.50E-05	1.00E-04	5.00E-05
HSF	11	0.00	0.55	Up	1.00E-04	7.50E-05	1.00E-04	5.00E-05
UPR	23	0.30	0.22	Up	3.00E-04	3.00E-04	1.00E-04	5.00E-05
NFE2L2	12	0.50	0.08	Down	0.0217	0.02165	1.00E-04	5.00E-05

LC90 vs CTRL

Pathway	NGenes	PropDown	PropUp	Direction	PValue	FDR	PValue.Mixed	FDR.Mixed
NF-κB	18	0.17	0.50	Up	1.00E-04	1.00E-04	1.00E-04	5.00E-05
AP-1	16	0.38	0.44	Up	1.00E-04	1.00E-04	1.00E-04	5.00E-05
HSF	11	0.18	0.64	Up	1.00E-04	1.00E-04	1.00E-04	5.00E-05
HIF1	28	0.21	0.39	Up	0.0021	0.003075	1.00E-04	5.00E-05
NFE2L2	12	0.50	0.25	Down	0.0041	0.00486	1.00E-04	5.00E-05
UPR	23	0.48	0.30	Down	0.0098	0.00975	1.00E-04	5.00E-05

LC90 vs LC50

Pathway	NGenes	PropDown	PropUp	Direction	PValue	FDR	PValue.Mixed	FDR.Mixed
HIF1	28	0.32	0.18	Down	1.00E-04	1.00E-04	1.00E-04	6.00E-05
UPR	23	0.61	0.22	Down	1.00E-04	1.00E-04	1.00E-04	6.00E-05
HSF	11	0.55	0.27	Down	1.00E-04	1.00E-04	1.00E-04	6.00E-05
AP-1	16	0.50	0.19	Down	0.0019	0.002775	1.00E-04	6.00E-05
NF-κB	18	0.33	0.11	Down	0.0053	0.0063	1.00E-04	6.00E-05
NFE2L2	12	0.25	0.25	Down	0.02	0.01995	4.00E-04	0.00035

Table S4. A ROAST gene set test was performed to determine whether a survival pathway was either up- (in red) or downregulated (in green). Pathways with a FDR < 0.05 are indicated in bold. Ngenes, number of genes in pathway; PropDown, proportion of genes in set with z-score < -sqrt(2); PropUp, proportion of genes in set with z-score > sqrt(2); Direction, direction of change, "'Up'" or "'Down'"; Pvalue, two-sided directional P-value; FDR: two-sided directional false discovery rate; PValue.Mixed, non-directional P-value; FDR.Mixed, non-directional false discovery rate.

Table S5 can be accessed at https://static-content.springer.com/esm/art%3A10.1007%2Fs00018-016-2401-0/MediaObjects/18_2016_2401_MOESM6_ESM.xlsx.

		Log2 fold-change (treatment / control)		
	Metabolite	**Vehicle**	**LC50**	**LC90**
Amino acid metabolism	Phenylalanine	0.108	1.082	1.338
	Leucine	0.117	1.035	1.387
	Isoleucine	0.138	1.168	1.455
	Methionine	0.125	1.112	1.405
	Valine	0.118	1.140	1.417
	Tryptophan	0.098	1.110	1.358
	Proline	0.115	0.534	0.566
	Tyrosine	0.121	0.994	1.235
	Threonine	0.206	1.192	1.556
	Alanine	0.188	0.602	0.577
	Asparagine	0.099	0.603	0.913
	Glutamine	0.046	0.532	0.789
	Glutamate	0.002	-0.333	-0.451
	Glycine	-0.005	0.243	0.248
	Aspartate	0.014	0.428	0.030
	Serine	0.040	0.756	1.082
	Histidine	0.127	0.975	1.184
	Lysine	0.207	1.893	2.167
	Arginine	0.130	1.392	1.635
	Creatinine	0.164	1.297	1.520
	Creatine	0.151	-0.483	-0.656
	N-Acetyl-glutamate	0.061	-0.860	-1.712
	Citrulline	0.089	-0.363	-0.464
	Ornithine	0.323	1.713	1.926
	Ophtalmic acid	0.127	-1.550	-2.228
	Glutathione	-0.084	-0.871	-1.332
	Glutathione disulfide	0.356	-0.073	-1.069
	Betaine	0.093	0.324	0.560
	Homocysteine	0.009	1.033	1.321
	S-Adenosylhomocysteine	0.078	-1.404	-1.364
	Cystine	0.224	1.767	2.143
	S-Adenosylmethionine	-0.072	-0.098	-0.841
	Choline	0.229	0.776	1.018
Carbohydrate metabolism	Lactate	0.256	0.895	0.868
	Glucose	0.097	1.487	1.787
	Hexose-phosphate	0.061	-1.419	-1.992
	Dihydroxyacetone phosphate	0.088	-0.052	-0.667
	Glyceraldehyde-3-phosphate	0.063	-1.908	-2.229
	Glucose-6-phosphate	0.289	-0.699	-0.858

	2/3-Phosphoglycerate	-0.070	0.961	1.467
	Phosphoenolpyruvate	0.213	2.864	4.009
	Acetyl-CoA	0.244	-0.260	-1.210
	Citrate/Isocitrate	0.002	-0.773	-1.241
	cis-Aconitate	-0.128	-1.234	-2.174
	2-Ketoglutarate	0.053	-1.170	-1.857
	Succinate	0.026	1.335	1.784
	Malate	0.023	-0.044	-0.745
	Fumarate	0.030	-0.059	-0.805
	Erythrose-4-phosphate	0.328	0.155	-0.875
	Pentose-phosphate	0.356	1.084	0.644
	Sedoheptulose-7-phospate	0.008	-0.167	0.548
	6-phosphogluconate	0.267	1.795	1.766
	N-Acetyl-glucosamine-6-phosphate	0.116	-0.087	-0.509
	UDP-N-Acetyl-glucosamine	0.024	-0.380	-1.247
Nucleotide metabolism	Adenosine	0.096	3.541	4.701
	Adenine	0.161	2.483	2.145
	Hypoxanthine	0.096	2.341	2.596
	Inosine	-0.052	2.647	3.741
	Guanine	0.530	4.262	3.933
	AMP	0.123	1.829	4.009
	IMP	0.000	8.474	10.393
	GMP	-4.867	3.885	5.743
	Uracil	-0.057	1.006	1.299
	Orotate	0.194	-3.479	-3.829
	Uridine	0.000	8.386	9.368
	UMP	0.101	1.484	2.973
Energy Metabolism	NADH	-0.052	-0.350	-0.660
	NAD+	0.016	-0.544	-1.103
	NADP+	0.121	0.659	0.647
	NADPH	0.116	-0.223	-0.626
Cofactors and vitamins	Nicotinamide	0.179	1.449	1.474
	Methylnicotinamide	0.059	-0.811	-1.572

Table S6. Overview of log_2 fold-changes in metabolite levels after ZPCL-PDT of SK-ChA-1 cells.

Chapter 5

Inhibition of hypoxia inducible factor 1 and topoisomerase with acriflavine sensitizes perihilar cholangiocarcinomas to photodynamic therapy

Oncotarget (2015)

RUUD WEIJER*
MANS BROEKGAARDEN*
MASSIS KREKORIAN
LINDY K. ALLES
ALBERT C. VAN WIJK
CLAIRE MACKAAIJ
JOANNE VERHEIJ
ALLARD C. VAN DER WAL
THOMAS M. VAN GULIK
GERT STORM
MICHAL HEGER

*authors contributed equally

Abstract

Photodynamic therapy (PDT) induces tumor cell death by oxidative stress and hypoxia but also survival signaling through activation of hypoxia-inducible factor 1 (HIF-1). Since perihilar cholangiocarcinomas are relatively recalcitrant to PDT, the aims were to (1) determine the expression levels of HIF-1-associated proteins in human perihilar cholangiocarcinomas, (2) investigate the role of HIF-1 in PDT-treated human perihilar cholangiocarcinoma cells, and (3) determine whether HIF-1 inhibition reduces survival signaling and enhances PDT efficacy.

Increased expression of VEGF, CD105, CD31/Ki-67, and GLUT-1 was confirmed in human perihilar cholangiocarcinomas. PDT with liposome-delivered zinc phthalocyanine caused HIF-1α stabilization in SK-ChA-1 cells and increased transcription of HIF-1α downstream genes. Acriflavine was taken up by SK-ChA-1 cells and translocated to the nucleus under hypoxic conditions. Importantly, pretreatment of SK-ChA-1 cells with acriflavine enhanced PDT efficacy via inhibition of HIF-1 and topoisomerases I and II.

The expression of VEGF, CD105, CD31/Ki-67, and GLUT-1 was determined by immunohistochemistry in human perihilar cholangiocarcinomas. In addition, the response of human perihilar cholangiocarcinoma (SK-ChA-1) cells to PDT with liposome-delivered zinc phthalocyanine was investigated under both normoxic and hypoxic conditions. Acriflavine, a HIF-1α/HIF-1β dimerization inhibitor and a potential dual topoisomerase I/II inhibitor, was evaluated for its adjuvant effect on PDT efficacy.

HIF-1, which is activated in human hilar cholangiocarcinomas, contributes to tumor cell survival following PDT *in vitro*. Combining PDT with acriflavine pretreatment improves PDT efficacy in cultured cells and therefore warrants further preclinical validation for therapy-recalcitrant perihilar cholangiocarcinomas.

Keywords

Cancer therapy, drug delivery system, extrahepatic cholangiocarcinoma, hypoxia, tumor targeting

Introduction

Photodynamic therapy (PDT) is a non-to-minimally invasive treatment modality for a variety of solid cancers. This therapy is based on the accumulation of a light-sensitive drug (photosensitizer) in the tumor following systemic administration. Next, the photosensitizer-replete tumor is locally irradiated with (laser) light, resulting in the activation of the photosensitizer and subsequent production of reactive oxygen species (ROS) via type I (superoxide) and/or type II (singlet oxygen) photochemical reactions. Consequently, PDT locally induces a state of hyperoxidative stress, culminating in tumor cell death, destruction of the microvasculature that causes tumor hypoxia and hyponutrition, and an anti-tumor immune response [1, 2].

PDT is effective in the curative treatment of (pre-)malignant skin lesions (actinic keratosis, basal/squamous cell carcinoma) [3], but is also employed as (last-line) treatment of head and neck cancer [4], early central stage lung tumors [5], esophageal cancer [6], nasopharyngeal carcinomas [7], bladder cancer [8], and non-resectable perihilar cholangiocarcinomas [9]. Although PDT yields complete response rates of 50–90% in the majority of the abovementioned cancers, nasopharyngeal-, urothelial-, and perihilar cholangiocarcinomas are relatively refractory to PDT. This may be in part due to hypoxia-mediated survival signaling that is triggered by the stabilization of hypoxia inducible factor 1 (HIF-1) following PDT [10–12]. In nasopharyngeal and superficial urothelial carcinomas, the overexpression of HIF-1α has been associated with poor overall survival [13, 14]. HIF-1 expression levels in perihilar cholangiocarcinomas are currently elusive but may account for the recalcitrance of these tumors to therapy [15].

HIF-1 is a transcription factor composed of HIF-1α and HIF-1β subunits. During normoxia, prolyl-hydroxylases (PHD) and factor inhibiting HIF (FIH) mediate the hydroxylation of Pro402, Pro564, and/or Asn803 of HIF-1α [16]. In turn, Von Hippel-Lindau tumor suppressor protein (VHL) binds to hydroxylated HIF-1α, resulting in complexation with E3 ubiquitin ligase and subsequent proteasomal degradation of HIF-1α [17, 18]. In contrast, hypoxia inhibits the activity of both PHDs and FIH, leading to HIF-1α stabilization and nuclear translocation [19]. After translocation to the nucleus, HIF-1α dimerizes with HIF-1β and mediates the transcription of various genes [20] that are involved in glycolysis, angiogenesis, survival, and apoptosis [21–23]. Alternatively, HIF-1 may be activated through ROS, which also deter the activity of PHDs and FIH, leading to the stabilization and nuclear translocation of HIF-1α [24, 25].

HIF-1 is constitutively active in most tumors since the tumor growth rate exceeds the rate of neoangiogenesis [21, 23]. Moreover, HIF-1 is responsible for resistance to chemotherapy and radiotherapy [26, 27]. PDT increases HIF-1 activity in mouse mammary carcinoma (EMT-6) cells [28] and human bladder cancer (UROtsa, RT112, and J84 but not RT4) cells [29] as well as in murine Kaposi's sarcoma- [30], BA mouse

mammary carcinoma- [31, 32], and CNE2 nasopharyngeal carcinoma xenografts [33]. Inhibition of HIF-1 activity and corollary survival signaling may consequently improve the therapeutic efficacy of PDT.

This study therefore investigated the therapeutic potential of the HIF-1 dimerization inhibitor acriflavine (ACF) in an *in vitro* PDT setting for the treatment of human perihilar cholangiocarcinoma (SK-ChA-1) cells [34], *i.e.*, a cell line derived from a type of cancer that is recalcitrant to different types of treatment. The photosensitizer used in this study was zinc phthalocyanine (ZnPC), a second-generation photosensitizer that was encapsulated in cationic liposomes designed to target tumor cells and tumor endothelium [35, 36]. ACF was selected due to its selective inhibition of HIF-1 activation [37] and due to its clinical safety [38]. In a recent study, it was shown that ACF downregulates the HIF-1 target gene vascular endothelial growth factor (*VEGF*) and reduces the amount of tumor microvessels in murine breast carcinoma (4T1)-bearing mice [39]. Moreover, Wong *et al*. revealed that treatment of human breast carcinoma (MDA-MB-231 and MDA-MB-435)-xenografted mice with ACF inhibited HIF-1-mediated invasion and metastasis [40]. Besides HIF-1 inhibition, ACF was also investigated in the context of its dual topoisomerase I and II inhibitor activity, as discovered by Hassan *et al*. [41]. Topoisomerases are involved in the cleavage and resealing of DNA breaks during transcription and cell replication, and inhibition of these topoisomerases may lead to cell cycle arrest and apoptosis in dividing cells (reviewed in [42]).

The most important findings were that HIF-1 is activated by sublethal PDT in SK-ChA-1 cells. Immunostaining of patient-derived perihilar cholangiocarcinoma biopsies demonstrated extensive neovascularization in desmoplastic tissue and heterogeneous glucose transporter 1 (GLUT-1) overexpression, hinting towards the possible involvement of hypoxia- and HIF-1-mediated angiogenesis. *In vitro*, pretreatment of tumor cells with ACF improved PDT outcome and reduced the PDT-induced expression of VEGF and PTGS2. Lastly, incubation of SK-ChA-1 cells with ACF resulted in induction of S-phase cell cycle arrest, DNA damage, and apoptosis, altogether underscoring ACF's dual topoisomerase I/II inhibition potential and utility to act as a neoadjuvant chemotherapeutic in PDT.

Results

Expression of hypoxia-related proteins in human perihilar cholangiocarcinoma

Although the incidence of tumor hypoxia and the importance of HIF-1 expression in a large variety of tumors have been widely established, literature on this phenomenon in perihilar cholangiocarcinomas is scarce. Therefore, it was investigated whether hypoxia-related proteins (VEGF for angiogenic signaling, CD105 and CD31/Ki-67 for neovascularization, and GLUT-1 for glycolysis) were present in perihilar

cholangiocarcinoma resection specimens. Of note, immunostaining for HIF-1α directly was not performed due to its high instability (protein half-life of 5–8 minutes) [43]. Representative differently stained serial images are presented in **Figure 1**.

The hematoxylin and eosin staining (**Fig. 1A**) revealed that perihilar cholangiocarcinomas were characterized by clusters of tumor cells surrounded by relatively large areas of desmoplastic tissue (*i.e.*, stroma). The tumor mass stained positively for VEGF (as did liver tissue), whereas VEGF staining was less prominent in the tumor stroma (**Fig. 1B**). Nevertheless, the tumor stroma was densely vascularized. The vasculature in the desmoplastic tissue was not of pre-existent nature, as the endothelium stained positively for CD105, a marker for angiogenic endothelium (**Fig. 1C**), and Ki-67, a marker of proliferation (**Fig. 1D**). Of note, the tumor mass was largely devoid of Ki-67-positive cells, indicating that the perihilar cholangiocarcinomas in our patient population were slowly proliferating tumors. GLUT-1 was largely absent in the tumor cell mass and stroma (**Fig. 1E**), albeit several regions containing GLUT-1-expressing cell clusters were observed in other sections of the tumor (**Fig. 1F**).

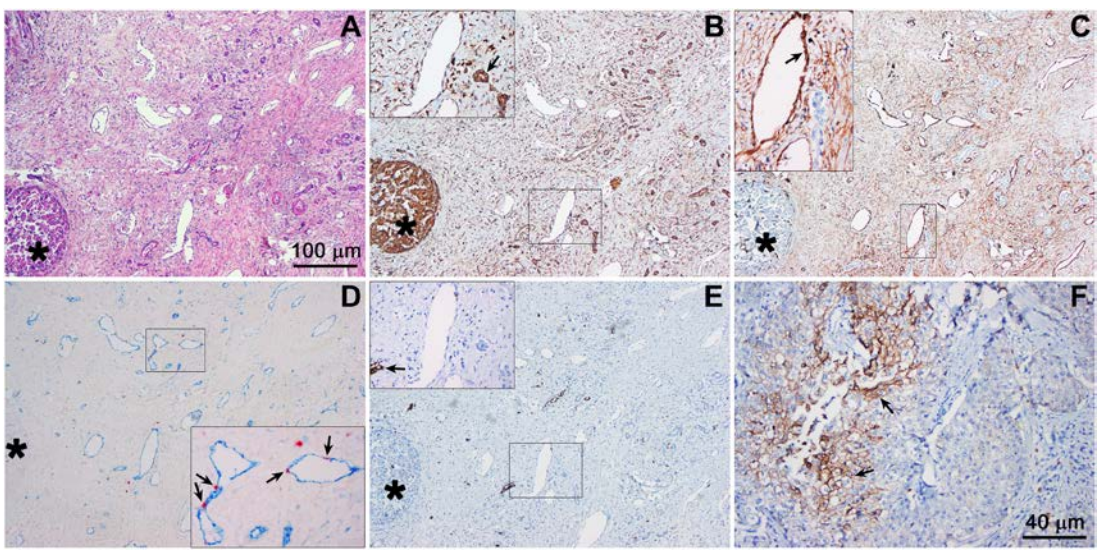

Fig. 1. Hypoxia-related protein expression in an extrahepatic perihilar cholangiocarcinoma (Klatskin tumor) resection specimen. Serial histological sections were used for protein profiling in the same region. **A**. Hematoxylin and eosin staining of a cholangiocarcinoma section containing tumor mass (intense purple staining, circular structure, bottom left, marked with an asterisk in panels **A**-**E**), tumor stroma, and native tissue (*e.g.*, pre-existent arterial structures). **B**. VEGF staining (brown), showing intense staining of the tumor mass and vascular endothelium (insert) as well as pre-existent biliary structures (insert, arrow). The insert corresponds to the demarcated region in the low-magnification image. **C**. CD105 staining (brown), showing no staining in the tumor mass and positive staining of the vascular endothelial cells in the tumor stroma (insert, arrow, indicates neovessel formation). **D**. Angiogenesis was further confirmed with CD31 (blue) and Ki-67 (red) double staining, showing that the blood vessels in the tumor stroma contain proliferating endothelial cells (insert, arrows). **E**. GLUT-1 staining (brown) was largely absent in the tumor mass and stroma, indicating that these regions were not affected by hypoxia. In some regions of the tumor, however, positive staining was observed (insert, arrow). **F**. Strong GLUT-1 staining was found in another region of the histological specimen. Magnification: 4× (**A**-**E**, scale bar = 100 µm) and 10× (**F**, scale bar = 40 µm).

Accordingly, these results provide compelling evidence for the presence of hypoxia and HIF-1 activation in perihilar cholangiocarcinomas, which likely drive angiogenesis and regional upregulation of glycolysis. Moreover, the perihilar cholangiocarcinomas are replete with vasculature that may serve as a conduit for the delivery of liposome-encapsulated photosensitizers.

HIF-1 is activated after PDT

To establish whether HIF-1 was activated by PDT, the optimal PDT dose was first determined in perihilar cholangiocarcinoma (SK-ChA-1) cells. SK-ChA-1 cells were incubated with increasing concentrations of ZnPC-encapsulating cationic liposomes (ZnPC-ETLs) and subsequently treated with PDT (500 mW, 15 J/cm^2).

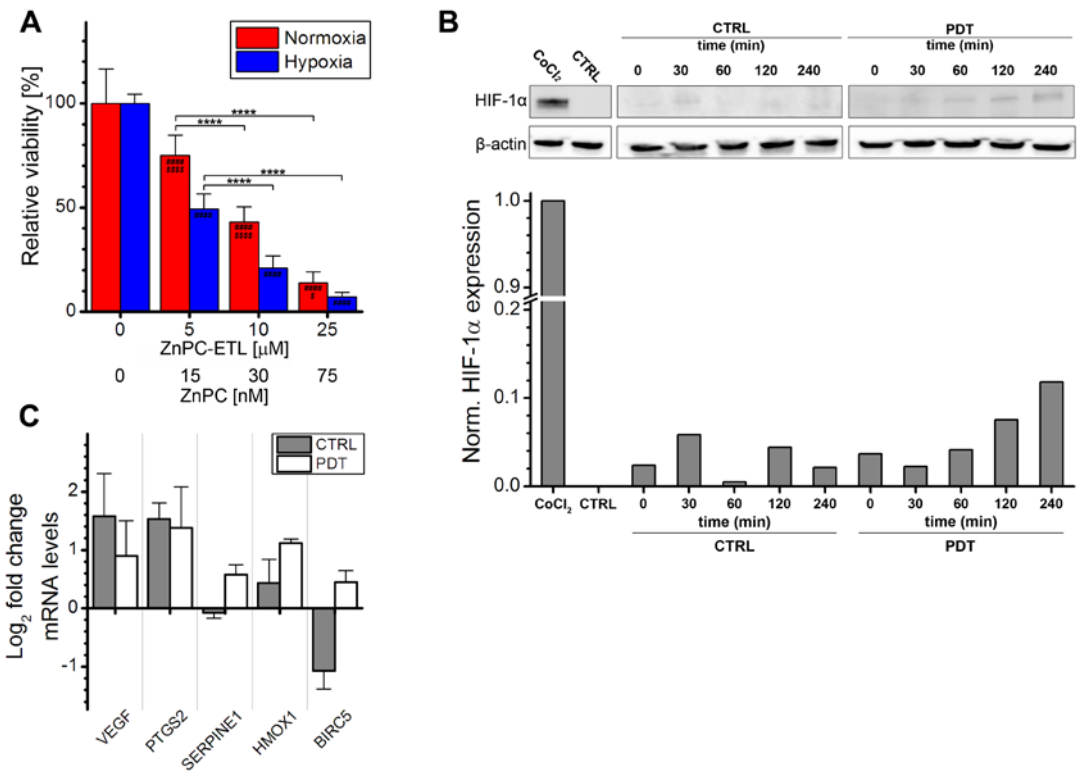

Fig. 2. Analysis of HIF-1α activation after PDT. **A**. SK-ChA-1 cells were incubated with increasing concentration of ZnPC-ETLs, treated with PDT, and maintained at normoxic (red bars) or hypoxic (blue bars) culture conditions. Cell viability was determined 24 hours post-PDT (n = 6 per group). **B**. SK-ChA-1 cells were treated with PDT (10 μM ZnPC-ETLs, final lipid concentration) or received a control (CTRL) treatment, after which the cells were placed in a hypoxic chamber up to 240 minutes (min) post-PDT. HIF-1α protein levels were determined using Western blotting. As a positive control, cells were incubated with 500 μM $CoCl_2$ for 24 hours (top panel). Next, the HIF-1α protein bands and their corresponding β-actin protein bands were quantified using ImageJ software [74] and each HIF-1α value was divided by its corresponding β-actin value. All values were normalized to the positive control ($CoCl_2$) (bottom panel). **C**. SK-ChA-1 cells were either left untreated (grey bars) or treated with PDT (white bars), and subsequently placed at hypoxic conditions for 4 hours. Thereafter, downstream targets of HIF-1 were analyzed with qRT-PCR (n = 3 per group). Readers are referred to the experimental section for the significance of the statistical symbols.

These liposomes have been shown to selectively accumulate in tumor endothelium [44], which is expected to translate to vascular shutdown and exacerbated tumor hypoxia following PDT [15]. Moreover, the ZnPC-ETLs are taken up by tumor cells, including SK-ChA-1 cells (manuscript in preparation). After PDT, the cells were either maintained under normoxic or hypoxic culture conditions (**Fig. 2A**) to mimic the PDT-induced vascular shutdown [45, 46]. Cell viability was determined 24 hours after PDT using the WST-1 assay. Cells exhibited a ZnPC concentration-dependent decrease in cell viability following PDT, whereby the extent of cell death was exacerbated by hypoxia (**Fig. 2A**). Since the IC_{50} concentration in normoxic and hypoxic cells were approximately 10 and 5 μM ZnPC-ETLs (final lipid concentration), respectively, these concentrations were used in the rest of the experiments.

Next, the stabilization of HIF-1α and induction of HIF-1α transcriptional targets were investigated following PDT. As shown in **Figure 2B**, normoxic SK-ChA-1 cells exhibited no notable HIF-1α expression. Stimulation of cells with cobalt chloride is commonly used to induce hypoxic signaling [47, 48] and was therefore used as positive control. Indeed, cobalt chloride caused extensive HIF-1α stabilization. Accordingly, SK-ChA-1 cells that were placed in a hypoxic chamber stabilized HIF-1α in a time-dependent manner, albeit less extensively than after cobalt chloride stimulation. HIF-1α stabilization was enhanced upon PDT.

The HIF-1α stabilization was associated with upregulated transcription of several HIF-1 target genes, including *VEGF* (angiogenesis), *PTGS2* (survival), and *HMOX1* (survival) (**Fig. 2C**). SK-ChA-1 cells also upregulated *SERPINE1* (angiogenesis) and baculoviral inhibitor of apoptosis repeat-containing 5 (*BIRC5*, survival) after PDT. It was therefore concluded that HIF-1α is upregulated in SK-ChA-1 cells following PDT, albeit to a minor extent in comparison to the cobalt chloride treatment.

ACF is translocated to the nucleus upon hypoxia and/or PDT

Since PDT induced HIF-1 signaling in SK-ChA-1 cells, which may be responsible for the therapeutic recalcitrance *in vivo*, we investigated whether the HIF-1α/HIF-1β dimerization inhibitor ACF would enhance PDT efficacy. First, the intracellular localization of ACF was determined by confocal microscopy, whereby the intrinsic fluorescence of ACF (λ_{ex} = 453 nm and λ_{em} = 507 nm) in combination with (intra) cellular membrane staining (**Fig. 3**). SK-ChA-1 cells were incubated with ACF during normoxia, hypoxia, and/or after PDT to study the cytosolic-to-nuclear translocation of ACF during these processes.

As shown in **Figure 3A**, ACF was localized in both the nucleus and cytosol under normoxic conditions. PDT treatment was accompanied by a translocation of ACF towards the nucleus under normoxic conditions, which was further characterized by altered cell morphology that entailed cell shrinkage and blebbing (**Fig. 3B**). Hypoxia (in the absence of PDT) triggered prominent translocation of ACF from the cytosol to

the nucleus (**Fig. 3C**). Interestingly, PDT-treated SK-ChA-1 cells that were placed in a hypoxic environment revealed a similar ACF distribution pattern as PDT-treated cells under normoxic conditions. ACF was mainly found in the nucleus in PDT-treated hypoxic cells, albeit at relatively lower levels compared to untreated hypoxic cells (**Fig. 3D**).

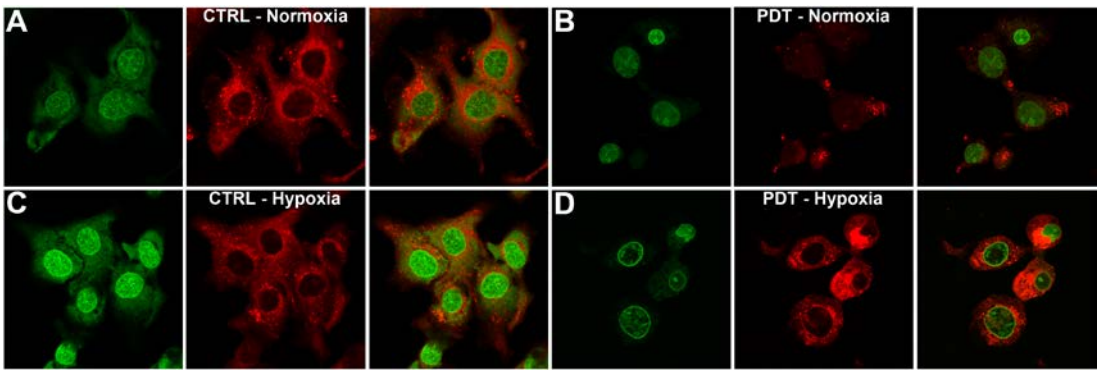

Fig. 3. Intracellular ACF localization. **A–D**. SK-ChA-1 cells were either left untreated or treated with PDT and subsequently incubated with ACF for 4 hours under normoxic (**A**, **B**) or hypoxic culture conditions (**C**, **D**). ACF localization was determined using confocal microscopy (ACF in green; Nile Red (membrane staining) in red).

ACF potentiated PDT efficacy

For clinical application purposes, ACF should remain stable during the application of PDT and during conditions of oxidative stress in order to inhibit HIF-1 activation after PDT and the subsequent microvascular shutdown. A model system was therefore used to study the stability of ACF during PDT. ACF was dissolved in buffer solution and exposed to increasing amounts of cell phantoms (*i.e.*, artificial cells) loaded with ZnPC, of which it was demonstrated that ROS is produced upon irradiation [36]. As shown in **Figure 4A**, the application of PDT only marginally affected ACF fluorescence, confirming that ACF remained stable during illumination and conditions of hyperoxidative stress.

To determine the most suitable concentration of ACF for the improvement of PDT efficacy, the concentration-dependent uptake and toxicity of ACF were tested in SK-ChA-1 cells. ACF uptake followed a concentration-dependent linear pattern up to 5 μM ACF (**Fig. 4B**). The toxicity of ACF was determined during a 24-hour incubation period under either normoxic or hypoxic conditions (**Fig. 4C**). The IC_{50} concentration during normoxia and hypoxia, determined with the WST-1 assay, was 29 and 73 μM, respectively. Inasmuch as SK-ChA-1 cells exhibited a relative viability of ~90% at 3 μM ACF during normoxia, this concentration was used in the rest of the experiments.

Next, SK-ChA-1 cells were incubated with ACF for 24 hours under normoxic conditions and treated with PDT (**Fig. 4D**) to investigate ACF's adjuvant efficacy. As indicated, ACF was mildly toxic, which translated to slightly increased cytotoxicity when combined with PDT and normoxic incubation (**Fig. 4D**). A similar trend was

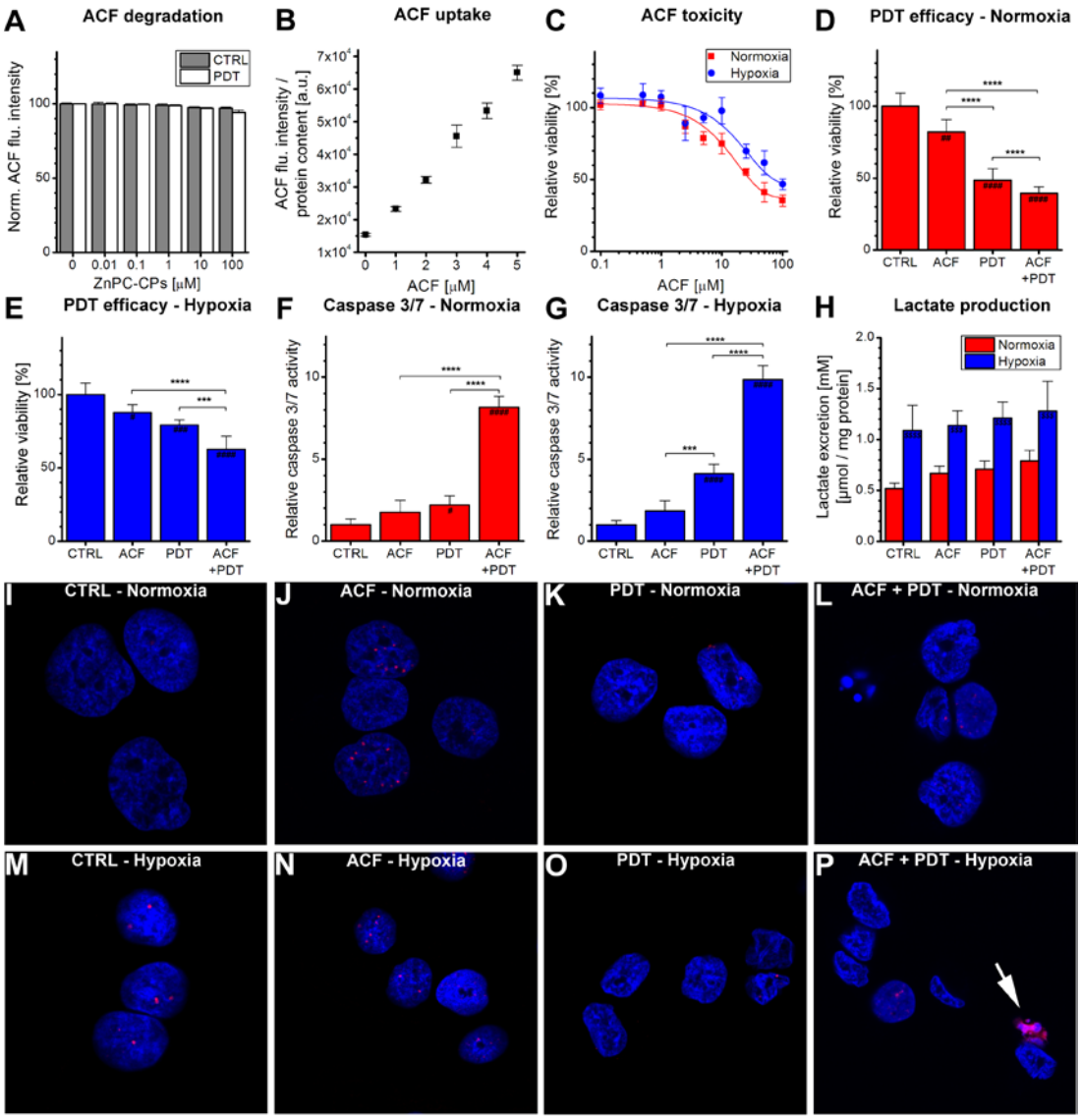

Fig. 4. Combination treatment of ACF with PDT. **A**. Evaluation of ACF stability using increasing concentrations of ZnPC-containing cell phantoms (ZnPC-CPs) with or without irradiation. ACF degradation was monitored using fluorescence spectroscopy (n = 4 per concentration). **B**. Cells were incubated with ACF for 24 hours, after which the uptake of ACF was determined using fluorescence spectroscopy. Data were normalized to protein content (n = 4 per concentration). **C**. ACF toxicity was determined after 24-hour incubation under either normoxic (red line) or hypoxic (blue line) conditions using the WST-1 method (n = 4 per group). Treatment efficacy of ACF and ACF + PDT was tested in SK-ChA-1 cells after 4 hours at **D**. normoxic and **E**. hypoxic culture conditions (n = 6 per group). (**F**, **G**) Relative caspase 3/7 activity was determined 4 hours after PDT at incubation at **F**. normoxic or **G**. hypoxic culture conditions (n = 6 per group). **H**. Lactate production by SK-ChA-1 cells treated with ACF and ACF + PDT was evaluated after 24 hours at normoxic (red bars) or hypoxic (blue bars) culture conditions (n = 6 per group). **I–P**. Analysis of DNA damage after control (CTRL), ACF, PDT, and ACF + PDT treatment. Cells were kept for 4 hours under normoxic (**I-L**) or hypoxic conditions (**M-P**) post-treatment. Cells were stained with DAPI (nuclei, blue) and phospho-H2AX (DNA double-strand breaks, red). The arrowhead in **panel P** indicates apoptosis. Readers are referred to the experimental section for the significance of the statistical symbols.

observed in cells that were maintained under hypoxic conditions after PDT (**Fig. 4E**). In addition, the levels of caspase 3 and 7 (*i.e.*, apoptosis markers) were assayed 4 hours post-treatment (**Fig. 4F**, **4G**). Under normoxic conditions, neither ACF nor PDT significantly affected caspase 3/7 levels, however, ACF + PDT resulted in a 8-fold higher caspase 3/7 activity in SK-ChA-1 cells (**Fig. 4G**). During hypoxia, PDT resulted in a 4-fold increase in caspase 3/7 activity and ACF + PDT resulted in a 10-fold higher caspase 3/7 activity, indicating that apoptosis constitutes an important mode of cell death following combination treatment of ACF + PDT. None of the conditions induced the formation of DNA double-strand breaks, as assessed by a phospho-H2AX staining 4 hours after treatment (**Fig. 4I–4P**), indicating that neither hypoxia nor ACF or PDT induce direct damage to DNA in the acute phase.

Lastly, inasmuch as HIF-1 signaling is a driving force behind glycolysis and the consequent production of lactate [49], the production of lactate was quantified in the cell culture medium 24 hours after ACF and PDT treatment (**Fig. 4H**). Lactate excretion levels were substantially increased under hypoxic conditions in all treatment groups compared to normoxic cells, validating our hypoxic incubation model. However, no further intergroup differences were observed in this cell line with respect to lactate production. Neither ACF nor PDT therefore induced notable metabolic catastrophe in cells.

ACF interferes with the regulation of HIF-1-induced target genes

To study whether pre-treatment with ACF influences post-PDT HIF-1α signaling, SK-ChA-1 cells were incubated with ACF and subsequently treated with PDT and maintained under hypoxic conditions. HIF-1 downstream targets were clustered in angiogenesis-, glycolysis-, and survival-associated genes and analyzed by quantitative reverse transcriptase polymerase chain reaction (qRT-PCR) at different time points after PDT (**Fig. 5**). Moreover, additional HIF-1 target genes were included in the ACF-related transcriptomic analysis.

PDT induced the expression of *VEGF*, *HMOX1*, and *PTGS2*, corroborating the data in **Figure 2C**. ACF reduced the degree of *PTGS2* upregulation (only in the 0-h and 2-h group) and *VEGF* transcription post-PDT. Conversely, *EDN1* was downregulated by hypoxia and PDT but upregulated by ACF. In addition, *SERPINE1* was highly induced upon ACF treatment - an effect that was also observed after PDT in the presence of ACF. Altogether, these findings indicate that ACF by itself and in combination with PDT modulates several important HIF-1-induced transcriptional targets. However, the direction of the regulation is not always consistent within one functional class.

Long-term exposure to ACF causes cell cycle arrest and apoptosis

Although ACF is generally considered a specific HIF-1α/HIF-1β dimerization inhibitor [37], Hassan *et al.* have reported that ACF may also act as a dual topoisomerase

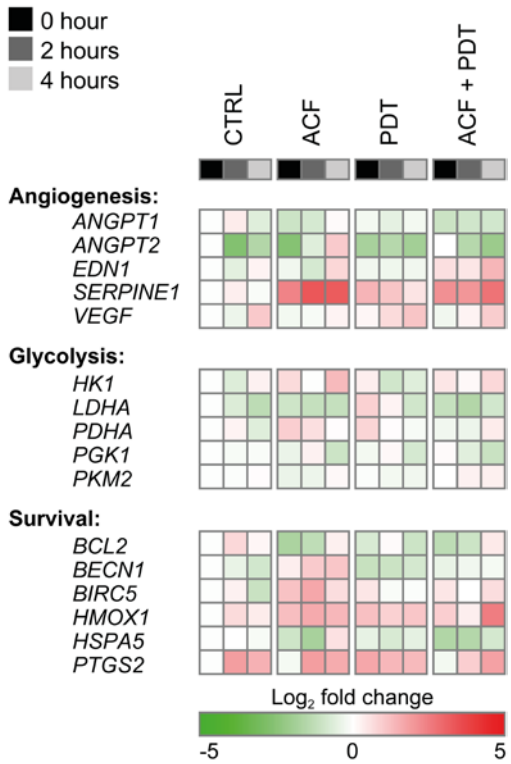

Fig. 5. Gene expression analysis after control (CTRL), ACF, PDT, and ACF + PDT treatment. Gene expression levels were obtained by qRT-PCR from SK-ChA-1 cells as analyzed 0 hours, 2 hours, or 4 hours post-treatment under hypoxic conditions. The plotted heat map data represents the log_2-transformed fold change of each data point in relation to the 0-hour normoxic CTRL. Upregulated genes are depicted in red, downregulated genes in green. Numeric values are provided in **Table S2.**

I/II inhibitor [41]. Topoisomerase I/II inhibition is associated with cell cycle arrest and consequent apoptosis as a result of DNA double-strand breaks (reviewed in [42, 50]). In the acute phase after PDT, DNA double-strand breaks were not observed (**Fig. 4I–4P**) but apoptotic signaling was pronounced, particularly in the ACF + PDT and hypoxia groups (**Fig. 4F** and **4G**). To investigate the potential topoisomerase I/II inhibitory effects, SK-ChA-1 cells were exposed to ACF for longer time frames (24 and 48 hours) under normoxic conditions, after which the cell cycle profile was analyzed using propidium iodide staining (**Fig. 6A–6D**).

As shown in **Figure 6B** and **6D**, ACF led to an increased fraction of cells in both the S- and G2/M-phase after 24 and 48 hours of incubation. The most significant effect of ACF was characterized by cell cycle arrest in the S-phase after 48 hours of incubation. Furthermore, ACF treatment was associated with increased apoptosis, but not necrosis, after 24 and 48 hours (**Fig. 6E**, **6F**), which concurred with elevated ROS production in cells (**Fig. 6G**, **6H**). Finally, incubation of SK-ChA-1 cells with ACF for 24 or 48 hours led to the formation of DNA double-strand breaks (**Fig. 6I–6P**), although not in a concentration-dependent manner.

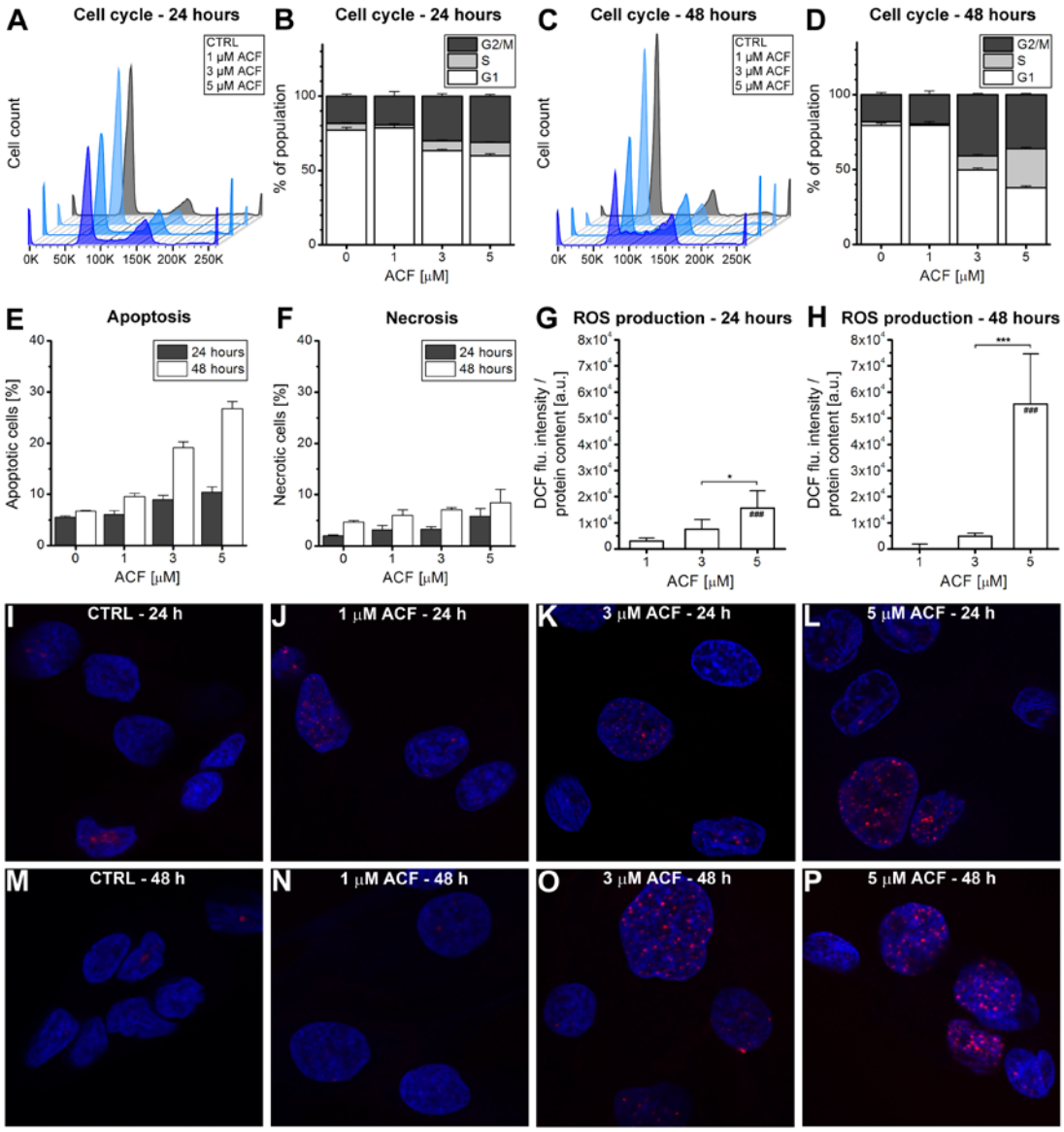

Fig. 6. **A–D**. SK-ChA-1 cells were incubated with ACF for either (**A**, **B**) 24 hours or (**C**, **D**) 48 hours, after which the cell cycle profile was analyzed with flow cytometry using propidium iodide staining (n = 3 per group). **E**. Flow cytometric analysis of SK-ChA-1 cells that were incubated with ACF for either 24 hours (in grey) or 48 hours (in white), after which the fraction of apoptotic (annexin V-positive) and **F**. necrotic (TO-PRO-3-positive) cells was determined (n = 3 per group). (**G**, **H**) SK-ChA-1 cells were exposed to ACF for **G**. 24 hours or **H**. 48 hours and intracellular DCF fluorescence was determined as a measure of ROS production. **I–P**. Analysis of DNA damage after control (CTRL) or ACF treatment. SK-ChA-1 cells received ACF or CTRL treatment for (**I-L**) 24 hours or (**M-P**) 48 hours, and were subsequently stained with DAPI (nuclei, blue) and phospho-H2AX (DNA double-strand breaks, red).

Discussion

Perihilar cholangiocarcinoma is a relatively rare cancer that is non-resectable in 70–80% of patients at the time of diagnosis [51]. Although PDT is not curative in these patients, the treatment does prolong the median survival of 6–9 months (stenting) to 21 months post-diagnosis (stenting + PDT) [9]. Driven by these promising results, novel avenues are being explored to enhance PDT efficacy in these refractory and rather lethal cancers. PDT is associated with microvasculature shutdown and consequent HIF-1 signaling that may contribute to therapeutic recalcitrance [10]. Therefore, this study was conducted to investigate the expression of HIF-1-induced proteins in perihilar cholangiocarcinomas to gauge whether inhibition of HIF-1 may be exploited as a therapeutic target in the context of PDT. Histological analysis revealed that human perihilar cholangiocarcinomas overexpress VEGF homogeneously and GLUT-1 heterogeneously and are replete with neoangiogenic vessels in the desmoplastic tissue, suggesting that HIF-1 is constitutively active in these tumors. Second, PDT of SK-ChA-1 cells with ZnPC-encapsulating liposomes caused HIF-1α stabilization and transcriptional upregulation of downstream targets of HIF-1. Third, ACF was taken up by SK-ChA-1 cells, especially during hypoxia, and translocated to the nucleus upon hypoxia and PDT. Lastly, ACF pretreatment was associated with S-phase cell cycle arrest and apoptosis and enhanced PDT efficacy, likely via inhibition of HIF-1 inhibition and topoisomerase I/II.

HIF-1α stabilization after PDT has been observed in various experimental settings. Ferrario *et al*. revealed that porfimer sodium-PDT resulted in HIF-1α stabilization in murine Kaposi's sarcoma [30]. PDT also upregulated the HIF-1-associated targets VEGF and COX-2 [30]. In mouse mammary carcinoma (BA) xenografts [31], porfimer-PDT led to an increase in HIF-1α, BIRC5, and VEGF protein levels. Lastly, murine mammary carcinoma (EMT-6) cells that were treated with porfimer sodium-PDT exhibited HIF-1α stabilization and its consequent translocation to the nucleus [28]. In line with these findings, our study demonstrated that HIF-1α was stabilized in SK-ChA-1 cells after incubation in a hypoxic chamber (to mimic vascular shutdown) and after PDT. PDT also led to the differential regulation of HIF-1-regulated genes, including *VEGF*, *PTGS2*, *SERPINE1*, *HMOX1*, and *BIRC5*. Consistent with these results, it was recently demonstrated that SK-ChA-1 cells subjected to sublethal PDT with neutral ZnPC-encapsulating liposomes significantly upregulated HIF-1-associated genes 90 minutes post-PDT [52]. Altogether, these findings attest that HIF-1α is activated following PDT and that this transcription factor constitutes an important therapeutic target, particularly in light of the fact that HIF-1 regulates biological processes that are important in PDT, such as glycolysis, angiogenesis, and survival [10].

The combinatorial use of HIF-1 inhibitors with PDT is a relatively new concept.

For instance, Chen *et al.* used HIF-1α siRNAs in combination with Photosan-PDT in a head-and-neck cancer mouse model, which resulted in regression of tumor volume by ~40% within 10 days [53]. Besides HIF-1 inhibition, its downstream target VEGF has been inhibited in various studies [32, 54, 55], which generally led to improved therapeutic efficacy. Although downstream targets of HIF-1 may be inhibited, from a pharmacology point of view it would be more attractive to inhibit HIF-1 itself, inasmuch as all the downstream targets are blocked concomitantly. As such, the HIF-1α/HIF-1β dimerization inhibitor ACF was evaluated for its adjuvant potential in SK-ChA-1 cells. ACF specifically binds the PER-ARNT-SIM (PAS) domain of HIF-1α and HIF-2α, which prevents the dimerization of HIF-1, thereby deterring its activation [37]. It was observed that ACF was taken up by SK-ChA-1 cells and translocated to the nucleus after hypoxia and/or PDT, presumably due to its binding to HIF-1α and HIF-2α. Moreover, ACF remained stable during the application of intense (laser) light exposure as well as during conditions of oxidative stress, suggesting that ACF will be able to inhibit HIF-1 after PDT and consequent vascular shutdown. The IC_{50} value of ACF in SK-ChA-1 cells was 29 μM during normoxia, which is in the range that has been observed for other cell lines [56]. Strese *et al.* found that human leukemic monocyte lymphoma (U937) was most susceptible to ACF, as demonstrated by an IC_{50} value of 4.6 μM, whereas human breast cancer (MCF-7) cells exhibited an IC_{50} value of 61 μM [56]. Pretreatment of SK-ChA-1 cells with ACF significantly improved therapeutic efficacy, which was partially mediated by the increase in caspase 3/7 levels (apoptosis).

In addition to HIF-1 inhibition, ACF has also been shown to act as a dual topoisomerase I/II inhibitor [41]. Of note, topoisomerase inhibitors (*e.g.*, topotecan [57]) may also repress gene transcription, but to what extent ACF is able to inhibit HIF-1-mediated signaling via this mechanism is currently elusive. Topoisomerase class I and II inhibitors cleave either one or both strands of DNA, respectively. Both topoisomerase I and II inhibitors may induce the formation of DNA double-strand breaks, inasmuch as the single-strand break that is induced by topoisomerase I inhibitors may turn into a double-strand break when the topoisomerase I cleavable complex collides with the replication fork [58]. This type of DNA damage may culminate in cell cycle arrest via tumor protein 53 (p53)-mediated $p21^{WAF1/CIP1}$ induction, cellular senescence, and both p53-dependent and p53-independent apoptosis [42, 50, 58, 59]. To determine whether the observed cell death could (in part) be explained by topoisomerase I/II inhibition, SK-ChA-1 cells were incubated with ACF for 24 and 48 hours (*i.e.*, a full cell cycle requires 48 hours [34]). It should be noted that, although SK-ChA-1 cells have a mutation (at codon 282) in the DNA binding domain of p53 [60], their p53 is still functional. ACF incubation led to cell cycle arrest in both the S-phase and the G2/M-phase and was associated with an increased percentage of apoptotic cells. SK-ChA-1 cells also exhibited DNA double-strand breaks as a result of ACF incubation.

Collectively, these findings support the notion that ACF exhibits topoisomerase I/II inhibition activity that may contribute to greater therapeutic efficacy.

An interesting finding of this study is the upregulation of *SERPINE1* after ACF treatment. *SERPINE1* is a downstream target of both HIF-1 and p53 [61] and its protein product plasminogen activator inhibitor 1 (PAI1) is known to exhibit pleiotropic effects. PAI1 is involved in the inhibition of extracellular matrix remodeling, but it also has anti-apoptotic and pro-proliferative capacities and is involved in angiogenesis [62, 63]. This has been exemplified by Devy *et al*., who demonstrated that cultured mouse aortic rings from PAI1-deficient mice, which were stimulated with PAI1, exhibited a dose-dependent angiogenic response [64]. Whereas low-dose levels of PAI1 were associated with increased angiogenesis, high-dose levels of PAI1 inhibited microvessel formation [64]. To what extent p53 is responsible for *SERPINE1* induction after ACF treatment is currently elusive, as are the consequences of PAI1 induction in the context of PDT.

As stated earlier, the use of inhibitors of specific survival pathways with PDT is a relatively novel strategy. Several studies have indicated that inhibition of survival pathways in conjunction with PDT may be an attractive means to enhance PDT efficacy (reviewed in [10]). Consistent with these results, the present findings also encourage the use of small molecule inhibitors (*e.g.*, HIF-1 inhibitors) of survival pathways together with PDT. These small molecule inhibitors can be co-encapsulated with a photosensitizer into a single drug delivery system, such as liposomes, in order to improve treatment outcome.

In conclusion, HIF-1 is overexpressed in a variety of solid cancers and is often associated with therapeutic recalcitrance, inasmuch as it stimulates glycolysis, angiogenesis, and survival. This study demonstrated that HIF-1 inhibition via ACF may be an attractive method to potentiate PDT efficacy in perihilar cholangiocarcinoma. Interestingly, not only HIF-1 inhibition, but also topoisomerase I/II inhibition by ACF may further contribute to increased PDT efficacy. *In vivo* studies as addressed in [65] are necessary to validate the potential of ACF in combination with PDT.

Materials and Methods

Chemicals

1,2-dipalmitoyl-*sn*-glycero-3-phosphocholine (DPPC), 1,2-dipalmitoyl-*sn*-glycero-3-phospho-L-serine (DPPS), and 3β-[N-(N',N'-dimethylaminoethane)-carbimoyl]cholesterol (DC-chol) were purchased from Avanti Polar Lipids (Alabaster, AL). L-α-phosphatidylethanolamine, distearoyl methoxypolyethylene glycol conjugate (DSPE-PEG, average PEG molecular mass of 2,000 amu), ZnPC, 4-(2-hydroxyethyl)-1-piperazineethanesulfonic acid (HEPES), fibronectin, sodium chloride (NaCl), β-mercaptoethanol, cholesterol, chloroform, Nile Red, paraformaldehyde, sucrose,

bovine serum albumin (BSA), Tween 20, $CoCl_2$, ACF, and pyridine were obtained from Sigma-Aldrich (St. Louis, MO). Tris-HCl and dimethyl sulfoxide (DMSO) were purchased from Merck KgaA (Darmstadt, Germany). Ethanol was obtained from Biosolve (Valkenswaard, the Netherlands). Protease inhibitor cocktail and water-soluble tetrazolium-1 (WST-1) were purchased from Roche Applied Science (Basel, Switzerland). 2',7'-dichlorodihydrofluorescein diacetate ($DCFH_2$-DA) was obtained from Life Technologies (Carlsbad, CA).

All lipids were dissolved in chloroform, purged with nitrogen gas, and stored at −20°C. Phospholipid stock concentrations were determined by the inorganic phosphate assay modified from [66]. ZnPC was dissolved in pyridine at a 178-μM concentration and stored at room temperature (RT) in the dark, $CoCl_2$ was dissolved in MilliQ at a concentration of 50 mM, and ACF and $DCFH_2$-DA were dissolved in DMSO at a concentration of 50 mM.

Histology

Histology was performed on two patient-derived, paraffin-embedded perihilar cholangiocarcinoma biopsies. Tissue sections were dewaxed in xylene and rehydrated in graded steps of ethanol. Endogenous peroxidase activity was blocked with methanol containing 0.3% peroxide (20 min, RT). Heat-induced epitope retrieval (HIER) was performed in a pretreatment module (Thermo Fisher Scientific, Fremont, CA) using Tris-EDTA (VEGF, Ki-67, CD31, GLUT-1) or citrate buffer (CD105) for 20 minutes at 98°C. Throughout the staining procedure all washing steps were performed with Tris-buffered saline. Superblock (Immunologic, Duiven, the Netherlands) was applied as a protein block prior to staining with primary antibodies.

All antibodies were diluted with antibody diluent (Scytek, Logan, UT). Single stains for CD105 (rabbit anti-human, polyclonal, cat. # RB-9291, Thermo Fischer Scientific), VEGF (rabbit anti-human, polyclonal, cat. # sc-152, Santa Cruz Biotechnology, Santa Cruz, CA), and GLUT-1 (rabbit anti-human, polyclonal, cat. # RB-9052, Thermo Fischer Scientific) were performed. These primary antibodies were visualized with BrightVision HRP-conjugated anti-rabbit polymer (Immunologic) and BrightDAB. The sections were counterstained with hematoxylin.

Sequential double staining [67] was performed for CD31 (mouse anti-human, clone JC70A, cat. # M0823, Dako, Glostrup, Denmark) and Ki-67 (rabbit anti-human, clone SP6, cat. # RM9106, Thermo Fischer Scientific). Ki-67 was visualized with BrightVision AP-conjugated anti-rabbit polymer (Immunologic) and Vector Red (Vector Labs, Burlingame, CA). Next, an intermediate HIER step using Tris-EDTA buffer (10 minutes at 98°C) was applied to remove all antibodies but leaving the chromogen intact [68]. Finally, CD31 was visualized with BrightVision AP-conjugated anti-mouse polymer (Immunologic) and PermaBlue plus/AP (Diagnostics Biosystems, Pleasanton, CA). All slides were dried on a hotplate (50°C) and permanently mounted

with Vectamount (Vector Labs).

It should be noted that, as part of the clinical diagnostics protocol at the Department of Pathology, all antibodies had been validated for their cross-reactivity and immunohistological staining efficacy using tissue that overexpresses the respective marker. Immunostaining for HIF-1α directly was not performed due to the instability of the HIF-1α antigen (degrades within a few minutes after biopsy).

Liposome preparation

ZnPC-ETLs were composed of DPPC:DC-chol:cholesterol:DSPE-PEG (66:25:5:4, molar ratio) and ZnPC was incorporated at a ZnPC:lipid molar ratio of 0.003. Liposomes were prepared using the lipid film hydration technique as described previously [36]. ZnPC-ETLs were characterized for size and polydispersity by photon correlation spectroscopy (Zetasizer 3000, Malvern Instruments, Malvern, Worcestershire, UK). Liposomes were purged with nitrogen and stored in the dark at 4°C until use.

Cell culture

Human perihilar cholangiocarcinoma (SK-ChA-1) cells were grown at standard culture conditions (37°C, 5% CO_2, and 95% air) and cultured in Roswell Park Memorial Institute (RPMI) 1640 culture medium supplemented with 10% fetal bovine serum (FBS) (v/v) (both from Gibco, Invitrogen, Carlsbad, CA), 1% penicillin/streptomycin (v/v), 1% L-glutamine (v/v) (both from Lonza, Walkersville, MD), and 1×10^{-5}% β-mercaptoethanol (v/v) (Sigma-Aldrich). Cells were passaged weekly at a 1:10 ratio. For all experiments, SK-ChA-1 cells were seeded in 24-wells (500 µL/well) or 6-wells plates (2 mL/well) (Corning, Corning, NY) at a density of 2×10^5 cells/mL. Confluent monolayers were achieved 48 hours after cell seeding, whereas 70–80% confluency was reached 24 hours after cell seeding.

PDT protocol

Cells were seeded in either 24-wells or 6-wells plates as indicated in the specific subsections and cultured until confluence. In case of ACF pre-treatment, cells were incubated with 3 µM ACF (in serum-free supplemented RPMI 1640 medium) for 24 hours prior to PDT. Next, cells were washed with PBS and incubated with ZnPC-ETLs (in serum-free supplemented RPMI 1640 medium) for 1 hour at standard culture conditions. Cells were washed twice with PBS and fresh serum- and phenol red-free supplemented RPMI 1640 was added to the cells. Serum was deliberately withdrawn after PDT in order to emulate the hyponutritional status of PDT-treated tumor cells *in vivo*, which is caused by the vascular shutdown. PDT was performed with a 671-nm solid state diode laser (CNI Laser, Changchun, China) at a power of 500 mW to achieve a cumulative radiant exposure of 15 J/cm^2. After PDT, cells were either placed at

standard culture conditions (normoxia) or placed in a hypoxic chamber [69] (hypoxia) to mimic vascular shutdown.

Cell viability

Cell viability was assessed using the WST-1 assay as described previously [36].

Western blotting

Cells were seeded in 6-wells plates and cultured until confluence. Cells were incubated with 10 μM ZnPC-ETLs (final lipid concentration) and treated with PDT (section "PDT protocol"). At 0, 30, 60, 120, and 240 minutes after PDT, cells were placed on ice and lysed in ice-cold Laemmli buffer [70] supplemented with protease inhibitor cocktail (1 tablet per 5 mL buffer). A 20-hour incubation with 500 μM $CoCl_2$ served as a positive control for HIF-1α stabilization [71]. The lysates were passed 10 × through a 25-gauge needle (BD Biosciences, San Jose, CA) to shear DNA. Next, samples were placed in a heat block for 10 minutes at 95°C, after which the samples were centrifuged for 15 minutes at 13,000 × g (4°C). Samples (30 μg) were loaded on a 10% SDS-PAGE precast gel (50 μL slot volume, Bio-Rad Laboratories, Hercules, CA) and the electrophoresis was performed for 90 minutes at 125 V. The gels were blotted onto methanol-primed PVDF membranes (Millipore, Billerica, MA) for 1 hour at 330 V at 4°C. Protein membranes were blocked for 1 hour with 5% dried milk powder (Protifar, Nutricia, Cuijk, the Netherlands) in 0.2% Tween 20 Tris-buffered saline (TBST, 20 mM Tris-HCl, 150 mM NaCl, pH = 7.5). The membranes were incubated overnight at 4°C on a rocker with anti-HIF-1α (1:500, clone 54/HIF-1α, BD Transduction Laboratories (Franklin Lakes, NJ)) and anti-β-actin (1:4,000, AC-74, Sigma-Aldrich). Next, the membranes were washed 4 times in TBST and incubated with HRP-conjugated goat-anti-mouse IgG_1 (1:1,000, Dako Cytomation (Glostrup, Denmark)) for 1 hour at RT. Subsequently, membranes were washed 3 times with TBST and 2 times with TBS. The enhanced chemiluminescence (ECL) kit (Thermo Scientific) was used as substrate for β-actin and ECL plus (Thermo Scientific) was used as substrate for HIF-1α. Protein bands were visualized on an ImageQuant LAS 3000 luminometer (GE Healthcare, Little Chalfont, UK).

qRT-PCR

Cells were seeded in 6-wells plates and treated with PDT as described in the section "PDT protocol". RNA was extracted using TRIzol according to the manufacturer's protocol (Life Technologies). RNA was quantified and analyzed with a Nanodrop 2000 UV-VIS spectrophotometer (Thermo Scientific). cDNA synthesis and RT-qPCR reactions were performed according to [52]. The primers that were used in this study are listed in **Table S1**. The data was analyzed using the LinRegPCR software in which relative starting concentrations of each cDNA template (N_0) were calculated

[72], after which the N_0 values of the target genes were corrected for the respective N_0 of the S18 rRNA. All S18 rRNA-corrected N_0 values of each gene were compared to the average N_0 of the untreated normoxic control samples. A $\log_2$ transformation was performed in order to obtain absolute fold-differences in expression levels of the genes of interest.

Confocal microscopy

Microscope cover slips (24 × 40 mm, VWR, Lutterworth, UK) were first coated with 5×10^{-4}% (w/v) fibronectin in 0.9% NaCl (Fresenius Kabi, Bad Homburg, Germany) for 2 hours at 37°C. Next, the fibronectin-containing solution was aspirated and cells were seeded and allowed to grow overnight. To determine the ACF subcellular localization, cells were either untreated or subjected to PDT as described in the section "PDT protocol", and subsequently incubated with 3 μM ACF for 4 hours under normoxia and hypoxia as specified. Next, cells were washed with 1 mL of PBS and fixed with a mixture of 4% paraformaldehyde and 0.2% sucrose for 5 min. Cells were washed with 1 mL of PBS and stained with 1 μM Nile Red (in PBS) for 1 min. Cells were washed thrice with 1 mL PBS and mounted on microscope slides using Vectashield mounting medium (Vector Laboratories, Burlingame, CA). After 1 h, the slides were sealed with nail polish.

For the assessment of DNA damage, cells were fixed with a mixture of 4% paraformaldehyde and 0.2% sucrose for 5 min and permeabilized in 0.1% TX-100 (in PBS) for 5 min. Next, cells were washed with 1 mL of PBS and incubated for 16 hours with mouse anti-human phospho-H2AX-AlexaFluor647 (Cell Signaling Technology, Danvers, MA) at a 1:100 dilution in 0.5% BSA and 0.15% glycine (in PBS, staining buffer) at 4°C. Next, cells were washed thrice with staining buffer and mounted on microscope slides using Vectashield mounting medium with 4',6-diamidino-2-phenylindole (DAPI) (Vector Laboratories). After 1 h, the slides were sealed with nail polish.

Cells were imaged on a Leica SP8 laser scanning confocal microscopy system (Leica Microsystems, Wetzlar, Germany). Fluorescence intensities were measured at λ_{ex} = 405 nm, λ_{em} = 415–480 nm for DAPI, λ_{ex} = 470 nm, λ_{em} = 480–550 nm for ACF, λ_{ex} = 540 nm, λ_{em} = 550–650 nm for Nile Red, and λ_{ex} = 660 nm, λ_{em} = 670–750 nm for phospho-H2AX. All experiments were performed using the same laser and microscope hardware settings.

ACF degradation

To evaluate the stability of ACF during PDT, 450 μL of ACF (80 μM) in serum-free and phenol red-free RPMI 1640 medium was added to 24-wells plates. Next, 50 μL of increasing concentrations of ZnPC-containing cell phantoms (85% DPPC, 10% DPPS, 5% cholesterol, molar ratio; ZnPC:lipid ratio of 0.003) in physiological buffer

(10 mM HEPES, 0.88% (w/v) NaCl, pH = 7.4, 0.292 osmol/kg) was added to the wells. The baseline ACF fluorescence was read at λ_{ex} = 460 ± 40 nm and λ_{em} = 520 ± 520 nm using a BioTek Synergy HT multi-well plate reader (Winooski, VT). Subsequently, the cells were subjected to PDT (500 mW, 15 J/cm^2) and ACF fluorescence was determined as a measure of ACF degradation. The data was normalized to control wells (n = 4 per group).

ACF uptake

Cells were cultured in 24-wells plates until confluence. Cells were washed with PBS and incubated with ACF in supplemented serum-free RPMI 1640 medium for 24 hours. After incubation, cells were washed with PBS and fresh supplemented serum-free RPMI 1640 medium was added to the wells. Next, ACF fluorescence, as a measure of uptake, was read at λ_{ex} = 460 ± 40 nm and λ_{em} = 520 ± 520 nm using a BioTek Synergy HT multi-well plate reader. Data were normalized to protein content per well (n = 4 per group) as determined with the SRB assay [73].

Caspase 3/7 activity

Cells were cultured in 24-wells plates and subjected to treatment as described above. Cells were incubated in 200 μL of serum- and phenol-red free medium and maintained at either normoxic or hypoxic conditions for 3.5 hours post-treatment. After treatment and normoxic/hypoxic incubation, 25 μL of Caspase-Glo assay reagent (Promega, Madison, WI) was added and cells were incubated for 30 minutes under the aforementioned conditions. Luminescence was read on a BioTek Synergy HT multiplate reader at 560 ± 20 nm and a signal integration time of 1 s. Data were obtained from n = 5 measurements and corrected for background luminescence.

Lactate production

Cells were cultured in 24-wells plates until confluence and treated with ACF and PDT as indicated in the section "PDT protocol". After 24 hours, extracellular lactate levels were determined using The Edge blood lactate analyzer (Apex Biotechnology, Hsinchu, Taiwan). Lactate concentrations were determined from a standard curve and corrected for the average protein content per group as determined with the bicinchoninic acid assay (Thermo Scientific).

Flow cytometry

For cell cycle analysis, cells were seeded in 6-wells plates and cultured until 70–80% confluence. Cells were incubated with ACF (in supplemented serum-free RPMI 1640 medium) for 24 or 48 hours, after which cell cycle analysis was performed using flow cytometry according to ref. 69.

The mode of cell death following ACF incubation was analyzed by flow

cytometry using APC-conjugated Annexin V (eBioscience, San Diego, CA) for apoptosis and TO-PRO-3 (Life Technologies) for necrosis. Cells were seeded in 6-wells plates and cultured until 70–80% confluence. Next, cells were incubated with ACF (in supplemented serum-free RPMI 1640 medium) for 24 or 48 hours. After incubation, the samples were prepared as described previously [36] and assayed on a FACSCanto II (Becton Dickinson, Franklin Lakes, NJ). Ten thousand events were recorded in the gated region and data was analyzed using FlowJo software (Treestar, Ashland, OR).

Intracellular ROS assay

Cells were seeded in 24-wells plates and cultured until 70–80% confluence. Thereafter, cells were washed with PBS and incubated with ACF or vehicle (DMSO) in supplemented serum-free RPMI 1640 medium for 24 or 48 hours. After the indicated time points, the medium was removed, cells were washed with serum- and phenol red-free RPMI 1640 medium, and cells were incubated with 100 μM $DCFH_2$-DA (in serum- and phenol red-free RPMI 1640 medium) for 1 hour at standard culture conditions. Next, cells were washed with serum- and phenol red-free RPMI 1640 medium, and fresh serum- and phenol red-free RPMI 1640 medium was added to the wells. Intracellular 2',7'-dichlorofluorescein (DCF) fluorescence, which is a measure of ROS production, was read on a BioTek Synergy HT multiplate reader at λ_{ex} = 460 ± 40 nm and λ_{em} = 520 ± 520 nm. Data were obtained from n = 6 measurements and corrected for ACF fluorescence, protein content using the SRB assay, and DCF fluorescence (basal metabolic rate) of control cells.

Statistical analysis

Data were analyzed in GraphPad Prism software (GraphPad Software, San Diego, CA). Data were analyzed for normality using a Kolmogorov-Smirnov test. Normally distributed data sets were analyzed with either a student's t-test or a one-way ANOVA and subsequent Bonferroni post-hoc test. Non-Gaussian data were statistically analyzed using a Mann-Whitney U or Kruskal-Wallis test and a Dunn's post-hoc test. All data are reported as mean ± standard deviation. In the figures, intergroup differences are indicated with (*) and differences between treated groups versus the untreated (CTRL) group are indicated with (#). Differences between normoxic and hypoxic data are, when relevant, indicated with ($). The level of significance is reflected by a single ($p < 0.05$), double ($p < 0.01$), triple ($p < 0.005$), or quadruple sign ($p < 0.001$).

Acknowledgements

The authors are grateful to Marcel Dirkes and Adrie Maas for input regarding the hypoxic incubator, and Ron Hoebe and Daisy Picavet for the technical assistance with confocal microscopy.

References

1. Garg AD, Nowis D, Golab J and Agostinis P. Photodynamic therapy: illuminating the road from cell death towards anti-tumour immunity. Apoptosis. 2010; 15:1050-1071.
2. Castano AP, Mroz P and Hamblin MR. Photodynamic therapy and anti-tumour immunity. Nature Reviews Cancer. 2006; 6:535-545.
3. Szeimies RM, Morton CA, Sidoroff A and Braathen LR. Photodynamic therapy for non-melanoma skin cancer. Acta Dermato-Venereologica. 2005; 85:483-490.
4. de Visscher SA, Dijkstra PU, Tan IB, Roodenburg JL and Witjes MJ. mTHPC mediated photodynamic therapy (PDT) of squamous cell carcinoma in the head and neck: a systematic review. Oral Oncology. 2013; 49:192-210.
5. Moghissi K and Dixon K. Update on the current indications, practice and results of photodynamic therapy (PDT) in early central lung cancer (ECLC). Photodiagnosis and Photodynamic Therapy. 2008; 5:10-18.
6. Qumseya BJ, David W and Wolfsen HC. Photodynamic therapy for Barrett's esophagus and esophageal carcinoma. Clinical Endoscopy. 2013; 46:30-37.
7. Wildeman MA, Nyst HJ, Karakullukcu B and Tan BI. Photodynamic therapy in the therapy for recurrent/ persistent nasopharyngeal cancer. Head & Neck Oncology. 2009; 1:40.
8. Pinthus JH, Bogaards A, Weersink R, Wilson BC and Trachtenberg J. Photodynamic therapy for urological malignancies: past to current approaches. Journal of Urology. 2006; 175:1201-1207.
9. Lee TY, Cheon YK and Shim CS. Current status of photodynamic therapy for bile duct cancer. Clinical Endoscopy. 2013; 46:38-44.
10. Broekgaarden M, Weijer R, van Gulik TM, Hamblin MR and Heger M. Tumor cell survival pathways activated by photodynamic therapy: a molecular framework for inhibition strategies. Cancer and Metastasis Reviews, in press. 2015.
11. Casas A, Di Venosa G, Hasan T and Al B. Mechanisms of resistance to photodynamic therapy. Current Medicinal Chemistry. 2011; 18:2486-2515.
12. Gomer CJ. Induction of prosurvival molecules during treatment: rethinking therapy options for photodynamic therapy. Journal of the National Comprehensive Cancer Network. 2012; 10 Suppl 2:S35-39.
13. Kitagawa N, Kondo S, Wakisaka N, Zen Y, Nakanishi Y, Tsuji A, Endo K, Murono S and Yoshizaki T. Expression of seven-in-absentia homologue 1 and hypoxia-inducible factor 1 alpha: Novel prognostic factors of nasopharyngeal carcinoma. Cancer Letters. 2013; 331:52-57.
14. Theodoropoulos VE, Lazaris AC, Kastriotis I, Spiliadi C, Theodoropoulos GE, Tsoukala V, Patsouris E and Sofras F. Evaluation of hypoxia-inducible factor 1α overexpression as a predictor of tumour recurrence and progression in superficial urothelial bladder carcinoma. BJU International. 2005; 95:425-431.
15. Weijer R, Broekgaarden M, Kos M, van Vught R, Rauws EAJ, Breukink E, van Gulik TM, Storm G and Heger M. Enhancing photodynamic therapy of refractory solid cancers: Combining second-generation photosensitizers with multi-targeted liposomal delivery. Journal of Photochemistry and Photobiology C: Photochemistry Reviews. 2015; 23:103-131.
16. Ratcliffe PJ. Oxygen sensing and hypoxia signalling pathways in animals: the implications of physiology for cancer. Journal of Physiology. 2013; 591:2027-2042.
17. Salceda S and Caro J. Hypoxia-inducible factor 1alpha (HIF-1alpha) protein is rapidly degraded by the ubiquitinproteasome system under normoxic conditions. Its stabilization by hypoxia depends on redox-induced changes. Journal of Biological Chemistry. 1997; 272:22642-22647.
18. Maxwell PH, Wiesener MS, Chang GW, Clifford SC, Vaux EC, Cockman ME, Wykoff CC, Pugh CW, Maher ER and Ratcliffe PJ. The tumour suppressor protein VHL targets hypoxia-inducible factors for oxygen-dependent proteolysis. Nature. 1999; 399:271-275.
19. Chilov D, Camenisch G, Kvietikova I, Ziegler U, Gassmann M and Wenger RH. Induction and nuclear translocation of hypoxia-inducible factor-1 (HIF-1): heterodimerization with ARNT is not necessary for nuclear accumulation of HIF-1alpha. Journal of Cell Science. 1999; 112:1203-1212.
20. Schodel J, Oikonomopoulos S, Ragoussis J, Pugh CW, Ratcliffe PJ and Mole DR. High-resolution genome-wide mapping of HIF-binding sites by ChIP-seq. Blood. 2011; 117:e207-217.
21. Denko NC. Hypoxia, HIF1 and glucose metabolism in the solid tumour. Nature Reviews Cancer. 2008; 8:705-713.
22. Bracken CP, Whitelaw ML and Peet DJ. The hypoxiainducible factors: key transcriptional regulators of hypoxic responses. Cellular and Molecular Life Sciences. 2003; 60:1376-1393.
23. Semenza GL. Targeting HIF-1 for cancer therapy. Nature Reviews Cancer. 2003; 3:721-732.
24. Lu H, Dalgard CL, Mohyeldin A, McFate T, Tait AS and Verma A. Reversible inactivation of HIF-1 prolyl hydroxylases allows cell metabolism to control basal HIF-1. Journal of Biological Chemistry. 2005; 280:41928-41939.
25. Schofield CJ and Ratcliffe PJ. Oxygen sensing by HIF hydroxylases. Nature Reviews Molecular Cell Biology. 2004; 5:343-354.
26. Rohwer N and Cramer T. Hypoxia-mediated drug resistance: novel insights on the functional interaction of HIFs and cell death pathways. Drug Resistance Updates. 2011; 14:191-201.
27. Meijer TW, Kaanders JH, Span PN and Bussink J. Targeting hypoxia, HIF-1, and tumor glucose metabolism to improve radiotherapy efficacy. Clinical Cancer Research. 2012; 18:5585-5594.
28. Mitra S, Cassar SE, Niles DJ, Puskas JA, Frelinger JG and Foster TH. Photodynamic therapy mediates the oxygenindependent

activation of hypoxia-inducible factor 1alpha. Molecular Cancer Therapeutics. 2006; 5:3268-3274.
29. Krieg RC, Herr A, Raupach K, Ren Q, Schwamborn K and Knuechel R. Analyzing effects of photodynamic therapy with 5-aminolevulinic acid (ALA) induced protoporphyrin IX (PPIX) in urothelial cells using reverse phase protein arrays. Photochemical & Photobiological Sciences. 2007; 6:1296-1305.
30. Ferrario A and Gomer CJ. Avastin enhances photodynamic therapy treatment of Kaposi's sarcoma in a mouse tumor model. Journal of Environmental Pathology, Toxicology and Oncology. 2006; 25:251-259.
31. Ferrario A and Gomer CJ. Targeting the 90 kDa heat shock protein improves photodynamic therapy. Cancer Letters. 2010; 289:188-194.
32. Ferrario A, von Tiehl KF, Rucker N, Schwarz MA, Gill PS and Gomer CJ. Antiangiogenic treatment enhances photodynamic therapy responsiveness in a mouse mammary carcinoma. Cancer Research. 2000; 60:4066-4069.
33. Zhou Q, Olivo M, Lye KY, Moore S, Sharma A and Chowbay B. Enhancing the therapeutic responsiveness of photodynamic therapy with the antiangiogenic agents SU5416 and SU6668 in murine nasopharyngeal carcinoma models. Cancer Chemotherapy and Pharmacology. 2005; 56:569-577.
34. Knuth A, Gabbert H, Dippold W, Klein O, Sachsse W, Bitter-Suermann D, Prellwitz W and Meyer zum Buschenfelde KH. Biliary adenocarcinoma. Characterisation of three new human tumor cell lines. Journal of Hepatology. 1985; 1:579-596.
35. Broekgaarden M, Kos M, Jurg FA, van Beek AA, van Gulik TM and Heger M. Inhibition of NF-kappaB in tumor cells exacerbates immune cell activation following photodynamic therapy. International Journal of Molecular Sciences. 2015; 16:19960-19977.
36. Broekgaarden M, de Kroon AI, Gulik TM and Heger M. Development and in vitro proof-of-concept of interstitially targeted zinc-phthalocyanine liposomes for photodynamic therapy. Current Medicinal Chemistry. 2014; 21:377-391.
37. Lee K, Zhang H, Qian DZ, Rey S, Liu JO and Semenza GL. Acriflavine inhibits HIF-1 dimerization, tumor growth, and vascularization. Proceedings of the National Academy of Sciences of the United States of America. 2009; 106:17910-17915.
38. Wainwright M. Acridine—a neglected antibacterial chromophore. Journal of Antimicrobial Chemotherapy. 2001; 47:1-13.
39. Yin T, He S, Shen G and Wang Y. HIF-1 dimerization inhibitor acriflavine enhances antitumor activity of sunitinib in breast cancer model. Oncology Research. 2015; 22:139-145.
40. Wong CC-L, Zhang H, Gilkes DM, Chen J, Wei H, Chaturvedi P, Hubbi ME and Semenza GL. Inhibitors of hypoxia-inducible factor 1 block breast cancer metastatic niche formation and lung metastasis. Journal of Molecular Medicine. 2012; 90:803-815.
41. Hassan S, Laryea D, Mahteme H, Felth J, Fryknas M, Fayad W, Linder S, Rickardson L, Gullbo J, Graf W, Pahlman L, Glimelius B, Larsson R and Nygren P. Novel activity of acriflavine against colorectal cancer tumor cells. Cancer Science. 2011; 102:2206-2213.
42. Dwarakanath BS, Khaitan D and Mathur R. Inhibitors of topoisomerases as anticancer drugs: problems and prospects. Indian Journal of Experimental Biology. 2004; 42:649-659.
43. Berra E, Roux D, Richard DE and Pouysségur J. Hypoxiainducible factor-1α (HIF-1α) escapes O_2-driven proteasomal degradation irrespective of its subcellular localization: nucleus or cytoplasm. EMBO Reports. 2001; 2:615-620.
44. Thurston G, McLean JW, Rizen M, Baluk P, Haskell A, Murphy TJ, Hanahan D and McDonald DM. Cationic liposomes target angiogenic endothelial cells in tumors and chronic inflammation in mice. Journal of Clinical Investigation. 1998; 101:1401-1413.
45. Krammer B. Vascular effects of photodynamic therapy. Anticancer Research. 2001; 21:4271-4277.
46. Chen B, Pogue BW, Hoopes PJ and Hasan T. Combining vascular and cellular targeting regimens enhances the efficacy of photodynamic therapy. International Journal of Radiation Oncology, Biology, and Physics. 2005; 61:1216-1226.
47. Wang GL, Jiang BH, Rue EA and Semenza GL. Hypoxiainducible factor 1 is a basic-helix-loop-helix-PAS heterodimer regulated by cellular O_2 tension. Proceedings of the National Academy of Sciences of the United States of America. 1995; 92:5510-5514.
48. Semenza GL, Roth PH, Fang H-M and Wang GL. Transcriptional regulation of genes encoding glycolytic enzymes by hypoxia-inducible factor 1. Journal of Biological Chemistry. 1994; 269:23757-23763.
49. Papandreou I, Cairns RA, Fontana L, Lim AL and Denko NC. HIF-1 mediates adaptation to hypoxia by actively downregulating mitochondrial oxygen consumption. Cell Metabolism. 2006; 3:187-197.
50. Vos SM, Tretter EM, Schmidt BH and Berger JM. All tangled up: how cells direct, manage and exploit topoisomerase function. Nature Reviews Molecular Cell Biology. 2011; 12:827-841.
51. Ruys AT, van Haelst S, Busch OR, Rauws EA, Gouma DJ and van Gulik TM. Long-term survival in hilar cholangiocarcinoma also possible in unresectable patients. World Journal of Surgery. 2012; 36:2179-2186.
52. Weijer R, Broekgaarden M, van Golen RF, Bulle E, Nieuwenhuis E, Jongejan A, Moerland PD, van Kampen AHC, van Gulik TM and Heger M. Low-power photodynamic therapy induces survival signaling in perihilar cholangiocarcinoma cells. Manuscript in preparation. 2015.
53. Chen W-H, Lecaros RLG, Tseng Y-C, Huang L and Hsu Y-C. Nanoparticle delivery of HIF1α siRNA combined with photodynamic therapy as a potential treatment strategy for head-and-neck cancer. Cancer Letters. 2015; 359:65-74.
54. Bhuvaneswari R, Yuen GY, Chee SK and Olivo M. Hypericin-mediated photodynamic therapy in combination with Avastin (bevacizumab) improves tumor response by downregulating angiogenic proteins. Photochemical & Photobiological Sciences. 2007; 6:1275-1283.
55. Solban N, Selbo PK, Sinha AK, Chang SK and Hasan T. Mechanistic investigation and implications of photodynamic therapy

induction of vascular endothelial growth factor in prostate cancer. Cancer Research. 2006; 66:5633-5640.
56. Strese S, Fryknas M, Larsson R and Gullbo J. Effects of hypoxia on human cancer cell line chemosensitivity. BMC Cancer. 2013; 13:331.
57. Rapisarda A, Uranchimeg B, Sordet O, Pommier Y, Shoemaker RH and Melillo G. Topoisomerase I-mediated inhibition of hypoxia-inducible factor 1: Mechanism and therapeutic implications. Cancer Research. 2004; 64:1475-1482.
58. Beretta GL, Perego P and Zunino F. Targeting topoisomerase I: molecular mechanisms and cellular determinants of response to topoisomerase I inhibitors. Expert Opinion on Therapeutic Targets. 2008; 12:1243-1256.
59. McDonald A and Brown R. Induction of p53-dependent and p53-independent cellular responses by topoisomerase 1 inhibitors. British Journal of Cancer. 1998; 78:745.
60. Moon Y, Dahlberg W, Yu Y, Ohno T, Todoroki T and Little J. Radiosensitivity of human biliary tract cancer cell lines in vitro. International Journal of Oncology. 1997; 10:545-551.
61. Shetty S, Shetty P, Idell S, Velusamy T, Bhandary YP and Shetty RS. Regulation of plasminogen activator inhibitor-1 expression by tumor suppressor protein p53. Journal of Biological Chemistry. 2008; 283:19570-19580.
62. Gramling MW and Church FC. Plasminogen activator inhibitor-1 is an aggregate response factor with pleiotropic effects on cell signaling in vascular disease and the tumor microenvironment. Thrombosis Research. 2010; 125:377-381.
63. Kwaan HC, Mazar AP and McMahon BJ. The apparent uPA/PAI-1 paradox in cancer: more than meets the eye. Seminars in Thrombosis and Hemostasis. 2013; 39:382-391.
64. Devy L, Blacher S, Grignet-Debrus C, Bajou K, Masson V, Gerard RD, Gils A, Carmeliet G, Carmeliet P, Declerck PJ, Nöel A and Foidart J-M. The pro- or antiangiogenic effect of plasminogen activator inhibitor 1 is dose dependent. FASEB Journal. 2002; 16:147-154.
65. Heger M. Editor's inaugural issue foreword: perspectives on translational and clinical research. Journal of Clinical and Translational Research. 2015; 1:1-5.
66. Rouser G, Fkeischer S and Yamamoto A. Two dimensional then layer chromatographic separation of polar lipids and determination of phospholipids by phosphorus analysis of spots. Lipids. 1970; 5:494-496.
67. de Boer OJ, van der Meer JJ, Teeling P, van der Loos CM, Idu MM, van Maldegem F, Aten J and van der Wal AC. Differential expression of interleukin-17 family cytokines in intact and complicated human atherosclerotic plaques. Journal of Pathology. 2010; 220:499-508.
68. van der Loos CM. Chromogens in multiple immunohistochemical staining used for visual assessment and spectral imaging: the colorful future. Journal of Histotechnology. 2010; 33:31-40.
69. Broekgaarden M, Weijer R, van Wijk AC, Cox RC, Egmond MR, Hoebe R, Van Gulik TM and Heger M. Photodynamic therapy with liposomal zinc phtalocyanine and tirapazamine increases tumor cell death via DNA damage. Manuscript in preparation. 2015.
70. Laemmli sample buffer (2X). Cold Spring Harbor Protocols. 2006; 2006:pdb.rec10424.
71. Ji Z, Yang G, Shahzidi S, Tkacz-Stachowska K, Suo Z, Nesland JM and Peng Q. Induction of hypoxia-inducible factor-1alpha overexpression by cobalt chloride enhances cellular resistance to photodynamic therapy. Cancer Letters. 2006; 244:182-189.
72. Ruijter JM, Ramakers C, Hoogaars WM, Karlen Y, Bakker O, van den Hoff MJ and Moorman AF. Amplification efficiency: linking baseline and bias in the analysis of quantitative PCR data. Nucleic Acids Research. 2009; 37:e45.
73. Vichai V and Kirtikara K. Sulforhodamine B colorimetric assay for cytotoxicity screening. Nature Protocols. 2006; 1:1112-1116.
74. Schneider CA, Rasband WS and Eliceiri KW. NIH Image to ImageJ: 25 years of image analysis. Nature Methods. 2012; 9:671-675.

Supplementary information

Gene name	Fw primer sequence	Rv primer sequence	Amplicon size (bp)	PCR efficiency	Melting curve	Electrophoresis
HIF1A	GCGCGAACGACAAGAAAAAGA	CCAGAAGTTTCCTCACACGC	204	high	sp	sb
ANGPT1	GCTCCACACGTGGAACCGGA	CCAGCATGGTAGCCGTGTGGT	175	high	sp, shoulder	sb
ANGPT2	CCCTACGTGTCCAATGCTGT	CCGCTGTTTGGTTCAACAGG	172	medium	sp, wide peak	sb
EDN1	GGGCTGAAGGATCGCTTTGA	GCGCCTAAGACTGCTGTTTC	199	medium	sp	sb
SERPINE1	ATGCCCTCTACTTCAACGGC	TTCCAGTGGCTGATGAGCTG	289	high	sp	sb, mbp
VEGF	CCACACCATCACCATCGACA	CTAATCTTCCGGGCTCGGTG	204	high	sp	sb
HK1	CGCAGCTCCTGGCCTATTAC	CATGATTCACTTGCACCCGC	288	high	sp	sb
LDHA	GACGTCAGCATAGCTGTTCCA	GCAAGTTCATCTGCCAAGTCC	294	high	sp	sb
PDHA	GGAGGCCGGCATCAACC	TTAGCAGCACCATCGCCATA	288	high	sp	sb, mbp
PGK1	CCCTCGTTGACCGAATCACC	CAGCAGCCTTAATCCTCTGGTT	178	high	sp	sb, mbp
PKM2	GGGTTCGGAGGTTTGATG	ACGGCGGTGGCTTCTGT	415	high	sp	sb
BCL2	TTTGTGGAACTGTACGGCCC	CAGCCTGCAGCTTTGTTTCA	230	high	sp	sb
BECN1	ATCTGCGAGAGACACCATCC	TGTCACCATCCAGGAACTCA	137	high	sp	sb
BIRC5	AGGACCACCGCATCTCTACA	TGTTCCTCTATGGGGTCGTCA	187	high	sp	sb
HMOX1	AGGGAATTCTCTTGGCTGGC	GCTGCCACATTAGGGTGTCT	233	high	sp	sb
HSPA5	GGCATCGACCTGGGGACCAC	TCATTCCACGTGCGGCCGAT	215	high	sp	sb
PTGS2	GGCCATGGGGTGGACTTAAA	CCCCACAGCAAACCGTAGAT	192	high	sp	sb
S18 rRNA	TTCGGAACTGAGGCCATGAT	CGAACCTCCGACTTTCGTTCT	151	high	sp	sb

Table S1. Primer information for primer pairs used for qRT-PCR, including amplicon size, PCR efficiency, melting curve analysis, and electrophoretic analysis of the amplicon. PCR efficiencies were categorized as low (<1.7), medium (1.7 - 1.8), or high (>1.8). Melting curves were analyzed for the formation of a single product (sp). Electrophoretic analysis was performed to assess the formation of single bands (sb), where the occurrence of a minor byproduct (mbp) was deemed acceptable.

SK-ChA-1	*HIF1A*	*ANGPT1*	*ANGPT2*	*EDN1*	*SERPINE1*	*VEGF*	*HK1*	*LDHA*	*PDHA*
CTRL 0 h	0.00 ± 0.21	0.00 ± 0.15	0.00 ± 0.54	0.00 ± 0.48	0.00 ± 0.33	0.00 ± 0.35	0.00 ± 0.06	0.00 ± 0.63	0.00 ± 0.63
CTRL 2 h	0.13 ± 0.67	0.43 ± 0.29	-2.61 ± 0.05	-0.52 ± 0.35	0.38 ± 0.64	-0.31 ± 0.45	-0.14 ± 0.23	-0.68 ± 0.30	0.27 ± 0.46
CTRL 4 h	0.12 ± 0.67	-0.57 ± 0.10	-1.54 ± 0.27	0.28 ± 0.13	-0.08 ± 0.09	1.58 ± 0.73	1.16 ± 0.38	-1.30 ± 0.70	-0.57 ± 0.38
ACF 0 h	0.48 ± 0.36	-1.00 ± 0.42	-2.59 ± 0.00	-0.25 ± 0.13	2.44 ± 0.33	-1.01 ± 0.24	1.72 ± 0.68	-0.96 ± 0.84	0.98 ± 0.27
ACF 2 h	-0.20 ± 1.16	-0.28 ± 0.16	-0.58 ± 0.96	-0.79 ± 0.20	3.36 ± 0.37	-0.10 ± 0.71	0.47 ± 1.51	-1.12 ± 0.49	0.65 ± 0.75
ACF 4 h	-0.82 ± 0.85	-0.18 ± 0.50	1.15 ± 1.35	0.83 ± 0.66	3.28 ± 0.51	0.26 ± 0.54	2.21 ± 0.17	-1.14 ± 0.33	0.10 ± 0.22
PDT 0 h	0.27 ± 0.39	-0.21 ± 0.29	-1.78 ± 0.00	-0.22 ± 0.69	1.48 ± 0.48	0.22 ± 0.56	0.39 ± 0.23	0.96 ± 0.21	0.88 ± 0.64
PDT 2 h	0.28 ± 0.21	-0.79 ± 0.40	-1.44 ± 0.53	-0.28 ± 0.42	1.16 ± 0.41	0.76 ± 0.33	-0.44 ± 0.16	0.27 ± 0.27	0.11 ± 0.04
PDT 4 h	-0.50 ± 0.13	0.17 ± 0.25	-1.83 ± 0.14	-0.22 ± 1.01	0.58 ± 0.17	0.90 ± 0.60	-0.09 ± 0.14	-0.91 ± 0.70	-0.11 ± 0.77
ACF + PDT 0 h	-0.26 ± 0.45	-1.03 ± 0.25	0.05 ± 0.21	0.66 ± 0.47	2.21 ± 0.59	-0.23 ± 0.53	1.42 ± 0.28	-1.13 ± 0.93	-0.25 ± 0.29
ACF + PDT 2 h	0.35 ± 0.05	-0.91 ± 0.18	-1.46 ± 0.12	0.54 ± 0.26	2.09 ± 0.48	0.27 ± 0.37	1.07 ± 0.02	-1.51 ± 0.58	-0.30 ± 0.19
ACF + PDT 4 h	-0.38 ± 0.10	-0.85 ± 0.46	-2.07 ± 0.24	1.44 ± 0.60	2.79 ± 0.37	1.03 ± 0.46	1.27 ± 0.56	-0.86 ± 0.72	0.45 ± 0.31

Table S2. Overview of the mean, log_2-transformed fold-changes in mRNA levels and standard deviations of selected target genes obtained in SK-ChA-1 cells. (continued on next page)

SK-ChA-1	*PGK1*	*PKM2*	*BCL2*	*BECN1*	*BIRC5*	*HMOX1*	*HSPA5*	*PTGS2*
CTRL 0 h	0.00 ± 0.73	0.00 ± 0.18	0.00 ± 1.03	0.00 ± 0.21	0.00 ± 0.14	0.00 ± 0.23	0.00 ± 0.08	0.00 ± 0.00
CTRL 2 h	-0.13 ± 0.65	-0.03 ± 0.35	1.36 ± 1.13	-0.38 ± 0.59	0.30 ± 0.34	0.74 ± 0.14	0.09 ± 0.60	1.93 ± 0.30
CTRL 4 h	-0.07 ± 0.14	0.10 ± 0.31	0.22 ± 0.55	-0.86 ± 0.11	-1.07 ± 0.31	0.44 ± 0.40	-0.68 ± 0.40	1.53 ± 0.28
ACF 0 h	-0.37 ± 0.14	-0.35 ± 0.18	-1.68 ± 0.57	0.39 ± 0.98	1.21 ± 0.13	1.30 ± 0.06	-1.78 ± 0.39	-0.16 ± 0.00
ACF 2 h	0.33 ± 0.94	-0.30 ± 0.94	-1.25 ± 1.60	1.06 ± 0.56	1.74 ± 1.01	1.68 ± 1.21	-1.76 ± 0.21	1.93 ± 0.47
ACF 4 h	-0.99 ± 0.76	0.20 ± 0.44	0.37 ± 0.93	1.14 ± 0.52	0.71 ± 0.62	1.42 ± 0.40	0.63 ± 0.11	1.66 ± 1.25
PDT 0 h	-0.20 ± 0.71	-0.05 ± 0.18	-0.73 ± 1.46	-1.09 ± 0.65	0.54 ± 0.50	1.25 ± 0.49	-0.44 ± 0.12	1.71 ± 0.52
PDT 2 h	0.19 ± 0.40	-0.19 ± 0.30	1.12 ± 0.73	-1.01 ± 0.32	-0.07 ± 0.46	0.93 ± 0.55	-0.73 ± 0.15	1.43 ± 0.12
PDT 4 h	-0.78 ± 0.44	-0.25 ± 0.62	-0.99 ± 0.79	-0.81 ± 0.30	0.45 ± 0.20	1.12 ± 0.07	-0.49 ± 0.81	1.38 ± 0.70
ACF + PDT 0 h	0.14 ± 0.11	0.08 ± 0.14	-1.31 ± 0.68	-0.41 ± 0.18	0.54 ± 0.31	0.98 ± 0.38	-1.57 ± 0.59	-0.21 ± 0.43
ACF + PDT 2 h	-0.53 ± 0.24	0.31 ± 0.92	-0.97 ± 0.47	-0.22 ± 0.28	0.05 ± 0.52	0.39 ± 0.30	-1.50 ± 0.60	0.97 ± 0.42
ACF + PDT 4 h	-1.06 ± 0.55	0.34 ± 0.39	-0.49 ± 0.86	-0.13 ± 0.95	0.68 ± 0.60	2.53 ± 0.44	-0.82 ± 1.24	1.84 ± 0.88

Table S2. Overview of the mean, log_2-transformed fold-changes in mRNA levels and standard deviations of selected target genes obtained in SK-ChA-1 cells.

Chapter 6

Photodynamic therapy with liposomal zinc phthalocyanine and tirapazamine increases tumor cell death via DNA damage

Journal of Biomedical Nanotechnology (2016)

MANS BROEKGAARDEN
RUUD WEIJER
ALBERT C. VAN WIJK
RUUD C. COX
MAARTEN R. EGMOND
RON HOEBE
THOMAS M. VAN GULIK
MICHAL HEGER

Abstract

The efficacy of photodynamic therapy (PDT) in some solid tumors is limited by the poor biodistributive properties of conventional photosensitizers and a natural predisposition of tumor cells to survive hypoxia and oxidative stress. This study investigated the therapeutic potential of a third-generation photosensitizer, liposomal zinc phthalocyanine (ZnPC), in combination with the hypoxic cytotoxin tirapazamine (TPZ). TPZ induces DNA double strand breaks (DSBs) under hypoxic conditions and subsequent apoptosis via p53 signaling. Experiments were performed in tumor cells with functional p53 (Sk-Cha1) and dysfunctional p53 (A431).

The combination therapy of TPZ and PDT induced DNA DSBs and cell cycle stalling and enhanced the cytotoxicity of PDT by exacerbating apopotic and non-apoptotic tumor cell death. These phenomena occurred regardless of oxygen tension and the mechanism of cell death differed per cell line. Liposomes containing both ZnPC and TPZ exhibited no dark toxicity but were more lethal to both cell types after PDT compared to ZnPC-liposomes lacking TPZ – an effect that was more pronounced under hypoxic conditions.

In conclusion, TPZ is a suitable pharmaceutical compound to increase PDT efficacy by exploiting the post-PDT tumor hypoxia. The inclusion of TPZ and ZnPC into a single liposomal delivery system was feasible. The PDT strategy described in this study may be valuable for the treatment of PDT-recalcitrant tumors.

Keywords

Reactive oxygen species and oxidative stress, bile duct cancer, cell cycle analysis, phospho-H2AX, JC-1, dichlorodihydrofluorescein diacetate

Introduction

Perihilar holangiocarcinomas (PHCCs) are tumors that most frequently arise at the bifurcation of the common bile duct. The prevalence of these tumors with unknown etiology is merely ~0.0015% but is increasing in the Western population and is associated with a very high mortality rate [1]. The only curative treatment is radical resection of the malignancy, which is not possible in 50-90% of the cases, depending on the treatment center [2]. Patients with non-resectable PHCCs have a median survival time of 6-9 months post-diagnosis [3]. Current palliative radiotherapy and/or chemotherapy regimens can only marginally improve life expectancy (~12 months post-diagnosis) [4], contributing to the dismal prognosis associated with the malignancy. A relatively promising last-line intervention for non-resectable PHCCs is photodynamic therapy (PDT), a treatment modality that was shown to extend patients' average life expectancy to 16 months post-diagnosis [5]. Despite the high cure rates of PDT in many types of cancer [6], PDT of non-resectable PHCCs is not curative but only palliative. Accordingly, there is a clear medical need to develop a more effective last-line and preferably curative intervention for this group of patients.

PDT for solid tumors consists of the oral or systemic administration of a photosensitizer, which preferentially accumulates in endothelial cells of intratumoral vasculature and perivascular tumor mass [7-12], followed by illumination of the tumor with laser light. Illumination causes excitation of the photosensitizer to a singlet and subsequent triplet state and the transfer of energy or the triplet state electron to molecular oxygen (O_2), yielding singlet oxygen ($^1O_2$) or superoxide anion ($O_2^{\bullet -}$), respectively [13]. These reactive oxygen species (ROS) oxidize various intracellular biomolecules and cause necrotic, apoptotic, and/or autophagic death of the photosensitized tumor cells and tumor-associated cells as a result of oxidative stress [14]. Additionally, PDT inflicts shutdown of the tumor microvasculature, resulting in tumor tissue hypoxia/anoxia and hyponutrition [7]. Finally, the destruction of tumor(-associated) cells attracts phagocytic and antigen-presenting cells to the tumor site that fuel a prolonged anti-tumor immune response [15].

With respect to PDT, one experimental approach that may lead to improved therapeutic efficacy is nanoparticle-mediated delivery of the photosensitizer to pharmacologically relevant locations in solid tumors; namely the tumor cells, tumor vasculature, and tumor interstitium [16]. For these purposes our group has developed tumor-targeted liposomes [17], tumor endothelium-targeted liposomes (ETLs) (manuscript in preparation), and interstitium-targeted liposomes [18] that encapsulate the second-generation photosensitizer zinc phthalocyanine (ZnPC), which can be combined in a single PDT modality. Additionally, the liposomes may co-encapsulate pharmacological agents that detrimentally interfere with vital biological and biochemical processes in cancer cells before and/or after PDT so as to further

improve the therapeutic efficacy. Suitable pharmacological targets include the survival pathways that are activated in cancer cells after sublethal PDT, as addressed in [19, 20]. We have further investigated the hypoxia-inducible factor 1 and NF-κB transcription factors as potential therapeutic targets for a PDT-based combination therapy [21-23]. Promising results were obtained with acriflavine, a specific inhibitor of hypoxia inducible factor-1 dimerization and activity [21, 22].

Another important biological process that can be exploited therapeutically is intratumoral hypoxia insofar as a constitutive state of hypoxia is propitious to tumor survival and hence common in many types of cancer [6, 24]. This constitutive and PDT-induced state of hypoxia may be targeted by employing a cytotoxic agent that is activated at low oxygen tension, which can further reduce tumor viability after PDT. A candidate drug for this purpose is tirapazamine (TPZ), a hypoxic cytotoxin capable of inducing oxidative DNA damage at low intracellular oxygen tensions [25]. Several clinical trials in which TPZ was combined with chemotherapy or chemoradiotherapy yielded promising results in non-small cell lung cancer- [26, 27], head-and-neck cancer- [28, 29], and cervical cancer patients [30, 31]. However, clinical trials in which TPZ did not exhibit beneficial effects on the efficacy of chemotherapy have also been published [32]. TPZ has been combined with PDT in a RIF1 murine cancer model using Photofrin (a first-generation photosensitizer) on one occasion, in which the combined therapy yielded a small adjuvant effect [33].

This study therefore explored the potential of TPZ pretreatment to increase the efficacy of PDT with liposomal ZnPC and also explored the feasibility of using a single liposomal formulation that contains both TPZ and ZnPC. Since DNA damage and apoptosis are mainly linked via the tumor suppressor protein p53, experiments were performed with p53-functional Sk-Cha1 biliary adenocarcinoma cells (derived from a tumor type that is recalcitrant to PDT) and with the p53-dysfunctional A431 human epidermoid carcinoma cell line (PDT is generally highly effective in skin cancers) [34]. It is demonstrated that, despite obvious differences in the cellular responses to TPZ, PDT efficacy was significantly improved by TPZ in both cell lines. Furthermore, both TPZ and ZnPC can be combined in a singular drug delivery system to enhance PDT efficacy.

Materials and Methods

Chemicals and reagents

1,2-dipalmitoyl-*sn*-glycero-3-phosphocholine (DPPC), cholesterol, and 3β-[N-(N',N'-dimethylaminoethane)-carbimoyl]cholesterol (DC-cholesterol) were obtained from Avanti Polar Lipids (Alabaster, AL). L-α-Phosphatidylethanolamine, distearoyl methoxypolyethylene glycol conjugate (DSPE-PEG, average PEG molecular mass of 2,000 amu), ZnPC (97% purity), 4-(2-hydroxyethyl)-1-piperazineethanesulfonic acid

(HEPES), bovine serum albumin (BSA, fraction V), L-tryptophan, paraformaldehyde, sucrose, glycine, β-mercaptoethanol, fibronectin, cholesterol, TPZ, ferrous sulfate (Fluka), DMSO, Triton X-100, and pyridine were from Sigma-Aldrich (St. Louis, MO). MitoTracker Red CMX-ROS (MTR), 2',7'-dichlorodihydrofluorescein-diacetate ($DCFH_2$-DA), 5,5',6,6'-tetrachloro-1,1',3,3'-tetraethyl-benzimidazolylcarbocyanine iodide (JC-1), and propidium iodide (PI) were acquired from Life Technologies/ Molecular Probes (Eugene, OR). Ethanol and methanol were from Biosolve (Valkenswaard, the Netherlands). Water-soluble tetrazolium-1 (WST-1) and RNAse A were purchased from Roche Diagnostics (Basel, Switzerland). Anti-phospho-H2AX (Ser139)-AlexaFluor647 (clone 20E3) rabbit monoclonal antibody was from Cell Signaling Technology (Danvers, MA).

For the oxidation and antioxidant assays, $DCFH_2$ (40 mM stock in methanol) was prepared from $DCFH_2$-DA as described in [35]. All (derivatized) lipids were dissolved in chloroform, purged with nitrogen gas, and stored at -20 °C. ZnPC was dissolved in pyridine at a 178-μM concentration, purged with nitrogen gas, and stored at room temperature (RT). The following compounds (stock concentration) were dissolved in DMSO and stored at -20 °C: TPZ (10 mM), JC-1 (5 mg/mL), MTR (10 mM), $DCFH_2$-DA (5 mM), PI (1 mg/mL).

Absorption and fluorescence spectroscopy

Absorption and fluorescence emission and excitation spectroscopy were performed on a Lambda 18 spectrophotometer (Perkin Elmer, Wellesley, MA) and a Cary Eclipse luminescence spectrometer (Varian, Palo Alto, CA), respectively. Spectra were normalized to the maximum absorption or fluorescence emission intensity.

Oxidation assays in cell-free environment

The oxidative and antioxidant properties of TPZ were assayed using an *in vitro* test system as described in [18, 35]. In a first test arm, TPZ-mediated oxidation of the redox-sensitive fluorogenic molecular probe, $DCFH_2$, was assayed [35]. $DCFH_2$ is nonfluorescent at λ_{ex} = 500 nm but is converted to the highly fluorescent dichlorofluorescein (DCF) upon oxidation. Accordingly, 1,483 μL of 'HEPES buffer' (10 mM HEPES in MilliQ, pH = 7.4) was transferred to a cuvette containing a magnetic stirrer that was placed in a temperature-controlled (20 °C) cuvette holder of the spectrofluorometer (operated in kinetics mode). At t = 60 s, 1.5 μL of 40 mM $DCFH_2$ in methanol was added to the buffer. At t = 120 s, 15 μL of TPZ (10 mM in DMSO), DMSO (negative control for TPZ), the oxidizing agent $Fe(II)SO_4$ (30 mM in MilliQ, positive control for TPZ), or MilliQ (negative control for Fe(II)SO4) was added. Spectral acquisition was performed at λ_{ex} = 500 ± 5 nm and λ_{em} = 523 ± 5 nm (DCF fluorescence).

The antioxidant properties of TPZ were assessed in two separate runs using

$DCFH_2$ as a reducing agent and a similar approach as in the previous experiments. In the first run, Fe(II) was employed as an oxidizing agent, whereas in the second run laser-irradiated ZnPC-ETLs (Section Liposome Preparation and Characterization) were used as ROS generator. For run 1, the settings were as follows: t = 0 s, 1,468 µL of HEPES buffer; t = 60 s, 1.5 µL of $DCFH_2$; t = 120 s, 15 µL of 10 mM TPZ, 5 mM of TPZ, 1.25 mM of TPZ, or DMSO; t = 180 s, 15 µL of $Fe(II)SO_4$. Run 2: t = 0 s, 1,468 µL of HEPES buffer; t = 60 s, 1.5 µL of $DCFH_2$; t = 120 s, 15 µL of 10 mM TPZ or DMSO; t = 180 s, 15 µL of ZnPC-ETLs; t = 240-360 s, laser irradiation (300 mW, applied as described in [18]).

Data in all experiments were corrected for the average fluorescence intensity of the last 10 s of acquisition before addition of the last compound to the cuvette.

Liposome preparation and characterization

ZnPC-containing cationic liposomes (referred to as 'ZnPC-ETLs') were prepared according to the lipid film hydration technique [36]. DPPC (66 mol%), DC-cholesterol (25 mol%), cholesterol (5 mol%), DSPE-PEG (4 mol%), and ZnPC (at a 0.003 molar ratio relative to the final lipid concentration [18]) were mixed at the indicated ratios. Liposomes were prepared as described in [18]. ZnPC, with an octanol-water partition coefficient (logP) value of ~8, was incorporated into the lipid bilayer of the liposomes [21]. The ZnPC-ETLs had a diameter of 111.6 ± 3.3 nm, a polydispersity index (PDI) of 0.151 ± 0.038, and a ζ-potential of +4.3 ± 1.1 mV.

TPZ liposomes ('TPZ-ETLs') were prepared in a similar manner as the ZnPC-ETLs, with the exception that TPZ was added to the lipid mixture at predefined molar ratios. TPZ was dissolved in methanol:DMSO:water at a 20:0.2:0.2 volume ratio at a stock concentration of 1 mM. The solution was heated at 60-70 °C until complete dissolution was achieved. Unless indicated otherwise, unencapsulated TPZ was removed by size exclusion chromatography in a 2.5-mL syringe (Sephadex G50 fine, 2.5-mL column volume, centrifugation at 2,000 ×g for 3 min at 4 °C for column drying, 250 µL loading volume, elution at 800 × g for 8 min at 4 °C). The TPZ-ETLs were stored under nitrogen gas at 4 °C in the dark. Size exclusion chromatography was performed within 24 h prior to use. TPZ has a logP of -0.342 [37], is therefore water-soluble, and thus localizes to the aqueous core of the liposome. Following preparation of liposomes by the lipid-film hydration technique using the TPZ solution, the encapsulation efficacy can be derived from the entrapment volume in the liposomes on the basis of the premise that the intraliposomal and extraliposomal TPZ concentrations are equal. We calculated the entrapment volume in accordance with [38] using the abovementioned size, a bilayer thickness of 4.5 nm [39], an average lipid molecular area of 45 Å2 [40], a lipid concentration of 5 mM, and a sample volume of 1 mL. In accordance with these parameters, the encapsulation efficiency was calculated to be 2.4%, which is consistent with entrapment efficiencies reported by us and others for other hydrophilic molecules

[21, 41, 42].

Cell culture

Human epidermoid (A431) carcinoma cells were cultured in phenol red-containing Dulbecco's Modified Eagle's Medium (Gibco), 2 mM L-glutamine, penicillin/streptomycin (100 U/mL and 100 µg/mL, respectively, both from Lonza, Basel, Switzerland). A431 cells were typically subcultured once a week at a 1:25 ratio and seeded at 1.5×10^5 cells/mL. Seeding was performed in 24-wells plates (500 µL of medium per well) or 6-wells plates (2 mL of medium per well) (Costar, Corning, Corning, NY). For all procedures not involving standard cell culture (*i.e.*, the experimental steps), cells were incubated in serum- and phenol red-free, fully supplemented DMEM equilibrated at 37 °C. Human PHCC (Sk-Cha1) cells were cultured in Rosswell Park Memorial Medium (RPMI) 1640 as described in [18].

Cells were maintained at standard normoxic culture conditions (21% O_2, 5% CO_2, 37 °C) or at hypoxic culture conditions (<1% O_2, 5% CO_2, 37°C using a gas mixture of 95% nitrogen, 5% CO_2 (Linde Gas, Schiedam, the Netherlands)). Hypoxic culture conditions were achieved in a custom-built air-tight plastic incubator (11.6 × 9.1 × 5.4 inches) comprised of a gas inlet, a gas outlet connected to a bubble trap, a temperature regulation system (silicone tubing, closed loop system connected to a dual temperature circulator (model TLC 3, Tamson Instruments, Bleiswijk, the Netherlands), a metal grid for the placement of the wells plate, wetted gauze in a petri dish to obtain 99% humidity, and a 2-inch computer fan secured to the metal grid for homogenous gas distribution. The O_2 percentage in the chamber was measured with an OdaLog gas monitor (App-Tek International, Brendale, Australia). The temperature inside the incubator was continuously monitored using a wireless thermometer (Oregon Scientific, Tualatin, Oregon).

Photodynamic therapy and neoadjuvant therapy with TPZ

For PDT, the culture medium was replaced with fresh medium containing ZnPC-ETLs. The ZnPC-ETL final lipid concentration was 10 µM for cells in the normoxia group and 5 µM for cells in the hypoxia group. After 1-h incubation, cells were washed twice with PBS (RT) and resuspended in fresh medium. Next, the cells were irradiated with a 671-nm laser (CNI, Changchun, China) at 500 mW, 60-s pulse duration, and a spot size of 1.9 cm^2, corresponding to an irradiance of 263 mW/cm^2 and a cumulative radiant exposure of 15.8 J/cm^2. Following PDT, cells were incubated at either standard culture conditions or at hypoxic culture conditions, the duration of which is indicated separately per experiment.

Cells were subjected to PDT and normoxic incubation conditions post-PDT as follows. On day 0, all cells were seeded as described in Section Cell Culture and allocated to the control group (CTRL), TPZ group (only TPZ pretreatment), PDT

group (only PDT), or TPZ + PDT group (TPZ pretreatment followed by PDT). On day 1, cells received serum-free medium (CTRL and PDT groups) or serum-free medium containing either 50 μM (A431 cells) or 100 μM TPZ (Sk-Cha1 cells). On day 2, the medium was removed and cells received fresh, serum-free culture medium (CTRL and TPZ groups) or serum-free medium containing 10 μM ZnPC-ETLs (final lipid concentration, PDT and PDT + TPZ groups). Cells were incubated with ZnPC-ETLs for 1 h at standard culture conditions and irradiated as described in Section Cell Culture. Subsequently, cells were kept at standard culture conditions for 4 or 24 h.

Alternatively, cells were subjected to PDT and hypoxic incubation conditions post-PDT as follows. Cells were seeded on day 0 and received TPZ on day 1 (50 μM for A431 cells, 100 μM for Sk-Cha1 cells) for 24 h. Following replacement of medium on day 2, cells were incubated with 5 μM ZnPC-ETLs for 1 h, irradiated, and subsequently maintained under hypoxic culture conditions for 4 or 24 h to mimic vascular shutdown conditions post-PDT. All PDT experiments with TPZ-ETLs were performed with liposomes from which the non-encapsulated TPZ was removed by size exclusion chromatography (Section Liposome Characterization and Preparation).

Determination of cell viability

Cell viability was determined using the WST-1 assay as described in [18].

Measurement of intracellular reactive oxygen species formation

Intracellular ROS formation was detected using $DCFH_2$-DA. The cells were incubated with TPZ (50 μM final concentration) for 24 h, resuspended in fresh medium, and incubated for 4 h at either normoxic or hypoxic conditions (Section Photodynamic Therapy and Neoadjuvant Therapy with TPZ). The medium was then replaced by fresh medium containing 25 μM $DCFH_2$-DA (final concentration) and the cells were incubated for 30 min at standard culture conditions. Next, the cells were washed twice with 0.5 mL PBS (RT) and resuspened in 0.5 mL PBS (RT). Intracellular DCF formation was measured at $\lambda_{ex} = 460 \pm 40$ nm and $\lambda_{em} = 540 \pm 15$ nm in a fluorescence plate reader (BioTek Synergy HT). Immediately thereafter, the PBS was removed and the cells were lysed with lysis solution (20% methanol and 0.1% Triton X-100 in MilliQ, 300 μL/well). Total protein was determined with the bicinchoninic acid assay (Pierce, Rockford, IL). DCF fluorescence intensities were corrected for background fluorescence intensity (control cells not incubated with $DCFH_2$-DA) and divided by the total protein content.

Confocal laser scanning microscopy

For PDT/TPZ-induced DNA damage experiments, cells were seeded in 6-wells plates containing fibronectin-coated microscope coverslips (24 × 40 mm, VWR, Lutterworth, UK) at the densities described in Section Cell Culture. Two lines of experiments were performed in which cells were seeded, treated by PDT, and kept

under either normoxic or hypoxic conditions. In the normoxic test arm, the cells were untreated (CTRL; no TPZ or PDT) or treated with TPZ as described above, PDT (10 μM ZnPC-ETLs (final lipid concentration) for 1 h as described in Section Photodynamic Therapy and Neoadjuvant Therapy with TPZ), or TPZ + PDT. Cells in all groups were kept under normoxic culture conditions for 4 h after treatment. In the hypoxic test arm, the cells were treated as described for the normoxic groups except that a 5-μM ZnPC-ETL final lipid concentration was used in the PDT and TPZ + PDT groups and that the cells were kept for 4 h under hypoxic culture conditions after treatment. When indicated, cells were stained with 50 nM MTR in fresh medium for 30 min at standard culture conditions. For the staining of damaged DNA, cells were permeabilized with 0.1% Triton X-100 in PBS for 5 min and washed with 1 mL of PBS. Subsequently, cells were incubated with anti-phospho-H2AX-AlexaFluor-647 at a 1:100 dilution in 0.5% BSA and 0.15% glycine in PBS (staining buffer) for 16 h at 4 °C. Cells were washed thrice with staining buffer. Subsequently, cells were washed with 1 mL of PBS (RT), fixed in 1 mL of 4% (w/v) paraformaldehyde and 2% (w/v) sucrose for 5 min, and washed with 1 mL of PBS (RT). The coverslips were mounted onto microscope slides using 10 μL of 4',6-diamidino-2-phenylindole (DAPI)-containing Vectashield mounting medium (Vector Labs, Burlingame, CA). The slides were dried for 1 h and sealed with nail polish. Cells were imaged with a Leica TCS SP8 confocal laser scanning microscope (Leica Microsystems, Wetzlar, Germany). Fluorescence was acquired at λ_{ex} = 405 nm and λ_{em} = 415-480 nm for DAPI, λ_{ex} = 470 nm and λ_{em} = 480-550 nm for TPZ, λ_{ex} = 579 nm and λ_{em} = 589-650 nm for MTR, and λ_{ex} = 647 nm and λ_{em} = 657-750 nm for phospho-H2AX-AlexaFluor647.

Cell cycle analysis

For cell cycle analysis, A431 cells were seeded at 7.5×10^4 cells/mL and Sk-Cha1 cells at 1.25×10^5 cells/mL in 6-wells plates. Cells were cultured for 24 h at standard culture conditions until approximately 80% confluence was reached. Afterwards, the cells were incubated for 24 h in medium containing either 50 μM TPZ (A431) or 100 μM TPZ (Sk-Cha1). The cells were washed with PBS (RT) and resuspended in fresh medium containing either 10 μM (normoxia group) or 5 μM (hypoxia group) ZnPC-ETLs (final lipid concentration) for 1 h. Next, the cells were washed twice with PBS (RT), resuspended in fresh medium, and subjected to PDT as described in Section Photodynamic Therapy and Neoadjuvant Therapy with TPZ. After PDT the cells were incubated under either normoxic conditions or hypoxic conditions for 24 h. Next, cells were washed with PBS (RT, 1 mL/well) and harvested by Accutase treatment (250 μL/well, 10 min). The supernatant was removed and cells were resuspended in 0.3 mL PBS (RT) and kept on ice. Subsequently, cells were fixed by the dropwise addition of 0.7 mL of ice-cold 96% ethanol during gentle swerving. The cells were pelleted by centrifugation and the supernatant was aspirated, followed by resuspension of the pellet in 0.5 mL

PBS containing 50 μg/mL PI and 20 μg/mL RNAse A (both final concentrations) and incubation for 30 min at RT in the dark. Cell cycle profiles were obtained by flow cytometry (FACSCantoII, BD Biosciences, Franklin Lakes, NJ) at λ_{ex} = 488 nm and λ_{em} = 585 ± 42 nm (PI fluorescence) and analyzed with FlowJo software (Treestar, Ashland, OR) based on 10,000 events. Cell cycle quantitative metrics ('quantrics') were determined based on the PI fluorescence intensity histograms. The G1 population (one copy of the genome per cell) was characterized by a PI fluorescence peak between 80 and 120 a.u., the G2 population (two copies of the genome per cell) typically exhibited a peak between 180 and 220 a.u. The S-phase population was distinguishable between the G1 and G2 peaks (*i.e.*, PI fluorescence intensity between 120 and 180 a.u.).

Determination of mode of cell death

Loss of mitochondrial membrane potential (MMP) as a result of mitochondrial permeability transition (MPT) was measured with JC-1 as an early marker for apoptosis. Cells were grown in 6-wells plates as described in Section Cell Culture and treated by TPZ (Section Photodynamic Therapy and Neoadjuvant Therapy with TPZ), PDT (Section Photodynamic Therapy and Neoadjuvant Therapy with TPZ), or TPZ + PDT. Following irradiation, the cells were washed with 1 mL of PBS (RT) and resuspended in 500 μL of fresh medium containing JC-1 (10 μg/mL final concentration). The cells were incubated for 30 min at standard culture conditions, washed twice with 1 mL PBS (RT), and detached by Accutase treatment (250 μL/well, ~10 min) at standard culture conditions. Next, 1 mL of medium was added and the cells were centrifuged for 5 min at 400 ×g (4°C), followed by resuspension in 500 μL of ice-cold PBS and flow cytometric analysis (FACSCantoII). JC-1 aggregates in mitochondria (signifying intact MMP) were determined at λ_{ex} = 488 and λ_{em} = 585 ± 42 nm, whereas JC-1 monomers in the cytosol (signifying induction of MPT and loss of MMP) were determined at λ_{ex} = 488 and λ_{em} = 530 ± 30 nm. Viable cells were gated based on forward- and side-scattering properties and subsequently characterized based on their fluorescence properties; green fluorescence indicated cells with perturbed MMP, red fluorescence indicated cells with intact MMP. The percentage of green fluorescent cells was calculated from the total (red + green) events. The data were processed in FlowJo software and presented as average ± SD of 1×10^5 events for N = 3 measurements.

Intracellular TPZ determination

A431 and Sk-Cha1 cells were seeded into 6-wells plates as described Section Cell Culture and grown to confluence overnight. Cells were incubated for 1 h with 100 μM TPZ or 100 μM TPZ-ETLs that contained 1 mM intraliposomal TPZ. It should be noted that the liposomes were not subjected to size exclusion chromatography. The concentration of free TPZ in the medium was therefore 50 μM upon incubation of cells with 100 μM TPZ-ETLs. After incubation, cells were lysed by the addition of 200 μL

of ice-cold MilliQ and 10-min incubation on ice. The lysates were harvested and the residual cells on the plate were dissolved in 750 µL lysis solution (Section Measurement of Intracellular Reactive Oxygen Species Formation). Intracellular TPZ concentrations were measured by spectrophotometric analysis of the lysates (Lambda Bio, Perkin Elmer). The absorption was measured at 470 nm, corrected for background (lysates obtained from cells not incubated with TPZ), and the concentrations were calculated by means of a standard curve (linear regression). The intracellular TPZ concentration was corrected for total protein content using the bicinchoninic acid assay (Section Measurement of Intracellular Reactive Oxygen Species Formation).

Statistical analysis

Statistical analysis was performed in GraphPad Prism (GraphPad Software, La Jolla, CA). Normal distribution of data sets was evaluated with a Kolmogorov-Smirnov test ($N \geq 5$). Differences between normally distributed ordinal variables were tested with one-way ANOVA and a Bonferroni post-hoc test ($N \geq 5$). Non-Gaussian data was analyzed using a Mann-Whitney U-test or a Kruskal-Wallis analysis and Dunn's post-hoc test. In the figures, intergroup differences are indicated with an asterisk and differences between treated groups versus the untreated (CTRL) group are indicated with a pound sign. The level of significance is depicted as a single ($p < 0.05$), double ($p < 0.01$), triple ($p < 0.005$), or quadruple sign ($p < 0.001$). Data are presented as mean ± standard deviation throughout the manuscript.

Results

Oxidant and antioxidant properties of tirapazamine

Measuring the optical properties of TPZ yielded a strong absorption peak at 470 nm (**Fig. 1A**). As shown in **Fig. 1B**, TPZ was unable to oxidize $DCFH_2$, whereas the addition of $Fe(II)SO_4$ caused gradual oxidation of $DCFH_2$ by various ROS intermediates (*e.g.*, $O_2^{\bullet-}$, H_2O_2, $^{\bullet}OH$) formed as a result of reactions between Fe^{2+} and O_2 [43]. For a compound to be used as adjuvant in PDT, it is also essential that the compound possesses minimal-to-no antioxidant properties so that the photoproduced ROS are not scavenged. In a test system where $DCFH_2$ was used as ROS substrate for $Fe(II)SO_4$-produced ROS, the addition of TPZ decreased the oxidation of $DCFH_2$ in a concentration-independent manner by 32.2% on average (**Fig. 1C**). Similarly, the ZnPC-ETL-mediated oxidation of $DCFH_2$ by photoproduced $^1O_2$ [44] was reduced by 21.9% in the presence of TPZ, altogether indicating that TPZ is an antioxidant capable of quenching radical- and non-radical ROS (**Fig. 1D**). This may potentially interfere with PDT efficacy if the intracellular TPZ and ZnPC localization are similar, given the short diffusion distance of photoproduced ROS in a biological milieu [45, 46].

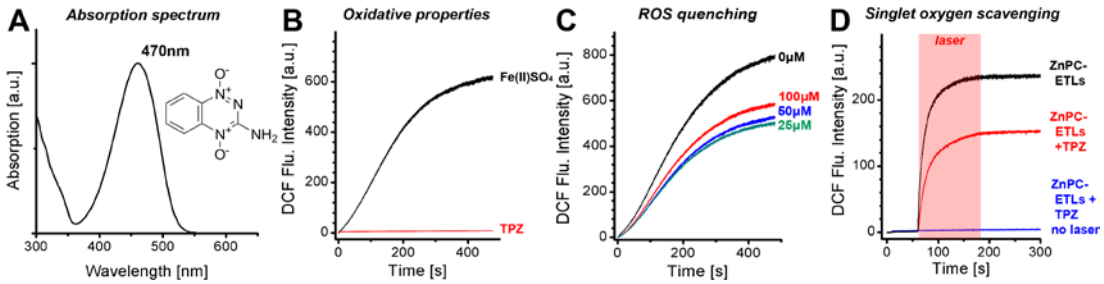

Fig. 1. (**A**) The chemical structure and absorption spectrum of TPZ, showing a maximum at 470 nm (in water). (**B**) The kinetics of the oxidation of non-fluorescent $DCFH_2$ to fluorescent DCF by TPZ and ferrous sulfate ($Fe(II)SO_4$, positive control) were measured by fluorescence spectroscopy. The ROS-quenching capacity of TPZ was measured using $DCFH_2$ as a reducing agent and $Fe(II)SO_4$ (**C**) and laser-irradiated ZnPC-ETLs (**D**) as oxidants. The ZnPC-ETLs were irradiated with a 671-nm laser (the red marquee signifies the irradiation time interval) to induce ROS production [18].

Tirapazamine is toxic under hypoxic conditions in a cell type-dependent manner

Before determining the adjuvant efficacy of TPZ, the inherent toxicity of increasing concentrations TPZ was assessed under normoxic and hypoxic conditions in A431 and Sk-Cha1 cells in the absence of PDT. Under normoxic conditions, TPZ was moderately toxic to A431 (**Fig. 2A**) and Sk-Cha1 cells (**Fig. 2E**) as evidenced by a relative viability of 66% and 60%, respectively, at a 100-μM TPZ concentration. Under hypoxic culture conditions, A431 cells experienced profound toxicity at a TPZ concentration of >10 μM. A similar pattern was observed for Sk-Cha1 cells, although hypoxic A431 cells were more susceptible to TPZ than hypoxic Sk-Cha1 cells. However, hypoxia sensitized both cell types to TPZ, which is potentially beneficial for an acute hypoxia-inducing treatment such as PDT.

Tirapazamine-induced cell death is associated with increased oxidative stress

Since intracellular TPZ is known to form radical species under hypoxic conditions, such as TPZ•, $O_2^{\bullet -}$, and •OH [47], we tested whether cancer cells exhibit increased oxidative stress in the presence of TPZ. Accordingly, cells were incubated with 50 μM (A431 cells) or 100 μM TPZ (Sk-Cha1 cells) for 24 h under normoxic or hypoxic conditions and assayed for oxidative stress using the cell-permeant and redox-sensitive probe $DCFH_2$-DA. In both cell lines, hypoxia resulted in a moderate increase in oxidative stress (**Fig. 2B** and **F**); a phenomenon that has been reported before [48]. TPZ did not result in increased oxidative stress in Sk-Cha1 cells and induced very mild oxidative stress in A431 cells (**Fig. 2B** and **F**). On the other hand, TPZ + hypoxia was associated with a 316% and 162% increase in the degree of oxidative stress in A431 and Sk-Cha1 cells, respectively. These results suggest that the cytotoxicity of TPZ is caused by ROS generation, which is significantly exacerbated under hypoxic conditions.

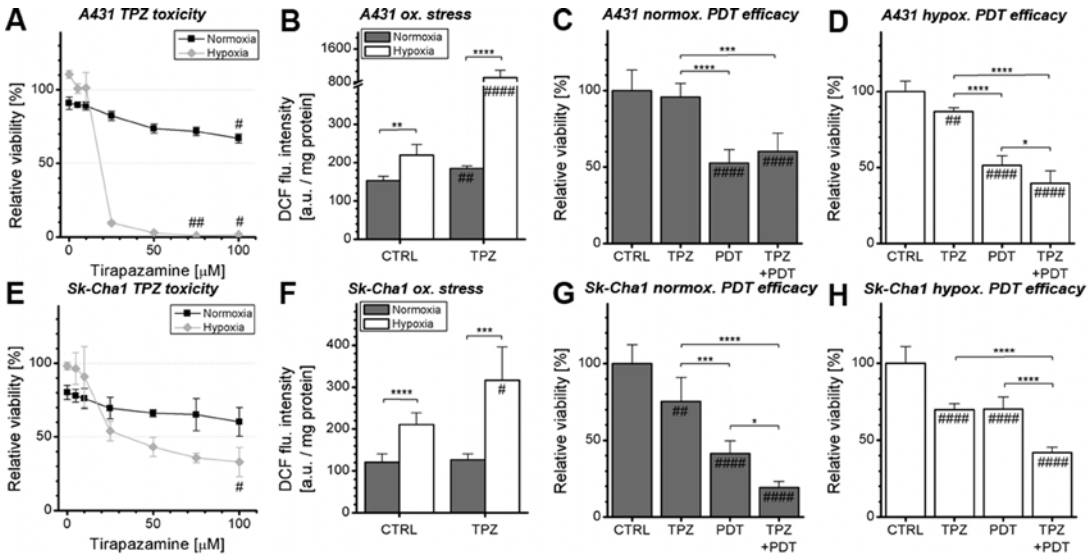

Fig. 2. Effect of TPZ on cell viability, oxidative stress, and PDT efficacy in A431 (**A-D**) and Sk-Cha1 (**E-H**) cells. (**A** and **E**) The 24-h toxicity of TPZ (0-100 μM) in A431 (**A**) and Sk-Cha1 (**D**) cells under normoxic (black) and hypoxic culture conditions (gray). Cells were incubated with serum-free medium containing TPZ and a 1% (v/v) DMSO concentration. The viability of the TPZ-treated cells was normalized to that of untreated cells incubated without DMSO (N = 3/concentration). (**B** and **F**) Oxidative stress was measured in A431 cells (**B**) and Sk-Cha1 cells (**F**) using $DCFH_2$-DA. Cells were exposed to 50 or 100 μM TPZ and kept under normoxic (gray) or hypoxic conditions (white) for 24 h (N = 6/treatment group/condition). Fluorescence intensities of DCF were corrected for protein content. (**C** and **G**) Viability of A431 and Sk-Cha1 cells that were incubated under normoxic conditions with serum-free medium for 24 h and left untreated (CTRL), with serum-free medium containing TPZ (TPZ), with serum-free medium and treated with PDT (PDT), or with serum-free medium containing TPZ and subsequently treated with PDT (TPZ + PDT) (N = 6/group). Viability was assayed 4 h after incubation under normoxic (**C** and **G**) or hypoxic conditions (**D** and **H**). The final TPZ concentrations used were 50 μM and 100 μM in A431 and Sk-Cha1 cells, respectively. PDT was performed with 10 μM of ZnPC-ETLs (normoxia groups) or 5 μM ZnPC-ETLs (hypoxia groups) (final lipid concentration). All data were normalized to control values. Readers are referred to section 2.13 for the significance of the statistical symbols.

Tirapazamine exacerbates PDT-induced cell death in a cell type-dependent manner

To test whether normoxic pre-incubation of cells with minimally toxic concentrations of TPZ could exacerbate PDT-induced cell death, cells were incubated for 24 h with either 50 μM TPZ (A431 cells) or 100 μM TPZ (Sk-Cha1 cells) as these concentrations resulted in a ~40% reduction in viability in the cell lines (**Fig. 2A** and **E**). Subsequently, cells were treated with PDT and cultured for 4 h under either normoxic or hypoxic conditions. It should be underscored that, when normoxic incubation was performed post-PDT, cells were photosensitized with 10 μM ZnPC-ETLs. When incubation was performed under hypoxic conditions post-PDT, cells were photosensitized with 5 μM ZnPC-ETLs. These regimens induced a ~50% reduction in viability under the given experimental conditions, and were employed in all experiments unless noted otherwise. The hypoxic conditions were tested to resemble the post-PDT tumor microenvironment (vascular shutdown-mediated hypoxia).

TPZ exhibited no normoxic toxicity and mild hypoxic toxicity in A431 cells (**Fig. 2C** and **D**). PDT alone decreased the relative viability of A431 cells to 52-51% under both normoxia and hypoxia. The combination of PDT with TPZ pre-incubation (TPZ + PDT) did not further reduce cell viability in normoxic A431 cells (relative viability of 60%) compared to PDT alone, but significantly decreased the viability to 39% when A431 cells were incubated under hypoxic conditions after PDT.

For Sk-Cha1 cells (**Fig. 2G** and **H**), TPZ pre-incubation was mildly toxic under both normoxic and hypoxic conditions (relative viability of 70-75%). PDT alone reduced the relative cell viability to 42% under normoxic conditions (10 μM ZnPC-ETLs) and to 70% under hypoxic conditions (5 μM ZnPC-ETLs). In contrast to A431 cells, Sk-Cha1 cells were more sensitive to TPZ + PDT compared to PDT alone, yielding an additional reduction in relative cell viability of 22% and 28% under normoxic and hypoxic conditions, respectively. As such, these data represent a 54% and 41% increase in efficacy when PDT was combined with TPZ versus PDT alone under normoxic and hypoxic conditions, respectively.

In sum, the findings indicate that TPZ preconditioning can be used to considerably increase the therapeutic efficacy of PDT in Sk-Cha1 cells and to a much lesser extent in A431 cells.

Tirapazamine induces DNA damage in a PDT-independent manner

To investigate the manifestation of TPZ-induced DNA damage after PDT in accordance with literature [49-51], cells were either left untreated or treated by TPZ for 24 h, PDT (5 μM ZnPC-ETLs), or TPZ + PDT, incubated for 4 or 24 h under hypoxic conditions to mimic the *in vivo* conditions, and stained with anti-phospho-H2AX; an epigenetic marker for DNA DSBs [52]. The DNA DSB data obtained at 4 h post-PDT are presented in **Fig. 3**. Representative cell cycle profiles of similarly treated cells were assayed after 24 h of hypoxic incubation post-PDT/CTRL treatment and are also presented in **Fig. 3**. The cell cycle quantrics are provided in **Fig. 4**.

A431 cells in the control (**Fig. 3A** and **B**) and PDT group (**Fig. 3E** and **F**) exhibited only minor levels of phospho-H2AX foci, indicating that neither hypoxia nor PDT induced DNA DSBs. Constitutive DNA damage was more prevalent in A431 cells compared to Sk-Cha1 cells (**Fig. 3E** versus **F** and **Fig 5A/E** versus **B/F**), which is consistent with the fact that A431 cells do not contain a functional p53 protein and thus better tolerate DNA damage [34], which is not the case for Sk-Cha1 cells [53]. P53 is responsible for DNA repair and initiation of DNA damage-induced apoptosis and regulates cell cycle progression based on the extent of DNA damage [54]. The cell cycle profiles confirm that the distribution of cells in G1, S, or G2/M phase was only minimally affected by PDT, although A431 cells did exhibit a mild proliferative tendency in response to PDT as evidenced by the slightly elevated S- and G2/M phase cell populations (**Fig. 3A** and **Fig. 4A**).

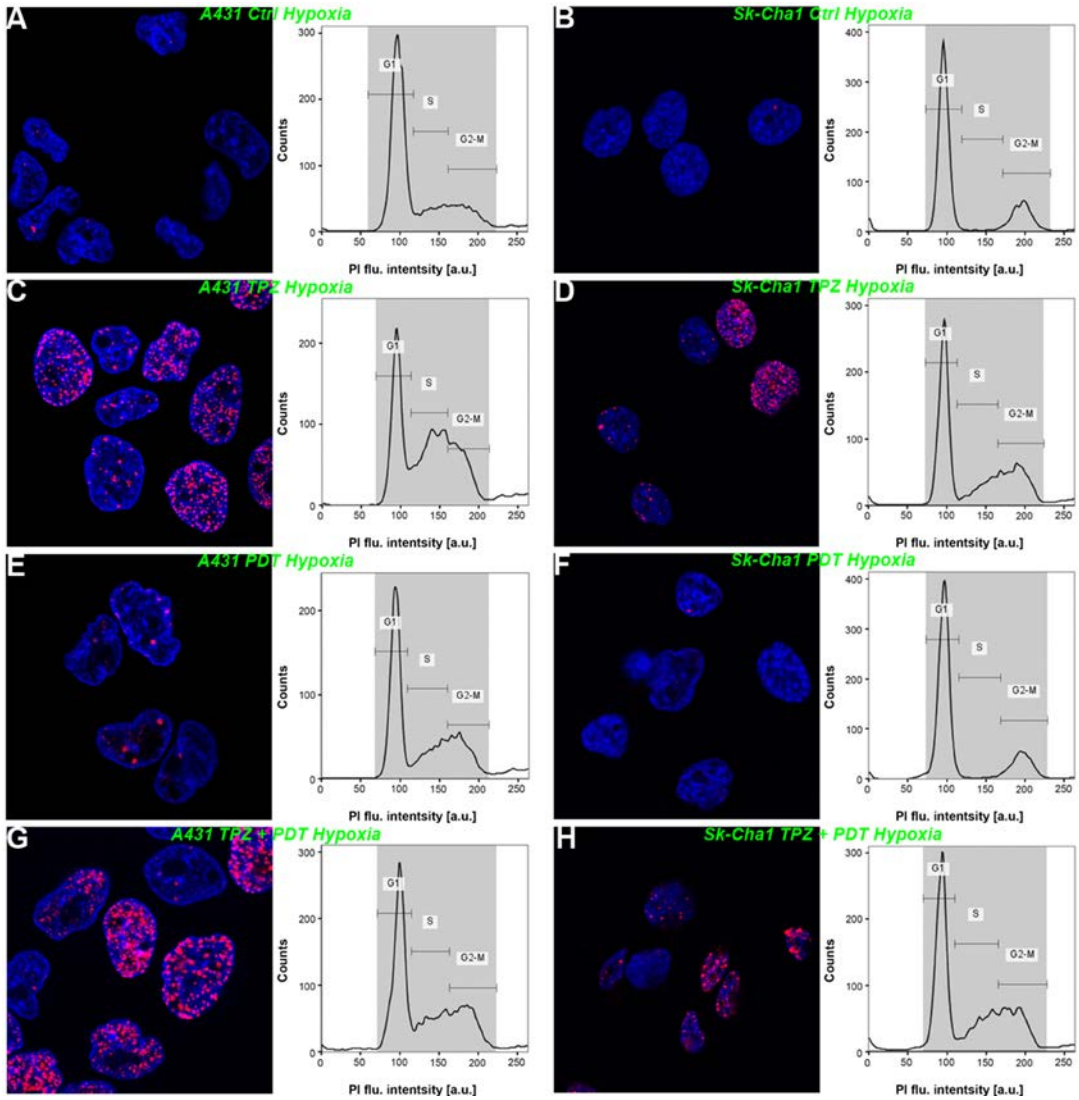

Fig. 3. Confocal laser scanning microscopy of DNA damage and cell cycle profiles of differently treated cells following hypoxic incubation. A431 (panels **A**,**C**,**E**,**G**) and Sk-Cha1 cells (panels **B**,**D**,**F**,**H**) were pretreated with non-supplemented medium (Ctrl and PDT) or medium supplemented with TPZ (A431, 50 μM; Sk-Cha1, 100 μM) and incubated under normoxic conditions for 24 h. Afterwards, cells were either not irradiated (Ctrl, TPZ) or treated by PDT (PDT and TPZ + PDT, 5 μM ZnPC-ETLs). All cells were incubated under hypoxic conditions for 4 h and assayed for DNA DSBs by confocal microscopy following phospho-H2AX (red) and DAPI (blue) staining. Additionally, the cell cycle profiles were determined in each group by flow cytometry after 24 h of hypoxic incubation. The G1, S, and G2/M populations are indicated in the histograms (representative histograms are provided from N = 3 experiments/group). The groups are labeled in green at the top of each panel set.

TPZ pretreatment and subsequent hypoxic incubation induced visibly higher levels of phospho-H2AX foci in both A431 and Sk-Cha1 cells (**Fig. 3C** and **D**, respectively). The DNA DSBs led to prominent changes in cell cycle profiles after 24 h. The distribution of cells in the S-phase reveals that S-phase inflow was increased

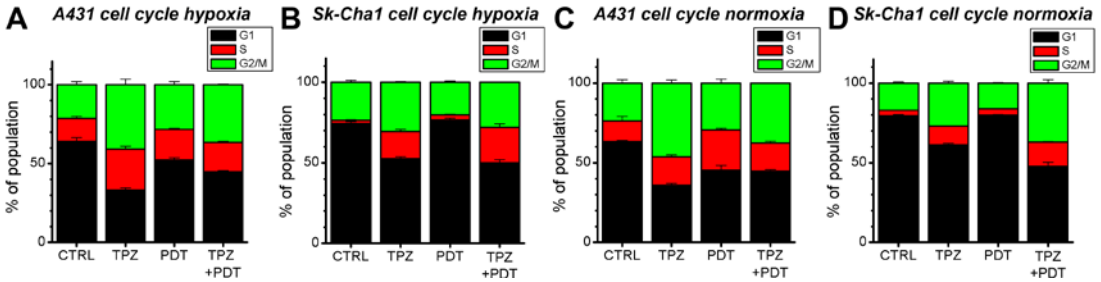

Fig. 4. Cell cycle quantrics in A431 and Sk-Cha1 cells per treatment group and incubation condition as indicated at the top of each panel. Cells were subjected to TPZ (50 μM for A431 and 100 μM for Sk-Cha1), PDT (5 μM ZnPC-ETLs for hypoxic cells and 10 μM ZnPC-ETLs for normoxic cells), or both (TPZ + PDT). Cells were kept under hypoxic or normoxic conditions for 24 h post-PDT.

in A431 cells (**Fig. 3C** and **Fig. 4A**) but unaltered in Sk-Cha1 cells (**Fig. 3D** and **Fig. 4B**) compared with control cells. Accumulation of cells in late S-phase occurred in both cell lines, supporting the hypothesis that the stalling of DNA replication forks during S-phase by inhibition of topoisomerase (necessary for DNA unwinding to allow replication) [55] leads to an intra-S-phase arrest in the presence of TPZ [56]. The increase in DNA DSBs in TPZ-treated hypoxic cells may also explain the increase in G2/M populations, since DNA damage typically stimulates G2 arrest prior to M-phase entry [57].

Similar results regarding DNA DSBs and effects on cell cycle profiles were observed in cells pre-incubated with TPZ and subsequently treated with PDT (**Fig. 3G** and **H** and **Fig. 4A** and **B**). Taken together, the reduction in cell viability following TPZ + PDT seems to stem from TPZ-induced DNA damage and cell cycle stalling.

Tirapazamine induces DNA damage under normoxia in a PDT-independent manner

As was shown in **Fig. 2C** and **G**, TPZ also affected cell viability under normoxic conditions. In order to determine whether TPZ exerts its DNA-damaging effects under normoxic conditions, A431 and Sk-Cha1 cells underwent similar treatments as in the previous section, with the exception that the cells were kept under normoxic conditions under all circumstances and were photosensitized with 10 μM ZnPC-ETLs.

The phospho-H2AX staining in untreated cells revealed that the nuclei of A431 cells contained multiple phospho-H2AX-positive foci, whereas these were largely absent in Sk-Cha1 cells (**Fig. 5A** and **B**, respectively). The DNA damage translated to similar cell cycle characteristics as reported for hypoxic cells in both cell lines (**Fig. 5A** and **B** and **Fig. 4C** and **D**). The degree of DNA DSBs did not increase in Sk-Cha1 cells after PDT (**Fig. 5F**), whereas the extent of DNA damage was slightly exacerbated after PDT in A431 cells (**Fig. 5E**), which was accompanied by a mild increase in cell populations in the S-phase and G2/M-phase (**Fig. 5E** and **Fig. 4C**). TPZ treatment increased the number of phospho-H2AX foci under normoxic conditions (**Fig. 5C** and **D**), although the effect was not as extensive as under hypoxic conditions (**Fig. 3C**

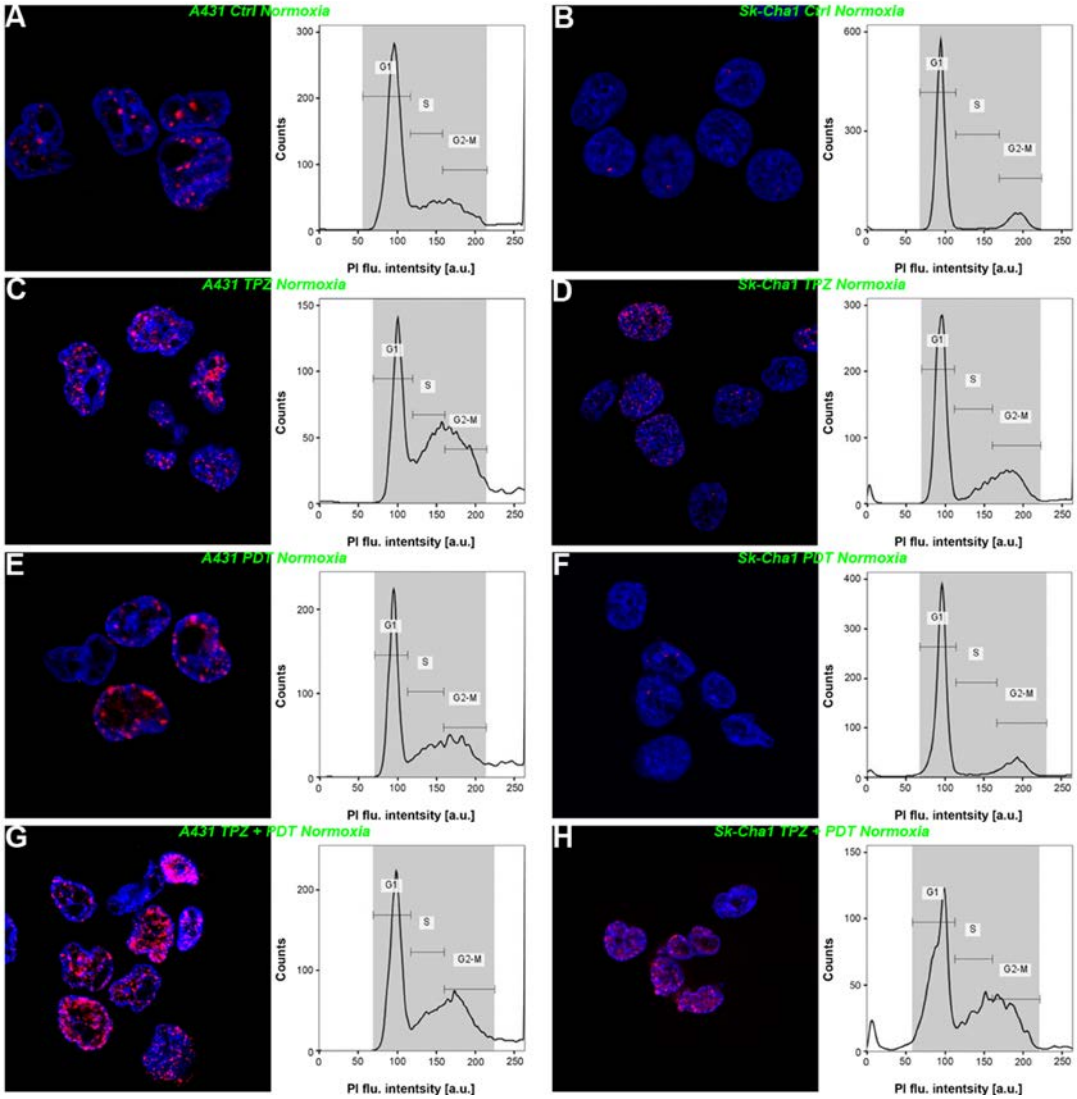

Fig. 5. Confocal laser scanning microscopy of DNA damage and cell cycle profiles of differently treated cells following normoxic incubation. A431 (panels **A**,**C**,**E**,**G**) and Sk-Cha1 cells (panels **B**,**D**,**F**,**H**) were pretreated with non-supplemented medium (Ctrl and PDT) or medium supplemented with TPZ (A431, 50 μM; Sk-Cha1, 100 μM) and incubated under normoxic conditions for 24 h. Afterwards, cells were either not irradiated (Ctrl, TPZ) or treated by PDT (PDT and TPZ + PDT, 10 μM ZnPC-ETLs). All cells were incubated under normoxic conditions for 24 h and assayed for DNA DSBs by confocal microscopy following phospho-H2AX (red) and DAPI (blue) staining. Additionally, the cell cycle profiles were determined in each group by flow cytometry after 24 h of normoxic incubation. The G1, S, and G2/M populations are indicated in the histograms (representative histograms are provided from N = 3 experiments/group). The groups are labeled in green at the top of each panel set.

and **D**). As reported for the hypoxic conditions, the cell cycle profiles under normoxic conditions revealed an increased proliferation rate in TPZ-subjected A431 cells (**Fig. 5C** and **Fig. 4C**) and an increase in the number of late-S-phase Sk-Cha1 cells (**Fig. 5D**

and **Fig. 4D**), which suggests that the implicated topoisomerase inhibition is hypoxia-independent. TPZ + PDT (**Fig. 5G-H**) visibly increased the phosho-H2AX foci to a comparable level as observed under hypoxic conditions (**Fig. 3G** and **H**). Accordingly, the transient depletion of oxygen by PDT (O_2 → ROS) may be sufficient to produce TPZ$^{\bullet}$ capable of inducing DNA oxidation and subsequent DNA DSBs insofar as prolonged hypoxia did not greatly exacerbate the occurrence of these lesions (**Fig. 3G** and **H**). Cell cycle analysis of cells treated with TPZ + PDT and subsequent normoxic incubation further confirms that the resulting DNA damage culminates in S-phase stalling and G2-arrested cells (**Fig. 5G/H** and **Fig. 4C/D**). Thus, the adjuvant effect of TPZ to the efficacy of PDT is not limited by oxygen tension, as TPZ induces DNA damage and increases the PDT effect even under normoxic culture conditions.

Tirapazamine is a potent inducer of apoptosis in combination with PDT

During imaging of DNA DSBs (**Fig. 3** and **5**) we frequently observed blebbing nuclei in the treated Sk-Cha1 cells, which is indicative of apoptosis. Additional confocal microscopy was therefore performed with Sk-Cha1 and A431 cells that had been treated with TPZ and TPZ + PDT and labeled with MTR, DAPI, and phospho-H2AX. Both treatments yielded a substantial amount of apoptotic Sk-Cha1 cells (exposed to 100 μM TPZ) with distinct blebbing morphology (**Fig. 6A-D**, arrows) regardless of

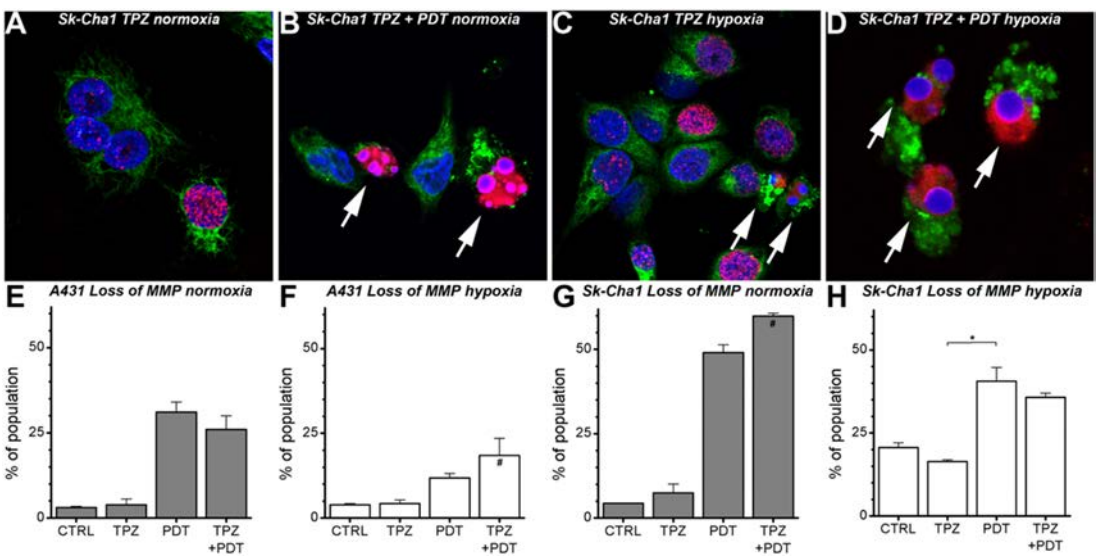

Fig. 6. (**A-D**) Confocal microscopy images of Sk-Cha1 cells subjected to 100 μM TPZ (**A**) or 100 μM TPZ + 10 μM ZnPC-ETL-PDT (**B**) and normoxic post-PDT conditions or to 100 μM TPZ (**C**) or 100 μM TPZ + 5 μM ZnPC-ETL-PDT (**D**) and hypoxic post-PDT conditions. All images were acquired 4 h after treatment. Nuclei are shown in blue, phospho-H2AX is depicted in red, and MitoTracker Red CMX-ROS is depicted in green. Arrows indicate apoptotic cells with typical nuclear blebbing morphology. (**E-H**) Loss of MMP in A431 and Sk-Cha1 cells per treatment group and incubation condition (indicated at the top of each panel). Readers are referred to Section Statistical Analysis for the significance of the statistical symbols.

oxygen tension. In addition, the apoptotic nuclei were intensely positive for phospho-H2AX, which may be a consequence of nuclease activity inherent to apoptosis [58] or the result of extensive TPZ/TPZ•-mediated DNA DSB formation. The apoptosis-associated blebbing was not observed in A431 cells incubated with 50 μM TPZ (not shown).

The intrinsic pathway of apoptosis is characterized by mitochondrial permeability transition (MPT) and loss of MMP, which ensues *e.g.*, p53-mediated pro-apoptotic BCL-2 protein activation (including BAX, PUMA, and NOXA). Loss of mitochondrial membrane integrity as a result of MPT can be measured with the fluorescent probe JC-1 [59] (Section Determination of Mode of Cell Death).

Under normoxic conditions, the majority of control and 50 μM TPZ-treated A431 cells did not exhibit mitochondrial membrane perturbations (**Fig. 6E**), which is in line with the viability data (**Fig. 2C**). PDT with ZnPC-ETLs (10 μM) caused a 31% increase in MPT, whereas the TPZ + PDT regime had no additional effect on mitochondrial integrity (**Fig. 6E**). These findings are in agreement with the viability profiles of comparably treated normoxic A431 cells (**Fig. 2C**). Similar trends were observed in hypoxic A431 cells in the control, TPZ (50 μM), and PDT (5 μM ZnPC-ETLs) groups (**Fig. 6F**), although the effect of PDT on MPT was dampened under hypoxic conditions relative to normoxic cells, while TPZ exacerbated the loss of mitochondrial integrity in PDT-treated A431 cells. These findings were mirrored by significantly increased oxidative stress by TPZ (**Fig. 2B**) and relative viability data (**Fig. 2D**) under hypoxia.

With respect to Sk-Cha1 cells, normoxic cells exhibited similar levels of MMP loss (4% of cells) as normoxic A431 cells, whereas hypoxia considerably increased MMP loss to 21% of cells (**Fig. 6G**). TPZ (100 μM) had no significant effect on MMP loss under normoxic conditions (**Fig. 6G**), despite the fact that it was associated with reduced cell viability (**Fig. 2G**) in a ROS-independent manner (**Fig. 2F**). Furthermore, 100 μM TPZ exhibited a tendency towards cytoprotection (albeit not significant) under hypoxia (**Fig. 6G**) despite the considerable TPZ-induced increase in oxidative stress (**Fig. 2F**) and reduction in cell viability (**Fig. 2H**). PDT (10 μM ZnPC-ETLs) caused MMP loss in a significantly higher percentage of normoxic cells (49%), which was further aggravated in cells treated with 100 μM TPZ + 5 μM ZnPC-ETL PDT (60%). The effect of PDT on MMP loss was slightly reduced under hypoxic conditions, where TPZ exhibited no additional effect on MMP loss in PDT-subjected Sk-Cha1 cells (**Fig. 6H**), suggesting that other cell death pathways may cause the reduction in cell viability (**Fig. 3H**).

Encapsulation of tirapazamine in ZnPC-ETLs increases the efficacy of PDT

TPZ is very poorly taken up by cells [60] yet exacerbates the extent of PDT-induced cell death in hypoxic A431 cells (**Fig. 2D**) and in Sk-Cha1 cells regardless of

oxygen tension (**Fig. 2G** and **H**). The inclusion of TPZ into ZnPC-ETLs may therefore increase the intracellular availability of TPZ and further increase PDT efficacy using a single drug delivery system. In the last set of experiments, ZnPC- and TPZ-ETLs were prepared with fixed ZnPC content and increasing TPZ concentrations. To investigate whether these liposomes remain stable in the presence of ZnPC, the size and PDI of TPZ-ETLs were assayed during 7 days post preparation, whereby the liposomes were either stored at 4 °C or 37 °C. The results (**Table 1**) indicate that the size and PDI remained stable throughout the experiment, and were not affected by the storage temperature or the presence of ZnPC.

Formulation: DPPC:chol:DC-chol:DSPE-PEG (66:5:25:4), 1 mM TPZ				
	4 °C		**37 °C**	
Day	**Size [nm]**	**PDI**	**Size [nm]**	**PDI**
0	114.0 ± 1.8	0.189 ± 0.034	114.0 ± 1.8	0.189 ± 0.034
1	114.4 ± 1.1	0.205 ± 0.044	113.1 ± 2.2	0.219 ± 0.032
3	110.5 ± 0.9	0.143 ± 0.018	111.6 ± 1.4	0.178 ± 0.014
7	112.5 ± 1.2	0.199 ± 0.037	114.6 ± 2.2	0.194 ± 0.019
Formulation: DPPC:chol:DC-chol:DSPE-PEG (66:5:25:4), ZnPC (0.003 ZnPC:lipid), 1 mM TPZ				
	4 °C		**37 °C**	
Day	**Size [nm]**	**PDI**	**Size [nm]**	**PDI**
0	108.8 ± 1.7	0.170 ± 0.013	108.8 ± 1.7	0.170 ± 0.013
1	111.1 ± 2.2	0.202 ± 0.014	107.8 ± 2.7	0.189 ± 0.026
3	108.0 ± 1.7	0.172 ± 0.016	107.8 ± 2.2	0.130 ± 0.019
7	111.3 ± 1.4	0.147 ± 0.018	111.7 ± 2.8	0.182 ± 0.021

Table 1. Stability of TPZ-ETLs in the absence and presence of ZnPC in terms of liposome size, PDI, and storage temperature.

Fig. 7A and **E** illustrate that incubation of cells with TPZ-ETLs (1 mM intraliposomal TPZ concentration) versus cells incubated with free TPZ (100 μM) resulted in an approximately 10-fold increase in intracellular TPZ in case of the TPZ-ETLs. This proved that liposomal encapsulation of TPZ results in increased intracellular availability of TPZ. All further experiments were performed with TPZ-ETL solutions from which the non-encapsulated TPZ had been removed. **Fig. 7B** and **F** show that there is no dark toxicity of TPZ-ETLs in A431 and Sk-Cha1 cells at a final lipid concentration of 10 μM. More importantly, the therapeutic efficacy of PDT with TPZ-ETLs was substantially higher compared to PDT with free TPZ preconditioning. Inclusion of 0.1 and 1 mM of TPZ into ZnPC-ETLs decreased A431 cell viability after PDT to 62% and 67% under normoxic conditions (**Fig. 7C**), respectively, and to 32% and 34% under hypoxic conditions (**Fig. 7D**), respectively, compared to PDT with TPZ-lacking ZnPC-ETLs (representing 100% relative viability). A similar dose effect was observed in Sk-Cha1 cells; incorporation of 0.1 and 1 mM of TPZ into ZnPC-ETLs decreased the relative viability after PDT to 73% and 63% under normoxic conditions (**Fig. 7G**),

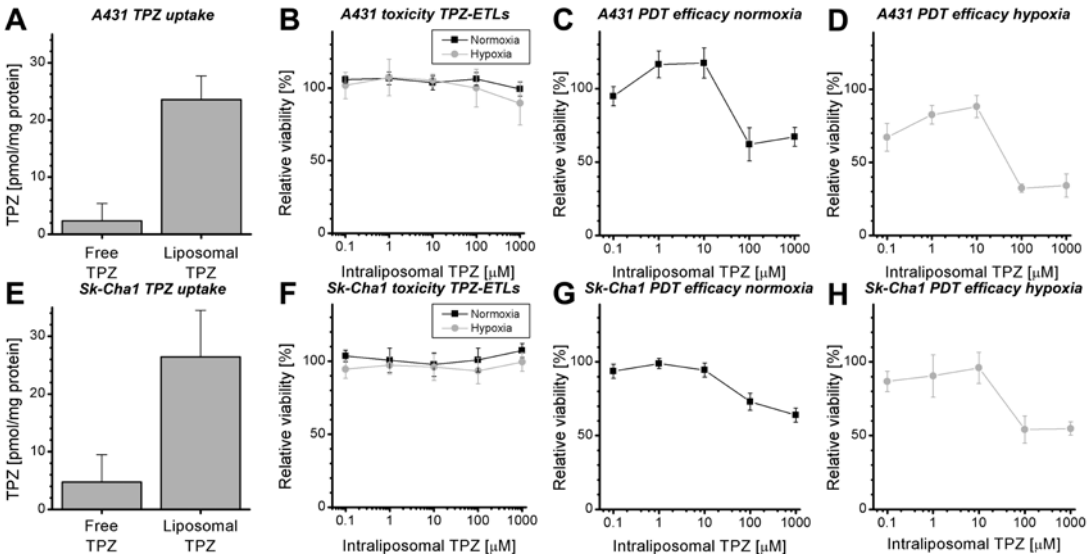

Fig. 7. Intracellular TPZ concentrations, dark toxicity, and PDT efficacy of TPZ-containing ZnPC-ETLs in A431 cells (**A**-**D**) and Sk-Cha1 cells (**E**-**H**) under normoxic- (black squares) or hypoxic conditions (grey circles). (**A**, **E**) Cells were exposed to either 100 μM TPZ or 100 μM of ZnPC-ETLs (final lipid concentration, medium contained 50 μM free TPZ) containing 1 mM intraliposomal TPZ for 1 h, after which the intracellular TPZ concentration was determined (N = 3). (**B**, **F**) Cells were exposed to 10 μM of ZnPC-ETLs (final lipid concentration) containing increasing intraliposomal TPZ concentrations for 24 h under normoxic- or hypoxic culture conditions in the absence of PDT (N = 4). (**C**, **G**) The normoxic PDT efficacy was determined after incubation of cells for 1 h with 10 μM of ZnPC-ETLs containing increasing intraliposomal TPZ concentrations, after which cells were subjected to PDT and subsequently maintained under normoxic conditions. After 4 h the relative viability was determined relative to cells that had been subjected to PDT with ZnPC-ETLs without TPZ (N = 4). (**D**, **H**) The same procedure was followed as in (**B** and **E**), only the cells were incubated under hypoxic conditions after PDT (N = 4).

respectively, and to 54% and 55% under hypoxic conditions (**Fig. 7H**), respectively, compared to ZnPC-ETLs not containing TPZ. The data provide compelling *in vitro* proof-of-concept for the use of fourth-generation photosensitizers (*i.e.*, a second-generation photosensitizer (ZnPC) encapsulated in a targeted photosensitizer delivery system (liposomes) with co-encapsulated adjuvant chemotherapeutics (TPZ)) for PDT.

Discussion

This study investigated the adjuvant effect of TPZ on PDT efficacy in cells derived from a therapy-resistant tumor (PHCC, Sk-Cha1) and in cells (A431) derived from a tumor that is equally relevant for PDT but that is distinct from Sk-Cha1 cells with respect to p53 functionality. Although Sk-Cha1 cells carry a missense mutation in the *TP53* gene that encodes the DNA binding domain, there is ample evidence that p53 is functional in these cells [61]. In contrast, A431 cells have lost a *TP53* allele and carry a missense mutation in the region that encodes the DNA binding domain of the remaining protein, substantially lowering their p53 signaling capability [34, 62].

The most important findings of this study were that, firstly, TPZ exacerbated

PDT-induced cell death under hypoxic conditions in both cell lines. This appeared to be the result of a chain of events that included TPZ• formation by nuclear reductases, the consequent induction of DNA DSBs, stalling of cell division, loss of MMP, and cell death via apoptosis. However, there were several important differences observed between the cell lines. Under hypoxic conditions, TPZ was more toxic to A431 cells compared to Sk-Cha1 cells, yet TPZ exhibited an adjuvant effect on PDT efficacy under normoxic conditions in Sk-Cha1 cells but not in A431 cells (albeit at a two-fold higher TPZ concentration than was used for A431 cells). Secondly, the extent of TPZ's adjuvant efficacy was not reliant on the p53 protein insofar as a decrease in post-PDT cell viability was observed in both cells lines under hypoxic conditions. Thirdly, these positive results prompted the development of liposomes that included both TPZ and ZnPC in a single liposomal formulation so as to enable the optimal delivery of both compounds to tumor cells. The TPZ-ETLs exhibited no dark toxicity but were more lethal to either cell type after PDT compared with ZnPC-ETLs lacking TPZ – an effect that was more pronounced in A431 cells than in Sk-Cha1 cells, especially under hypoxic conditions.

Before discussing the neoadjuvant effect of TPZ on PDT efficacy, it is imperative to address TPZ as a stand-alone pharmaceutical compound in the absence of PDT. The putative mechanism of action entails the TPZ → TPZ• conversion in the nucleus under hypoxic conditions, resulting in oxidative damage to DNA bases [63] through the formation of formamidopyrimidine and 5-hydroxy-6-hydropyrimidine [64], potentially leading to mismatches and single strand breaks (SSBs) [65]. This type of base damage is either repaired via base excision repair [66] or results in DNA DSBs when cells with DNA lesions progress through S phase [67, 68]. Accordingly, TPZ•-induced DNA base damage, SSBs, and DSBs have been reported previously [50]. The different types of DNA damage may emanate from TPZ's hypoxia-independent inhibition of topoisomerases [55] and the hypoxia-dependent formation of TPZ• and subsequent base oxidation.

Although the hypoxia-driven mechanism of action was confirmed by our experiments, TPZ/TPZ• also exerted a pharmacological effect under normoxic conditions when combined with PDT. Since PDT rapidly depletes intracellular O_2 levels by the conversion into ROS [69], the transient post-PDT hypoxia appeared to be sufficient to form TPZ• and induce DNA DSBs and subsequent cell death, even under normoxic culture conditions. The reason behind TPZ being more toxic to p53-dysfunctional A431 cells compared to p53-functional Sk-Cha1 cells is currently elusive. In addition, non-irradiated, TPZ-treated hypoxic Sk-Cha1 and A431 cells exhibited a considerable increase in intracellular oxidative stress as well as an elevated degree of DNA DSBs. This TPZ-mediated increase in oxidative stress translated to augmented MPT in PDT-subjected A431 cells but not Sk-Cha1 cells, suggesting that the mechanism behind the cell death exacerbation in the TPZ + PDT groups differed between Sk-Cha1

and A431 cells. These phenomena may be a consequence of the higher proliferation rate of A431 cells versus Sk-Cha1 cells, causing the DNA damage to be propagated more quickly in A431 cells, resulting in mitotic catastrophe and cell death.

In contrast to the above, the other results were in agreement with the p53-status of the two cell types. TPZ induced oxidative stress under hypoxic conditions that led to DNA DSBs in both cell lines. The cell cycle of p53-dysfunctional A431 cells was minimally affected by adjuvant TPZ, whereas the cell cycle was affected in Sk-Cha1 cells. In addition, while increased cell death occurred in both cell lines, the increased cell death was associated with more extensive MPT in Sk-Cha1 cells but not A431 cells. Thus, the augmented cell death signaling in TPZ + PDT-treated A431 cells appeared to circumvent the p53-MPT route, whereas cell death and growth arrest in Sk-Cha1 cells may have proceeded through p53 via DNA DSB-induced MPT and activation of the p21 cell cycle inhibitor, respectively. Based on the above it appears that TPZ has prominent adjuvant potential in combination with PDT, although the mechanism of cell death appears to be dependent on the p53 status and proliferation rate of the tumor cells.

Given TPZ's confirmed hypoxic cytotoxin properties, we tested whether PDT-induced hypoxia, which was emulated by the incubation of PDT-subjected cells under hypoxic conditions, would be a potent activator of TPZ that would exacerbate cancer cell death via auxiliary pathways not induced by PDT, such as DNA damage. Most photosensitizers localize predominantly to the (membranes of) the endoplasmic reticulum, Golgi apparatus, mitochondria, and/or lysosomes. Their intracellular localization in combination with the fact that ROS have a short action radius in a biological milieu causes PDT-induced damage to be typically confined to the aforementioned organelles [13, 46], whereby the nucleus is left unscathed. Nuclear 'protection' from PDT was corroborated by the absence of increased phospho-H2AX staining of DNA DSBs [52] in both cell lines. Although TPZ exhibited mild antioxidative properties in a cell-free environment (**Fig. 1**), TPZ did not reduce the therapeutic efficacy of PDT. This may be due to the induction of DNA damage by TPZ in the nucleus and not the cytoplasm, although the intracellular distribution of TPZ was not investigated. The damage inflicted by PDT is mainly cytoplasmic as a result of the non-nuclear localization of ZnPC (unpublished results). The TPZ-induced DNA damage and corollary induction of apoptosis were hence expected to have an additive impact on the extent of cell death following PDT. Furthermore, increased cell cycle arrest and cell death following PDT + TPZ treatment were hypothesized to mainly occur in hypoxic Sk-Cha1 cells, *i.e.*, cells that are able to regulate these processes via p53 following DNA damage.

There is a large range of applications for liposomal drug delivery in biomedicine that includes delivery of cytostatic or diagnostic drugs for cancer [18, 70-74], leishmaniasis [75], heart disease [76, 77], port wine stains [78], and thrombosis

[79]. Liposomes are versatile drug carriers since the liposome surface can be modified to gain long circulating capacity using *e.g.*, glucoronide or PEG [80, 81], cross the blood-brain barrier by adding p-aminophenyl-α-d-mannopyranoside [82], and target specifically to tumor cells using antibody- or nanobody conjugation [17, 83-87]. Moreover, the lipid composition of liposomes can be modified to bestow specific biodistributive properties upon the liposomes. For instance, cationic liposomes have the ability to accumulate specifically at tumor vascular endothelium *in vivo* [88]. A distorted blood flow in angiogenic tumor vessels and the consequential shedding of the barrier-forming glycocalyx of endothelial cells is believed to be the underlying mechanism for an increased interaction of the cationic liposomes and the anionic endothelial cell membrane [89, 90]. Cationic liposomes are suitable carriers for *in vitro* drug delivery since they are effectively taken up by many different cell types in culture. For example, cationic liposomes composed of DPPC, cholesterol, and stearylamine (45:45:10 mol%, 120 nm) were previously used to assess the delivery of the radiosensitizer 5-bromo-2-deoxy-uridine (BrdU) to human HMV-II melanoma cells *in vitro* [91]. The cationic BrdU-containing liposomes were substantially more effective in radiosensitizing HMV-II cells compared to anionic or neutral liposomes. Taken together, liposomes constitute a promising carrier for target-specific delivery of hydrophilic and hydrophobic pharmacological agents, including ZnPC and TPZ.

Clinically, TPZ has been employed as a stand-alone treatment or as a radio- and chemosensitizer in the treatment of non-squamous cell lung cancer, head and neck cancer, cervical cancer, and melanoma, which are hypoxic tumor types [92]. TPZ has shown limited clinical efficacy in non-hypoxic tumors [92], and the functionality of p53 has been implicated in the responsiveness of tumor cells to TPZ inasmuch as neuroblastoma cell lines without a functional p53 were significantly less sensitive to TPZ-induced apoptotis than their wild type counterparts [93]. Contrastingly, p53-deficient cell lines have also been shown to be hypersensitive to TPZ [94]. The exact mechanism notwithstanding, the results presented in **Fig. 2** are in favor of a combined treatment approach of TPZ + PDT for PHCCs, especially since merely 14-26% of PHCC patients carry a mutation in the *TP53* gene [95]. However, there are three major drawbacks of TPZ in regard to clinical use, which include (1) poor cellular uptake [61], (2) suboptimal pharmacokinetics [96], and (3) the moderate adverse events reported in completed and ongoing clinical trials [26, 27]. Poor uptake enforces the use of higher TPZ dosing to achieve a desired clinical effect. Since TPZ has been associated with muscle cramping, anemia, diarrhea, skin rash, nausea, vomiting, and even (reversible) blindness [26, 27], the use of higher TPZ dosages is contra-indicated. Moreover, the plasma half-life of TPZ is extremely short, namely 36 min in mice and 47 min in humans at LD_{10} doses [96], resulting in poor drug delivery efficiency.

In order to resolve these drawbacks for clinical use, TPZ can be co-encapsulated with ZnPC in ETLs to specifically deliver these compounds to pharmacologically

important locations in the tumor [16] and achieve an adjuvant therapeutic effect after PDT. Liposomal encapsulation and tumor targeting of TPZ may prevent some of the pharmacokinetic and toxicity hurdles mentioned above and improve pharmacodynamic efficacy. Indeed, it was shown that the encapsulation of TPZ into ZnPC-ETLs resulted in a substantial increase in intracellular TPZ concentrations and PDT efficacy, yet did not exert the toxic effects induced by free TPZ. This increase in efficacy was observed in both A431 and Sk-Cha1 cells, indicating that the adjuvant effect of liposome-delivered TPZ on PDT efficacy occurs in a p53-independent manner. Taken altogether, it was demonstrated that TPZ and ZnPC can be combined in a singular drug delivery system for the treatment of tumor cells. Moreover, the study provides compelling evidence for the use of a fourth-generation liposomal formulation (*i.e.*, a liposome-encapsulated second-generation photosensitizer with co-encapsulated TPZ or pharmacological agents that for example inhibit survival pathways) for PDT of recalcitrant solid cancers.

Conclusions

TPZ is a hypoxic cytotoxin that confers an adjuvant effect on PDT outcome, despite the varying responses of cells to TPZ treatment. The adjuvant effect stems from TPZ-mediated radical formation, DNA damage, loss of MMP, and consequent induction of cell death. These phenomena occurred under both normoxic and hypoxic conditions and independently of p53 functionality. The poor uptake of TPZ by tumor cells as well as unfavorable pharmacokinetics was circumvented by liposomal co-encapsulation, which nearly doubled the PDT efficacy. These *in vitro* results provide proof-of-concept for the use of fourth-generation photosensitizers and furnish mechanistic insight into the adjuvant potential of TPZ in PDT.

Acknowledgments

This work was sponsored by grants from the Dutch Anti-Cancer Society (Stichting Nationaal Fonds Tegen Kanker, Amsterdam, the Netherlands) and the Phospholipid Research Center (Heidelberg, Germany). The authors are grateful to Gerben Koning (Erasmus Medical Center, Rotterdam, the Netherlands) for provision of the A431 cells, Alexander Knuth and Claudia Matter (Department of Oncology, University Hospital Zurich) for providing the Sk-Cha1 cells, Adrie Maas (Department of Experimental Surgery, Academic Medical Center, University of Amsterdam) for construction of the hypoxic incubator, and Berend Hooibrink (Department of Cell Biology and Histology, Academic Medical Center, University of Amsterdam) for assistance with flow cytometry. The authors would like to thank Remko van Vught for fruitful discussions.

References

1. S. A. Khan, H. C. Thomas, B. R. Davidson, and S. D. Taylor-Robinson, Lancet. 366, 1303-1314 (2005)
2. N. Ramírez-Merino, S. P. Aix, and H. Cortés-Funes, World J Gastrointest Oncol. 5, 171-176 (2013)
3. T. Y. Lee, Y. K. Cheon, and C. S. Shim, Clin Endosc. 46, 38-44 (2013)
4. M. Aljiffry, M. J. Walsh, and M. Molinari, World J Gastroenterol. 15, 4240-4262 (2009)
5. M. E. J. Ortner, K. Caca, F. Berr, J. Liebetruth, U. Mansmann, D. Huster, W. Voderholzer, G. Schachschal, J. Mössner, and H. Lochs, Gastroenterol. 125, 1355-1363 (2003)
6. M. Broekgaarden, R. Weijer, T. M. van Gulik, M. R. Hamblin, and M. Heger, Cancer Metast Rev. 34, 643-690 (2015)
7. V. H. Fingar, J Clin Laser Med Surg. 14, 323-328 (1996)
8. V. H. Fingar, P. K. Kik, P. S. Haydon, P. B. Cerrito, M. Tseng, E. Abang, and T. J. Wieman, Br J Cancer. 79, 1702-1708 (1999)
9. V. H. Fingar, T. J. Wieman, P. S. Karavolos, K. W. Doak, R. Ouellet, and J. E. van Lier, Photochem Photobiol. 58, 251-258 (1993)
10. B. Chen, B. W. Pogue, P. J. Hoopes, and T. Hasan, Int J Radiat Oncol Biol Phys. 61, 1216-1226 (2005)
11. V. H. Fingar, T. J. Wieman, S. A. Wiehle, and P. B. Cerrito, Cancer Res. 52, 4914-4921 (1992)
12. D. J. H. Roberts, F. Cairnduff, I. Driver, B. Dixon, and S. B. Brown, Int J Oncol. 5, 763-768 (1994)
13. K. Plaetzer, B. Krammer, J. Berlanda, F. Berr, and T. Kiesslich, Lasers Med Sci. 24, 259-268 (2009)
14. D. E. J. G. J. Dolmans, D. Fukumura, and R. K. Jain, Nat Rev Cancer. 3, 380-387 (2003)
15. A. P. Castano, P. Mroz, and M. R. Hamblin, Nat Rev Cancer. 6, 535-545 (2006)
16. R. Weijer, M. Broekgaarden, M. Kos, R. Vught, E. Rauws, T. M. van Gulik, and M. Heger, J Photochem Photobiol C Photochem Rev. 23, 103-131 (2015)
17. M. Broekgaarden, R. van Vught, S. Oliveira, R.C. Roovers, P. M. van Bergen en Henegouwen, R.J. Pieters, T. M. van Gulik, E. Breukink, and M. Heger, Nanoscale. 8, 6490 (2016)
18. M. Broekgaarden, A. I. de Kroon, T. M. van Gulik, and M. Heger, Curr Med Chem. 21, 377-391 (2013)
19. A. Casas, G. Di Venosa, T. Hasan, and A. Batlle., Curr Med Chem. 18, 2486-2515 (2011)
20. C. J. Gomer, J Natl Compr Cancer Netw. 10, S-35-S-39 (2012)
21. M. Broekgaarden, R. Weijer, M. Krekorian, B. van den IJssel, M. Kos, L. K. Alles, A. C. van Wijk, Z. Bikadi, E. Hazai, T. M. van Gulik, and M. Heger, Nano Res. 9, 1639 (2016)
22. R. Weijer, M. Broekgaarden, M. Krekorian, L. K. Alles, A. C. van Wijk, C. Mackaaij, J. Verheij, A. C. van der Wal, T. M. van Gulik, G. Storm, and M. Heger, Oncotarget 7, 3341 (2015)
23. M. Broekgaarden, M. Kos, F. A. Jurg, A. A. van Beek, T. M. van Gulik, and M. Heger, Int. J. Mol. Sci. 16, 19960 (2015).
24. G. L. Semenza, Trends Pharmacol Sci. 33, 207-214 (2012)
25. J. S. Daniels, K. S. Gates, C. Tronche, and M. M. Greenberg, Chem Res Toxicol. 11, 1254-1257 (1998)
26. J. von Pawel, R. von Roemeling, U. Gatzemeier, M. Boyer, L. O. Elisson, P. Clark, D. Talbot, A. Rey, T. W. Butler, V. Hirsh, I. Olver, B. Bergman, J. Ayoub, G. Richardson, D. Dunlop, A. Arcenas, R. Vescio, J. Viallet, and J. Treat, J Clin Oncol. 18, 1351-1359 (2000)
27. M. Gatineau, O. Rixe, and T. L. Chevalier, Clin Lung Cancer. 6, 293-298 (2005)
28. E. E. W. Cohen, D. Rosine, D. J. Haraf, E. Loh, L. Shen, A. Lusinchi, E. E. Vokes, and J. Bourhis, Int J Radiat Oncol Biol Phys. 67, 678-684 (2007)
29. D. Rischin, L. Peters, R. Hicks, P. Hughes, R. Fisher, R. Hart, M. Sexton, I. D'Costa, and R. von Roemeling, J Clin Oncol. 19, 535-542 (2001)
30. D. Rischin, R. J. Hicks, R. Fisher, D. Binns, J. Corry, S. Porceddu, and L. J. Peters, J Clin Oncol. 24, 2098-2104 (2006)
31. A. Covens, J. Blessing, D. Bender, R. Mannel, and M. Morgan, Gynecol Oncol. 100, 586-590 (2006)
32. P. A. DiSilvestro, S. Ali, P. S. Craighead, J. A. Lucci, Y.-C. Lee, D. E. Cohn, N. M. Spirtos, K. S. Tewari, C. Muller, W. H. Gajewski, M. M. Steinhoff, and B. J. Monk, J Clin Oncol. 32, 458-464 (2014)
33. P. Baas, H. Oppelaar, M. Stavenuiter, N. V. Zandwijk, and F. A. Stewart, Int J Radiat Oncol Biol Phys. 27, 665-670 (1993)
34. Reiss M., Brash D.E., Muñoz-Antonia T., Simon J.A., Ziegler A., Vellucci V.F., and Z. Z.L., Oncol Res. 4, 349-357 (1992)
35. J. J. Kloek, X. Marechal, J. Roelofsen, R. H. Houtkooper, A. B. van Kuilenburg, W. Kulik, R. Bezemer, R. Neviere, T. M. van Gulik, and M. Heger, Antioxid Redox Signal. 17, 1109-1123 (2012)
36. J. Lasch, V. Weissig, and M. Brandl, in Liposomes, Edited V. P. Torchilin and V. Torchilin, Oxford University Press, New York, USA (2003)
37. F. B. Pruijn, J. R. Sturman, H. D. S. Liyanage, K. O. Hicks, M. P. Hay, and W. R. Wilson, J Med Chem. 48, 1079-1087 (2005)
38. X. Xu, M. A. Khan, and D. J. Burgess, Int J Pharm. 423, 410-418 (2012)
39. Z. V. Leonenko, E. Finot, H. Ma, T. E. S. Dahms, and D. T. Cramb, Biophys J. 86, 3783-3793 (2004)
40. O. Edholm, and J. F. Nagle, Biophys J. 89, 1827-1832 (2005)
41. L. S. Mendonça, J. N. Moreira, M. C. de Lima, and S. Simões, Biotechnol Bioeng. 107, 884-893 (2010)
42. M.I. van Raath, R. Weijer, G.H. Nguyen, B. Choi, A.I. de Kroon, and M. Heger, J. Biomed. Nanotechnol. 12, 1617-1640 (2016)
43. J. Weiss, Naturwissenschaften. 23, 64 (1935)
44. M. van Leeuwen, A. Beeby, I. Fernandes, and S. H. Ashworth, Photochem Photobiol Sci. 13, 62-69 (2014)
45. C. D. Georgiou, I. Papapostolou, N. Patsoukis, T. Tsegenidis, and T. Sideris, Anal Biochem. 347, 144-151 (2005)

46. A. E. O'Connor, W. M. Gallagher, and A. T. Byrne, Photochem Photobiol. 85, 1053-1074 (2009)
47. W. R. Wilson, and M. P. Hay, Nat Rev Cancer. 11, 393-410 (2011)
48. Y. Park, S. Kanekal, and J. P. Kehrer, Am J Physiol. 260, H1395-H1405 (1991)
49. G. Chowdhury, V. Junnotula, J. S. Daniels, M. M. Greenberg, and K. S. Gates, J Am Chem Soc. 129, 12870-12877 (2007)
50. J. W. Evans, S. B. Chernikova, L. A. Kachnic, J. P. Banath, O. Sordet, Y. M. Delahoussaye, A. Treszezamsky, B. H. Chon, Z. Feng, Y. Gu, W. R. Wilson, Y. Pommier, P. L. Olive, S. N. Powell, and J. M. Brown, Cancer Res. 68, 257-265 (2008)
51. J. P. Banáth, and P. L. Olive, Cancer Res. 63, 4347-4350 (2003)
52. E. P. Rogakou, D. R. Pilch, A. H. Orr, V. S. Ivanova, and W. M. Bonner, J Biol Chem. 273, 5858-5868 (1998)
53. D. Y. Shen, J. H. Kang, W. Song, W. Q. Zhang, W. G. Li, Y. Zhao, and Q. X. Chen, Phytother Res. 25, 1519-1526 (2011)
54. D. P. Guimaraes, and P. Hainaut, Biochimie. 84, 83-93 (2002)
55. K. B. Peters, and J. M. Brown, Cancer Res. 62, 5248-5253 (2002)
56. B. Hong, V. W. Y. Lui, E. P. Hui, M. H. L. Ng, S. H. Cheng, F. L. Sung, C. M. Tsang, S. W. Tsao, and A. T. Chan, Invest New Drugs. 29, 401-410 (2011)
57. M. J. O'Connell, N. C. Walworth, and A. M. Carr, Trends Cell Biol. 10, 296-303 (2000)
58. M. M. Compton, Cancer and Metastasis Rev. 11, 105-119 (1992)
59. L. Piccotti, C. Marchetti, G. Migliorati, R. Roberti, and L. Corazzi, J Biol Chem. 277, 12075-12081 (2002)
60. K. O. Hicks, F. B. Pruijn, J. R. Sturman, W. A. Denny, and W. R. Wilson, Cancer Res. 63, 5970-5977 (2003)
61. Y. Moon, W. Dahlberg, Y. Yu, T. Ohno, T. Todoroki, and J. Little, Int J Oncol. 10, 545-551 (1997)
62. T. T. Kwok, C. H. Mok, and L. Menton-Brennan, Cancer Res. 54, 2834-2836 (1994)
63. D. Kotandeniya, B. Ganley, and K. S. Gates, Bioorg Med Chem Lett. 12, 2325-2329 (2002)
64. M. Birincioglu, P. Jaruga, G. Chowdhury, H. Rodriguez, M. Dizdaroglu, and K. S. Gates, J Am Chem Soc. 125, 11607-11615 (2003)
65. B. Ganley, G. Chowdhury, J. Bhansali, J. S. Daniels, and K. S. Gates, Bioorg Med Chem. 9, 2395-2401 (2001)
66. H. E. Krokan, and M. Bjøras, Cold Spring Harb Perspect Biol. 5, a012583 (2013)
67. O. A. Sedelnikova, C. E. Redon, J. S. Dickey, A. J. Nakamura, A. G. Georgakilas, and W. M. Bonner, Mutation Res. 704, 152-159 (2010)
68. E. Markkanen, U. Hübscher, and B. van Loon, Cell Cycle. 11, 1070-1075 (2012)
69. M. A. Weston, and M. S. Patterson, Photochem Photobiol. 90, 878-888 (2014)
70. W. Yuan, R. Kuai, W. Cai, L. Fu, Y. Yang, Y. Qin, Y. Liu, Y. Tang, H. Fu, Q. Zhang, M. Yuan, Z. Zhang, F. Gao, and Q. He, J Biomed Nanotechnol. 10, 1563-1573 (2014)
71. M. Liu, H. Yu, T. Wang, N. Chang, J. Zhang, D. Du, M. Liu, S. Sun, R. Wang, H. Tao, Z. Shen, Q. Wang, and H. Peng, J Mater Chem B. 2, 1619-1625 (2014)
72. F. Jia, X. Liu, L. Li, S. Mallapragada, B. Narasimhan, and Q. Wang, J Control Release. 172, 1020-1034 (2013)
73. A. L. de Barros, L. G. Mota, D. C. F. Soares, C. M. de Souza, G. D. Cassali, M. C. Oliveira, and V. N. Cardoso, J Biomed Nanotechnol. 9, 1636-1643 (2013)
74. T. L. Lapenda, W. A. Morais, F. J. F. Almeida, M. S. Ferraz, M. C. B. Lira, N. P. S. Santos, M. A. M. Maciel, and N. S. Santos-Magalhães, J Biomed Nanotechnol. 9, 499-510 (2013)
75. R. M. Lopes, M. M. Gaspar, J. Pereira, C. V. Eleutério, M. Carvalheiro, A. J. Almeida, and M. E. M. Cruz, J Biomed Nanotechnol. 10, (2014)
76. M. Liu, M. Li, S. Sun, B. Li, D. Du, J. Sun, F. Cao, H. Li, F. Jia, T. Wang, N. Chang, H. Yu, Q. Wang, and H. Peng, J Biomed Nanotechnol. 35, 3697-3707 (2014)
77. M. Liu, M. Li, G. Wang, X. Liu, D. Liu, H. Peng, and Q. Wang, J Biomed Nanotechnol. 10, (2014)
78. G. Aguilar, B. Choi, M. Broekgaarden, O. Yang, B. Yang, P. Ghasri, J. Chen, R. Bezemer, J. Nelson, A. van Drooge, A. Wolkerstorfer, K. Kelly, and M. Heger, Ann Biomed Eng. 40, 486-506 (2013)
79. M. Heger, I. I. Salles, W. van Vuure, I. H. Hamelers, A. I. de Kroon, H. Deckmyn, and J. F. Beek, Microvas Res. 78, 57-66 (2009)
80. N. Oku, Y. Namba, and S. Okada, Biochim Biophys Acta. 1126, 255-260 (1992)
81. Z. Amoozgar, and Y. Yeo, Wiley Interdiscip Rev Nanomed Nanobiotechnol. 4, 219-233 (2012)
82. D. Du, N. Chang, S. Sun, M. Li, M. Liu, X. Liu, G. Wang, H. Li, X. Liu, Q. Wang, and H. Peng, J Control Release. 182, 99-110 (2014)
83. P. Marqués-Gallego, and A. I. P. M. De Kroon, Biomed Res Int. 2014, 129458 (2014)
84. Y. Mir, S. A. Elrington, and T. Hasan, Nanomedicine. 9, 1114-1122 (2013)
85. S. Oliveira, R. M. Schiffelers, J. van der Veeken, R. van der Meel, R. Vongpromek, P. M. van Bergen en Henegouwen, G. Storm, and R. C. Roovers, J Control Release. 145, 165-175 (2010)
86. K. Papadia, E. Markoutska, and S. G. Antimisiaris, J Biomed Nanotechnol. 10, 871-876 (2014)
87. S. Oliveira, R. Heukers, J. Sornkom, R. J. Kok, and P. M. van Bergen en Henegouwen, J Control Release. 172, 607-617 (2013)
88. G. Thurston, J. W. McLean, M. Rizen, P. Baluk, A. Haskell, T. J. Murphy, D. Hanahan, and D. M. McDonald, J Clin Invest. 101, 1401-1413 (1998)
89. R. B. Campbell, B. Ying, G. M. Kuesters, and R. Hemphill, Jf Pharm Sci. 98, 411-429 (2009)
90. A. Abu Lila, T. Ishida, and H. Kiwada, Pharm Res. 27, 1171-1183 (2010)
91. S. Kato, M. Kimura, and N. Miwa, J Biomed Nanotechnol. 10, 3280-3290 (2014)

92. S. B. Reddy, Williamson, S. K., Exp Opin Investig Drugs. 18, 77-87 (2009)
93. B. Yang, and C. P. Reynolds, Clinical Cancer Research. 11, 2774-2780 (2005)
94. J. M. Brown, Br J Cancer. 77 Suppl, 12-14 (1998)
95. S. A. Khan, H. C. Thomas, M. B. Toledano, I. J. Cox, and S. D. Taylor-Robinson, Liver Int. 25, 704-716 (2005)
96. M. A. Graham, S. Senan, H. Robin, N. Eckhardt, D. Lendrem, J. Hincks, D. Greenslade, R. Rampling, S. B. Kaye, R. von Roemeling, and P. Workman, Cancer Chemother Pharmacol. 40, 1-10 (1997)

Chapter 7

Summarizing discussion and future perspectives

1. Summarizing discussion

Photodynamic therapy (PDT) is a treatment strategy that is employed for a variety of medical conditions, including antibiotic-resistant bacterial infections [1], atherosclerosis [2], wet age-related macular degeneration [3], and (palliative) treatment of solid cancers [4]. In case of solid cancer treatment, PDT requires the accumulation of a light-sensitive molecule (photosensitizer) in the tumor environment, which can be either administered systemically or locally depending on the location of tumor. Thereafter, the tumor site is locally irradiated with light to excite the photosensitizer. The activated photosensitizer then undergoes a photochemical reaction with oxygen that is present in the tumor tissue, thereby producing highly toxic singlet oxygen and other forms of reactive oxygen species (*e.g.*, superoxide). As a result of the oxidation of biomolecules in tumor cells and its vasculature, the therapeutic insult induces tumor cell death, shutdown of the tumor (micro)vasculature, and may initiate an anti-tumor immune response as a result of the damaged tumor cells [5].

Currently, PDT is employed as a treatment strategy for cancer patients with either curative or palliative intentions. In this thesis, we have focused on the optimization of PDT strategies for the treatment of perihilar cholangiocarcinoma. This cancer type is typically diagnosed at a late tumor stage due to its asymptomatic course, after which the tumor is no longer resectable. Interestingly, PDT has been shown to improve the median survival from 7 months in case of biliary stenting to 21 months where stenting was combined with PDT [6]. A recent meta-analysis also demonstrated that PDT is able to significantly improve the median survival time of non-resectable cholangiocarcinoma patients, as evidenced by a median survival of 3 - 7.4 months for stenting alone versus 9.8 - 21 months for PDT plus stenting [7]. Despite these promising results, PDT is still a palliative treatment strategy. Hence, novel ways were explored to enhance therapeutic efficacy.

As described in **Chapter 2**, PDT may be improved by selecting photosensitizers that are amongst others efficient singlet oxygen generators, are able to strongly absorb light in the red spectrum, and are safe for clinical use. As such, the photosensitizer zinc phthalocyanine (ZnPC) was selected. To ensure bioavailability (*i.e.*, ZnPC is highly lipophilic) and to selectively target ZnPC towards to the pharmacologically important sites within a tumor, ZnPC was encapsulated in three distinct liposomal formulations. These formulations are designed to either target to tumor cells (tumor cell-targeting liposomes), tumor endothelium (endothelial cell-targeting liposomes, ETLs), and tumor interstitial spaces (interstitially targeted liposomes, ITLs). With this approach, we aim to augment therapeutic efficacy and reduce potential photosensitivity (*i.e.*, due to non-specific accumulation of photosensitizer in the skin) as a result of specific targeting.

In response to PDT, tumor cells may initiate various protection mechanisms that

are programmed to stimulate survival which has been extensively described by [8]. To evaluate the safety of ZnPC-encapsulating ITLs and to assess the response of perihilar cholangiocarcinoma (SK-ChA-1) cells to PDT, SK-ChA-1 cells were treated with ZnPC-ITL-PDT and analyzed by microarray analysis (**Chapter 3**). Furthermore, *in vivo* toxicity was also assessed in chicken embryos and C57BL/6 mice. These experiments indicated that ZnPC-ITLs were non-toxic *in vitro* as well as *in vivo*. Importantly, PDT-treated SK-ChA-1 cells that were treated with a suboptimal treatment regimen revealed extensive HIF-1- and NF-κB-mediated survival signaling. These results also constituted the basis for **Chapter 4**. Here, we also evaluated the transcriptomic response of tumor-comprising cells, namely endothelial cells, macrophages, and perihilar cholangiocarcinoma and epidermoid carcinoma cells, following PDT with cationic ZnPC-encapsulating liposomes at a low (lethal concentration, 50% (LC_{50})) and high (LC_{90}) photosensitizer concentration. In accordance with previous findings, PDT-treated tumor cells exhibited survival signaling via HIF-1- and NF-κB, which was most prominent in the LC_{50} groups. Additionally, SK-ChA-1 cells were also subjected to (phospho)proteomics and metabolomics to further decipher the post-PDT response. SK-ChA-1 cells that were treated with high-dose PDT exhibited a downregulation of proteins involved in cytoskeletal organization as well as metabolites that are responsible for the redox status and energy production by mitochondria. Interestingly, the frequently exploited tumor target epidermal growth factor receptor (EGFR) was downregulated at both the proteomic and mRNA level after high-dose PDT, which may be partly responsible for the PDT-induced cell death.

The latter studies were performed to gain understanding of the behavior of tumor cells to PDT, but also to exploit potential vulnerabilities of tumor cells to make them more susceptible to PDT. In the *in vivo* situation, PDT may damage the tumor vasculature leading to vascular occlusion, thereby depleting tumor cells from hypoxia. Furthermore, PDT relies on the conversion of oxygen to reactive oxygen species, whereby the oxygen concentration in the tumor environment may drop. In response to both processes, the survival factor HIF-1 may be activated that enhances the survival of tumor cells under low oxygen conditions. Therefore, in **Chapter 5** it was examined whether the HIF-1 inhibitor acriflavine could sensitize tumor cells to PDT. This study revealed that the PDT efficacy using cationic ZnPC-encapsulating liposomes was enhanced in perihilar cholangiocarcinoma in combination with acriflavine under hypoxic conditions. The enhanced PDT efficacy not only stemmed from HIF-1 inhibition, as acriflavine is also known as a dual topoisomerase I/II inhibitor [9] that may lead to cell cycle arrest and lethal DNA damage during transcription and cell replication [10].

The hypoxic state of tumor cells following PDT was further exploited in **Chapter 6**. Here, the hypoxic cytotoxin tirapazamine (TPZ) was used as a strategy to augment therapeutic efficacy. TPZ is a molecule that is converted into a radical by

nuclear reductases when the concentration drops below a certain threshold (*i.e.*, < 10% O_2 [11]), which causes the formation of DNA double-strand breaks leading to cell death. In this study, TPZ and ZnPC were both encapsulated in one cationic liposomal formulation which showed an enhanced PDT efficacy in hypoxic conditions compared to their TPZ-lacking counterparts. These findings underscore the safety and feasibility of this approach as a way to improve PDT efficacy.

2. Future perspectives

The work in this thesis forms the basis for the development of second-generation photosensitizers (*i.e.*, metallated phthalocyanines) in combination with a multi- targeting liposomal delivery platform as introduced in **Chapter 2**. Future research shall be focused on the development of an *in vivo* proof-of-concept and exploit the tumor survival mechanisms that may induced by PDT to make tumor cells more vulnerable to the therapeutic insult. Potential drugs that may be tested in such a platform include acriflavine (**Chapter 5**) and TPZ (**Chapter 6**). In addition to the optimization of this PDT strategy, future work should also include the development of an orthotopic perhilar cholangiocarcinoma *in vivo* model, since these models are currently lacking. Hence, novel treatment strategies for perihilar cholangiocarcinoma may be tested in a setting that better mimics the clinical situation that should lead to more clinically translatable results.

References

1. Liu Y, Qin R, Zaat SA, Breukink E, Heger M, Liu Y: Antibacterial photodynamic therapy: overview of a promising approach to fight antibiotic-resistant bacterial infections. 2015.
2. Waksman R, McEwan PE, Moore TI, Pakala R, Kolodgie FD, Hellinga DG, Seabron RC, Rychnovsky SJ, Vasek J, Scott RW et al: PhotoPoint photodynamic therapy promotes stabilization of atherosclerotic plaques and inhibits plaque progression. J Am Coll Cardiol 2008, 52(12):1024-1032.
3. Kawczyk-Krupka A, Bugaj AM, Potempa M, Wasilewska K, Latos W, Sieron A: Vascular-targeted photodynamic therapy in the treatment of neovascular age-related macular degeneration: Clinical perspectives. Photodiagnosis Photodyn Ther 2015, 12(2):161-175.
4. Huang Z: A review of progress in clinical photodynamic therapy. Technol Cancer Res Treat 2005, 4(3):283-293.
5. Castano AP, Mroz P, Hamblin MR: Photodynamic therapy and anti-tumour immunity. Nat Rev Cancer 2006, 6(7):535-545.
6. Zoepf T, Jakobs R, Arnold JC, Apel D, Riemann JF: Palliation of nonresectable bile duct cancer: improved survival after photodynamic therapy. Am J Gastroenterol 2005, 100(11):2426-2430.
7. Lu Y, Liu L, Wu JC, Bie LK, Gong B: Efficacy and safety of photodynamic therapy for unresectable cholangiocarcinoma: A meta-analysis. Clin Res Hepatol Gastroenterol 2015, 39(6):718-724.
8. Broekgaarden M, Weijer R, van Gulik TM, Hamblin MR, Heger M: Tumor cell survival pathways activated by photodynamic therapy: a molecular basis for pharmacological inhibition strategies. Cancer Metastasis Rev 2015, 34(4):643-690.
9. Hassan S, Laryea D, Mahteme H, Felth J, Fryknas M, Fayad W, Linder S, Rickardson L, Gullbo J, Graf W et al: Novel activity of acriflavine against colorectal cancer tumor cells. Cancer Sci 2011, 102(12):2206-2213.
10. Dwarakanath BS, Khaitan D, Mathur R: Inhibitors of topoisomerases as anticancer drugs: problems and prospects. Indian J Exp Biol 2004, 42(7):649-659.
11. Wilson WR, Hay MP: Targeting hypoxia in cancer therapy. Nat Rev Cancer 2011, 11(6):393-410.

Appendices

Summary & Nederlandse samenvatting
Portfolio
List of publications
Dankwoord
Biography

Summary

Photodynamic therapy (PDT) is a minimally-to-non-invasive therapy in which a light-sensitive molecule is activated by light to locally produce highly destructive reactive oxygen species (ROS). When employed for cancer treatment, PDT is able to induce tumor cell death, microvascular damage, and an anti-tumor immune response. All these factors contribute to tumor destruction. Although PDT is successfully applied for a variety of tumor types, PDT yields promising yet unsatisfactory results in non-resectable perihilar cholangiocarcinoma patients. This is partly due to the use of suboptimal photosensitizers and the activation of survival signaling in PDT-subjected but sublethally afflicted tumor cells. Consequently, novel PDT strategies are needed to treat these patients in a selective and effective manner. For this purpose, we (1) incorporated a photosensitizer with superior photochemical properties into a multi-targeting liposomal delivery system, (2) analyzed survival signaling in PDT-treated tumor cells, and (3) pharmacologically intervened in survival programs to improve therapeutic efficacy.

The first part of this thesis describes the rationale for the proposed PDT modality and the response of (tumor) cells to this therapy. The PDT modality is based on the photosensitizer zinc phthalocyanine (ZnPC) that is incorporated into three distinct liposomal formulations that are targeted to the pharmacologically most important regions in a tumor, namely tumor cells, tumor vascular endothelium, and tumor interstitial spaces (**Chapter 2**). **Chapter 3** revealed that ZnPC-encapsulating interstitially targeted liposomes are non-toxic in various *in vitro* and *in vivo* models. Moreover, suboptimally treated perihilar cholangiocarcinoma cells showed extensive survival signaling that may account for a suboptimal therapeutic response. This study was followed up by investigating the molecular responses of tumor-associated cell types (*i.e.*, vascular endothelial cells, macrophages, perihilar cholangiocarcinoma cells, epidermal growth factor receptor (EGFR)-overexpressing epidermoid cancer cells) to PDT with ZnPC-encapsulating endothelial cell-targeting liposomes (**Chapter 4**). The study revealed that sublethal PDT activates multiple pathways in tumor-associated cell types that transcriptionally regulate cell survival, proliferation, energy metabolism, detoxification, inflammation/angiogenesis, and metastasis. Interestingly, optimal PDT resulted in downregulation of proteins involved in EGFR signaling, which is a well-known therapeutic target in various cancer therapies.

The second part of this thesis exploited the knowledge obtained in the previous chapters to develop so-called fourth generation photosensitizers. These are second-generation photosensitizers (ZnPC) encapsulated in a photosensitizer delivery system (*i.e.*, liposomes) with co-encapsulated small-molecular inhibitors of PDT-activated survival pathways. Hypoxia-inducible factor 1 (HIF-1) is a survival factor that is overexpressed in a variety of tumor types. However, PDT may also activate HIF-1

as PDT depletes oxygen during the production of ROS. In addition, tumor cells may experience hypoxia due to the obstructed influx of oxygen into the tumor as a result of PDT-induced vascular damage. In **Chapter 5** it was found that HIF-1 is expressed in human hilar cholangiocarcinoma and that HIF-1 contributes to tumor cell survival following PDT *in vitro*. We found that pretreatment with the HIF-1 inhibitor acriflavine improved PDT efficacy in cultured cells, which warrants further *in vivo* validation for therapy-recalcitrant perihilar cholangiocarcinomas. Lastly, in **Chapter 6** it was evaluated whether tirapazamine (TPZ) is a suitable compound to increase PDT efficacy by exploiting the post-PDT tumor hypoxia. Under low oxygen conditions, TPZ is converted into a TPZ radical that causes DNA damage and consequent cell death. We found that it was feasible to incorporate TPZ into ZnPC-encapsulating endothelial cell-targeting liposomes. Moreover, the combination treatment of TPZ with PDT improved PDT efficacy under hypoxic conditions by inducing an additional mode of cell death via TPZ radical-induced DNA double strand breaks.

In conclusion, this thesis describes a novel PDT strategy that may be used for the treatment of refractory solid cancers. The modality appeared safe in a variety of models and it was feasible to incorporate pharmacological agents into our multi-targeted delivery platform. We believe that PDT-induced survival signaling may contribute to a suboptimal therapeutic response as well as potential tumor recurrence. Therefore, future research should be focused on targeted PDT strategies that exploit the post-PDT survival response and evaluate its clinical potential in animal models.

Nederlandse samenvatting

Fotodynamische therapie (PDT) is een minimaal- tot niet-invasieve therapie waarbij een lichtgevoelig molecuul door licht wordt geactiveerd licht om lokaal destructieve reactieve zuurstofverbindingen te produceren. In het geval van kankerbehandeling heeft PDT de mogelijkheid om tumorceldood te induceren, evenals microvasculaire schade en de opwekking van een anti-tumor immuunrespons. Al deze factoren dragen bij aan de verwijdering van de tumor. PDT wordt succesvol toegepast in verschillende tumortypes, maar leidt tot veelbelovende, maar nog onbevredigde resultaten bij patiënten met niet-resectabel perihilair cholangiocarcinoom. Dit wordt deels veroorzaakt door suboptimale fotosensitizers en de activatie van signaalroutes die de overleving stimuleren in tumorcellen die suboptimaal behandeld zijn met PDT. Daarom zijn nieuwe PDT strategieën nodig om deze patiënten te behandelen op een selectieve en effectieve wijze. Voor dit doel hebben wij (1) een fotosensitizer met superieure fotochemische eigenschappen geïncorporeerd in een liposomaal transportsysteem met multi-targeting eigenschappen, (2) de signaalroutes die overleving stimuleren geanalyseerd in PDT-behandelde tumorcellen en (3) farmacologisch ingegrepen om de overlevingsroutes te blokkeren om de therapeutische effectiviteit te verhogen.

Het eerste deel van de thesis beschrijft de rationaal voor de voorgestelde PDT modaliteit en de respons van (tumor)cellen op deze therapie. De PDT modaliteit is gebaseerd op de fotosensitizer zink ftalocyanine (ZnPC) dat is verpakt in drie verschillende liposomale formuleringen die worden gestuurd naar de belangrijkste farmacologische gebieden in het tumorgebied, namelijk de tumorcellen, de bloedvaten van de tumor en de interstitiële ruimte van de tumor (**Hoofdstuk 2**). **Hoofdstuk 3** toont aan dat ZnPC-bevattende interstitieel-gestuurde liposomen niet toxisch zijn in verschillende *in vitro* en *in vivo* modellen. Bovendien laten suboptimaal behandelde cellen van het perihilair cholangiocarcinoom zien dat zij de overlevingsroutes sterk stimuleren wat voor een suboptimale therapeutische respons kan zorgen. Deze studie is opgevolgd door de moleculaire respons van tumor-geassocieerde cellen te onderzoeken (vasculaire endotheelcellen, macrophagen, perihilaire cholangiocarcinoomcellen, epidermaalcellen die epidermale groeifactor receptor (EGFR) tot overexpressie brengen) na de PDT behandeling met ZnPC-bevattende endotheel-gestuurde liposomen (**Hoofdstuk 4**). Deze studie liet zien dat sublethale schade na PDT verschillende signaalroutes activeert in tumor-geassocieerde celtypen die transcriptioneel de celoverleving, proliferatie, energiemetabolisme, detoxificatie, inflammatie/angiogenese en metastase reguleren. Een interessante vinding was dat optimale PDT leidt tot een vermindering van eiwitten die betrokken zijn bij de signaalroutes van EGFR, een welbekend therapeutisch doel in verschillende kankerbehandelingen.

Het tweede deel van de thesis heeft gebruik gemaakt van de kennis die is

opgedaan in de vorige hoofdstukken om zogenoemde vierde generatie fotosensitizers te ontwikkelen. Dit zijn tweede generatie fotosensitizers (ZnPC) die worden verpakt in een fotosensitizer afleveringssysteem (liposomen) waarin ook moleculaire inhibitors van overlevingsroutes worden verpakt. Hypoxie-induceerbare factor 1 (HIF-1) is een overlevingsfactor dat abundant aanwezig is in verschillende tumortypen. PDT kan ook HIF-1 activeren aangezien PDT zuurstof gebruikt bij de vorming van ROS. Hierbij komt dat tumorcellen hypoxie kunnen ervaren door de obstructie van zuurstof naar de tumor als gevolg van vaatschade. In **Hoofdstuk 5** is gevonden dat HIF-1 aanwezig is in het humaan cholangiocarcinoom en dat HIF-1 bijdraagt aan de overleving van tumorcellen na PDT *in vitro*. Ook hebben wij gevonden dat voorbehandeling met de HIF-1 inhibitor acriflavine de effectiviteit van PDT verhoogt *in vitro* wat aanleiding geeft tot *in vivo* validatie van deze behandeling voor therapieresistente perihilaire cholangiocarcinomen. Tot slot, in **Hoofdstuk 6** is onderzocht of tirapazamine (TPZ) een geschikt middel is om de effectiviteit van PDT te verhogen door gebruik te maken van de hypoxie die ontstaat na PDT. Tijdens lage zuurstofcondities wordt TPZ omgezet in een TPZ radicaal dat DNA schade kan induceren, en als gevolg daarvan celdood. We hebben gevonden dat het mogelijk is om TPZ te verpakken in ZnPC-bevattende endotheel-gestuurde liposomen. Bovendien verhoogde een combinatiebehandeling van TPZ met PDT de effectiviteit van PDT onder hypoxische condities door een additionele manier van celdood te induceren, namelijk door TPZ radicaal-geïnduceerde dubbelstrengse beschadigingen aan het DNA.

In conclusie, deze thesis beschrijft een nieuwe PDT strategie dat mogelijk zou kunnen worden gebruikt voor de behandeling van refractoire solide kankertypen. De modaliteit is veilig gebleken in verschillende modellen en het was mogelijk om farmacologische agentia te incorporeren in het multi-targeting afleveringssysteem. Wij geloven dat PDT-geïnduceerde signaalroutes die overleving stimuleren kunnen bijdragen aan een suboptimale therapeutische respons evenals tumor recidief. Daarom zal toekomstig onderzoek gefocust moeten zijn op getargete PDT strategieën die de overlevingsrespons na PDT exploiteren en het klinische potentiaal evalueren in diermodellen.

Portfolio

Name: Ruud Weijer
PhD period: April 2012 - June 2016
PhD supervisor: Prof. dr. T.M. van Gulik

1. PhD training

Courses	**Year**	**Workload (ECTS)**
Mass Spectrometry, Proteomics and Protein Research	2014	2.1
R_2 course	2014	0.3
Practical Biostatistics	2014	1.1
Basic Microscopy Course	2015	1.6
Advanced qPCR	2015	0.7
Workshops and seminars	**Year**	**Workload (ECTS)**
Weekly department seminars	2012-2016	4
Horizon 2020 Crash Course	2016	0.15
Honest Networking	2016	0.1
Presentations	**Year**	**Workload (ECTS)**
Invited lecture, École Polytechnique Fédérale de Lausanne, Lausanne, Switzerland	2016	0.5
International conferences	**Year**	**Workload (ECTS)**
Society for Free Radical Research Europe, Athens, Greece	2013	1
European Association for Cancer Research, Munich, Germany	2014	1.25
Journal reviewer	**Year**	**Workload (ECTS)**
PLoS One	2013, 2016	1
Journal of Photochemistry and Photobiology B: Biology	2014	0.5
Journal of Pharmacology and Experimental Therapeutics	2014	0.5

2. Teaching

Tutoring	**Year**	**Workload (ECTS)**
Experimental Surgery, BSc. course, University of Amsterdam	2012	2
Experimental Surgery, BSc. course, University of Amsterdam	2013	2
Experimental Surgery, BSc. course, University of Amsterdam	2015	2
Supervising	**Year**	**Workload (ECTS)**
Esther Bulle and Esther Nieuwenhuis, individual elective internship, MD program, Academic Medical Center, University of Amsterdam	2013-2014	2
Robert van Kooten, individual elective internship, MD program, Academic Medical Center, University of Amsterdam	2014	1

Robert van Kooten, bachelor thesis, MD program, Academic Medical Center, University of Amsterdam	2014-2015	0.5
Daniël Ernst, research internship, bachelor program, Higher Laboratory Education, Hogeschool Rotterdam	2014-2015	1
Maud Pijls, bachelor internship, Health and Life Sciences program, VU University, Amsterdam	2015	1
Massis Krekorian, master internship, Molecular and Cellular Life Sciences program, University of Utrecht, Utrecht	2015	1
Lionel Mendes Diaz, PhD internship, PhD program in Biomedicine, University of Beira Interior, Covilhã, Portugal	2015-2016	1
DJ van Doorn, Loïc Gorge, Jordi Heemskerk, Gideon Saelman, and Minne Schepers, bachelor thesis, MD program, Academic Medical Center, University of Amsterdam	2015-2016	1
3. Parameters of Esteem		
Awards and prizes		
Young Investigator Award, Society for Free Radical Research, Athens, Greece	2013	

List of publications

In this thesis

Enhancing photodynamic therapy of refractory solid cancers: combining second-generation photosensitizers with multi-targeted liposomal delivery
R. Weijer, M. Broekgaarden, M. Kos, R. van Vught, E.A.J. Rauws, E. Breukink, T.M. van Gulik, G. Storm, M. Heger
Journal of Photochemistry and Photobiology C: Photochemistry Reviews, 23, 2015, 103-131

Low-power photodynamic therapy induces survival signaling in perihilar cholangiocarcinoma cells
R. Weijer, M. Broekgaarden, R.F. van Golen, E. Bulle, E. Nieuwenhuis, A. Jongejan, P.D. Moerland, A.H. van Kampen, T.M. van Gulik, M. Heger
BMC Cancer, 15, 2015, 1014

Multi-OMIC profiling of survival and metabolic signaling networks in cells subjected to photodynamic therapy
R. Weijer, S. Clavier*, E.A. Zaal*, M.M.E. Pijls*, R.T. van Kooten*, K. Vermaas, R. Leen, A. Jongejan, P.D. Moerland, A.H.C. van Kampen, A.B.P. van Kuilenburg, C.R. Berkers[$], S. Lemeer[$], M. Heger[$]
Cellular and Molecular Life Sciences, 2016. doi:10.1007/s00018-016-2401-0

Inhibition of hypoxia inducible factor 1 and topoisomerase with acriflavine sensitizes perihilar cholangiocarcinomas to photodynamic therapy
R. Weijer*, M. Broekgaarden*, M. Krekorian, L.K. Alles, A.C. van Wijk, C. Mackaaij, J. Verheij, A.C. van der Wal, T.M. van Gulik, G. Storm, M. Heger
Oncotarget, 7, 2015, 3341-3356

Photodynamic therapy with liposomal zinc phthalocyanine and tirapazamine increases tumor cell death via DNA damage
M. Broekgaarden, R. Weijer, A.C. van Wijk, R.C. Cox, M.R. Egmond, R. Hoebe, T.M van Gulik, M. Heger
Journal of Biomedical Nanotechnology, 12, 2016

Other

Tumor cell survival pathways activated by photodynamic therapy: a molecular basis for pharmacological inhibition strategies
M. Broekgaarden, R. Weijer, T.M. van Gulik, M.R. Hamblin, M. Heger
Cancer and Metastasis Reviews, 2015, 1-48

Inhibition of hypoxia inducible factor 1 with acriflavine sensitizes tumor cells to photodynamic therapy with zinc phthalocyanine-encapsulating cationic liposomes.
M. Broekgaarden, R. Weijer, M. Krekorian, B. van den IJssel, M. Kos, L.K. Alles, A.C. van Wijk, Z. Bikadi, E. Hazai, T.M. van Gulik, M. Heger
Nano Research, 9, 2016, 1639-1662

Tranexamic acid-encapsulating thermosensitive liposomes for site-specific pharmaco-laser therapy of port wine stains
M.I. van Raath, R. Weijer, G.H. Nguyen, B. Choi, A.I. de Kroon, M. Heger
Journal of Biomedical Nanotechnology, 12, 2016, 1617-1640

*authors contributed equally
$shared senior authorship

A

Dankwoord

Prof. van Gulik, Thomas, allereerst bedankt dat u mijn promotor wilde zijn. Ik wil u ook graag bedanken voor uw hulp in de afgelopen vier jaar (bijna vijf), uw klinische visie op het project en de uiteindelijke afronding van het project.

Michal, de drijvende kracht achter dit project. Ik wil jou heel erg bedanken voor de kans die jij mij gaf om het PDT onderzoek uit te voeren. Het waren soms roerige tijden, maar ik denk dat het onderzoek veel interessante dingen heeft opgeleverd en nieuwe aanknopingspunten voor vervolgonderzoek. Bedankt voor jouw kritische blik, gedrevenheid, enthousiasme, steun, vertrouwen in mij en het hart dat je hebt voor het onderzoek. De kritische blik was wel even wennen in het begin. Zeker als je een manuscript opstuurt, deze vervolgens terug krijgt en denkt: "Ik had mijn tekst toch zwart opgemaakt?". Achteraf gezien ben ik hier gelukkig geen uitzondering in geweest.

Graag wil ik ook alle commissieleden, dr. Bonnet, prof. Eldering, prof. Ince, prof. van Laarhoven, dr. Rauws en prof. Sterenborg bedanken dat ze deel uit willen maken van mijn commissie.

Roomies

Mans, jij hebt de basis gelegd voor het project, heel erg bedankt daarvoor. Ook al zijn wij bijna twee tegenpolen, het heeft in ieder geval tot heel mooie dingen geleid! Ivo en Marcel, de ervaren heren op het lab. Bedankt voor de tijd waarin we samen op één kamer hebben gezeten. Jimme, de stoïcijnse werker met zijn fameuze Beats by Dre hoofdtelefoon. Het was een goede tijd. Kasia, de eerste vrouw op de kamer. Ik moest in het begin even wennen aan het hardop denken van jou, maar je hebt de tijd op het lab een stuk aangenamer gemaakt. Joost, ooit heb ik (stilletjes) gewenst dat je een cocon om je heen zou krijgen vanwege de vele telefoontjes die je kreeg. Ook al was je een beetje luidruchtig, je bleek uiteindelijk een heel leuke collega te zijn. Tot slot, de roomies waarmee ik mijn laatste tijd op het lab mee heb doorgebracht Pim, Julia en Zehra. Criticus Pim, bedankt voor het geouwehoer en de kritische blik naar alles en iedereen. Ik vond het leuk en gezellig dat je op de kamer zat. Julia en Zehra, ook al heb ik jullie minder goed leren kennen, ik vond het gezellig dat jullie er waren. Heel veel succes de komende tijd met jullie onderzoek.

Lab

Daarnaast zijn er een nog een aantal mensen van het lab die ik wil bedanken. Rowan en Megan (of Megwan, thanks to Michal) bedankt voor het samenwerken, de kritische houding en de fijne tijd. En Rowan, natuurlijk ook bedankt dat jij mij bij wil staan op 24 februari. Robert-Jan jij ook bedankt, zowel voor de samenwerking (virus project), het boek dat ik eigenlijk voor de start van mijn PhD moest lezen en je speech. Lionel, thank you for working together on the PDT project. You are probably one of

the kindest and modest people I know and I sincerely hope that everything works out with your PhD. Misschien heeft het wel met de plek in het lab te maken, maar rasoptimisten Floor en Eva bedankt voor de gezelligheid. Martien en Sebastiaan jullie ook bedankt voor alles. Succes allebei met de afronding van jullie promotie! Matthanja, bedankt voor de goede tijd en natuurlijk heel erg bedankt dat ik je huis kon overnemen. Ruurdtje en Vincent jullie ook heel erg bedankt, zowel voor advies voor experimenten, de nuchterheid, alswel de vele lunches die we samen hebben gehad. Albert, bedankt voor de gezelligheid, het overal een oplossing voor hebben als ik weer ergens tegen aan liep en natuurlijk de mogelijkheid om altijd een praatje te maken. Esther, jij ook bedankt voor de goede tijd, het orde op zaken stellen en je hulp. Lindy, party animal en PCR expert, ik zou denk ik wel een boek over je kunnen schrijven. Bedankt voor je hulp, je enthousiasme en gezelligheid, je fantantische uitspraken, de poffertjes met poeiersuiker en ik wens je heel veel succes toe in Utrecht. Adrie ~~M~~Baas, ik wil jou heel erg bedanken voor je expertise en hulp bij onze muizenexperimenten. Goos en Erik, jullie ook bedankt voor alles. Tot slot, Andrea heel erg bedankt voor het altijd klaar staan voor van alles en nog wat, de koekjes en de hulp bij de afronding!

Meer lab

Er zijn in de loop van de tijd heel wat studenten de revue gepasseerd. 'Chickies' Esther en Esther, jullie waren de eerste studenten op een vrij complex project. Bedankt voor jullie goede werk. Maud, de control freak, bedankt voor de gezelligheid, goede hulp en mooie data, ondanks een stageperiode van slechts vier maanden. Ilvana en Ali, de SRB experts, en Milan de DAMP man, ik heb jullie wat meer van de zijlijn begeleid, maar ik vond het fijn om met jullie samen te werken. Bas, bedankt dat je er was en ik hoop dat alles goed is afgelopen? En dan nu het rijtje studenten waarvoor één stage niet genoeg was: Massis, Robert, Daniël. Massis, de hardwerkende student die elke dag met de trein uit Deventer naar Amsterdam reist. Respect hoor. Dank voor je goede hulp en de soms fantastische uitspraken. Robert, je hebt gewerkt aan een vrij moeilijk project, maar ik vind dat je goed hebt doorgezet, ondanks de kritiek die je soms te verwerken kreeg. Daniël, 'de eeuwige student', bedankt voor het samenwerken en de vele vragen die ik te verwerken kreeg. Ik vond het leuk dat je er was en heel veel succes met de Master. Jaylen, de man van de deadlines, de Aziatische precisie, en de duizend en één cellijnen. Bedankt voor je inzet.

Projecten

Voor veel van onze projecten hebben we samen gewerkt met groepen uit het AMC als wel de Universiteit Utrecht. Allereerst wil ik Perry, Aldo en Antoine bedanken voor de goede samenwerking wat betreft alle bioinformatische aangelegenheden. Graag wil ik ook ik Joanne, Claire en prof. van der Wal bedanken voor de hulp met de pathologie van de perihilaire cholangiocarcinomen. Lisette P., bedankt voor je allround

hulp! Ook wil ik graag de mensen uit Utrecht bedanken voor jullie hulp en het gebruik maken van jullie lab. Prof. Killian, Toon, Eefjan, Martijn, Remko, Paulien, Saran, Jonas, bedankt! Simone, Celia, Séverine, Esther Z., het was fijn om met jullie samen te werken en bedankt voor de goede inzet bij onze OMICS paper. Yao, bedankt voor de hulp, de interesse, de gastvrijheid en de gesprekken die we hebben gehad!

Niet-werk

Tot slot wil ik de mensen bedanken waarmee het leven een stuk aangenamer is. Bedankt Martijn S., Mirjam, Martijn de V., Madelon voor de gezellige tijd, de evaluaties en de support! Ook wil ik iedereen bedanken uit Coevorden (ook jij Ellie), Dalen/ Amsterdam (dit wisselt af en toe), Amersfoort, Groningen en Goor voor de goede tijd, hulp waar het nodig was en uiteraard de ontspanning. Graag wil ik ook iedereen bedanken van mijn trainingsgroepje van Phanos voor de gezellige, leuke en goede trainingen waardoor je weer frisse moed krijgt. Last, but not least, Anne. Bedankt dat jij er bent. Ik wil je heel erg bedanken voor je eeuwige support, hulp, evaluaties, de bier en burgers bij iedere publicatie en het samen zijn! En, we hadden gewoon met zijn tweeën op één paper kunnen staan ;).

Biography

Ruud Weijer was born in Coevorden on July 7, 1987. After attending atheneum at De Nieuwe Veste in Coevorden, he started his first year of the Bachelor study Health and Life Sciences at Windesheim, Zwolle. Due to accreditation issues, he continued his second year at the VU University of Amsterdam. He obtained his Bachelor in Health and Life Sciences in 2009, after which he started the Master's Oncology program also at the VU University. He completed his first internship at the department of Pathology at the Cancer Center Amsterdam where he focused on the role of Epstein–Barr virus-encoded small RNAs and their putative transport mechanisms into exosomes. He performed a second internship at the Netherlands Cancer Institute where he screened three small molecule inhibitors targeting the RAS/RAF mitogen-activated protein kinase pathway as a new treatment for glioblastoma multiforme.

After obtaining his Master's degree in Oncology in October 2011, he started his PhD at the Academic Medical Center in Amsterdam in April 2012. Under the supervision of dr. Michal Heger and prof. dr. Thomas van Gulik he focused on novel strategies to enhance photodynamic therapy for the treatment of refractory solid cancers.